# Size and doping effect on the structure, transitions and optical properties of multiferroic BiFeO particles for photocatalytic applications

Xiaofei Bai

NNT : 2016SACLC013

# THESE DE DOCTORAT
DE
L'UNIVERSITE PARIS-SACLAY
PREPAREE A
CENTRALESUPELEC

ECOLE DOCTORALE N °573
Structures, Propriétés et Modélisation des Solides

Spécialité de doctorat : Sciences des Matériaux

Par

**M Xiaofei BAI**

## Effet de taille et du dopage sur la structure, les transitions et les propriétés optiques de particules du multiferroïque $BiFeO_3$ pour des applications photocatalytiques

**Thèse présentée et soutenue à Châtenay-Malabry, le 16 Février 2016**

**Composition du Jury :**

| | | |
|---|---|---|
| M | Raphaël HAUMONT | Président du jury |
| Mme | Catherine ELISSALDE | Rapporteur |
| M | Damien LENOBLE | Examinateur |
| M | Philippe PAPET | Examinateur |
| Mme | Ingrid CANERO INFANTE | Co-encadrant de thèse |
| M | Brahim DKHIL | Directeur de thèse |

université PARIS-SACLAY
ÉCOLE DOCTORALE
INTERFACES
Approches Interdisciplinaires : Fondements, Applications et Innovation

**Titre :** Effet de taille et du dopage sur la structure, les transitions et les propriétés optiques de particules du multiferroïque $BiFeO_3$ pour des applications photocatalytiques

**Mots clés :** $BiFeO_3$, multiferroïque, photocatalysis, propriétés optiques, nanoparticules

**Résumé :**

Ce travail de thèse expérimentale a été consacré à la synthèse par des méthodes de chimie par voie humide de nanoparticules à base du multiferroïque $BiFeO_3$ et à leur caractérisation, avec comme objectif finale des applications photocatalytiques. Ce matériau présente une bande interdite, avec un gap de ~2.6 eV, qui permet la photogénération de porteurs de charges dans le visible faisant ainsi de $BiFeO_3$ un système intéressant pour des processus photoinduits. Ce travail s'est en particulier focalisé à caractériser les propriétés de nanoparticules à base de $BiFeO_3$ en vue de comprendre l'effet de ses propriétés sur leur potentiel dans des applications liées à la photocatalyse. Tout d'abord, l'étude des effets de taille sur les propriétés structurales, de transitions de phase, et physicochimiques des particules a été réalisée, en gardant comme principal objectif de découpler les propriétés liées à la surface de celles du massif/coeur de la particule. Pour cela, une maîtrise et une optimisation des procédés de synthèse de particules aux échelles nanoet micromicrométriques de $BiFeO_3$ a été nécessaire pour obtenir des composés de taille variable et de très bonne qualité cristalline. Malgré la diminution de la taille des particules, on constate que, grâce au contrôle de paramètres de synthèse, nos nanoparticules présentent des propriétés très proches à celles du massif de $BiFeO_3$, gardant la structure rhomboédrique *R3c* avec des faibles effets de contrainte. Afin de contrôler indirectement par le dopage les propriétés optiques des composés à base de $BiFeO_3$, on a réussi à réaliser un dopage très homogène en $La^{3+}$, et un dopage partiel en $Ca^{2+}$, sur le site de $Bi^{3+}$. Les propriétés optiques des nanoparticules et leurs applications dans les premières expériences photocatalytiques sur la dégradation du colorant rhodamine B ont montré la complexité de la physicochimie de leur surface et du processus d'interaction lumièreparticule. Après analyse des données d'absorbance optique en fonction de la taille de nanoparticules, on observe que la bande interdite déduite pour ces différentes particules n'est pas le facteur prédominant sur les performances photocatalytiques. D'autres facteurs ont pu être identifiés comme étant à l'origine de la localisation de charges photogénérées, tels que des états de surface liés à une fine couche de peau ou skin layer sur les nanoparticules, présentant des défauts structuraux, une réduction de l'état d'oxydation du $Fe^{3+}$ vers le $Fe^{2+}$ et la stabilisation d'autres adsorbats, tels que FeOOH ; tous ces facteurs peuvent contribuer au changement dans les performances photocatalytiques. Les résultats photocatalytiques restent très encourageants pour poursuivre les études de nanoparticules à base de $BiFeO_3$, montrant une dégradation de la rhodamine B à 50% au bout de 4 h de réaction photocatalytique pour certaines des nanoparticules étudiées.

**Université Paris-Saclay**
Espace Technologique / Immeuble Discovery
Route de l'Orme aux Merisiers RD 128 / 91190 Saint-Aubin, France

**Title :** Size and doping effect on the structure, transitions and optical properties of multiferroic $BiFeO_3$ particles for photocatalytic applications

**Keywords :** $BiFeO_3$, multiferroics, photocatalysis, optical properties, nanoparticles

**Résumé :**

This experimental PhD work has been dedicated to the synthesis, by wet chemistry methods, and characterization of nanoparticles based on multiferroic $BiFeO_3$, with the aim of using them for photocatalytic applications. This material presents a bandgap of ~2.6 eV, which allows the charge carrier photoexcitation in the visible range, making $BiFeO_3$ a very interesting system for photoinduced processes. This thesis has been particularly focused on characterizing the properties of $BiFeO_3$ nanoparticles in view of understanding the relationship of their properties on their potential use for photocatalytic applications. First of all, the topic of the size effect on the structural properties, phase transitions, and physics and chemistry of the particles has been developed, keeping as first aim to separate the properties related to the surface from those arising from the bulk/core of the particle. To do so, the mastering and optimization of the synthesis processes of $BiFeO_3$ particles at the nano and microscale were needed, to finally obtain different size compounds with high crystalline quality. Despite the size reduction of the particles, we notice that, thanks to the control of the synthesis process, our $BiFeO_3$ nanoparticles present properties very close to those of the bulk $BiFeO_3$ material, keeping the rhombohedral structure *R3c* with weak strain effects. In order to indirectly tune the optical properties exploiting the doping, we have succeeded in realizing a homogenous $La^{3+}$ doping, and a partial $Ca^{2+}$ doping, on the $Bi^{3+}$ site. The optical properties of the nanoparticles and their use on the first photocatalytic experiments for degrading rhodamine B dye have shown the complexity of the physics and chemistry phenomena at their surface and of the light-particle processes. After analyzing optical absorbance data as a function of the particle size, we observe that the deduced bandgap for different particles is not the main parameter directing the photocatalytic performances. Other factors have been identified to be at the origin of the localization of the photoexcited charges, as the surface states linked to the skin layer of the nanoparticles, depicting structural defects, a reduction of the oxidation state of $Fe^{3+}$ towards $Fe^{2+}$ and the stabilization of other adsorbates, such as FeOOH; all these parameters may contribute to the change on the photocatalytic performances. The photocatalytic results are very encouraging, motivating to continue the study of $BiFeO_3$ based nanoparticles, though depicting a 50% rhodamine B degradation after 4 h of photocatalytic reaction using some of the present nanoparticles.

CentraleSupélec

**THÈSE**

Présentée par

Xiaofei BAI

**Pour l'obtention du**

**GRADE DE DOCTEUR**

**Spécialité:** Sciences des Matériaux

**Laboratoire d'accueil:** Structures, Propriétés et Modélisation des Solides

**SUJET:**

# Size and doping effect on the structure, transitions and optical properties of multiferroic $BiFeO_3$ particles for photocatalytic applications

Devant un jury compose de :

| | | |
|---|---|---|
| Mme | Ingrid CANERO INFANTE | Co-encadrant de thèse |
| M | Brahim DKHIL | Directeur de thèse |
| Mme | Catherine ELISSALDE | Rapporteur |
| M | Raphaël HAUMONT | Rapporteur |
| M | Damien LENOBLE | Examinateur |
| M | Philippe PAPET | Examinateur |

## Acknowledgements

First of all I would like to thank my supervisor Dr. Brahim DKHIL for giving me the opportunity and freedom to work with this project. His enthusiasm, his confidence in my work and his broad knowledge of materials science has been an invaluable source of encouragement and motivation. I am also grateful to my co-supervisor Dr. Ingrid CANERO INFANTE for her support and valuable comments to my work. Most of the work of this subject is finished under her guidance. Her insight and complementary perspective as a physicist have been very important to me.

I would like to thank everyone in SPMS for making it such a wonderfully diverse, inspiring and fun environment to work in. Especially Pascale SALVINI, Christine BOGICEVIC and Fabienne KAROLAK, Gilles BOEMARE, Nicolas GUIBLIN and Hubert JUBEAU, Christine VINEE-JACQUIN and Pascale GEMEINER, Pierre-Eymeric JANOLIN, Guihem DEZANNEAU.

I am indebted to the PhD and Post doc in SPMS: Fabien BRIEUC, Désirée CIRIA, Charles PAILLARD, BoBo TIAN, WenJing LI, ChenYi LI, Yang LIU, XiaoXuan SHI, Halyna VOLKOVA, Ze Yin YAN, Zheng Yu ZHANG and also Charlotte COCHARD, Anastasia IAKOVLEVA who have graduated in 2015. A big thank you goes to my former and present office mates Gentien THORNER, Romain FAYE and Cintia HARTMANN for all our numerous non-scientific discussions and brakes.

I thank Dr. Soma SALAMON at University of Duisburg-Essen for the one week very enjoyable days for intense learning Mössbauer and magnetic properties. I would also like to thank Prof. Wei jie at Xi'an jiaotong University for our ongoing collaboration. We meet in SPMS and discuss everyday for scientific questions.

In my PhD period, I have also had the joy of my friends, they help me familiarize the French life and help me solve lots of problems. Thank you, Zhao hang and Shen chen.

I have spent three wonderful years in France, and I own that to all my friends here, thank you, all of you! Finally, I would like to thank my parents and my wife for their encouragement and support.

## Table of contents

Table of contents ..... I
List of abbreviations ..... V
1 Background and motivation ..... 1
2 Aim of the present work ..... 3
3 Introduction to ferroics and their photo-induced properties ..... 5
3.1 Short overview on ferroic pervoskite oxides ..... 5
3.1.1 Ferroelectricity ..... 5
3.1.2 Ferromagnetism ..... 7
3.2 Photo-induced properties in ferroelectrics ..... 9
3.3 $BiFeO_3$: room temperature photomultiferroic ..... 13
3.3.1 General introduction to $BiFeO_3$ ..... 13
3.3.2 Light phenomena related to $BiFeO_3$ ..... 15
3.3.3 Photocatalysis and $BiFeO_3$ ..... 20
4 Experimental ..... 23
4.1 State of art on the synthesis of $BiFeO_3$ powders ..... 23
4.2 Pure $BiFeO_3$ and doping samples for nano and microparticles: Optimizing wet chemical methods and solid state method. ..... 25
4.2.1 Wet chemical synthesis of nano crystalline $BiFeO_3$ ..... 25
4.2.2 Synthesis of bulk $BiFeO_3$ by solid state methods ..... 28
4.3 Characterization techniques ..... 29
4.3.1 X-ray diffraction and analysis using Rietveld refinement ..... 29
4.3.2 Raman spectroscopy ..... 31
4.3.3 X-ray photoelectron spectroscopy (XPS) ..... 32
4.3.4 Electron Microscopy techniques ..... 33
4.3.4.1 Scanning Electron Microscopy ..... 33
4.3.4.2 Transmission Electron Microscopy and related techniques ..... 34
4.3.5 Thermal analysis ..... 36
4.3.6 Magnetic measurements ..... 36
4.3.6.1 Vibrating sample magnetometry ..... 36
4.3.6.2 Mössbauer spectroscopy ..... 37

4.3.7 Optical properties ..... 38
4.3.7.1 Diffuse reflectance ..... 38
4.3.7.2 Kubelka-Munk theory and Tauc plot for band structure investigation ..... 38
4.3.7.3 Urbach analysis ..... 39
4.3.8 Photocatalysis ..... 40
5 Synthesis of $BiFeO_3$ compounds ..... 43
5.1 $BiFeO_3$ with nano particle size synthesized by wet chemical methods ..... 43
5.2 Crystal growth mechanisms of different size $BiFeO_3$ ..... 50
5.3 Nanostructure through Electron Microscopies ..... 55
5.4 Results on the synthesis of A-site doped $BiFeO_3$ samples comment size in this part ..... 58
5.5 Conclusion ..... 60
6 Structure, electronic/chemical states and magnetic properties of $BiFeO_3$ particles ..... 61
6.1 X-ray diffraction results ..... 61
6.1.1 X-ray diffraction results of nano-$BiFeO_3$ ..... 61
6.1.2 X-ray diffraction results of A-site doped nano-$BiFeO_3$ ..... 66
6.1.3 Temperature dependence of X-ray diffraction results of different size $BiFeO_3$ particles ..... 70
6.2 Raman spectra for different size $BiFeO_3$ ..... 73
6.2.1 Room temperature Raman spectra of $BiFeO_3$ nanoparticles ..... 74
6.2.2 Temperature dependence of $BiFeO_3$ Raman spectrum ..... 79
6.2.3 Raman spectra of A-site doped $BiFeO_3$ particles ..... 83
Nanostructure through Electron Microscopies ..... 91
6.3 ..... 91
6.3.1 High Resolution Scanning Transmission Electron Microscopy for atomic scale structural characterization ..... 91
6.3.2 Chemical analysis of pure $BiFeO_3$ and 10% La doped $BiFeO_3$ nanoparticles by Electron Energy Loss Spectroscopy ..... 94
6.3.3 Surface chemical states from X-ray photoelectron spectroscopy ..... 96
6.4 Magnetism from magnetometry and Mössbauer spectroscopy ..... 99
6.4.1 Magnetometry ..... 99

6.4.2 Mössbauer spectroscopy ..... 103
6.5 Conclusion ..... 105
7 Light interaction with $BiFeO_3$ particles ..... 107
7.1 Mechanisms for charge transition in $Fe^{3+}$ oxides ..... 107
7.1.1 $Fe^{3+}$ ligand field transitions or $Fe^{3+}$ *d-d* transitions ..... 107
7.1.2 Pair excitations or double exciton processes ..... 110
7.1.3 Ligand to metal charge-transfer transitions ..... 110
7.1.4 Band edge and narrow *d* bands ..... 110
7.2 Optical properties of pure $BiFeO_3$: effect of particle size and temperature 111
7.2.1 Room temperature behavior ..... 111
7.2.2 High temperature behavior ..... 120
7.2.3 Band gap as a function of temperature for $BiFeO_3$ nano and microparticles ..... 129
7.2.4 Low energy *d-d* transition as a function of temperature for $BiFeO_3$ nano and microparticles ..... 137
7.3 Optical properties of A-site doped $BiFeO_3$ ..... 140
7.3.1 Low energy *d-d* transition as a function of temperature for A-site doped $BiFeO_3$ nano and microparticles ..... 140
7.3.2 Band gap as a function of temperature for A-site doped $BiFeO_3$ microparticles ..... 143
7.4 Conclusion ..... 146
8 Photocatalysis using $BiFeO_3$ nanoparticles on Rhodamine B dye ..... 149
9 Summary ..... 159
References ..... 161

## List of abbreviations

| | |
|---|---|
| AFM | Antiferromagnetic |
| DFT | Density functional theory |
| DM | Dzyaloshinskii-Morlya |
| DSC | Differential scanning calorimetry |
| EELS | electron energy loss spectroscopy |
| EG | Ethylene glycol |
| FC | Field cooling |
| FE | Ferroelectric |
| FWHM | Full width at half maximum |
| HS | High spin |
| HTXRD | High temperature X-ray diffraction |
| K-M | Kubelka-Munk |
| LS | Low spin |
| PLZT | $PbLa_xZr_{1-y}Ti_yO_3$ |
| RhB | Rhodamine-B |
| SEM | Scanning electron microscopy |
| STEM | Scanning transmission electron microscopy |
| TA | Tartaric acid |
| VSM | Vibrating sample magnetometry |
| XPS | X-ray photoelectron spectroscopy |
| XRD | X-ray diffraction |
| ZFC | Zero field cooling |

# 1 Background and motivation

The development of modern technology based on multifunctional materials is opening the path to new applications answering to continuous technological challenges. As one of the potential materials, complex oxide materials are of particular interest since they exhibit a fascinating range of behaviors: from colossal magnetoresistance and high temperature superconductivity to ferroelectricity and mutiferroicity. This made them capable to possess many different phase transition related to this different properties (ferromagnetic, ferroelectric, metal-to-insulator, and superconducting). The multifunctional character of such materials brings the possibility of unusual response to external stimuli that can be exploited for instance in the framework of conversion of electric stimuli in magnetic response, *i.e.* the magnetoelectric effect. In these oxide materials, it exists an intimate relationship between structure and properties, making oxides more sensitive to crystalline structure, strain or shape conditions. As a novel application, multifunctional oxides have recently attracted attention as candidates for their use in photoactive devices using the coupling of light absorption with other functional properties, such as photovoltaicity, photoelasticity and photocatalysis, capable to provide photo-excited carriers used for different purposes.

Actually, the environmental pollution as well as the lack of sufficient clean and nature energy resources are some of the most serious problems faced on a global scale. Photocatalytic processes, in which the inexhaustibly abundant, clean, and safe energy of the sun can be harnessed for sustainable, nonhazardous, and economically viable technologies, are a major advance in this direction. Semiconductor photocatalysis has received much attention as a real solution for counteracting environmental degradation. As one of the pioneer photocatalytic materials, titanium oxide $TiO_2$ materials have shown great potential as ideal and powerful photocatalysts due to their chemical stability, nontoxicity, high reactivity, and large light absorption wavelength scale. Intense research has been carried out on $TiO_2$ photocatalysis, which has been focused on understanding the fundamental principles, enhancing the photocatalytic activity, and expanding the scope of

application. Unfortunately, $TiO_2$ is not ideal for all purposes and performs rather poorly in processes associated with solar photocatalysis due to its wide band gap (~3.2 eV). During the past decade, much effort has been devoted to exploit other semiconductor oxide as novel photocatalytic materials.

One kind of these oxide materials that has come into sight gradually are multiferroics. Considered as semiconductors and directly compared to $TiO_2$, similarities can be found such as the band gap values and structural characteristics, since the existence of octahedral cages centered on transition metal ions is a basic brick in both systems. Moreover, in multiferroics presenting ferroelectric order, a spontaneous electric polarization may promote an electrically tunable separation of the photo-exited carriers, making them movable to the surface for easily interact and react with molecules or other particles in the surrounding media. Within these mutiferroic materials, bismuth ferrite ($BiFeO_3$), with perovskite structure, is one of the most promising materials exhibiting interesting properties. $BiFeO_3$ is a room temperature multiferroic presenting coexistence of ferroelectricity, characterized by a strong polarization value and very high Curie temperature, and an antiferromagnetic order with high Néel temperature. Added to its great potential in spintronics and other magnetoelectric and strain mediated applications, though exhibiting ferroelasticity, it has been recently at the focus of large interest though a photovoltaic effect has been reported in $BiFeO_3$ systems. Besides, $BiFeO_3$ band gap value being lower than other ferroelectric materials, it has been expected a larger photon efficiency and enhanced interaction with electrons/holes. These properties of $BiFeO_3$ have opened a new field for photo-induced properties.

$BiFeO_3$ has obvious future potential for technological applications. However, several fundamental questions still remain unsolved and the present work has been developed in such direction. Additionally, with the development of different synthesis routes, it will be possible to design and create different shapes, composites, core shells or decoration based on this multiferroic material, with the objective of obtaining more suitable systems presenting enhanced thermodynamic and chemical compatibility and directed to respond to different photocatalytic issues. These factors are crucial for fabrication and integration of these materials into devices.

## 2 Aim of the present work

The aim of this work is the synthesis and characterization of $BiFeO_3$ based compounds using soft chemistry routes, in particular a wet chemistry. In the framework to understand the potential photocatalytic properties in these compounds, this work has been focused on studying the surface, structure and physico-chemical effects by playing with the (nano)particle size and the doping on the Bi-site. Micrometric samples were in parallel studied as a reference state for the nanosized samples results. The main objective of this work is thus to unveil the relationship between photocatalytic properties and band structure, optically driven charge transition of different size $BiFeO_3$ powders.

Wet chemical synthesis and traditional solid state route are used for obtaining high quality $BiFeO_3$ nano and micro particles. Optimized synthesis processes are obtained through thermal analysis and the crystalline growth mechanisms are presented.

Band structure and optically driven charge transition of different size samples at room temperature and high temperature are investigated. These results help understanding the photocatalytic of these samples through deducing not only the optical bandgap but also other charge transitions producing localized carriers. Photocatalytic properties of different size $BiFeO_3$ are studied at visible light range and the photocatalytic mechanisms are explained in view of the band structure information determined from optical characterization. Moreover, in a more fundamental approach, the investigation of these optical properties as a function of temperature has been carried out, contributing to understand the physics of $BiFeO_3$ compounds.

The new results reported in this work are classified into four chapters:

5 Synthesis of $BiFeO_3$ compounds;

6 Structure, electronic/chemical states and magnetic properties of $BiFeO_3$ particles;

7 Light interaction with $BiFeO_3$ particles;

8 Photocatalysis using $BiFeO_3$ nanoparticles on Rhodamine B dye.

# 3 Introduction to ferroics and their photo-induced properties

## 3.1 Short overview on ferroic pervoskite oxides

Generally speaking , multiferroics are defined as materials that exhibit more than one ferroic order parameter simultaneously[1]. The ferroic (or anti-ferroic) order parameters include the polarization, the magnetization and the deformation. In multiferroics they can coexist and potentially couple[2-4]. All ferroelectric materials that display a spontaneous polarization switchable under an electric field are intrinsically multiferroic as they are also usually ferroelastic. Indeed the ferroelectricity is related to the splitting of the barycenter of positive and negative charges in the unit cell, which induces the unit cell deformation[3, 5]. Nevertheless when dealing with multiferroics, usually people have in mind materials within which polarization and magnetization coexist. As a matter of fact, when the polarization and magnetization couple the multiferroic becomes magnetoelectric and can be useful for applications, as instead of using a magnetic field and thus a current to switch the magnetization, one can rather use an electric field and thus a voltage which is much favorable from energy consumption point of view..

### 3.1.1 Ferroelectricity

To be ferroelectric, a material should exhibit a switchable spontaneous polarization, which gives rise to an hysteresis loop of the polarization versus the applied electric field. The ferroelectricity appears from the centrosymmetric paraelectric state below a critical temperature $T_c$, the Curie temperature. As a result a peak in the dielectric susceptibility associated to the appearance of the polarization takes place at $T_c$. As stressed above, the ferroelectricty appears by symmetry breaking (loss of the inversion symmetry) and is thus linked to the structure modifications. The structure of interest in this thesis work is the perovskite. Such structure presents a wide spectrum of properties: superconductor to insulator, magnetism, ferroelectricity, piezoelectricity, dielectric, ionic conductivity, ... It is therefore an important structure of technical as well as fundamental interest. For instance, the perovskite structure is one of the most technologically important classes of ferroelectric materials. The

perovskite oxides has the general chemical formula $ABO_3$, where A and B are cations with various charges, spins and radii expalining the plethora of properties related to this structure. It consists of a network of corner-linked $BO_6$ octahedra, within which is enclosed the large A cation[6-7]. The basic criteria for the structure to be stable is that the valence of the ions should balance and that the ionic radii meet the Goldschmidt criteria[8-9] though the tolerance factor *t* which is defined by:

$$t = \frac{r_A + r_O}{\sqrt{2}(r_B + r_O)},$$

where $r_x$ is the ionic radii of the *X* cation. The structure will be stable with $0.85<t<1.05$.

The prototype non-polar perovskite unit cell is cubic and belongs to the space group $Pm\bar{3}m$ and is shown in Figure 3.1 (a). In conventional ferroelectric perovskites, the shift in the cation sublattice relative to the anion sublattice causes a net polarization. Figure 3.1 (b), (c) and (d) show the displacement along [001], [110], [111] inducing tetragonal, orthorhombic and rhombohedral unit cell respectively.

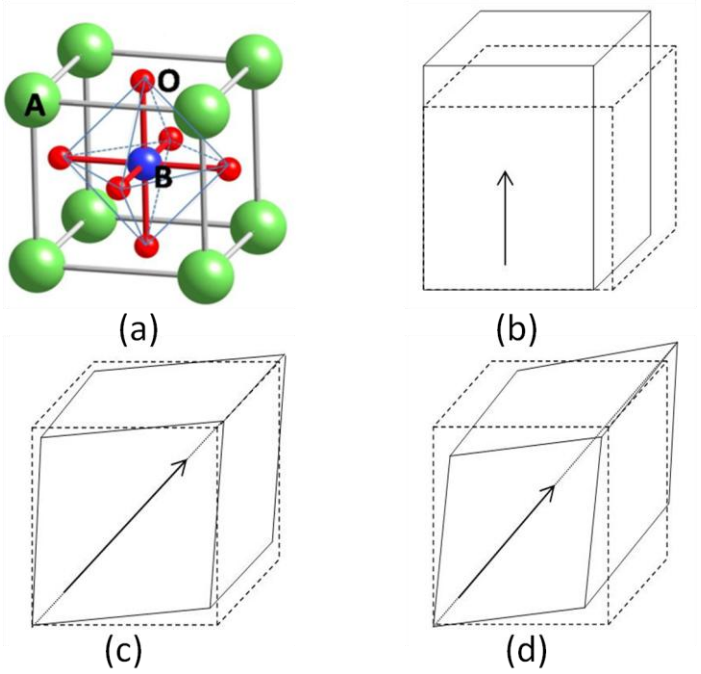


Figure 3.1 Classical perovskite unit cell ($ABO_3$ structure). (b), (c) and (d) are the tetragonal, monoclinic and rhombohedral distortion of the cubic unit cell, respectively. The arrows indicate the direction of polarization for each of the distortions.

Ferroelectric perovskites are usually considered as ionic compounds being $A^{1+}B^{5+}(O^{2-})_3$, $A^{2+}B^{4+}(O^{2-})_3$ or $A^{3+}B^{3+}(O^{2-})_3$[6, 10-12]. Although the covalent contribution to bonding is small, it has been shown theoretically, for example for $BaTiO_3$ or $KNbO_3$, that the reason of the displacement of the cation sublattices is linked to a covalent bonding between O 2*p* and B 3*d* electrons[13]. As a result when removing this covalent bond contribution, the ferroelectricity vanishes. In lead-based or bismuth-based perovskites, there is a the so-called "lone pair" of electrons which involves hybridization of the n$s^2$ and $p^0$ orbitals of $Pb^{2+}$ or $Bi^{3+}$ that can stabilize the distorted structure[14-16] and can lead to displacive distortions[13, 17-18].

The strong sensitivity of ferroelectrics to chemistry, defects, electrical boundary conditions and mechanical stresses arise from a delicate balance between long-range Coulomb forces (which favour the ferroelectric state) and short-range repulsions (which rather favour the non-polar cubic structure)[19-20]. In general, for ferroelectric perovskites, hybridization between B cation and O is essential to weaken the short-range repulsions and allow the ferroelectric transition[2, 21]. The A cation can also hybridize as we already mention, leading indirectly to change the B-O interactions and modify the ground state and nature of the transition[2, 22].

### 3.1.2 Ferromagnetism

The field created by a magnet is associated with the motions and interaction of its electrons. Electricity is the movement of electrons, so each atom represents a tiny permanent magnet in its own right[23-24]. The circulating electron produces its own orbital magnetic moment, and there is also a spin magnetic moment because the electron itself spins[1, 25]. In most materials, these magnetic moments cancel each other out with each electronic magnet compensating the field produced by another[23, 26]. From Figure 3.2, it can be seen that the total magnetic moment is caused by spin magnetic moment and orbital magnetic moment[27].

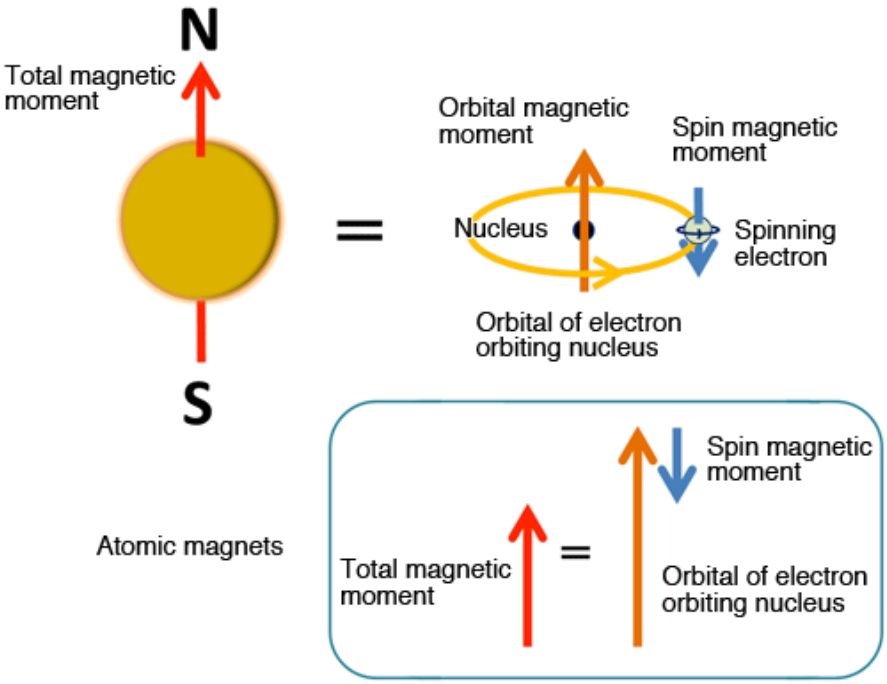


Figure 3.2 The orbit of a spinning electron about the nucleus of an atom

As in ferroelectrics, ferromagnetics exhibit an hysteresis loop of the magnetization versus magnetic field (in case of ferroelectrics, it is polarization versus electric field) as shown in Figure 3.3 with a coercive field $H_c$, a remanent $M_r$ and saturation $M_s$ magnetization. [28].

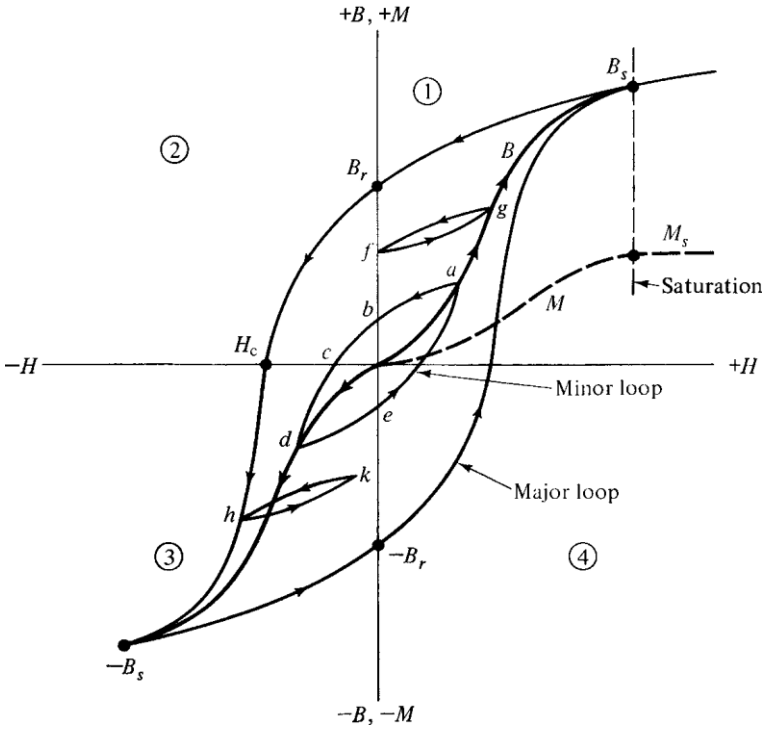


Figure 3.3 Ferromagnetization curves and hysteresis loop.

Depending on the exchange interactions between spin moments of each magnetic ion, several magnetic ordering can be observed. Basically in the perovskite structure, the spin on the B cations may couple through oxygen anions by the electron transfer mechanism known as superexchange[29-30] and lead to antiferromagnetic arrangement while double exchange interaction between B-B cations favours a ferromagnetic state[31-32]. Superexchange between $e_g$ orbitals is stronger than superexchange between $t_{2g}$ orbitals ; degeneracy of the *d* orbitals are lifted in an octahedral crystal field[13]. For perovskites with tilted $BO_6$ octahedra the B-O-B angle is smaller than 180°[6], leading to a less overlap of the O 2*p* and B *d* orbitals. The Néel temperature ($T_N$) associated to the antiferromagnetic ordering is then related to the B-O-B angle[33-34]. Therefore with decrease of B-O-B angle, $T_N$ increases[34-37]. For instance, a hydrostatic pressure can increase the overlap of B-O-B angle and then $T_N$ can increase[38-39].

## 3.2 Photo-induced properties in ferroelectrics

The ferroelectric properties are usually considered to be sensitive to change of temperature, pressure, electric field, strain or chemical composition. Recently, fostered by energy and environment concerns, photo-induced properties in ferroelectric have attracted much more attention. The intrinsic component which is the spontaneous polarization in ferroelectric materials may serve as an internal electric field to separate the photogenerated charge carriers. As a matter of fact, in contrast to traditional semiconductor solar cell[40] where the internal field is located at the p-n junction, the internal field in ferroelectric exist within the whole ferroelectric domain. This is directly related to the so-called anomalous or abnormal bulk photovoltaic effect[46]. When a non-centrosymmetry material (it is the case for ferroelectrics) is illuminated with uniform light wavelength corresponding to the absorption edge of the material, a steady photocurrent is generated[41]. This phenomenon is different from the mechanism involved in *p-n* junction of semiconductors[42]. The bulk photovoltaic effect correspond to a third rank tensor and depends on the light polarization[41, 43]. Therefore, it disappears in the paraelectric phase[41, 43-44]. It is believed that because of the non-centrosymmetry, the probability

for the photogenerated carriers to move from k to k' momentum is different from that to move from k' to k (such probability is the same in centrosymmetric systems) and therefore a shift current can be photogenerated. It is worth mentioning that in addition to the above described bulk photovoltaic, it has been also proposed that the domain wall contribute to the photocurrent[45-46]. Indeed, because the bounding charges are not fully compensated at this domain-to-domain interface, it appears an internal field (resembling to that of the p-n junction) which helps to photogenerate charges. It is not clear yet if this mechanism does exist or if it is not rather related to some point defect like oxygen vacancies. There is still a strong controversy on this aspect and today the existence as well as the contribution of both mechanisms is still actively debated.

Figure 3.4 illustrates a possible model for anomalous photovoltaic effect for $Pb_{1-x}La_x(ZrTi)O_3$ ceramics[47]. The energy band is basically generated by the hybridization of oxygen *p*-orbitals with the *d*-orbitals of Ti/Zr. The donor impurity levels (La doping) are present slightly above the valence band. The transition from these levels with the asymmetric potential due to the crystallographic anisotropy may provide a preferred momentum to the electron. The electromotive force is generated when electrons that are excited by the light move in a certain direction of the ferroelectric crystal (spontaneous polarization)[48].

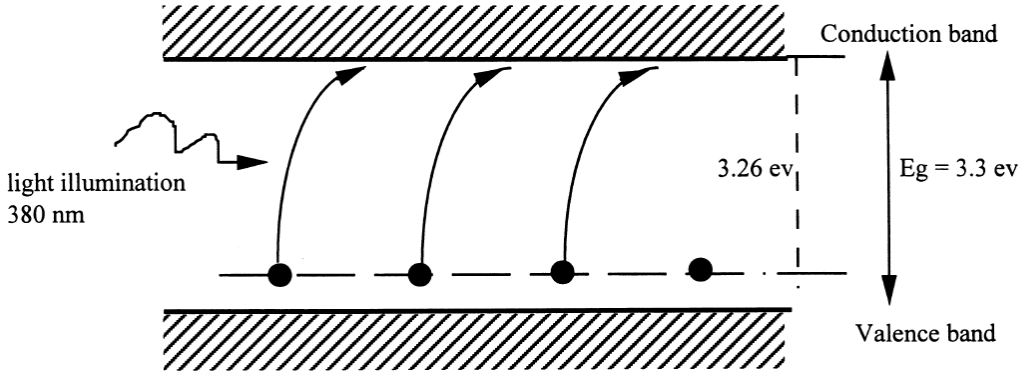


Figure 3.4 Energy band gap model of excited transition from impurity level in PLZT.

Finally, for typical perovskite structure ($ABO_3$), the excitation across the band gap is in the most often cases a charge transition from the oxygen (O) 2*p* states at the valence band maximum to the transition metal *d* states at the conduction band

minimum[47]. Owing to a large difference in electronegativity between oxygen and transition metal atoms, the band gap is usually quite large (3-5 eV).

The main features of the photovoltaicity in ferroelectrics can be presented as follow[41, 43, 47, 49-52]: (1) This effect appears in poled uniform single crystals or ceramics with noncentrosymmetry and is entirely different in nature from the *p*-*n* junction effect observed in semiconductors. (2) Constant photo current and voltage are generated in the spontaneous polarization direction under uniform illumination in the ferroelectric phase and disappears in the paraelectric phase. (3) The magnitude of the photoinduced voltage is proportional to crystal length along the polarization direction and is much greater than the band gap energy of the crystal.

Another important potential application of ferroelectrics concerns their photocatalytic properties. From the point of view of semiconductor photochemistry, the photocatalysis is used to accelerate the redox reaction through the irradiation of semiconductor, as shown in Figure 3.5. If the ferroelectric material with a reasonable band gap is irradiated by a light, the separation of electron-hole pairs happened[48, 53]. Due to the spontaneous polarization in the ferroelectric, it can prevent the electron-hole recombination, improve the migration of the carriers towards the surface of the particle and thus can permit to enhance the photocatalytic activity[47, 54]. The band edge position of common materials which have been used in photocatalysts are presented in Figure 3.6. The left side of the figure indicates the energy position of the bands for some given and common semiconductors. The band position of siliver halides have also been included as they are usually used in redox reaction for Ag nano-particles. In the middle of the figure the work function of some common noble metals are shown, while some typical redox group are given in the right side of the figure.

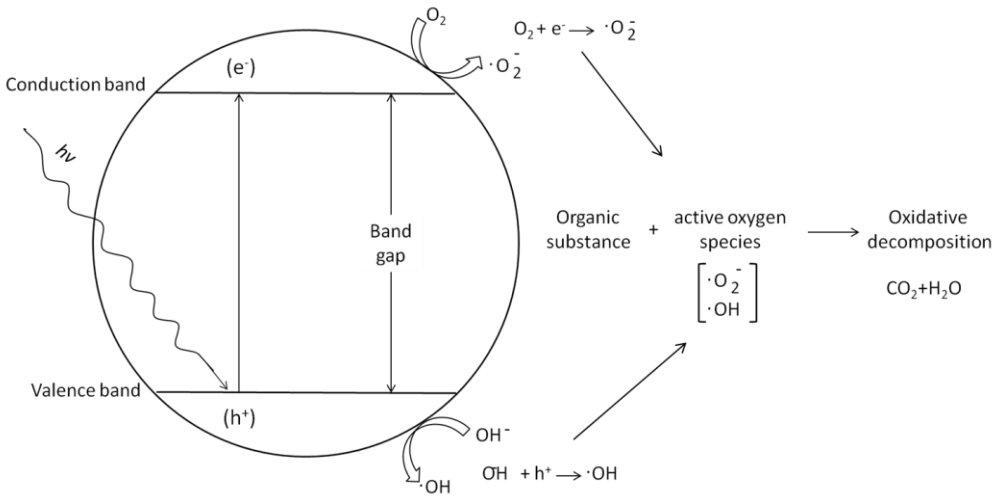


Figure 3.5 Principles of oxidative decomposition of photocatalysts. After it undergoes illumination, charge carrier of photo-generation in a photocatalytic material is separated. Valence band hole and conduction band electrons are represented by $h^+$ and $e^-$.

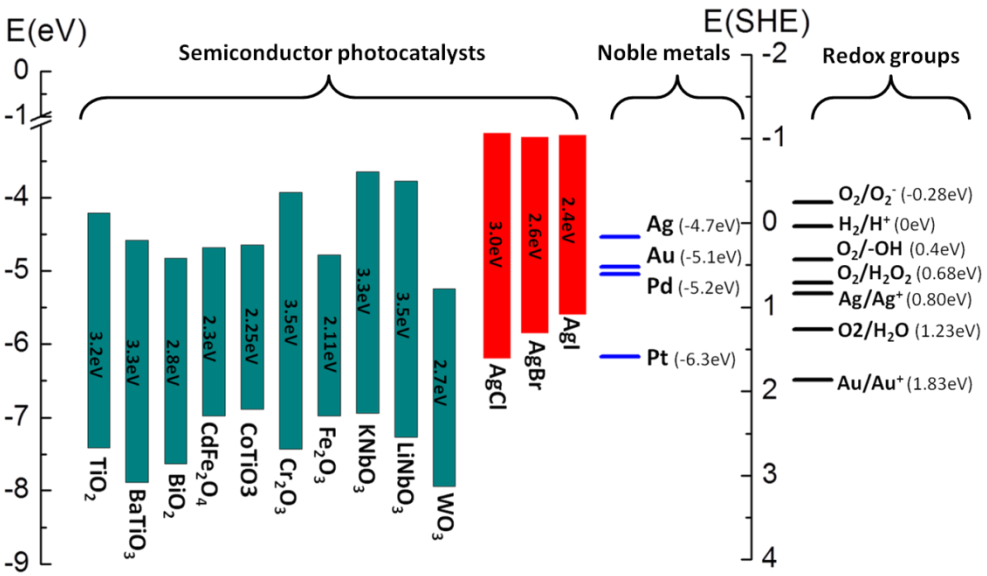


Figure 3.6 Energy band position of common semiconductor materials in photocatalysis, the work function of noble metals, and the electrochemical potentials of redox groups

For a fully polarized particle, the spontaneous polarization produces positive bound charges on the $C^+$ surface and negative bound charges on the $C^-$ surface (Figure 3.7). In turn, these bound charges if not fully screened by the external charges at the surface, like for instance adsorbed species, produce a depolarization field that makes the inner free electrons to move from the $C^-$ surface to $C^+$ one. After photo-induced charge carriers creation, the internal electric field moves the electrons to the $C^+$

surface and the holes towards $C^-$ surface. It results in an accumulation of positive and negative charges that takes place at different surfaces, a band bendingoccurs.

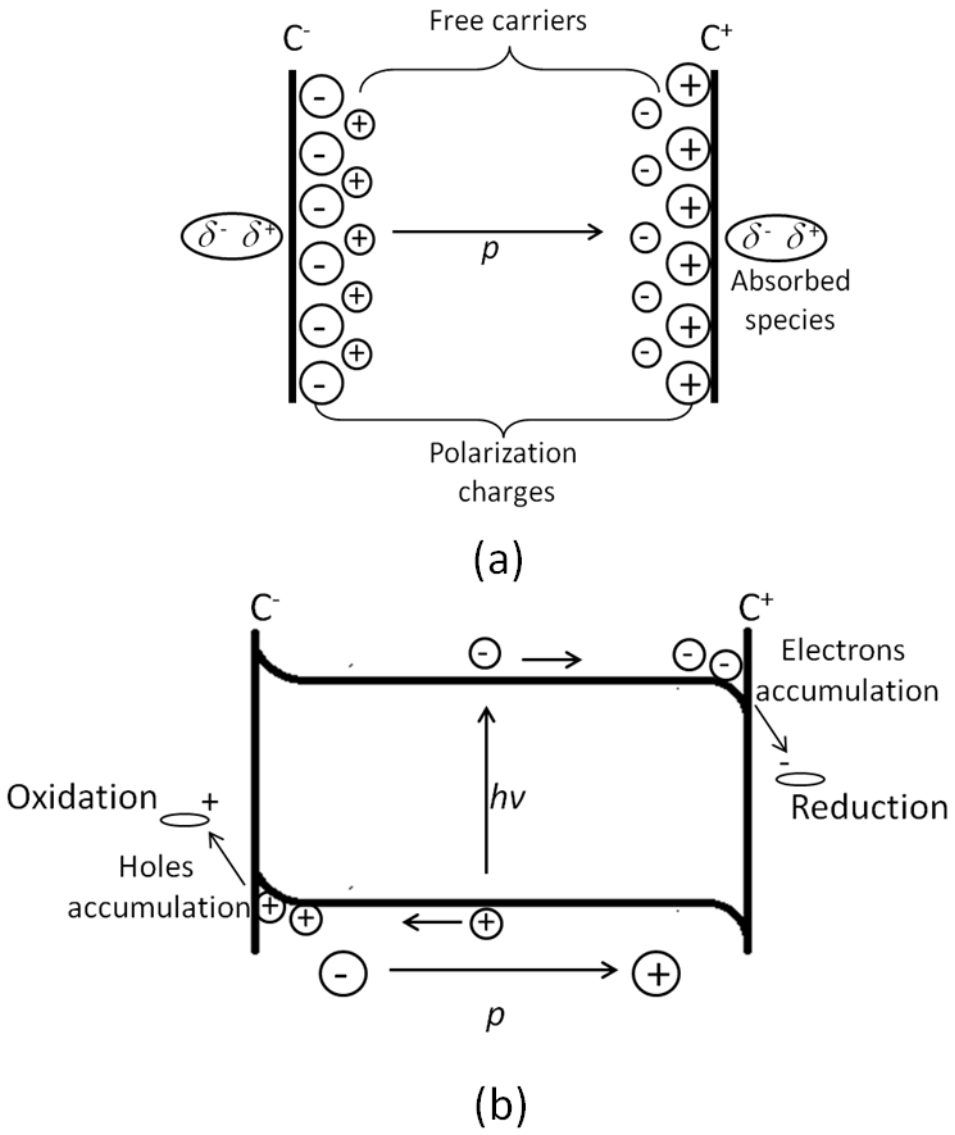


Figure 3.7 Schematic of ferroelectric materials in which (a) exists the spontaneous polarization fields and depolarization field causing by free carriers and external absorbed species and (b) the reorganization of free carrier and the band structure in ferroelectric materials.

## 3.3 $BiFeO_3$: room temperature photomultiferroic

### 3.3.1 General introduction to $BiFeO_3$

$BiFeO_3$ is a room temperature multiferroic exhibiting simultaneously a ferroelectric state with a strong polarization up to 100 $\mu C/cm^2$ and an antiferromagnetic order which is superimposed to a long period cycloidal modulation[33]. Because of its multiferroic properties coexisting at room temperature, it has attracted a great

attention leading to interesting magnetoelectric coupling as well as the possibility to tune its properties by various external parameters such as temperature, pressure, electric and magnetic field, light, and so on[55-57]. Light interaction with these order parameters in $BiFeO_3$ has been studied through photovoltaic and photostriction effects[49, 58-59]. Structural details and the physical properties of $BiFeO_3$ are shown in Table 3.1.

Table 3.1 Structure and physical properties of $BiFeO_3$

| Property | Value | Ref |
|---|---|---|
| Crystal system[a] | Trigonal | 60 |
| | $a_{rh}$=5.6364 Å, $\alpha_{rh}$=59.348° | 60-62 |
| | $a_{hex}$=5.5787 Å, $c_{hex}$=13.8688 Å | |
| | $a_{pc}$=3.965 Å, $\alpha_{pc}$=89.35° | |
| Space group | R3c | 60 |
| Tolerance factor[b] | $t$=0.89 | |
| Polyhedral volume retio | $V_A/V_B$=4.727 | 63 |
| Density | 8.40 g/cm$^3$ | |
| Thermal expansion | Non-linear and anisotropic | 64-65 |
| Ferroelectricity | $T_C$=820-830 °C | 66-67 |
| Polarisation[c] | 90-100 $\mu$C/cm$^2$ | 68-72 |
| Dielectric constant | $\varepsilon_r$=30 | 73 |
| Antiferromagnetism | Canted G-type, $T_N$=370 °C | 62 |
| Piezoelectricity | D33=15-60 pm/V | 68, 71-72 |

[a]Trigonal crystals can be represented with rhombohedral, hexagonal or pseudocubic unit cell axes and lattice parameters.
[b]Assuming six-coordinated high spin $Fe^{3+}$ and eight-coordinated $Bi^{3+}$ with ionic radii from Shannon.
[c]Inferred from measurements on thin film, single crystals, bulk ceramics and Berry phase calculations.

The structure of $BiFeO_3$ can be characterized by two distorted perovskite blocks connected along the pseudocubic <111> direction, to build a rhombohedral unit cell[33]. In this structure the two oxygen octahedral of the cells connected along the <111> are rotated clockwise and counterclockwise around the <111> by ±13.8° and the Fe ion is shifted by 0.135 Å along the same axis away from the oxygen octahedron center position[74]. $Bi^{3+}$ plays the major role in the origin of ferroelectricity[75]. Bi ion has outer 6*s* electrons that do not participate in chemical

bonds and it has a high polarizability. The rotation angle of the oxygen octahedral is one of the very important parameter. When use the Goldschmid tolerance factor using the ionic radii of Shannon gives a value of $t$=0.88 has been obtained[76], which means the A cation is too small to fill the 12-coordinated void between $BO_6$ octahedra, the perovskite structure accommodates this size mismatch by tilting the octahedral to reduce the size of the dodecahedron. In $BiFeO_3$, the tilting of oxygen octahedral is direct related to Fe-O-Fe angle, $\theta$=ca.154-156°[77]. The Fe-O-Fe angle can modify the magnetic exchange and orbital overlap between Fe and O, and then it can affect the magnetic ordering temperature and the conductivity[78]. In terms of symmetry groups, the polar displacement alone would reduce the symmetry from cubic $Pm\bar{3}m$ to rhombohedral $R3m$[79], the rotation of the $FeO_6$ octahedra alone would lead to the paraelectric phase with the space group $R\bar{3}c$[80]. The incorporation of both kinds of distortion gives the actual ferroelectric phase of $BiFeO_3$ with the space group $R3c$[33]. The unit cell of $BiFeO_3$ arising from the cubic perovskite structure by two kind of distortions is shown in Figure 3.8.

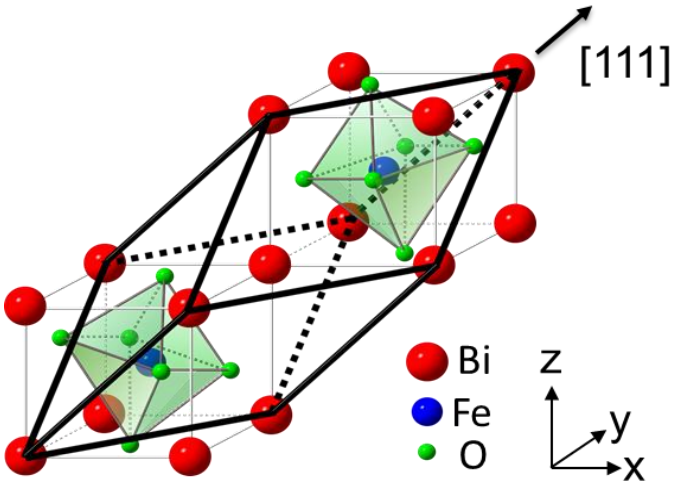


Figure 3.8 Schematic drawing of the crystal structure of perovskite BiFeO3 (space group R3c). Two crystals along [111] direction are shown in the Figure.

### 3.3.2 Light phenomena related to $BiFeO_3$

While mainly studied for its multiferroic properties, $BiFeO_3$ has been recently widely considered for its photoferroelectric properties. Actually, interaction of light with ferroelectrics is known for a long time[81] but only few works have been done in the

past. The revival of photoferroelectric came with $BiFeO_3$ because it displays a lower band gap (of ~2.6 eV) compared to classical ferroelectrics like $BaTiO_3$ or $PbTiO_3$ (up to 3 eV). This part mainly introduces the photo induced phenomena in $BiFeO_3$.

Photovoltaic are known as a methods for generating electric power by using solar cell to convert energy into a flow of electrons. The photovoltaic effect refers to photons of light exciting electrons into a higher state of energy, allowing them to act as charge carrier for an electric current[41].

As we already mentioned, the photoferroelectrics has been reconsidered thanks to the low gap of $BiFeO_3$. The aforementioned abnormal bulk photovoltaic effect has been proposed to exist in $BiFeO_3$ and explain its photovoltaicity like in any other non-centrosymettric material. However, in addition recent works on the photovoltaicity of $BiFeO_3$ shed light on the potential key role the domain walls can play. This leads to consider the domain wall as the active element rather than the domain. In other words, domain wall photovoltaicity has been proposed as an alternative or complement to the bulk photovoltaic effect. Actually, as the domain walls are very narrow, easily movable, can be created or annihilated and show particular properties that are absent in the adjacent domains, a new field of research was born. It concerns the investigation of such active nanoelements through the domain wall engineering.

The photovoltaic charge separation at ferroelectric domain walls in the complex oxide $BiFeO_3$ has been reported and voltage which is higher than the band gap has been produced[43, 82]. Figure 3.9 sketches the model for the photovoltaic effect in $BiFeO_3$ domain wall[51]. Under illumination, a net voltage is produced at the domain wall by the potential steps arising from the component of the polarization perpendicular to the domain wall. The higher local electric field enables a more efficient separation of the excitons, creating a net imbalance in charge carriers near the domain walls, and a net voltage is observed across the entire sample.

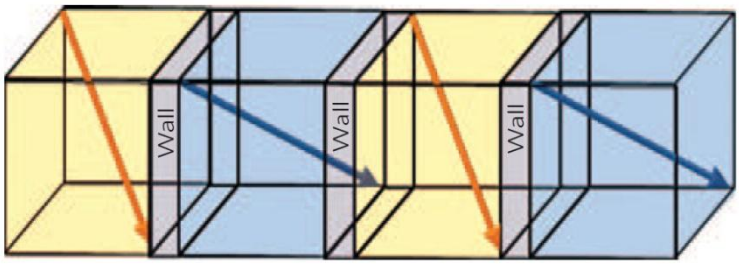


(a)

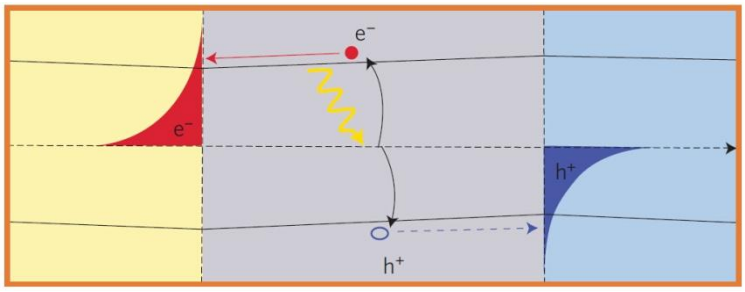


(b)

Figure 3.9 (a) Schematic of four domains (three domain walls) in an order array of 71° domain walls. (b) Detailed picture of the build-up of photo excited charge at a domain wall.

$BiFeO_3$ exhibits also photostrictive properties. In ferroelectrics, the photo-induced strain can be seen as a superposition of photovoltaic and piezoelectric effects. As light irradiates on the ferroelectric electron-hole pairs are generated producing a voltage[58]. These charges can partially screen the polarization and as a ferroelectric is also piezoelectric, it turns that a deformation occurs by reverse piezoelectric effect[59]. For $BiFeO_3$, such photostriction has been shown for the first time using either using a He-Ne laser or a white light (Figure 3.10).

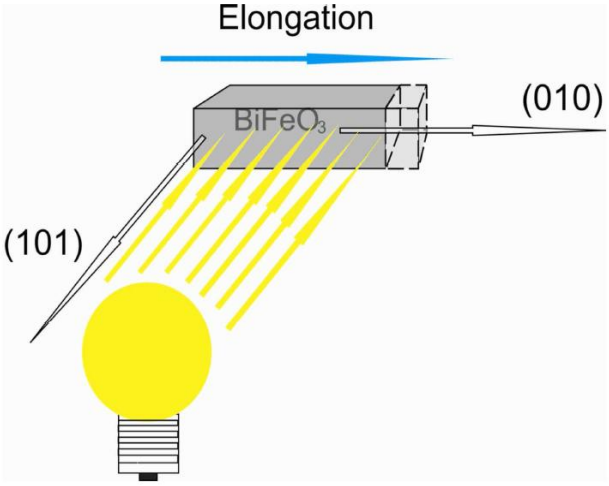


(a)

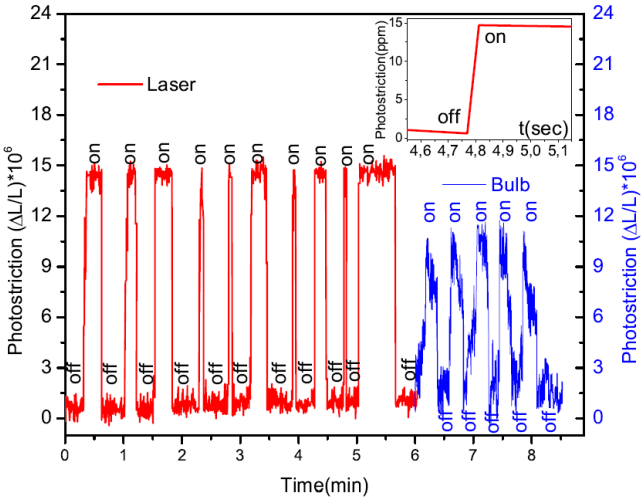


(b)

Figure 3.10 (a) schematic of the photoelastic stress measurements. (b) Time dependence of photostriction in $BiFeO_3$ using He-Ne laser and white light.

It is worth to mention that $BiFeO_3$ has been used for photo-induced strain under different wavelength excitation as shown in Figure 3.11. With the wavelength increasing, the observed deformation value shows a nonlinear behavior. The deformation response time is also wavelength dependent. Due to the faster momentum transfer for energy close to the band gap, the light with smaller light energy which is close to the band gap can cause faster deformation than illumination with other energy (wavelength) far away from the band gap energy. The larger deformation observed in the near UV region may be caused by the band-band

transitions in $BiFeO_3$ or impurity-defect absorption (oxygen vacancy) mechanism[83]. This example stresses another ingredient to the photo effect in ferroelectrics and especially in $BiFeO_3$ that are the defects which can play a crucial role to know that in these oxides oxygen vacancies are always present and Bi is very well known to be highly volatile.

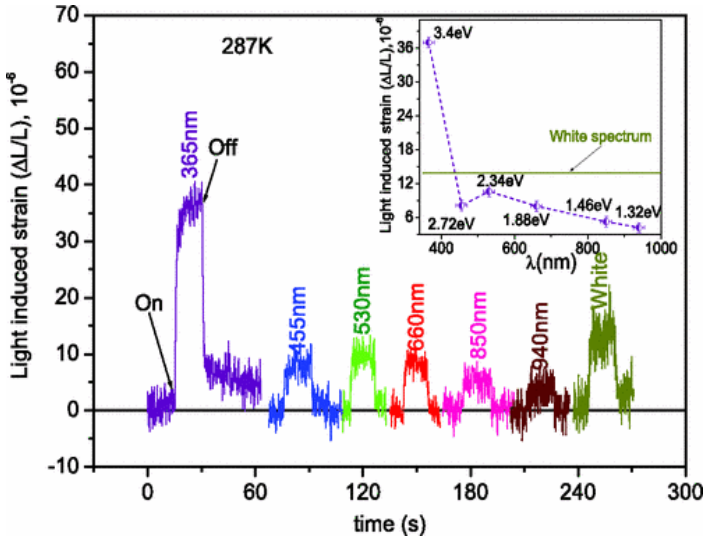


(a)

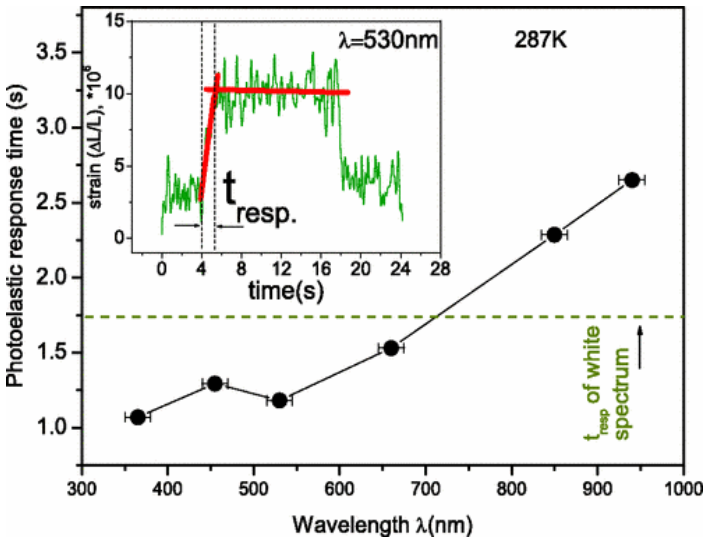


(b)

Figure 3.11 (a) Photoinduced strain of $BiFeO_3$ single crystal as a function of time. The inset shows the photoinduced strain at different wavelength. (b) Photoelastic response time of single crystal at different wavelength. The inset shows the response time determination approach using fits.

### 3.3.3 Photocatalysis and $BiFeO_3$

Among semiconductors considered for photocatalysis[84-85], the most used and investigated is $TiO_2$. However, several issues limit their efficiency: the wide band gap, the high recombination rate of the photogenerated charge carriers, photostability in water, ....[48] In $TiO_2$ notably, only 4% of the total solar spectrum can photoexcite charge carriers, conditioning the need for artificial UV radiation to drive efficiently the chemical reactions. Photovoltaic ferroelectrics might be considered as an alternative choice as most of them are non-toxic oxides, stable in water and crystallize in the perovskite structure which is close to that of $TiO_2$. In ferroelectrics, once the light excitation generates electrons-hole pairs, the polarization acts like an internal electric field favoring separation of the photo-induced charges carriers and thus increasing their lifetime by reducing their recombination. This is for instance revealed by the much larger decay time of photoluminescence in ferroelectric $LiNbO_3$ as compared to non-ferroelectric $TiO_2$[86] (9 $\mu$s against 0.1 $\mu$s).

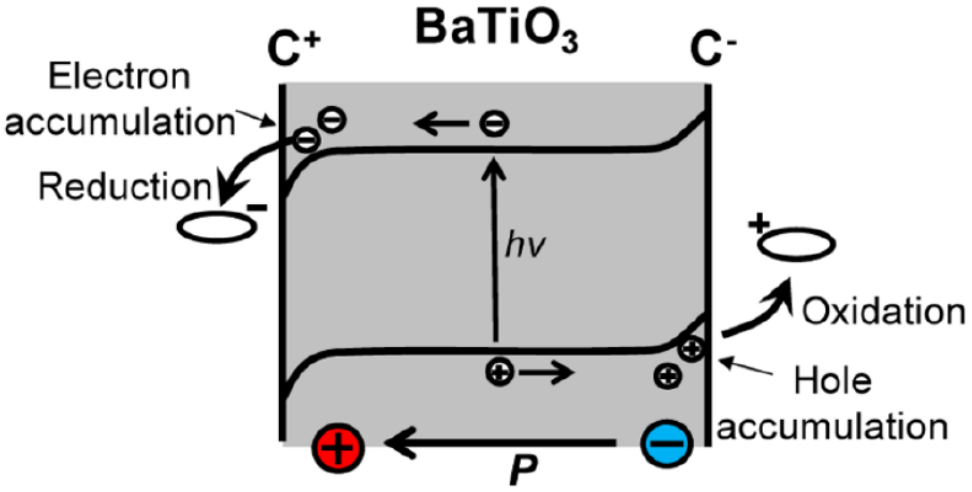


Figure 3.12 Band bending caused by the polarization in $BaTiO_3$ and the free photoexcited carriers act jointly to enhance redox chemical reaction. From Ref. ([87])

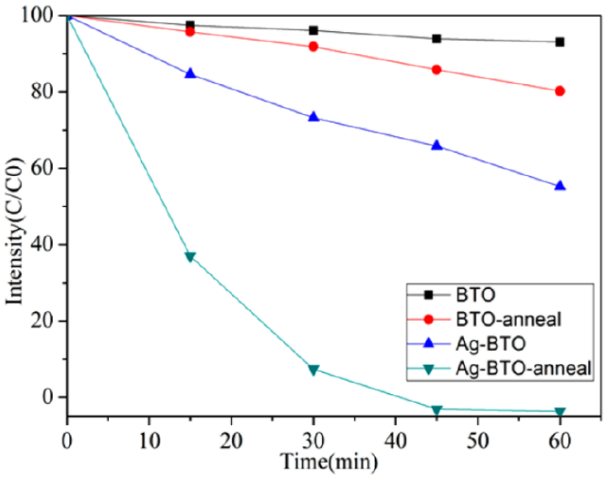


Figure 3.13 Ag nanoparticles coated $BaTiO_3$ are 7.25 times as fast as bare $BaTiO_3$ in degrading the dye molecule Rhodamine B. From Ref. ([87])

Interestingly, photogenerated charges can migrate to the materials surface (see Figure 3.12) and serve as efficient redox reaction sources for degradation of contaminant molecules[88-89] in wastewater treatment as well as water splitting[90-91] in sustainable hydrogen fuel cells. When using photo decolorization of a target dye-molecule, the decolorization rate is significantly enhanced when ferroelectric $BaTiO_3$ particles rather than non-ferroelectric ones are used[87]. A full (100% efficiency) photocatalytic degradation of the molecule is achieved after 40 min illumination under solar simulator using ferroelectric $BaTiO_3$ particles coated by Ag nanoparticles[87] (see Figure 3.13). Similarly photocatalytic effects of $BiFeO_3$ to oxidize organic dyes was demonstrated not only using UV irradiation[92] but also visible light[88, 93] thanks to its lower band gap. Moreover in ferroelectrics, the appearance of polarization gives rise to surface charges which in turn induce a depolarizing field that acts against the polarization. Adsorption or chemisorption of molecules onto the surface can minimize the effect of the depolarizing field by screening the polarization charges[94-95]. As a result a strong Stern layer can be formed favoring interactions with environment reactants. A stronger adsorption of dye molecules was observed in $LiNbO_3$ in comparison to $TiO_2$ powders (7.79% per unit area against 1.27%)[96]. By switching the polarization direction and thus the type of polarization charges at the surface of the ferroelectric, it is also possible to preferentially favor a type of reactions. For instance, $H_2$ production is enhanced on the positive surface of

Sr-doped Pb(ZrTi)$O_3$[97-98] while negative polarization charges are found to promote the oxidation reaction both experimentally and theoretically in case of $BiFeO_3$[98]. Interestingly, it was also proposed that molecules having (permanent or induced) dipole moment can interact with the polarization at the surface of the ferroelectric and reduces the energy required to break bonds which therefore enhances the photochemical activity[99]. Finally, we note that a piezo-electrochemical effect has been reported as an efficient photocatalytic mechanism in $BaTiO_3$ dendrites[100] suggesting that other cross-coupled processes could exist.

Compared to other semiconductors used for photocatalysis, $BiFeO_3$ has a low band gap[101], and combined with its specific photovoltaic-like properties[49], it is of interest to investigate its photocatalytic potentialities. It is known that the photocatalytic activity mainly depends on the band structure[48, 102] with respect to the energy levels of molecule to be degraded as well as the surface reactivity through the particle size[103] and morphology[54, 104]. In order to enhance the photocatalytic response, it is of importance to optimize the relation between these factors. For instance, it was reported that the band structure can be adjusted by the core-shell structured $BiFeO_3/TiO_2$ systems[93] because of electron excitation from *d* orbitals $Fe^{3+}$ to $Ti^{4+}$ 3*d* orbitals in the interfaces, which can significantly enhance the photocatalytic efficiency. In particular, due to the large surface area of small particle, using $BiFeO_3$ particle with nano scale size is beneficial to enhance the photocatalytic activity[105]. Wei *et.al*[106]. have reported that microcrystallite $BiFeO_3$ with different morphologies present preferable photocatalytic activity compared to smaller and coarse counterparts. However, despite the strong potentiality of $BiFeO_3$ as photocatalysis there are only few works reported and a flexible control of the size and morphology on photocatalytic properties of $BiFeO_3$ remains only rarely investigated.

# 4 Experimental

## 4.1 State of art on the synthesis of $BiFeO_3$ powders

Amount of methods have been reported to synthesize different particle size and morphology $BiFeO_3$, which is summarized in Table 4.1. Solid state reaction between $Bi_2O_3$ and $Fe_2O_3$ at high temperature is one of conventional methods to synthesize micro size $BiFeO_3$. However, it has been proved that it is difficult to avoid other two ternary phases in the $Bi_2O_3$-$Fe_2O_3$ system. The $Bi_2O_3$-$Fe_2O_3$ phase diagram indicated three equilibrium phases: the orthorhombic $Bi_2Fe_4O_9$ (space group *Pbam*, ICSD #20067), the rhombohedral perovskite $BiFeO_3$ (space group, *R3c*, ICSD #15299), which decomposes peritectically to $Bi_2Fe_4O_9$ and a liquid phase at ~935 °C, and cubic $Bi_{25}FeO_{39}$ (space group, 123, ICSD #62719), the latter exhibiting a peritectic decomposition to $Bi_2O_3$ and a liquid phase at ~790 °C. Experimental evidence for the high temperature instability of $BiFeO_3$ has been reported abundantly. Morozov *et al.*[107] showed that pure $BiFeO_3$ can be prepared by at high temperature 850 °C under short time (5-10 min), which is called "rapid liquid phase sintering". Another factor that can cause instability of $BiFeO_3$ is the impurity which is introduced during the process of sintering by $Al_2O_3$ or $SiO_2$ from sintering container[108]. Studies on $Bi_2O_3$-$Fe_2O_3$ diffusion couples, performed at 650 °C, revealed that bismuth diffuses several micrometers inside the $Fe_2O_3$, while there was little backward diffusion of iron into the $Bi_2O_3$. Assuming coupled diffusion of the $Bi^{3+}$ and $O^{2-}$ ions, which preserves the electroneutrality, and considering that the oxygen diffusion, it can be reasonably assume that the formation of $Bi^{3+}$ toward the $Fe_2O_3$. The low diffusion data, calculated for 700 °C: the trace diffusion coefficient of $Fe^{3+}$ in $Fe_2O_3$ ($D_{700°C} \sim 2.8\times10^{-25}$ $m^2/s$) is five orders of magnitude lower than that of $Bi^{3+}$ in $Bi_2O_3$ ($D_{700°C} \sim 6.8\times10^{-20}$ $m^2/s$)[108]. The faster bismuth diffusion explains the commonly observed microstructural features in $BiFeO_3$ ceramics, that is, a Fe-rich region inside a $BiFeO_3$ grain with the Bi-rich sillenite phase close to the $BiFeO_3$ grain boundary. So to understand as a kinetically stabilized phase coexistence is necessary to avoid unreacted phase in this system.

Soft chemistry technique are one of efficient methods for synthesizing different size and morphology samples, which include hydrothermal, microwave hydrothermal, deposition from solutions and methods based on chemical vapour deposition. It makes the precursor solution, gel and polymer precursor mixed in the atomic scale, which can disperse reaction ions uniformly and enhance the final sample quality. Generally, soft chemistry methods process at relative low temperature and it can control the stoichiometry of sample effectively. Recently, different morphologys of $BiFeO_3$ have been synthesized using hydrothermal methods. Fei. *et al* synthesized perovskite $BiFeO_3$ pills and robs with domain facets[109] and cubes with [110] exposed facets by adjusting the alkaline conditions of the precursor solution. Different size $BiFeO_3$ were also been synthesized by sol-gel methods and in which different precursors were used. Generally, for chelation, hydroxyl (-OH) is need in chelate since it has the strong chelate ability, which can hold the cation and ensure stoichiometric for different oxides[111]. In order to obtain the different size materials, different synthesis temperature is need to be controlled, since the recovery and recrystallisation are complete and further reduction in the internal energy can only be achieved by reducing the total area of grain boundary.

It is clearly that the closely relationship between structure and properties, thus, synthesizing the high quality sample for properties analysis is significant. In this study, different particle size and morphology nano-$BiFeO_3$ and doping samples have been synthesized by wet chemical process and conventional solid state methods, and the growth mechanism for wet chemical method has been presented for $BiFeO_3$ nanoparticles.

Table 4.1 The different methods of synthesizing $BiFeO_3$ and its compounds.

| Method | | Synthesis Temperature (°C) | Morphology | Size | Ref |
|---|---|---|---|---|---|
| Oxide Precursors | Conventional solide state reaction | 825-8 h | Amorphous | Micro (>200 nm) | [112] |
| | Rapid liquid sintering | 880-450 s | Amorphous | Micro (>200 nm) | [113] |
| | Mechanical activation | 760-6 h | Amorphous | Micro (>200 nm) | [108] |
| Wet Chemical Methods | Metal complex | 400-600 °C | sphere | 10-200 nm | [114] |
| | Modified Pechini | 400-600 °C | sphere | 10-200 nm | [112] |
| | Polymer complex | 400-700 °C | difform | 10-200 nm | [115] |
| | Glycol gel | 400-700 °C | difform | 15-250 nm | [116] |
| | Co-precipitation | 750-850 °C | difform | Micro (>200 nm) | [117] |
| | Hydrothermal | 200 °C | cube-shape | Micro (>200 nm) | [118] |
| | Microwave-Hydrothermal | 200 °C | difform | Micro (>200 nm) | [119] |
| | Sonochemical | 400-700 °C | difform | 4-50 nm | [120] |
| | Combustion | 200 °C | difform | 25 nm | [121] |

## 4.2 Pure $BiFeO_3$ and doping samples for nano and microparticles: Optimizing wet chemical methods and solid state method.

### 4.2.1 Wet chemical synthesis of nano crystalline $BiFeO_3$

The $BiFeO_3$ nanoparticles with different size have been synthesized using wet chemical methods[112]. All chemical reagents were of analytical grade and used without any further purification. In a typical synthesis process, an aqueous solution of 12 ml was first prepared by dissolving $Bi(NO_3)_3{\cdot}5H_2O$ (0.005 mol), $Fe(NO_3)_3{\cdot}9H_2O$ (0.005 mol) and nitric acid (4 ml) in deionized water (8 ml) in a beaker with a magnetic stirring at room temperature. After stirring continuously for 20min, the solution became clear and light yellow color. Keeping the stirred up condition, then

the tartaric acid (TA) (0.01 mol) was dissolved in the solution, after it dissolved completely, ethylene glycol (EG) (0.01 mol) was droped into the solution. Finally, the mole ratio of metal ions, TA and EG in the solution need be hold at ($Bi^{3+}$+$Fe^{3+}$):TA:EG=1:1:1. When the reagent in solution has been dissolved completely, control the temperature carefully and heat up to 60 °C under stirring continuously to ensure complexing of the cations. The solutions displayed a light yellow color homogeneously. Keeping this temperature until the solvent was evaporated completely, and at the same time the mixture will become viscous. Transfer the mixture to the air-blast oven and keep temperature at 80 °C for 10 h. The solution was finally transformed to a dry polymeric precursor. Amount of porous can be found on the dry polymeric precursor. After the precursor was completely dried, it was ground into a fine powder in an Agate mortar. Ground precursor powders were calcined in air with a heating rate of 400 °C/h, and kept for 2 h at different temperature to obtain a series of different particle size. A scheme of the synthesis route for $BiFeO_3$ is shown in Figure 4.1.

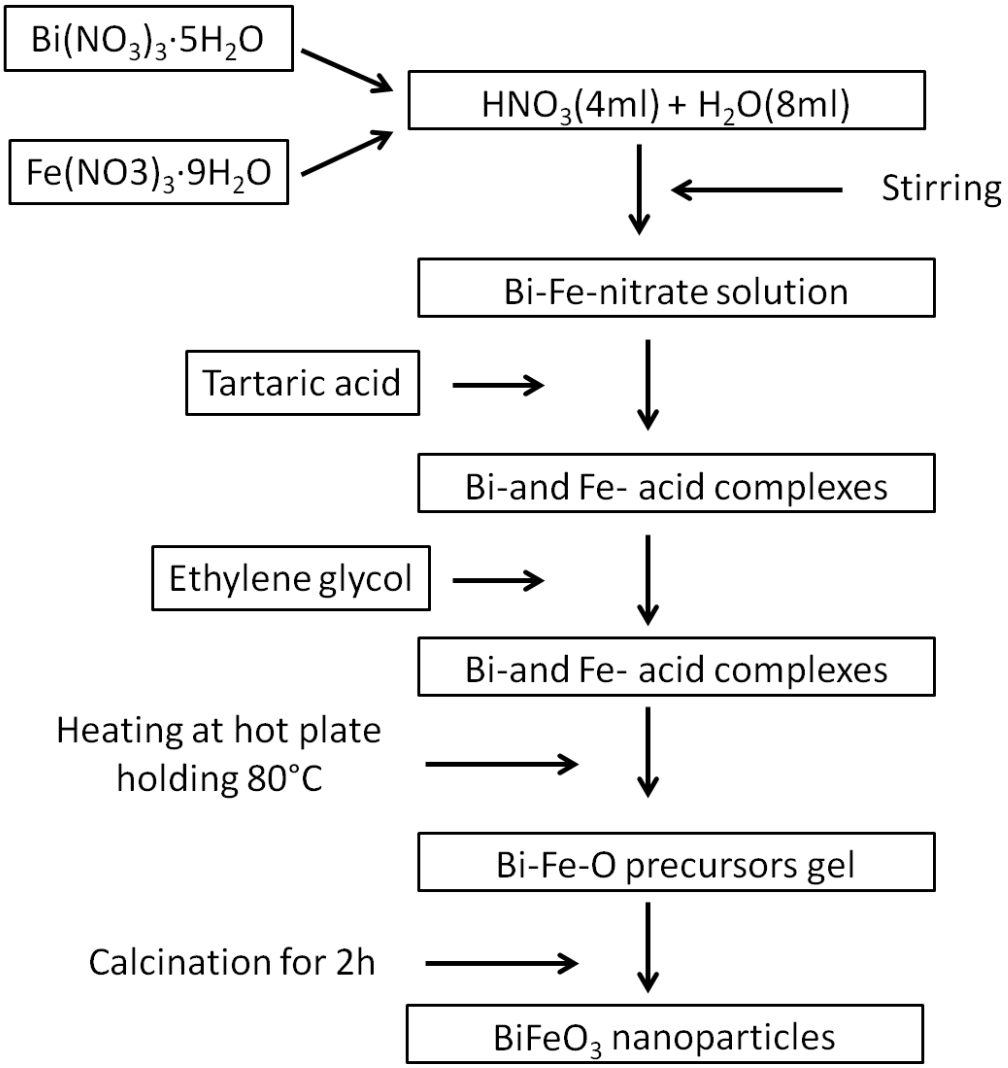


Figure 4.1 Scheme of wet chemical synthesis route for $BiFeO_3$

Ca and La doping nanoparticle samples in A site with different doping content (5%, 10%) were synthesized using the same process. $CaCO_3$, and $La(NO_3)_3{\cdot}6H_2O$ have been used for the source of doping ions. At the beginning, the nitric acid solution with same concentration has been used. After $Bi(NO_3)_3{\cdot}5H_2O$ and $Fe(NO_3)_3{\cdot}9H_2O$ were dissolved in the solution, different content of doping ions compound were added. In order to obtain the high quality sample, the mole ratio of metal ions, TA and EG in the solution need be hold at ($Bi^{3+}$+$Fe^{3+}$+doping ions):TA:EG=1:1:1. And then the same process as synthesis of nano-$BiFeO_3$ sample was used for synthesizing the different particle size $Bi_xA_{1-x}FeO_3$ (5%, 10%) doping samples.

### 4.2.2 Synthesis of bulk $BiFeO_3$ by solid state methods

$BiFeO_3$ ceramic was prepared by solid state reaction between $Fe_2O_3$ and $Bi_2O_3$. Precursor powders were carefully weighted to control the nominal stoichiometry. The ideal starting for solid state reaction synthesis is a homogenous mixture of binary oxide particles. The most successful with respect to time comsumption, control of stoichiometry and reproducibility in term of phase purity of fired product was to mix the binary oxides in ethanol using an Agate mortar and a pestle, since it can avoid induce impurities to the system comparing to the ball milling methods, since the impurities can destabilize the perovskite phase, which has been proved by Sverre *et al*[112]. Complete separation of the milled powder from ball milling also proved difficult, hindering control of the nominal stoichiometry.

The mixed binary oxide was uniaxially cold-pressed with 20-30 *MPa* pressure into 8 mm diameter pellets of 2 mm thickness. Then place the pellet in alumina disk. Sacrificial powder is necessary for coving the pellet in order to avoid evaporation of bismuth oxides ($Bi_2O_3$ and BiO) and separation between pellet and the alumina disk. A nominal Bi:Fe ratio close to unity was thus inferred for phase pure materials, which has been confirmed by a series of $BiFeO_3$ samples with intentional deviation from Bi:Fe ratio 1:1 and these samples contained the expected secondary phases $Bi_2Fe_4O_9$ and $Bi_{25}FeO_{39}$ due to non-stoichiometry and no variation in lattice parameters of $BiFeO_3$ with nominal composition was observed.

The sample was fired in air at 825 °C for 8 h. In order to avoid secondary phase, put the sample into the tube oven directly when temperature at 825 °C and quenching the sample in water after 8 h soaking time, which has been adopted for avoiding the parasitic keeping the purity.

Ca/La-doping A site $Bi_{1-x}A_xFeO_3$ samples were obtained as the process of $BiFeO_3$ and $Bi_2O_3$, $Fe_2O_3$, CaO and $La_2O_3$ have been used as the raw materials. Because of different rate of diffusion for different ions, $Bi_{1-x}Ca/La_xFeO_3$ samples with x=0.05 and 0.1 were fired at 830 °C by heating and cooling rate 400 °C/h and 8 h was chosen as the soaking time, which can confirm the foreign ions enter the corresponding crystal position.

Solid state method for synthesis of phase pure $BiFeO_3$ is difficult and with poor reproducibility, due to the sensitivity of secondary phase in the synthesis temperature region[122]. The isovalent substitution with larger cation on A site or a small cation on the B site would increase the stability of $BiFeO_3$ with respect to the binary oxides, and possible also with respect to the $Bi_2Fe_4O_9$ mullite and $Bi_{25}FeO_{39}$ sillenite phase[108, 123]. Substitution of a more acidic cation on the B site or a more basic cation on the A site is also expected to stabilise the perovskite phase[6, 124-125]. La is almost the same size as $Bi^{3+}$, and although the space group changes with high substitution levels, perovskite phase is obtained for all values of x in $Bi_{1-x}La_xFeO_3$[76, 126]. Through thermodynamics mechanism, it has been obtained the result that substitution with elements more soluble in $BiFeO_3$ than $Bi_2Fe_4O_9$ or $Bi_{25}FeO_{39}$ favors the formation of pure, single phase perovskite and La is more soluble in $BiFeO_3$[122]. When we consider Ca doping, because of divalent of Ca, it will cause the production of hole in the A site, in order to keep the charge balance in the oxide, the oxygen vacancies will also be produced at the same time[127-128], however, the concentration of holes and oxygen vacancies are not equivalent actually, which is caused by the experiment condition and the defect formation in the oxide[129]. Therefore, the band energy will be changed according to the concentration of holes and oxygen vacancies within the sample, which can affect the physical properties of materials.

## 4.3 Characterization techniques

### 4.3.1 X-ray diffraction and analysis using Rietveld refinement

X-ray diffraction (XRD) at ambient temperature was performed using Bruker D2 phase with XFLASH detector using Cu *Kα* radiation in Bragg-Brentano geometry. Data was collected from 10° to 90° 2θ with a step size of 0.005° 2θ, 1 sec. per step.

High temperature XRD (HTXRD) was performed with a high resolution goniometer with a rotating anodes Rigaku RA-HF18. Heat was provided by oven Rigaku 2311 (300 K-1000 K). A circular alumina crucible supported the sample in a cavity. Preliminary HTXRD pattern of $BiFeO_3$ and doping samples were collected in air from 20° to 60° 2θ with a step size of 0.02° 2$\theta$, 6 sec. per step and 0.2° fixed divergence slit. The sample

was held for 5 min at each temperature prior to data collection to ensure thermal equilibrium.

All Rietveld refinements were carried out using software JANA2006[130]. Sample displacements were refined, while zero errors were fixed. The peak profile was refined by Pseudo-Voigt peak shape function. The peak profile function giving the best fit to the experimentally observed data was chosen and kept for all patterns within a serious of patterns with varying composition, temperature and crystallite size.

Lattice parameters, background, displacement and peak profile parameters were allowed to converge before atomic position were added to the refinement. Systematically, the position parameters of the heaviest atom in the unit cell were refined to convergence before subsequently adding lighter atoms to the refinement. Isotropic thermal displacement parameters were added to the refinement after convergence of atomic position, and finally the anisotropic thermal displacement parameters.

For the doping samples, since the doping content has been controlled lower than 10% to keep the *R3c* space group, the refinement condition is same as the $BiFeO_3$ samples.

Crystallite sizes and micro strain were determined using the Williamson-Hall method[131] which is derived from profile matching or Rietveld analysis. In this method the widening of the Bragg peaks $\beta_{\text{strain}}$ (integral breath) follow the equation:

$$\beta_{strain} = 4\varepsilon \tan\theta \qquad [4.1]$$

Where $\varepsilon$ is the micro-strain. However experimentally there are multiples causes of broadening of Bragg peak, another one is due to size effect which follows the well known Scherrer's law:

$$\beta_{size} = \frac{K\lambda}{L\cos\theta} \qquad [4.2]$$

where factor *K* was set to 1.0 for integral breath, the radiation of wavelength $\lambda$=1.5418 Å, the Full Width at Half Maximum (FWHM) of the Bragg reflection is depicted by *L* and $\theta$ is the angle of the chosen Bragg reflection. FWHM values were obtained by JANA2006. The Williamson-Hall analysis is based in the sun of both kinds of broadening:

$$\beta_{tot} = \beta_{size} + \beta_{strain} = 4\varepsilon \tan\theta + \frac{K\lambda}{L\cos\theta} \qquad [4.3]$$

thus:

$$\beta_{tot} * \cos\theta = 4\varepsilon \sin\theta + \frac{K\lambda}{L} \qquad [4.4]$$

Plotting $\beta_{tot}$*cos$\theta$ versus 4sin$\theta$ allows separating and getting a measurement of both the size and micro-strain effect: the micro strain is obtained by the slope of the plot and the crystallite size is obtained by the intercept at sin$\theta$ = 0. The FWHM, $\beta$, was corrected for instrumental broadening using a diffraction pattern of standard material $LaB_6$ powder record with identical X-ray optics.

### 4.3.2 Raman spectroscopy

Raman scattering arises from the interaction of light with different vibrations within a material and it allows obtaining a unique spectroscopic image of the different vibrational and rotational modes, low-frequency modes related to long range order, strain or size effects, among a larger variety of characteristics of a given system. In the particular case of $BiFeO_3$, it is a highly useful tool to get insight theoretically and experimentally not only structural parameters, but also on ferroelectricity and magnetic effects[132, 133]. To obtain Raman spectroscopy data, the inelastic scattering of light with matter is performed using a monochromatic source of light, usually a laser in the visible, near infrared, or near ultraviolet range. The laser photons interact with molecular vibrations, phonons or other excitations in the system, resulting in the energy of the laser photons being shifted up or down. The shift in energy of these photons gives information on the vibrational modes in the system. Practically, the electromagnetic radiation from the illuminated spot is collected with

a lens and sent through a monochromator. Elastic scattered radiation at the wavelength corresponding to the laser line (Rayleigh scattering) is filtered out, while the rest of the collected light is dispersed onto a detector by either notch or a band pass filter[134-136].

Raman spectra presented in this manuscript were collected using a Labram Horiba Jobin Yvon spectrometer with laser He-Ne ($\lambda$=632.8 nm) in backscattering geometry. Scattered photons with wavenumber from 50 to 1000 $cm^{-1}$ were selected using an edge band pass filter. The temperature was controlled by using Linkam heating stage (80 K-870 K) placed under the Raman microscope. Typical optical magnification was attained using a x 10 objective lens having a numerical aperture of 0.25, to obtain a signal averaged within different grains. The sample was carefully deposited on the heating plate and then the laser was focused on it. After the temperature was stabilized, the beam focusing was again adjusted to obtain the maximum intensity, and suitable testing time was set.

### 4.3.3 X-ray photoelectron spectroscopy (XPS)

X photoelectron spectroscopy (XPS) is used for detecting the photoelectron emitted from the surface of materials by X-rays, which based on the photoelectric effect and gives the surface information (element composition, chemical state analysis) of materials[137] Because of high energy of X-ray, the inner shell electrons can be excited as photoelectrons with ionization and relaxation process. According to Einstein photoelectric emission law, the electron binding energy of each of the emitted electrons can be determined by

$$E_{binding} = E_{photon} - \left(E_{kinetic} + \Phi\right) \qquad [4.5]$$

Where $E_{binding}$ is the binding energy of the electron, $E_{photon}$ is the energy of the X-ray photons being used, $E_{kinetic}$ is the kinetic energy of the electron as measured by the instrument and $\Phi$ is work function. $E_{binding}$ represents the strength of the interaction of the electrons at different atomic core levels with the nuclear charge. Figure 4.2

shows a scheme of the XPS measurement mechanism and photoelectrons excitation process.

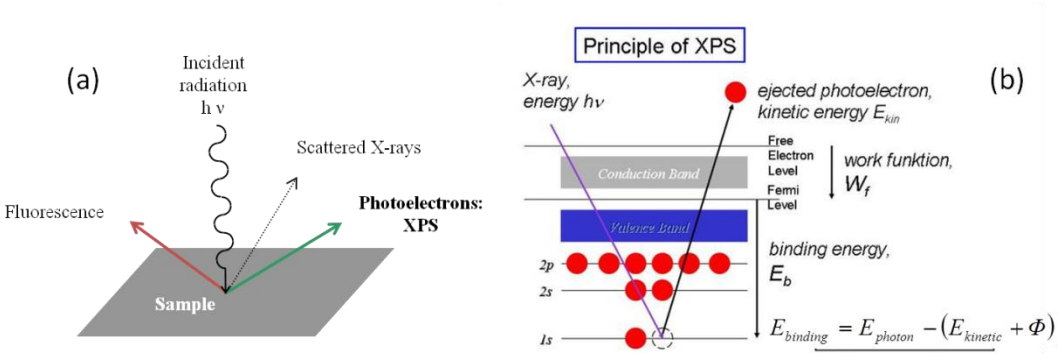


Figure 4.2 (a) Scheme of processes after irradiation of a sample by an X-ray beam; (b) the process of photoelectrons excitation under X-ray irradiation.

X-ray Photoelectron Spectroscopy (XPS) measurements were carried out with a Kratos Axis Ultra DLD spectrometer using a monochromatic Al Kα source of 1486.6 eV working at 150 W, which is the system situated at the Luxembourg Institute of Science and Technology (LIST). The experiments were performed and analyzed by Dr. J. GUILLOT and Y. Fleming. The powders were placed in a crucible and the base pressure in the analysis chamber was better than 5.10-9 Torr. The survey scans and the narrow scans were acquired with a pass energy of 150 eV and 20 eV respectively. In both cases, the take-off angle was 90° and the collection column was used in the hybrid lens mode. The analysis area of the samples surface was 700 μm x 300 μm. A neutralizer was used to limit the charging effect during the acquisition and the spectra were then calibrated in energy by shifting the energy scale so that the main C-C/C-H component of the C 1s peak, corresponding to the adventitious carbon, is at 285.0 eV.

### 4.3.4 Electron Microscopy techniques

#### 4.3.4.1 Scanning Electron Microscopy

Scanning electron microscopy (SEM) permits the observation and characterization of heterogeneous organic and inorganic materials on a nanometer to micrometer scale

by irradiating with a finely focused electron beam. Different particles are generated by the interaction of the electron beam with the sample, including secondary electrons, backscattered electrons, X-rays, *etc*. These electrons and photons are obtained from specific emission volumes within the sample and can be used to examine many characteristics of the samples (*e.g.* surface topography, crystallography, composition, *etc.*).

For morphology purposes, imaging is obtained using secondary and backscattered electrons, because their emission primarily depends on the differences in the surface topography. The secondary electron emission, confined to a very small volume near the beam impact area for certain choices of the beam energy, permits imaging to be obtained at a resolution close to the size of the focused electron beam (nanometer scale)[138].

The microscope used for the present experiments is a Carl Zeiss Leo 1530 Gemini field-emission scanning electron microscopy (FE-SEM) operating at a maximum electron accelerating voltage of 20 kV. SEM imaging was carried out by Françoise GARNIER and Fabienne KAROLAK.

#### 4.3.4.2 Transmission Electron Microscopy and related techniques

Transmission electron microscopy (TEM) is a microscopy technique which is capable of imaging at a significantly high resolution than light microscopes. Because of the small de Broglie wavelength of electrons, the electron beam can transmit through the ultra-thin specimen and an image is formed from the interaction of the electrons transmitted through the specimen. Electrons are generated by thermoionic discharge in a cathode, or by field emission; and afterwards they are accelerated by an electric field, typically in the 80-300 kV range, achieving equivalent electronic wavelengths of $\lambda \sim 10^{-12}$m[139].

Scanning transmission electron microscopy (STEM) works on the same principle as a normal scanning electron microscope by focusing an electron beam into a very small spot which is scanned over the TEM sample, and it needs the accelerated electrons beam pass through the sample. When operating in STEM mode using the High Angle

Annular Dark Field (HAADF) detector, dense areas as well as areas that contain heavy elements appear brighter due to larger angular scattering of the electrons and corresponding scattering probability, thus the image is typically a signature of the difference of the atomic number (Z-contrast) of the elements contained in the sample.

Electron Energy Loss Spectroscopy (EELS) is in short based on the physical principle of the inelastic scattering of the incident electrons with the electrons of the sample[140]. Information about the sample properties is obtained from the collected scattered electrons and the final analysis using an electron spectrometer allows interpreting the nature of the atoms found in the sample and their electronic state and environment. In a typical EELS spectrum, the main contribution to the collected electrons are those that have not undergone any inelastic scattering, forming the so-called Zero Loss Peak. Moreover, at larger energy losses, fingerprints of sample elements and their environment can be deduced from the electrons arising from interactions with the core levels electrons of the elements present in the sample.

The microscope used for the present experiments is a Jeol JEM ARM200F Cold-FEG (Universidad Complutense de Madrid), operating at an electron accelerating voltage of 200 kV and equipped with a EELS spectrometer with a GIF Gatan detector, which energy resolution about 0.5 eV. STEM-HAADF experiments as well as EELS spectra were carried out by María Varela del Arco, and co-analyzed by Pavan Nukala. Figure 4.3 shows the electron transmission channels of TEM, STEM and EELS.

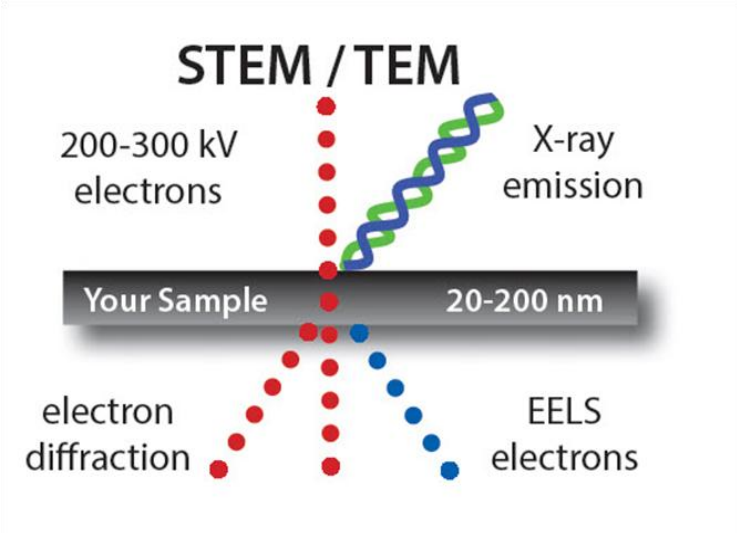


Figure 4.3 Sketch of the electron transmission channels of TEM, STEM and EELS. In reality, EELS electrons are not scattered at a different angle but at a different energy and collected through the spectrometer located at the direct beam position (Bright Field).

### 4.3.5 Thermal analysis

Differential scanning calorimetry (DSC) was performed with TG-DSC 92 SETARAM. Samples of 20-100 mg were encapsulated in aluminium sample pans and measurements were done in air with 10 to 40 °C/min heating and cooling rates in the temperature region 25-600 °C. Non-isothermal crystalline temperatures detection was determined using the same measurement process and the heating rate from 10 °C/min to 40 °C/min have been used for crystallite growth mechanism analysis.

### 4.3.6 Magnetic measurements

Magnetic properties are performed using vibrating sample magnetometry and Mössbauer spectroscopy which is situated at Faculty of Physics and Center for Nanointegration Duisburg-Essen (CENIDE). The experiment were performed and analyzed by Dr. S. Salamon. The Mössbauer data was fitted using PI program which is written by Dr. M. Escobar Castillo.

#### 4.3.6.1 Vibrating sample magnetometry

Vibrating sample magnetometry (VSM) was done with a Quantum Design MPMS SQUID VSM dc magnetometer from 5 to 300 K, collecting data every 1 K, using a 9 T

magnetic field. Standard procedures include the field and temperature dependent determination of sample magnetization, through the recording of *M*(*H*) hysteresis and *M*(*T*) ZFC-FC curves. The device is equipped with a temperature controller, allowing the sample temperature to be set between 1.8 and 1000 K. A superconducting magnet allows fields up to +/-9 T to be set. The machine is built as a closed-cycle system, being able to generate the liquid helium needed for operation via a pulse tube cooler.

#### 4.3.6.2 Mössbauer spectroscopy

In the Mössbauer spectra, the environment of the Fe nuclei is investigated. Mössbauer spectroscopy is based on the absorption of gamma-radiation by nuclei and their different energy levels which undergo and characterize the nuclei environment (valence state, local crystal field, spin configuration). In fact, the technique exploits the Doppler effect between the gamma rays source and sample, and thus the characteristic spectra is represented by an absorbed intensity as a function of the source to sample relative speed. The analysis of the collected spectra is compared to a given reference absorber. The energy levels of the nuclei are mainly modified by the isomer shift and the quadrupole and magnetic splittings. First, isomer shift accounts for the electron cloud surrounding the nuclei. Secondly, quadrupole splitting for the angular momentum of the nuclei, and thus it is sensitive to any local electric field gradient, such as the electric polarization. Finally, magnetic splitting is directly related to the Zeeman splitting of nuclei presenting non-zero nuclear spin moment, thus being sensitive to magnetic order, spin projection, and other spin-related features.

Mössbauer studies were performed in transmission geometry using a constant acceleration spectrometer and a $^{57}Co$ source (Rh-matrix) on samples with ~20 mg/cm$^2$ $BiFeO_3$. The MVC-450 from WissEI allows the calibration of the Mössbauer-drive by a laser interferometer. This device is used for high-speed measurements, widening the range by increasing the velocity of the Mössbauer driving unit, which can be used for high speed measurements for sample with strong temperature depending line broadening.

### 4.3.7 Optical properties

#### 4.3.7.1 Diffuse reflectance

Diffuse reflectance spectrophotometer has been used for studying the optical properties. Ultra Violet-visible diffuse reflectance spectra were measured on particle directly using a PerkinElmer spectrometer Lambda 850 in the wavelength range of 200 nm to 900 nm. Non-absorbing standard $BaSO_4$ has been used as reference sample.

High temperature diffuse reflectance was performed through Harrick equipment assessor with a high temperature reaction chambers which allow diffuse reflection spectroscopic measurements under controlled pressures and a wide range of temperatures. In our experiment, temperature range from 30 °C to 450 °C with a step size of 30 °C has been used for diffuse reflectance. The powder sample was hold for 5 min at each temperature prior to data collection to ensure thermal equilibrium.

In diffuse reflectance measurements, one of important accessory is integrating sphere which is an optical component consisting of a hollow spherical cavity with its interior covered with a diffuse white reflective coating, with small holes for entrance and exit ports. The simplified principle of the use of integrating sphere to measure the reflectance of a test sample has been shown in Figure. It can ensure a uniform scatting or diffusing effect and preserve power but destroys spatial information.

#### 4.3.7.2 Kubelka-Munk theory and Tauc plot for band structure investigation

Kubelka-Munk theory[141] provides an equation that relates the reflection of a sample under diffuse illumination to certain of its properties. In diffuse reflectance spectrum, scattered radiation is collected excluding specularly reflected light matching closely with the Kubelka-Munk function given by

$$F(R) = \frac{(1-R)^2}{2R} \qquad [4.6]$$

Where *R* is the reflectance. Kubelka-Munk parameter *F*(*R*) is related to the absorption spectrum, which can be used for obtaining the charge transition information in the range of reflectance wavelength.

In order to get the band gap value for different size samples, Tauc plot[141-142] has been used.

$$(h\nu\alpha)^{1/n} = A(h\nu - E_g) \qquad [4.7]$$

Where *h* is the Planck's constant, $\nu$ is frequency of vibration, $\alpha$ is absorption coefficient, $E_g$ is band gap and *A* is proportional constant.

The value of the exponent *n* denotes the nature of the sample transition.

For direct allowed transition, *n*=1/2; for direct forbidden transition, *n*=3/2; for indirect allowed transition, *n*=2; for indirect forbidden transition, *n*=3.

Generally, the direct allowed transition has been reported for $BiFeO_3$, *n*=1/2 is used in this work. The acquired diffuse reflectance spectrum is converted to Kubelka-Munk function. The $\alpha$ in the Tauc equation is substituted with *F*(*R*). Thus, in the actual experiment, the relational expression becomes

$$[h\nu F(R)]^2 = A(h\nu - E_g) \qquad [4.8]$$

A line is drawn tangent to the point of inflection on the curve of equ , and the $h\nu$ value at the point of intersection of the tangent line and the horizontal axis is the band gap $E_g$ value.

#### 4.3.7.3 Urbach analysis

Urbach energy describes the density-of-state tails above the valence band and below the conductor band, the shape and size of these tails depend on the presence of different types of disordering[143-145]. The function

$$\ln\alpha = h\nu / E_U \qquad [4.9]$$

can be used for obtaining the Urbach energy $E_U$. $\alpha$ is the absorption coefficient, in our case, it can be substituted by $F(R)$.

### 4.3.8 Photocatalysis

The photocatalytic properties were characterized by the degradation of Rhodamine-B (RhB) in aqueous solution under visible-light irradiation. The equipment of photocatalysis is shown in Figure 4.4 (a), the equipment is situated at the Electronic Materials Research Laboratory, Key Laboratory of Ministry of Education, Xi'an Jiaotong University, the equipment were performed and analyzed by Prof. J.Wei. The photocatalytic reaction was performed with 50 mg $BiFeO_3$ powders in a reactor under magnetic stirring, which was irradiated using a 500 W Xe lamp with a cutoff filter ($\lambda$>420 nm) (Figure 4.4 (b)). The reaction temperature was kept at room temperature by cooling water to prevent the thermal catalytic effect. The degradation efficiency of RhB was evaluated by centrifuging the retrieved samples and recording the intensity of absorption peak of RhB (553 nm) relative to its initial intensity ($C/C_0$) using a UV–Vis spectrophotometer.

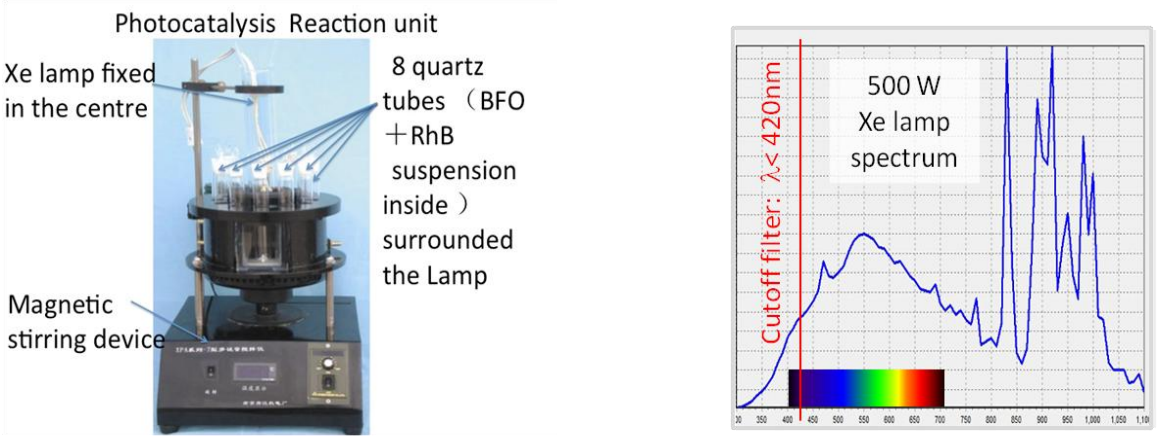


Figure 4.4 (a) The photocatalysis equipment which includes Xe lamp, magnetic stirring device, sample container. (b) The absorption spectrum of 500W Xe lapm spectrum.

The procedure of photocatalysis experiment is as follow:

1. Weight a certain amount of RhB and prepare RhB solution with 50 mL, 5 mg/L;
2. Weight 50 mg $BiFeO_3$ powder and put it in the quartz test tube which contains RhB solution. Then put the tube in the dark reaction chamber with

magnetic stirring, keep it 30 min in the dark condition and make the $BiFeO_3$ dispersion uniformly;

3. Turn on the light (500 W) for photocatalysis reaction;
4. Turn off the light and draw 10 ml mixture from the tube by pipette at regular interval (1 h); put the mixture in the centrifuge tube and remove the powder by centrifuging. Then measure the absorption spectrum by UV-visible spectrophotometer. And the peak summit of RhB absorption spectrum is the $C_x$ (x=1, 2, 3,….);
5. Repeat the step 4, until you get the enough data;
6. Note: measure the prepared RhB solution in step 1which doesn't process for photocatalysis reaction and get the RhB absorption spectrum, the peak summit is $C_0$;

The photocatalysis reaction temperature is controlled at room temperature by coolant system.

# 5 Synthesis of $BiFeO_3$ compounds

## 5.1 $BiFeO_3$ with nano particle size synthesized by wet chemical methods

Nano-$BiFeO_3$ particles are synthesized by wet chemical method at different synthesis temperature. A systematic investigation of synthesizing temperature and the effect of different chelates to complex $Bi^{3+}$ and $Fe^{3+}$ are performed. The synthesis route is introduced in detail in chapter 4.2.1.

An overview of syntheses and chelates identified by X-ray diffraction (XRD) after annealing at 600 °C are summarized in Table 5.1. X indicates presence of phases which have been detected in XRD and ICSD #20067 ($Bi_2Fe_4O_9$), ICSD #15299 ($BiFeO_3$), and ICSD #62719 ($Bi_{25}FeO_{39}$) are used as reference.

Table 5.1 Synthesis process, chelates, and products identified by XRD after annealing at 600°C

| Synthesis | Chelates | $BiFeO_3$ | $Bi_2Fe_4O_9$ | $Bi_{25}FeO_{39}$ | other |
|---|---|---|---|---|---|
| A | TA | X | X | | |
| B | TA+EG | X | | | |
| C | PVA | X | X | X | X |
| D | 2-M | X | X | X | |

Note: In the synthesis A and C, precipitation of white crystals, possibly $Bi(NO_3)_3$, on the wall of the beaker at the liquid air interface was observed during evaporation of the solution, and it may explain the traces of $Bi_2Fe_4O_9$ observed after calcination. TA, tartaric acid. EG, ethylene glycol. 2-M, 2-Methoxyethanol. PVA, polyvinyl alcohol.

Since the diluting nitric acid is used as the reaction solution, no precipitates are observed during the sol process for all syntheses in Table 5.1. The precursors from all syntheses displayed completely amorphous XRD patterns before calcinations. Compared with other synthesis process, in synthesis B the use of ethylene glycol (EG) creates a more porous polymeric precursor that can be seen through the overall expansion in the beaker. From summary results of Table 5.1., high quality $BiFeO_3$ particles can be synthesized by simultaneously using tartaric acid (TA) as chelant and ethylene glycol as assistant agent. In the following, the synthesis mechanism will be explained in detail.

Figure 5.1 shows the molecular structure of different chelants used in the syntheses. A requirement for the formation of a homogenous polyester precursor with segregation of cations is thus proposed to be COOH-group for complexing of $Bi^{3+}$ and $Fe^{3+}$, and OH-group for polyesterification with COOH-group[111]. $Bi^{3+}$ has been reported to form nine-coordinated complexes with tartaric acid[146]. The addition of equimolar amount of ethylene glycol with respect to the carboxylic acids yield phase pure $BiFeO_3$. Because the existence of OH-group in the ethylene glycol, it can react with hydroxyl-terminated group of tartaric acid[147]. A rigid 3D network (Figure 5.2) can form by polymerization between OH-group and COOH-group, which is beneficial to uniformly disperse the cations in the solution and finally obtain a high quality gel[148]. The polymerization reaction is shown in Figure 5.2. For other synthesis processes, which just include one chelant in the solution and lack of OH-group on the main branch, it also contains single bonds, allowing the COOH-group to rotate independently. Although the cations can be complexed, the uniform dispersion cannot be guaranteed[112]. It will be influent on the quality of the final products.

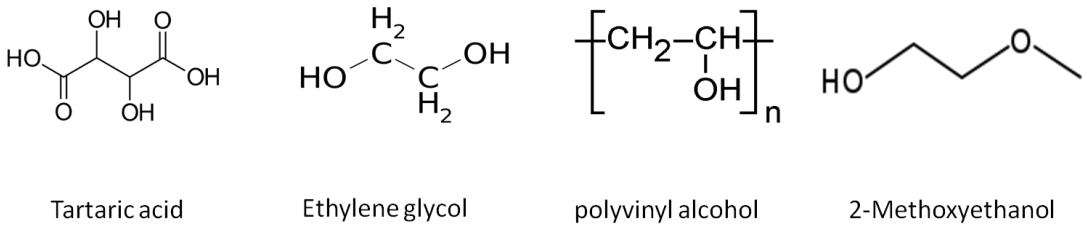


Figure 5.1 Molecular structure of different chelants used in the syntheses

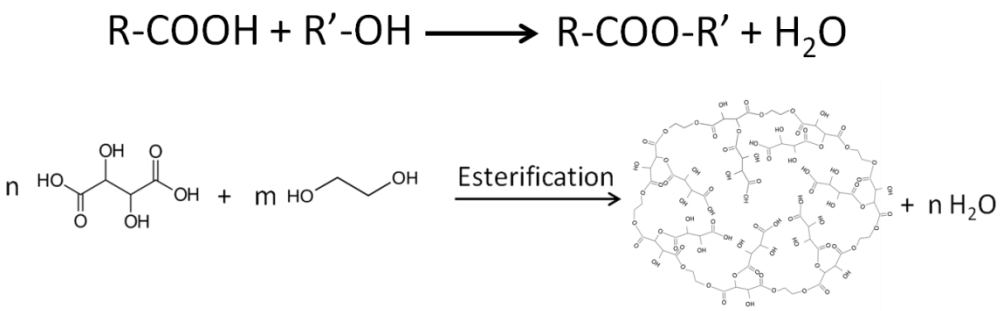


Figure 5.2 Polymerization reaction of esterification for precursors, in which tartaric acid and ethylene glycol have been used as chelant and assistant agent, respectively. 3D structure is formed in this reaction which can help fix the ions, improving sample quality.

When using different temperature program for Precursor powder of synthesis B with equimolar amounts of tartaric acid and ethylene glycol, different quality $BiFeO_3$ could be synthesized. If a one-step temperature program is used, which is shown in the top inset of Figure 5.3 (red line), parasitic phases can be detected in the XRD of the final powders (top data in Figure 5.3). We propose that $Fe^{3+}$ may catalyse the reaction. Detection of the iron rich phase $Bi_2Fe_4O_9$, but not a poor Fe phase as $Bi_{25}FeO_{39}$ in the XRD pattern (asterisk in Figure 5.3), is attributed to a higher local temperature and evaporation of the volatile phases, as $Bi_2O_3$[111-112]. From XRD data in Figure 5.3, it can be seen that the use of different temperature processes for the same precursor powders, while keeping the same final temperature (500 °C) but following a one-step (top) or a three-steps (bottom) temperature program, the corresponding XRD patterns depict the formation in the final powders of $BiFeO_3$ but in the first case it is accompanied by parasitic phases whereas in the latter case only pure $BiFeO_3$ powders are obtained.

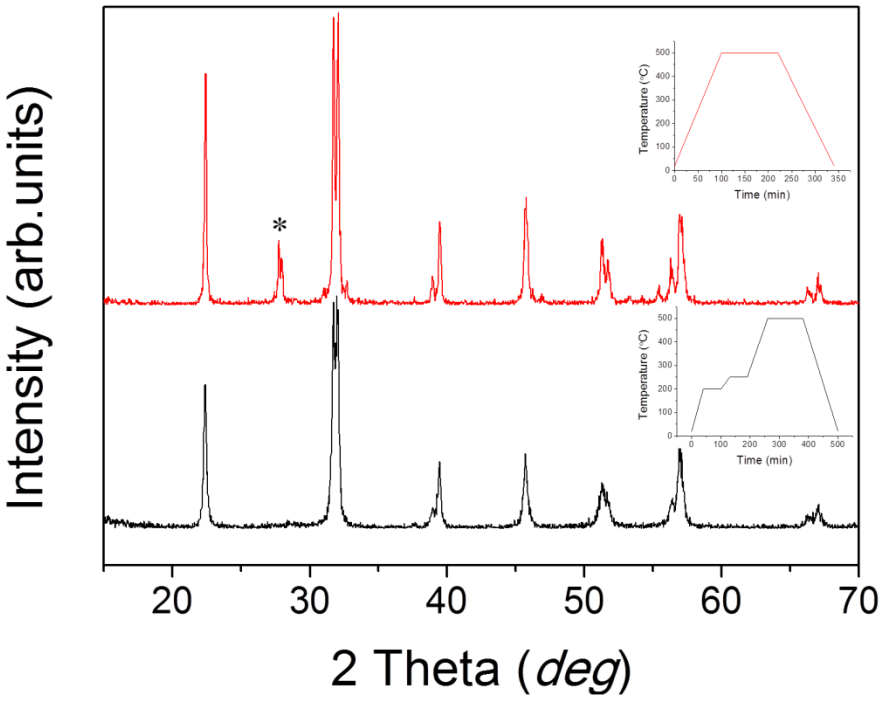


Figure 5.3 XRD data from the synthetized powders after the same sol-gel synthesis method is used to produce $BiFeO_3$ but applying different temperature process. Top (red): ordinary one-step temperature program (see inset for details). Bottom (black): Three-step temperature program (see inset for details). Bulk $BiFeO_3$ main phase is obtained in both cases, but for the one step temperature program, parasitic phases are also observed (marked by asterisks∗).

As we have acknowledged and proved experimentally with the different temperature programs presented before, the synthesis of pure $BiFeO_3$ powders is very difficult, because of the loss of Bi through the volatilization of $Bi_2O_3$ at high temperature, not keeping the stoichiometric ratio of $BiFeO_3$ and parasitic phases will appear. Furthermore, the size and morphology of the particles strongly depend on both crystal temperature and total reaction time. On the basis of our experimental results and previous reports, we propose a possible formation mechanism of different size $BiFeO_3$ particles synthesized via our wet chemical process with different synthesis temperature. We will present here how we have determined the optimum three-step temperature program in combination with the previously presented sol-gel process called synthesis process B (ethylene glycol and tartaric acid).

In order to obtain the optimal temperature process for synthesizing $BiFeO_3$ particles, the precursor powders have been analyzed using differential scanning calorimetry (DSC). From Figure 5.4, the DSC results show that with increase of temperature up to 400ºC, two endothermic peaks appear successively and no other peak is detected in the following, at higher temperature. In Figure 5.4, DSC results of these powders demonstrate that the precursors are ignited at around 200 °C, indicated by a sharp endothermic peak (blue area), caused by the progressive decomposing of tartaric acid, ethylene glycol and the network structure caused by the esterification reaction between tartaric acid and ethylene glycol. Since the decomposing temperature of tartaric acid and ethylene glycol is close to 200 °C, which means that a great amount of heat can be exchanged during a very short time, it can cause a local overheating and thus promote the evaporation of $Bi_2O_3$, affecting the stoichiometry of $BiFeO_3$[111]. After 250 °C, another endothermic peak appears (green area), which is caused by the complete destruction of the polymeric network structure.

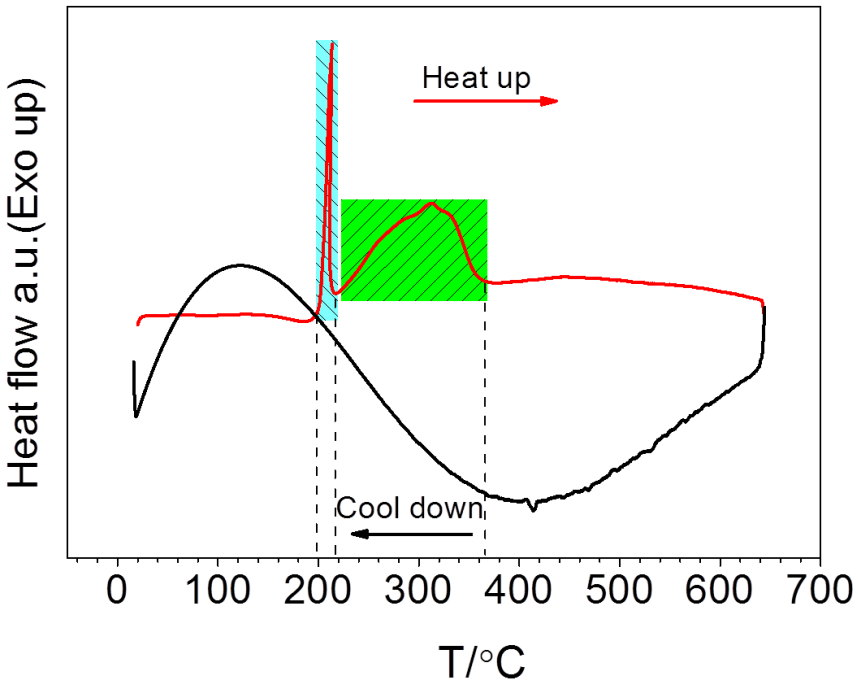


Figure 5.4 DSC analysis of precursor powders (from synthesis process B).Unit problems

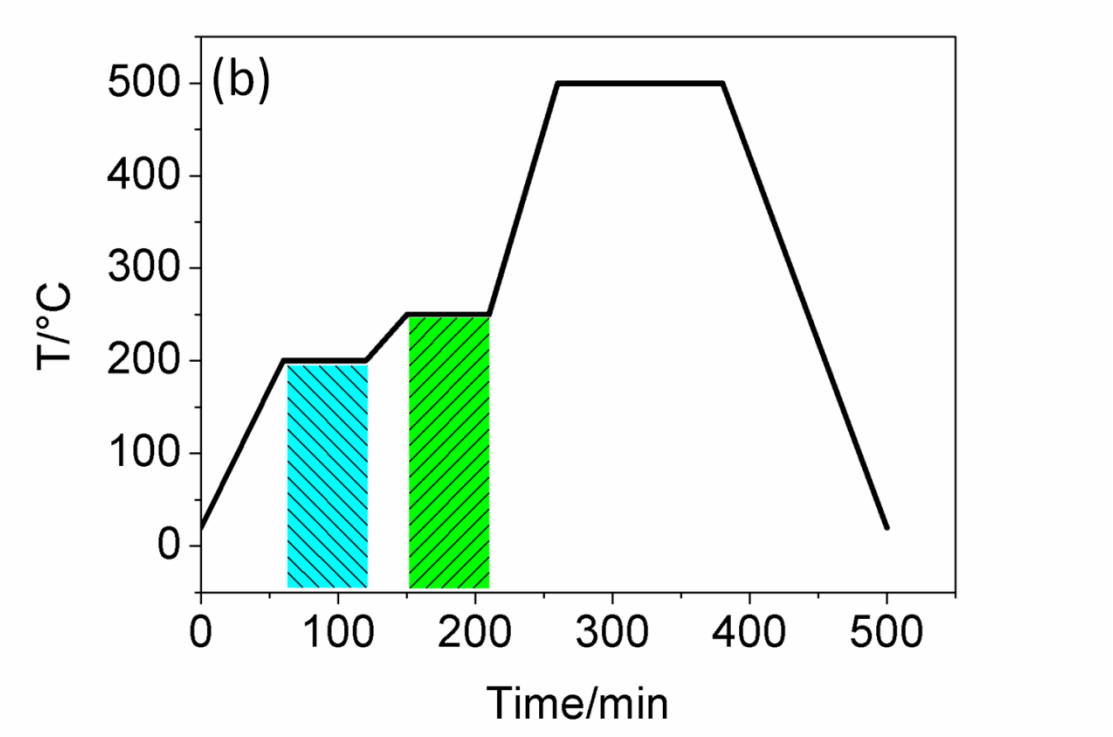


Figure 5.5 Detail of the optimized three-step temperature program determined on the basis of DSC data analysis of $BiFeO_3$-precursors to prevent parasitic phase formation.

On basis of these DSC results, the synthesis temperature process has been determined and shown in Figure 5.5. The different intermediate temperature steps are fixed for a relatively long time before the final synthesis temperature step is attained to prevent that the heat exchange is released in a short time thus allowing to keep the Bi-stoichiometry and finally improving the concentration of pure $BiFeO_3$ phase up to even suppressing any parasitic phase.

Analyzing in detail this wet chemical process, the use of tartaric acid as cationic chelate fastens the process by exploiting the OH-group reactivity with the metallic ions, which is a benefit to the final reaction process at low temperature. Furthermore, ethylene glycol being used, it reacts with tartaric acid through esterification, a homogeneous network can be formed and the metallic ions can be fixed in it, additionally. As a matter of fact, ethylene glycol has been proved to be a suitable solvent to prepare metal oxides (*i.e*. $SrBi_2TaO_9$ and $Ba_{0.5}Sr_{0.5}TiO_3$)[149-150] because the presence of two terminal hydroxyl groups in the molecule makes it easy to keep heterometallic units during hydrolysis reaction. It is reported that the linearly structured molecule of ethylene glycol is favorable for obtaining stable sol[151]. Ethylene glycol as solvent can thus prevent the hydrolysis of bismuth cation and keep bismuth and iron, although presenting different electronegativity, within the same network[152]. This may reduce the energy required for successful dissolution and recrystallization to form pure $BiFeO_3$ during the sol-gel process. In other words, the reaction kinetics of $BiFeO_3$ should be remarkably accelerated by using ethylene glycol as solvent[152-153]. Introducing ethylene glycol in aqueous solution should in principle decrease the dielectric constant in comparison to water [151], which would result in a higher nucleation rate of bismuth ferrite. Thus, ethylene glycol as a solvent gives rise to a faster nucleation and formation of a larger number of crystal nuclei with smaller size[154-157].

To sum up on this discussion on the polymerization process, all these different parameters (different solvents, temperature steps) allows controlling the stoichiometric equilibrium of $Bi^{3+}$ and $Fe^{3+}$ and ensuring the phase purity of $BiFeO_3$ particles. The details on the polymerization process are found in Figure 5.2.

Now we focus on the study of the crystallization process of the amorphous powder, observed from DSC, in Figure 5.6. Two separated exothermic peaks are observed, the peaks being shifted to higher temperature with the increase of the heating rate of the thermal process, which indicates that the events are thermally activated. We have studied the effect of the heating rate using the thermal process ending at 450 °C. Observation of two endothermic events and from the XRD data of the processed powder suggest that the amorphous precursors of $BiFeO_3$ evolves through a nucleation and crystalline growth process to form $BiFeO_3$, happening at different temperatures depending on the different heating exchange. Crystallite growth is also evident from XRD in the same temperature region as the peak in the DSC curves. The present finding shows that nano-crystalline $BiFeO_3$ can be obtained at 450 °C by the present wet chemical route.

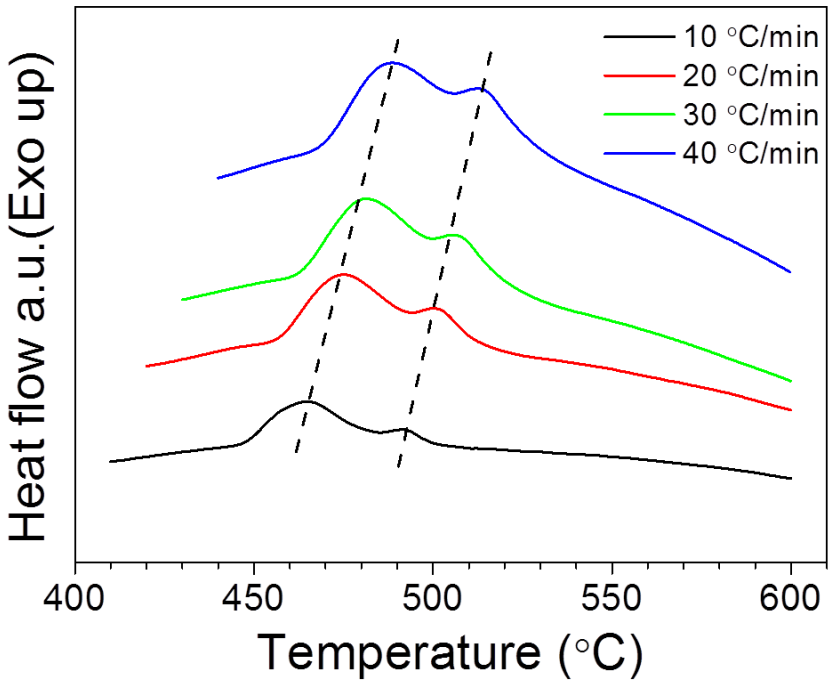


Figure 5.6 Crystallization of amorphous powders observed by DSC indicated from the 2 heat exchange peaks. The same precursors but different heating rates are used for the crystallization.

XRD patterns of precursor powders and powders after calcinations at various temperatures form synthesis B are shown in Figure 5.7 (a). Crystallization and crystallite growth of $BiFeO_3$ was evidenced by the XRD patterns recorded with

increasing calcination temperature. From the XRD patterns, it can be seen that the powder is amorphous after calcinations at 400 °C. Remarkably, detail investigation of the XRD data around (104) and (110) diffraction peaks (Figure 5.7 (b)) indicates a slight reduced separation of these two peaks, which is a signature a tiny evolution of the crystalline structure with grain size decreasing. These powders present all of them rhombohedral *R3c* structure, and the Rietveld refinement results will be presented in chapter 6.1.1.

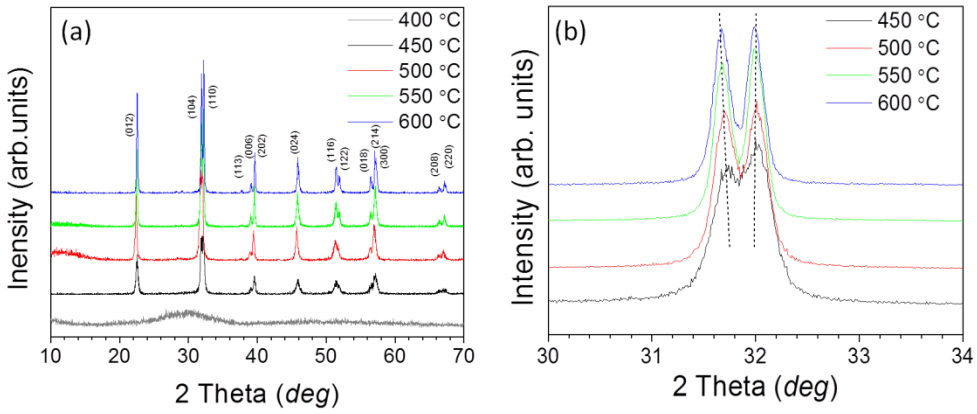


Figure 5.7 XRD patterns of different size $BiFeO_3$ synthesized at different end temperatures: (a) Full range data, (b) detail of the XRD data around (104) and (110) peaks.

In summary, crystallization kinetics and growth mechanism of the $BiFeO_3$ particles have been studied combining DSC and XRD results. Figure 5.6 shows the DSC curves for the crystallization of the $BiFeO_3$ particles at various heating rate ranging from 10 to 40 K $min^{-1}$. It can be found that the crystallization peaks shift to a higher temperature when the heating rate increases, meaning the nucleation and growth of $BiFeO_3$ crystals are delayed to higher temperature though the heating exchange is less efficient with quicker heating rates. The existence of two peaks suggests that an irregular $BiFeO_3$ crystal network is created (first peak) and secondly a periodic lattice of $BiFeO_3$ crystals is set (second peak).

## 5.2 Crystal growth mechanisms of different size $BiFeO_3$

Modified Johnson-Mehl-Avrami (JMA) function can be applied for obtaining the non-isothermal activation energy of $BiFeO_3$ particles crystallization[158], following the formulae:

$$\ln V = -\frac{E_C}{RT_c} + \ln C \qquad [5.1]$$

$$\ln h = -\frac{E_a}{1.985}\frac{1}{T_m} + C \qquad [5.2]$$

where $h$ is the heating rate, $E_a$ is the activation energy for crystallization, $T_m$ is the crystal peak temperature of DSC curve and $C$ is the constant. From the DSC results at different heating rates, a linear relationship between ln$h$ and $1/T_m$ is shown in Figure 5.8 and the activation energy (66.2 $kJ{\cdot}mol^{-1}$) can be obtained from the slope of fitted line.

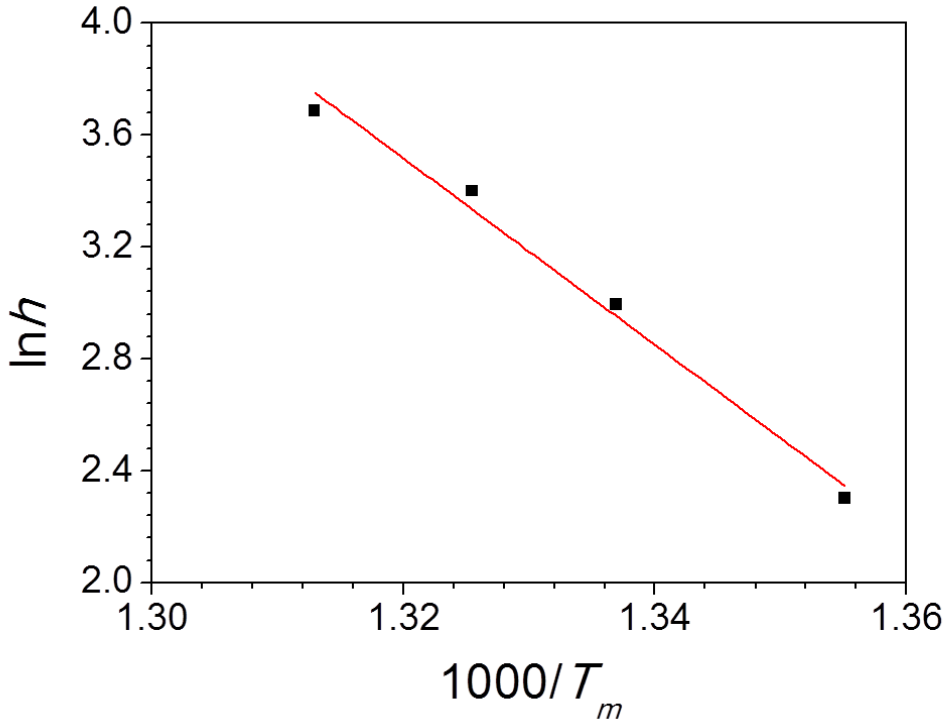


Figure 5.8 The Arrhenius relation of heating rate $h$ and crystallizing temperature $T_m$.

When the $BiFeO_3$ precursors are heated at a constant rate, the crystal nuclei are formed, eventually growing in size if the soaking time is increased. Since the number of crystallizing molecules is proportional to the heat release during a time interval, the total number of $BiFeO_3$ nuclei ($N$) formed per unit volume in the course of heating between $T_1$ and $T_2$ is expressed as[159-160]

$$N = \frac{1}{h}\int_{T_1}^{T_2} I(T)dT = \frac{N_0}{h} \qquad [5.3]$$

and the radius ($r$) of crystal particles is expressed by[159-161]

$$r = \frac{1}{h}\int_{T_1}^{T_2} U_0 \exp\left(-\frac{E_a}{RT}\right) dT \cong \frac{r_0}{h}\exp\left(-\frac{E_a}{RT}\right) \qquad [5.4]$$

where $N_0$ is the initial number of nuclei, $h$ is the heating rate, $I(T)$ is the nucleation rate, $U_0$ is the rate constant of crystal growth, $R$ is the gas constant. There are two types of crystallization; one is based on the bulk nucleation and the other on the surface nucleation. For the case of bulk nucleation, it means that the crystal particles grow towards three dimensions. The volume fraction of the crystal ($x$) is expressed as[161-162]

$$\frac{dx}{dt} = \frac{4N_0 r_0^2 U_0}{h^3}(1-x)exp\left(-\frac{nE_a}{RT}\right) \quad [5.5]$$

where $x=S_i/S$, $S$ is the area under DSC curve between the crystal formation started temperature ($T_1$) and the crystal formation completed temperature ($T_2$), $S_i$ is the area between $T_1$ and $T_i$ (intermediate temperature between $T_1$ and $T_2$) under DSC curve (Figure 5.9) and $n$ is the growth morphology parameter.

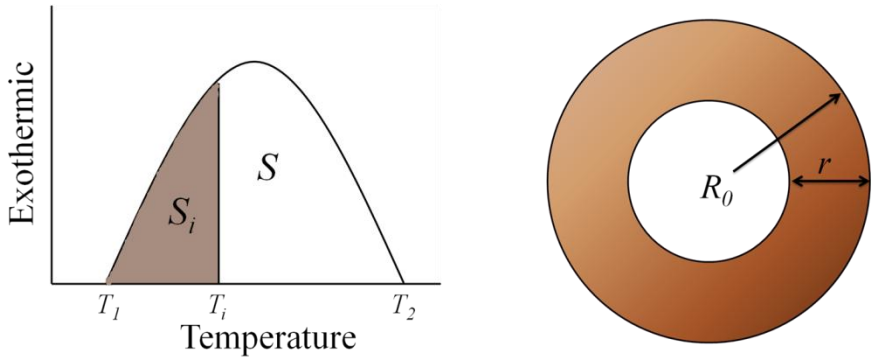


Figure 5.9 (a) Sketch of the integral area for different temperature range; (b) Sketch of surface nucleation in a particle.

That is,

$$\frac{dx}{1-x} = \frac{4N_0 r_0^2 U_0}{h^3} exp\left(-\frac{3E_a}{RT}\right) dT \qquad [5.6]$$

this integral not being expressed by any elementary function, thus the following approximation should be made:

$$-\ln(1-x) \cong \frac{K}{h^4}\exp\left(-\frac{3E_a}{RT}\right) \qquad [5.7]$$

In the case of surface nucleation (Figure 5.9 (b)), the nuclei are formed at the surface and not at the center of the particle. We thus assume that the crystal sphere of radius $R_0$ and the thickness $r$ of surface layer is crystallized. The volume fraction of the crystal is expressed as[161, 163]

$$x = 1 - \left(1 - \frac{r}{R_0}\right)^3 \qquad [5.8]$$

Thus:

$$1 - (1 - x)^{\frac{1}{3}} = \frac{r}{R_0} = \frac{1}{h}\frac{r_0}{R_0} exp\left(-\frac{E_a}{RT}\right) \qquad [5.9]$$

$$1 - (1 - x)^{\frac{1}{3}} \cong -\frac{1}{3}\ln(1 - x) \qquad [5.10]$$

$$-ln(1 - x) = \frac{3}{h}\frac{r_0}{R_0}\exp\left(-\frac{E_a}{RT}\right) \qquad [5.11]$$

Accordingly, combining the function of bulk and surface nucleation together, the following expression is derived:

$$-\ln(1 - x) = \frac{K'}{h^m} exp\left(-\frac{nE_a}{RT}\right) \qquad [5.12]$$

and the following simplified expression is derived:

$$\log[-\ln(1 - x)] = -m\log h - \frac{1}{2.303}\frac{nE_a}{RT} + constant \qquad [5.13]$$

where $n$ and $m$ are numerical factor which depend on the mechanism of crystallization. Different value of $n$ and $m$ mean different crystallization growth mechanism. For $m$=4, $n$=3, it describes the three dimensional growth, for $m$=3, $n$=2, it means two dimensional growth, for $m$=2, $n$=1, it means one dimensional growth. For the surface nucleation, $m$=$n$=1.

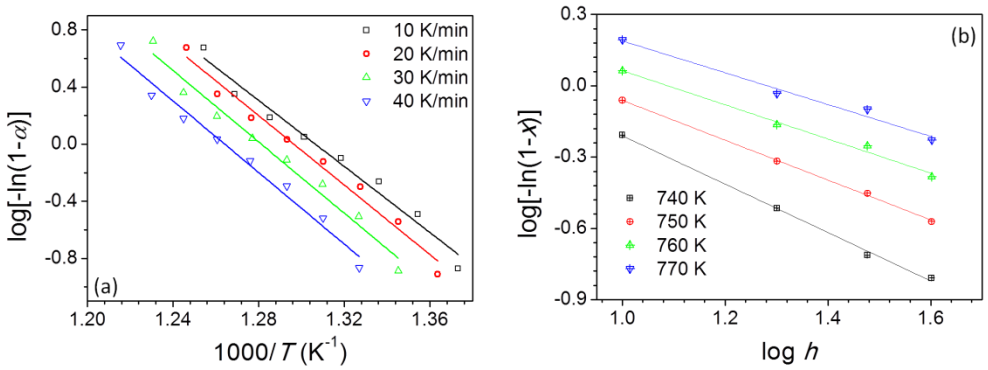


Figure 5.10 (a) Arrhenius plots of log[-ln(1-*x*)] against 1/*T* and (b) log-plots against log *h*, for $BiFeO_3$ precursor powders at various heating rates in (a) and at a fixed temperature in (b). The numerical factor *n* and *m* can be obtained from slope value of fitting results. Change the figure

Table 5.2 Growth morphology parameters of *n* and *m* at various heating rates

| **Heating rate (K $min^{-1}$)** | ***nE*$_a$ (kJ $mol^{-1}$)** | ***n*** | ***M*** |
|---|---|---|---|
| 10 | 84.515 | 1.276 | 1.017 |
| 20 | 86.066 | 1.300 | 0.839 |
| 30 | 88.785 | 1.341 | 0.718 |
| 40 | 98.148 | 1.483 | 0.708 |
| Average | 89.378 | 1.350 | 0.821 |

The plot of log[-ln(1-x)] against 1/*T* and log *h* for the $BiFeO_3$ precursor powders at various heating rate are shown in Figure 5.10. The value $nE_a$ and *m* are obtained from the slope of the fitted lines, which is shown in Table 5.2. For the *m*, *n* values of $BiFeO_3$ particles, it can be seen that it is approximately 1. According to the aforementioned function analysis, it means that $BiFeO_3$ crystallites are formed from the given precursors by a surface nucleation mechanism.  explain

Usually, the rate of crystal nucleation reaches the maximum at a high temperature and then decreases rapidly with temperature increasing, while the rate of crystal growth reaches the maximum at a temperature much higher than the temperature at which the nucleation rate is highest. When sample is heated at a constant rate, crystal nuclei formed at lower temperatures and grown in size at high temperature without any increasing in number.

From above analysis, we know that the crystal growth mechanism of our nanoparticles is surface nucleation and the crystallization started from surface. From Figure 5.6, it can be seen that the crystal temperature for different heating rate are between 450 °C and 500 °C. It means that the crystal nucleus can be formed in this temperature range. Above this temperature range, the leading role of crystallization is crystal nucleus growth. From XRD and SEM results (chapter 6.1.1 and 6.3.1), when we compare the particle size and crystal size, it can be found that when the $BiFeO_3$ nanoparticle is smaller, the particle size is same as crystal size, on the contrary, when particle size is bigger, one particle size includes two or three $BiFeO_3$ single crystal.

As mentioned above, the amount of crystal nuclei is fixed. Because of surface nucleation of nanoparticles, the single crystal is formed at lower temperature, however, when temperature increasing, bigger particles can be formed by single crystals mergering. Finally, it can be observed different size particles from SEM images, which will be shown in chapter 5.3.

## 5.3 Nanostructure through Electron Microscopies

In chapter 5.2, the crystallite growth mechanism by sol-gel solution has been presented through non-isothermal analysis, which has indicated that the crystallite is formed from surface nucleation mechanism of the precursors. From Scanning Electron Microscopy (SEM) images in Figure 5.11, the particle size growth increase with synthesis temperature is attributed to a larger degree of agglomeration.

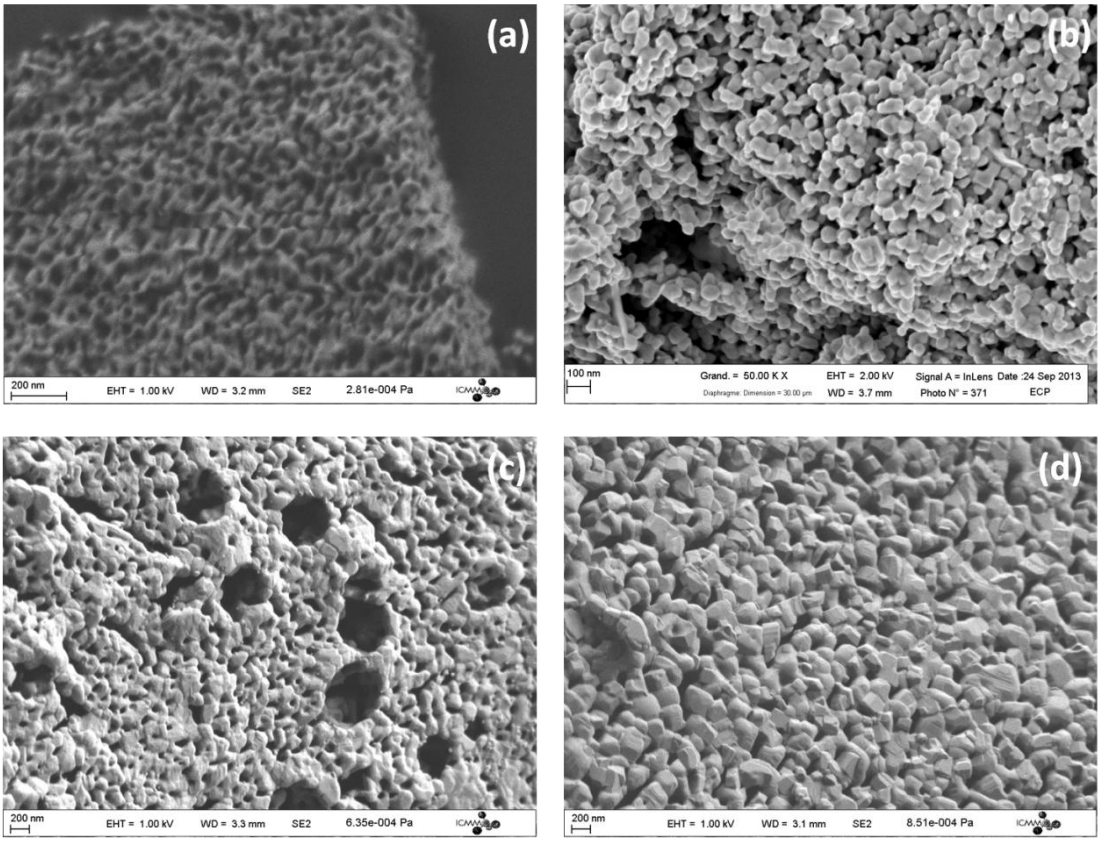


Figure 5.11 SEM images of different size $BiFeO_3$ nanoparticles synthesized at different temperatures: (a) 450 °C, (b) 500 °C, (c) 550 °C, and (d) 600 °C.

At first glance, the morphology of larger size samples is more faceted compared to the smaller ones. This is partially caused by the SEM resolution limits for the smaller nanoparticles. We have shown that from XRD patterns of different size samples (Figure 6.1), the crystallite size can be calculated by Williamson-Hall function. Thus, we can compare crystallite and particle sizes, both as a function of the synthesis temperature, shown in Figure 5.12. It can be seen that the particle size increases with the increase of synthesis temperature. However, when compared to the crystallite size obtained from XRD analysis, the particle size is much larger than the crystallite one for higher synthesis temperatures. In fact, the size of $BiFeO_3$ nanoparticles synthesized at 600 °C is three times larger than their crystallite size. We can thus speculate that the nanoparticles synthesized at 450 °C are equivalent to nanometric single crystals, whereas the nanoparticles synthesized at 600 °C are composed by three nanometric single crystals. Compared to the smaller size nanoparticles, the larger ones should present a less-defective surface as noticed

from the reduced strain noticed from XRD analysis (chapter 6), which can influence among others the optical properties.

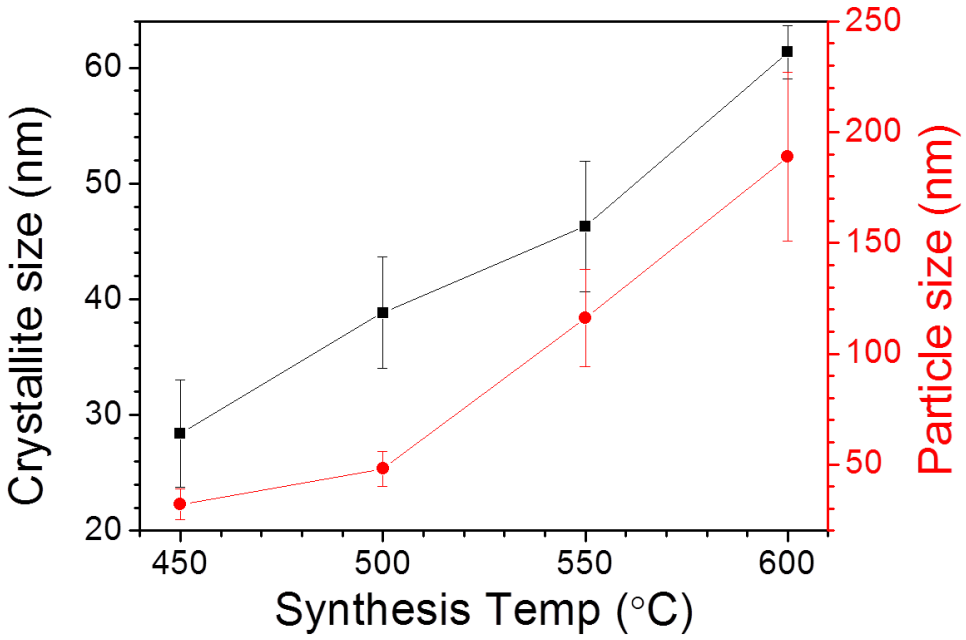


Figure 5.12 Crystallite size (black, squares) from XRD analysis and particle size (red, circles) from SEM images analysis of nano $BiFeO_3$ as a function of the synthesis temperature.

In order to obtain the size distribution of different nanoparticles, 150 particles of every sample (synthesizing at different temperature and the same soaking time) have been selected from SEM image for calculating the size distribution by one homemade program. The size distribution has been obtained in different size range. Figure 5.13 shows the size distribution for different synthesis temperature at the same soaking time. The mean sizes for different synthesis temperature are 32 nm, 49 nm, 120 nm and 189 nm. After analyzing the size deviation of different sample, we found that different size samples have the similar deviation value (20%), which means the growth mechanism for different nanoparticle is identical.

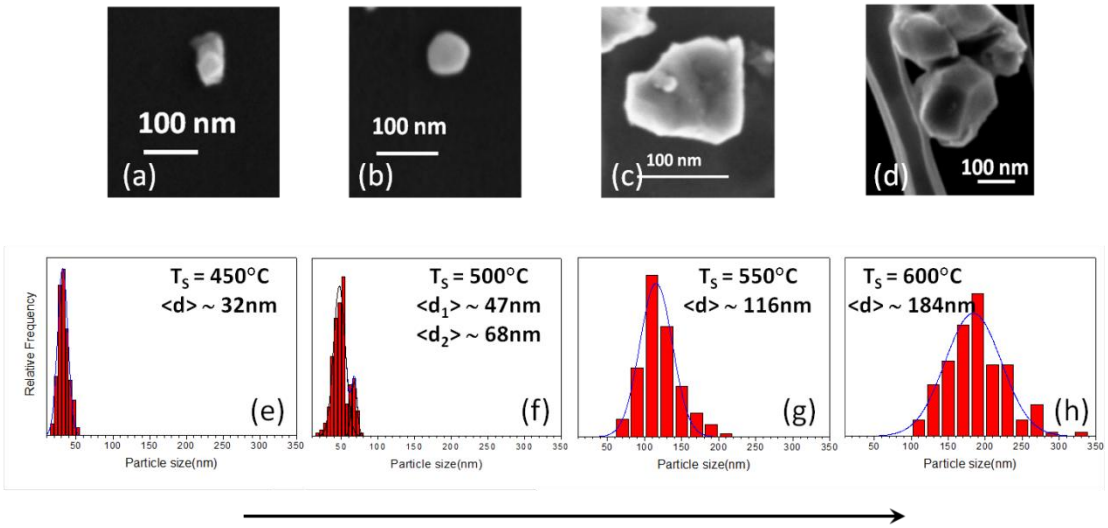


Figure 5.13 Zoom of the SEM images for $BiFeO_3$ nanoparticles synthesized at different temperatures, being (a) 450 °C, (b) 500 °C, (c) 550 °C, and (d) 600 °C, and the corresponding size distribution (e)-(h).

From above analysis, it can be observed that different size $BiFeO_3$ nanoparticles have been synthesized by three steps temperature program (chapter 5.1).

## 5.4 Results on the synthesis of A-site doped $BiFeO_3$ samples

Nanoparticles of A-site doped $BiFeO_3$ ($Bi_{1-x}A_xFeO_{3-\delta}$) using lanthanum (La) and calcium (Ca) have been synthesized using the same wet chemical methods, *i.e.* tartaric acid and ethylene glycol have been used as the complexant agents, fixing the cations through the 3D network structure as depicted in Figure 5.2. The mechanism has been presented in chapter 5.1. Furthermore, a similar temperature program is used during the synthesis process, however, one important point needs to be noticed, meaning that the first step in the temperature process is changed depending on the doping ions. The corresponding DSC and XRD analysis are shown in Figure 5.14.

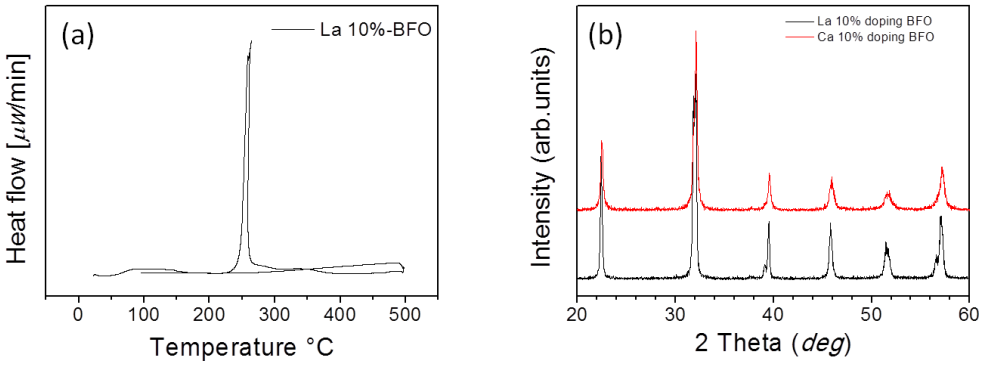


Figure 5.14 (a) DSC analysis of 10% La doping in $BiFeO_3$, compare to the result of non-doping result, the combustion exothermic peak shift to high temperature. (b) The XRD results of La/Ca 10% doping sample synthesizing at 600 °C through adjust the first temperature step.

In order to understand and optimize the synthesis process, analysis of the DSC results from room temperature to the higher calcined temperature (600 °C) is performed. As mentioned before, an intense peak corresponding to the decomposition of solvents is observed around 200 °C. However, in comparison to the process related to obtain pure $BiFeO_3$, it can be found that the heat exchange peak is shifted to a lower or higher temperature (Figure 5.14 (a)) depending on the doping cations[76, 164]. The violent decomposition reaction occurring around 250°C can be deemed as a self-heating, leading to an apparent acceleration of the decomposition. There may also be a contribution of an self-combustion reaction[165], with the nitrate acting as an oxidizer. In fact, different nitrates have different catalytic activity, thus mixing them with dopants in the base material, the dopant will have an influence on the heat exchange[166] directly seen from the temperature shift of the decomposition peak for different nitrates. For this doping level, after close inspection of XRD data (Figure 5.14 (b)), we deduce that both La and Ca 10% doping on the Bi-site allows keeping the *R3c* structure.

We can explain the doping process in the A-site of $BiFeO_3$ in the following manner: when introducing A-site doping ions, because of the different ionic radius, they can induce strain fields that may disturb grain growth process[78]. As a matter of fact, doping ions act as pinning centers located in the grain boundaries and therefore limiting grain boundary mobility[167]. The interaction between dopants and surface/grain boundaries may as well decrease the ratio between surface and grain boundary energies, thus, leading to the stabilization of surface and grain

boundaries[167-168], which is similar to the effect created by a surfactant used to reduce the surface energy and stabilize surfaces. In addition, during the synthesis process, the effect of lubrication by the dopants affects particle agglomeration[169], thus the mean particle size will consequently decrease. In addition, the dopant drag effect is produced when the dopant is segregated to the grain boundaries due to a low solubility on the host component. If located at the grain boundaries[170-171], the dopant will slow down the diffusion, resulting in an inhibition of grain growth. On the other hand, when doping with divalent cations having thus a different oxidation state than $Bi^{3+}$,other electronic defects should be formed in order to neutralize the charge imbalance introduced by the dopant[76, 172-173]. In the case of $Ca^{2+}$ cations, they will introduce an excess of negative charge that can be compensated by different defects, like the creation of oxygen vacancies or reduction of pre-existing cations, as it will be created the $Bi^{3+}$ cationic vacancies. These defects may also affect the grain growth. The grain size of different doping $BiFeO_3$ will be presented in the chapter 6.1.3.

## 5.5 Conclusion

In this part, different size $BiFeO_3$ and doped nanoparticles are synthesized by wet chemical methods. The crystal growth mechanism is studied through modified Johnson-Mehl-Avrami function and surface nucleation mechanisms for different size samples have been studied. For different synthesis temperature, we can obtain different size $BiFeO_3$, for smaller size $BiFeO_3$, the nanoparticle is single crystal, however, when particle size is bigger, it includes two or three single crystal $BiFeO_3$ in one $BiFeO_3$ particle. Doping samples synthesized by the same wet chemical method by controlling the ratio of chelants and metallic ions. When introducing other cations, these doping ions reduce the solvent decomposition temperature through the synthesis process, whereas defects can be introduced through the doping ions.

# 6 Structure, electronic/chemical states and magnetic properties of $BiFeO_3$ particles

## 6.1 X-ray diffraction results

### 6.1.1 X-ray diffraction results of nano-$BiFeO_3$

Rietveld method has been used to refine the XRD diffraction data as shown in Figure 6.1. Mean crystallite sizes estimated from XRD data of pure phase samples are obtained through the Rietveld refinement together with the structural parameters and micro-strain. All samples were determined to structurally correspond to rhombohedral symmetry, *R3c* space group. Lattice parameters, crystallite size and micro-strain values are refined by the Rietveld method and the corresponding results are given in Table 6.1. According to The Williamson-Hall function (4.4) and refinement results of different particle size $BiFeO_3$, the crystal size and microstrain can be obtained from the value of slope and intercept, which has been shown in Figure 6.2.

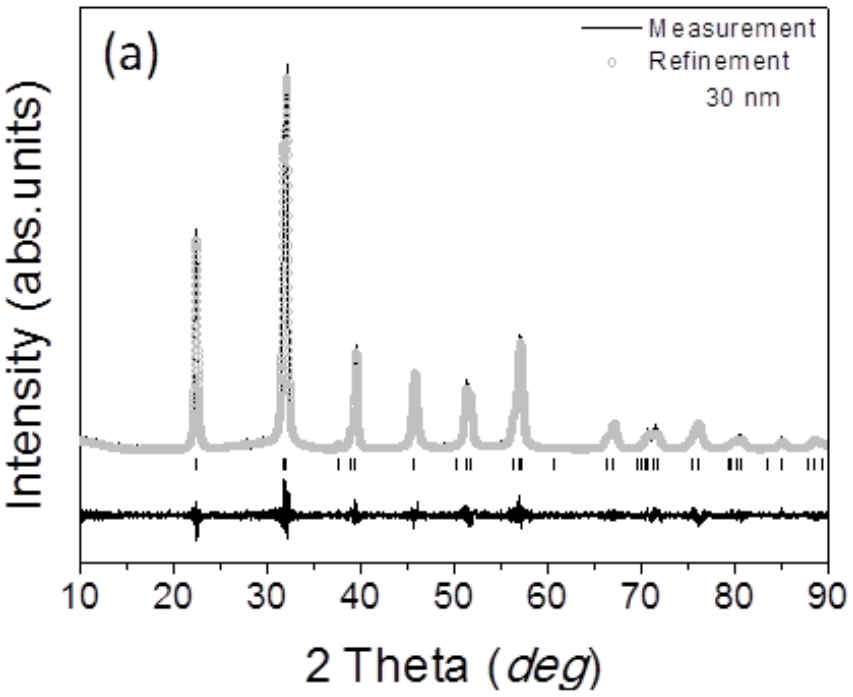
(a)
Measurement
Refinement
30 nm
Intensity (abs.units)
10
20
30
40
50
60
70
80
90
2 Theta (deg)

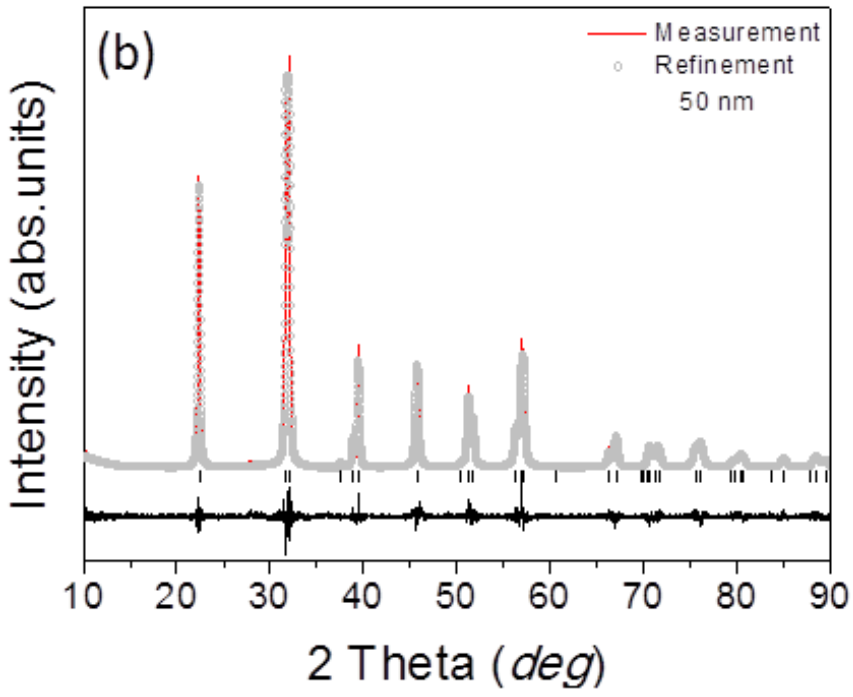
(b)
Measurement
Refinement
50 nm
Intensity (abs.units)
10
20
30
40
50
60
70
80
90
2 Theta (deg)

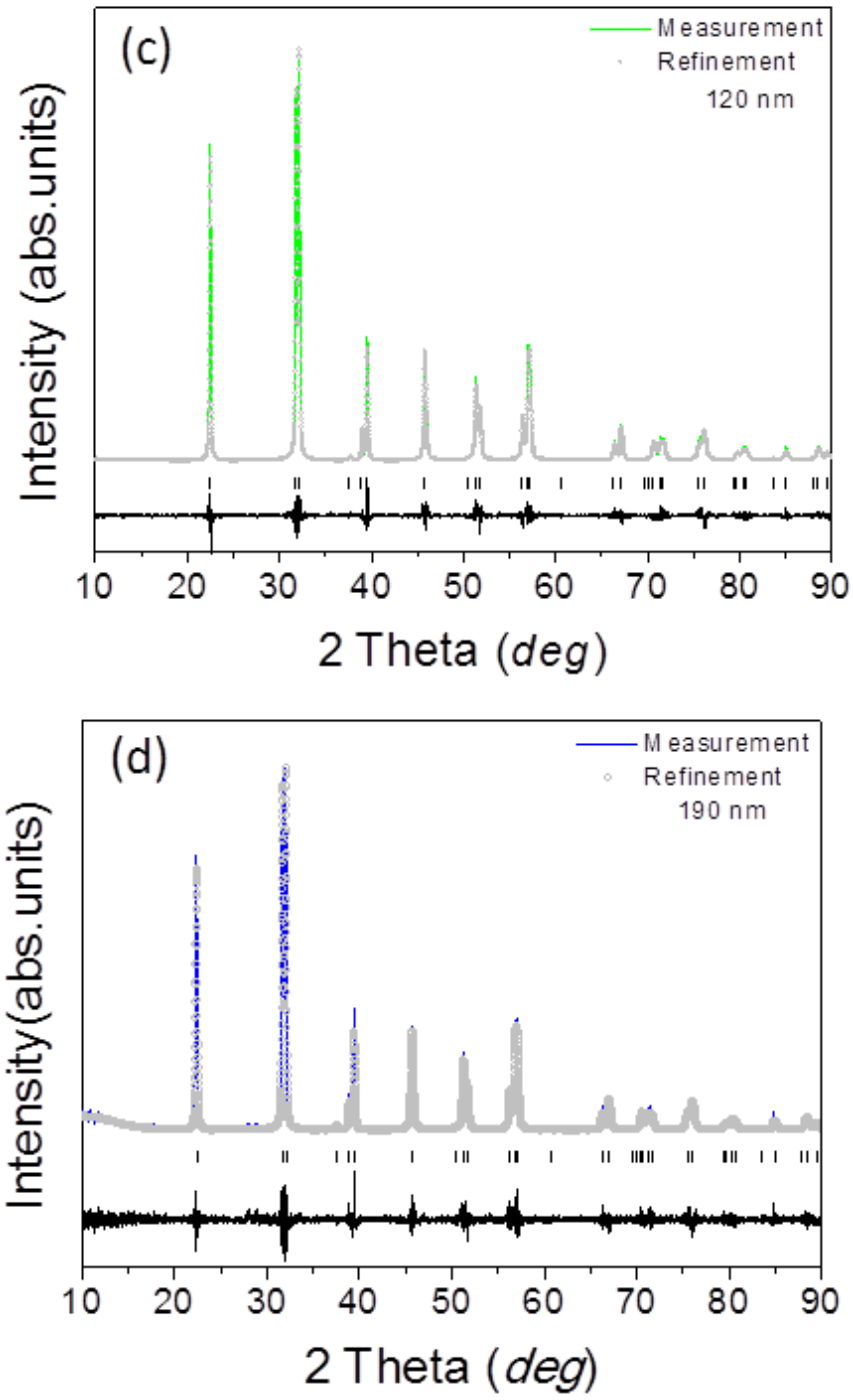


Figure 6.1 XRD data and corresponding Rietveld refinement results of different size nano-$BiFeO_3$: (a) 30nm, (b) 50nm, (c) 120nm, and (d) 190nm

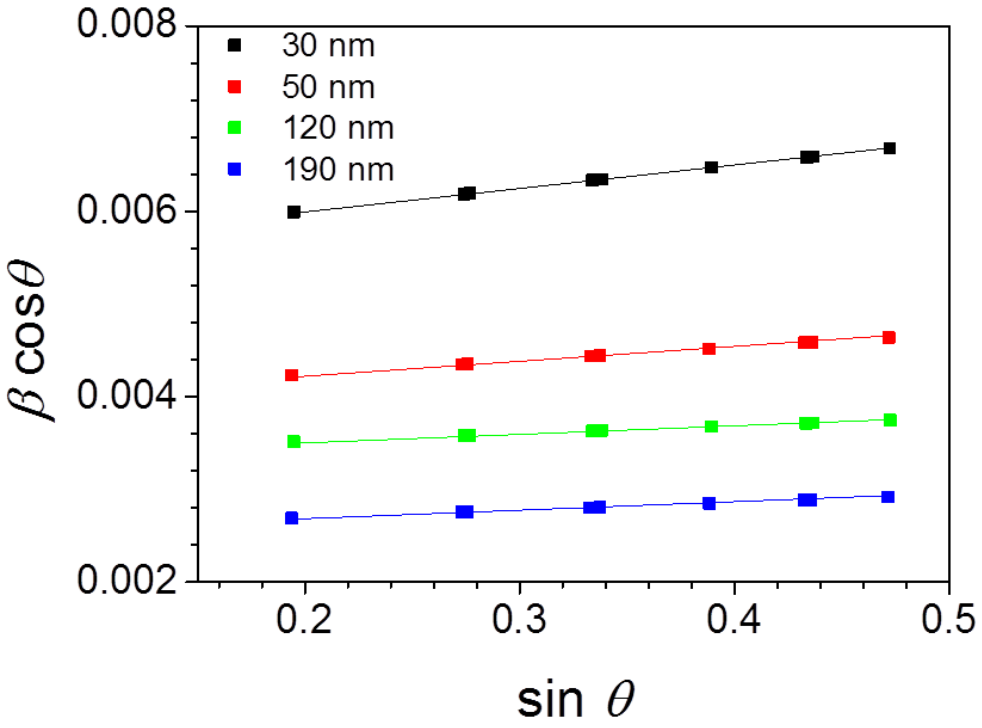


Figure 6.2 Williamson-Hall method for crystal size (intercept) and microstrain (slope)

Table 6.1 Structural parameters $a_{hex}$ and $c_{hex}$ in hexagonal notation, pseudocubic tetragonality $c_c / a_c$ calculated from corresponding pseudocubic $c_c$ and $a_c$ unit cell, unit cell volume $V_{hex}$, crystallite size and micro-strain for different nano-sized $BiFeO_3$ particles.

| | **30 nm** | **50 nm** | **120 nm** | **190 nm** |
|---|---|---|---|---|
| **$a_{hex}$ (Å)** | 5.5794(2) | 5.5781(5) | 5.5791(3) | 5.5781(6) |
| **$c_{hex}$ (Å)** | 13.8703(7) | 13.8682(5) | 13.8712(9) | 13.8683(9) |
| **$a_c$ (Å)** | 3.9452(5) | 3.9443(5) | 3.9450(4) | 3.9443(6) |
| **$c_c$ (Å)** | 4.0040(1) | 4.0030(4) | 4.0042(7) | 4.0034(3) |
| **$c_c / a_c$** | 1.0148(9) | 1.0149(7) | 1.0150(1) | 1.0149(8) |
| **$V_{hex}$ (Å$^3$)** | 373.9(4) | 373.7(1) | 373.9(2) | 373.7(1) |
| **$R_p$(%)** | 8.39 | 8.22 | 8.02 | 8.13 |
| **$R_{wp}$(%)** | 13.71 | 13.15 | 13.23 | 13.03 |
| **Crystallite (nm)** | 28±5 | 39±5 | 46±6 | 61±2 |
| **Microstrain ($\varepsilon$)** | $(24.7\pm4.8)\cdot10^{-4}$ | $(14.6\pm2.5)\cdot10^{-4}$ | $(8.4\pm3.0)\ 10^{-4}$ | $(8.2\pm2.8)\ 10^{-4}$ |

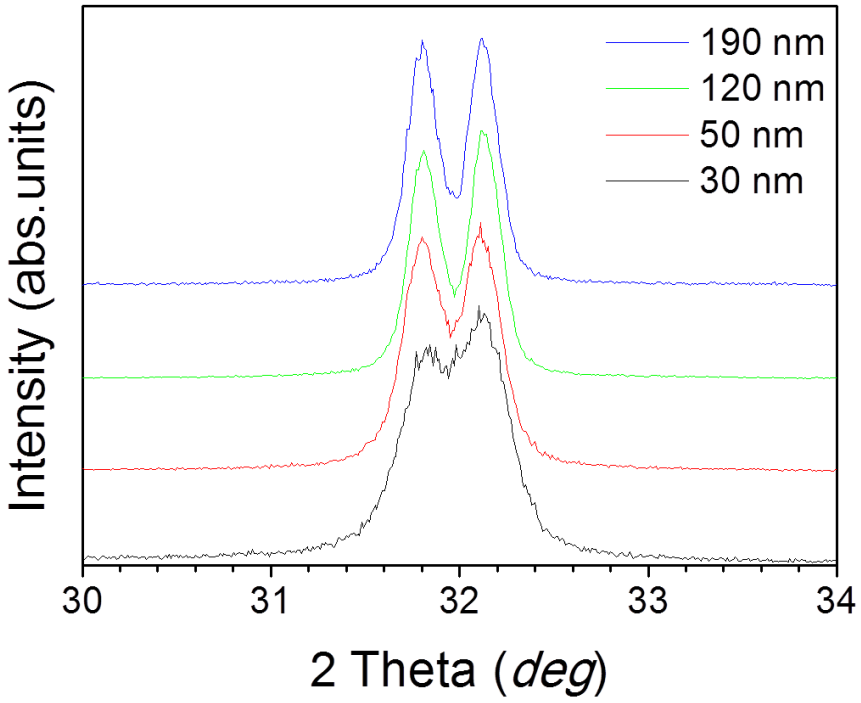


Figure 6.3 Zoom in of the XRD fine scanning patterns shown in Figure 6.1 around (104) and (110) peaks for different size BFO particles (bottom to top, particle size is 30nm, 50nm, 120nm and 190nm).

It can be seen that the lattice parameters *a* and *c* do not show much change as a function of crystal size, meanwhile, the $c_c/a_c$ ratio and rhombohedral distortion varying from 1.0148 to 1.0149 and from 1.46% to 1.47% respectively when the grain size is decreased from 190 nm to 30 nm. Therefore, the polarization which is directly proportional to the square-root of the distortion is believed to remain almost unchanged in the studied size range. From the detail of XRD pattern, the reduced separation of (104) and (110) peak positions [$\Delta 2\theta_{(104)-(110)}$] which would coalesce into a single (200) peak in the cubic phase (Figure 6.3). The symmetric broadening of the XRD peaks indicated that microscale internal strain varies from crystal to crystal. Using the Bragg peak widths extracted from the Rietveld analysis and applying the Williamson-Hall methods, we can access the crystallite size as well as the so called inhomogeneous strains (Table 6.1) or local distortions arising from defects including vacancies, dislocations or interfaces, among others.

It is worth mentioning that the crystallite size coincides with the size of the smallest particles while the bigger nanoparticles are constituted of some crystallites, as we

can determine from SEM images, presented in chapter 5.3 (Figure 5.12). By decreasing the particle size, the inhomogeneous strain corresponding to local distortion related to defects rises up by three times from the biggest to the smallest particles as reported in Table 6.1. That is, downscaling $BiFeO_3$ particles results then in an enhancement of the amount and/or strength of defects and their corresponding local strains. These details on the strain dependent on the size will be afterwards related to the effect on the optical properties of $BiFeO_3$ particles.

### 6.1.2 X-ray diffraction results of A-site doped nano-$BiFeO_3$

X-ray diffraction analysis of different size La or Ca doped $BiFeO_3$ particles are shown in Figure 6.4. Rietveld method is used for crystal parameter and the results are compared to those of undoped samples. The final structural parameters refined by the Rietveld method is shown in Table 6.2. The focus of our work being to induce variations on the optical properties but as few as possible changes on the ferroelectric properties, strongly linked to the structure, we limited the doping to 10% for each dopant.

About the different ionic radius of the dopants within the *R3c* $BiFeO_3$ structure, first we note that La ion having almost the same ionic radius than Bi ion, when La is occupying the A site of $BiFeO_3$, both the Fe-O bond within the $FeO_6$ octahedron and the off-centering of the ferroelectric polarization along the hexagonal $[001]_h$ direction are predicted to be substantially reduced[76, 174]. La doping mainly induces the oxygen octahedral tile in $BiFeO_3$, which can affect the photo-induced properties and it will be explained in next chapter 7. Bivalent Ca ion having a much smaller ionic radius than Bi ion, when used for doping in the A site of $BiFeO_3$, two effects will be produced[78, 128-129, 173]: the unit cell crystal volume is compressed as the Fe-O-Fe angle increases; the $Ca^{2+}$ divalent dopant, in contrast to the trivalent one $Bi^{3+}$, creates positive charge imbalance, thus to maintain valence equilibrium, oxygen vacancies and/or holes can be produced, affecting the band structure of materials and probably leading to new localized electronic states.

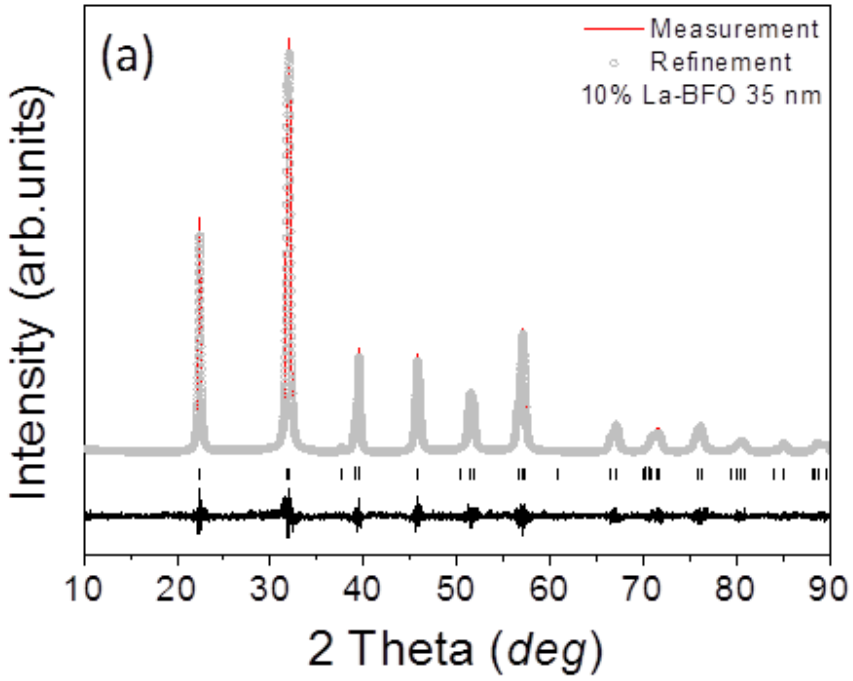
(a)
Measurement
Refinement
10% La-BFO 35 nm
Intensity (arb.units)
10
20
30
40
50
60
70
80
90
2 Theta (deg)

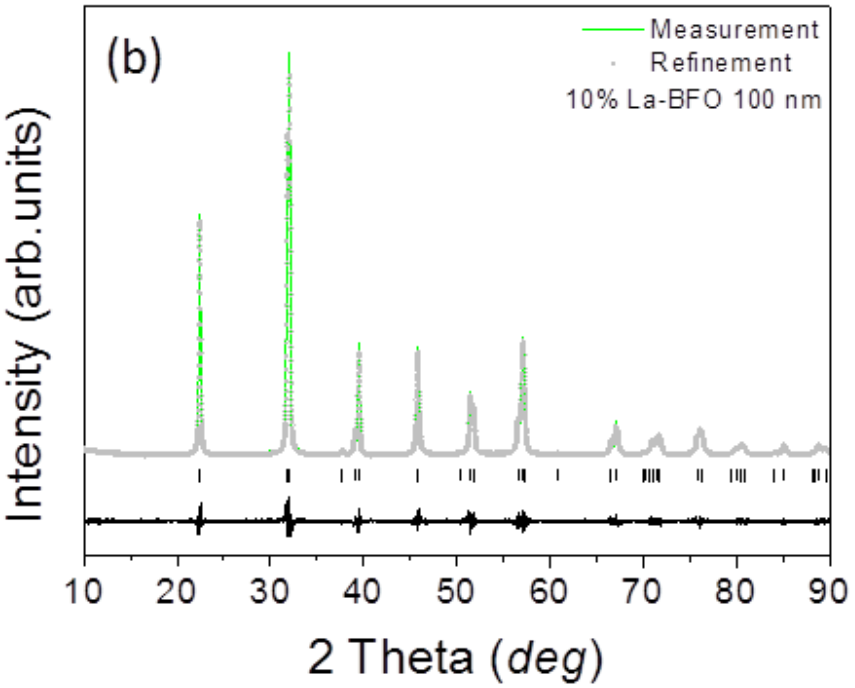
(b)
Measurement
Refinement
10% La-BFO 100 nm
Intensity (arb.units)
10
20
30
40
50
60
70
80
90
2 Theta (deg)

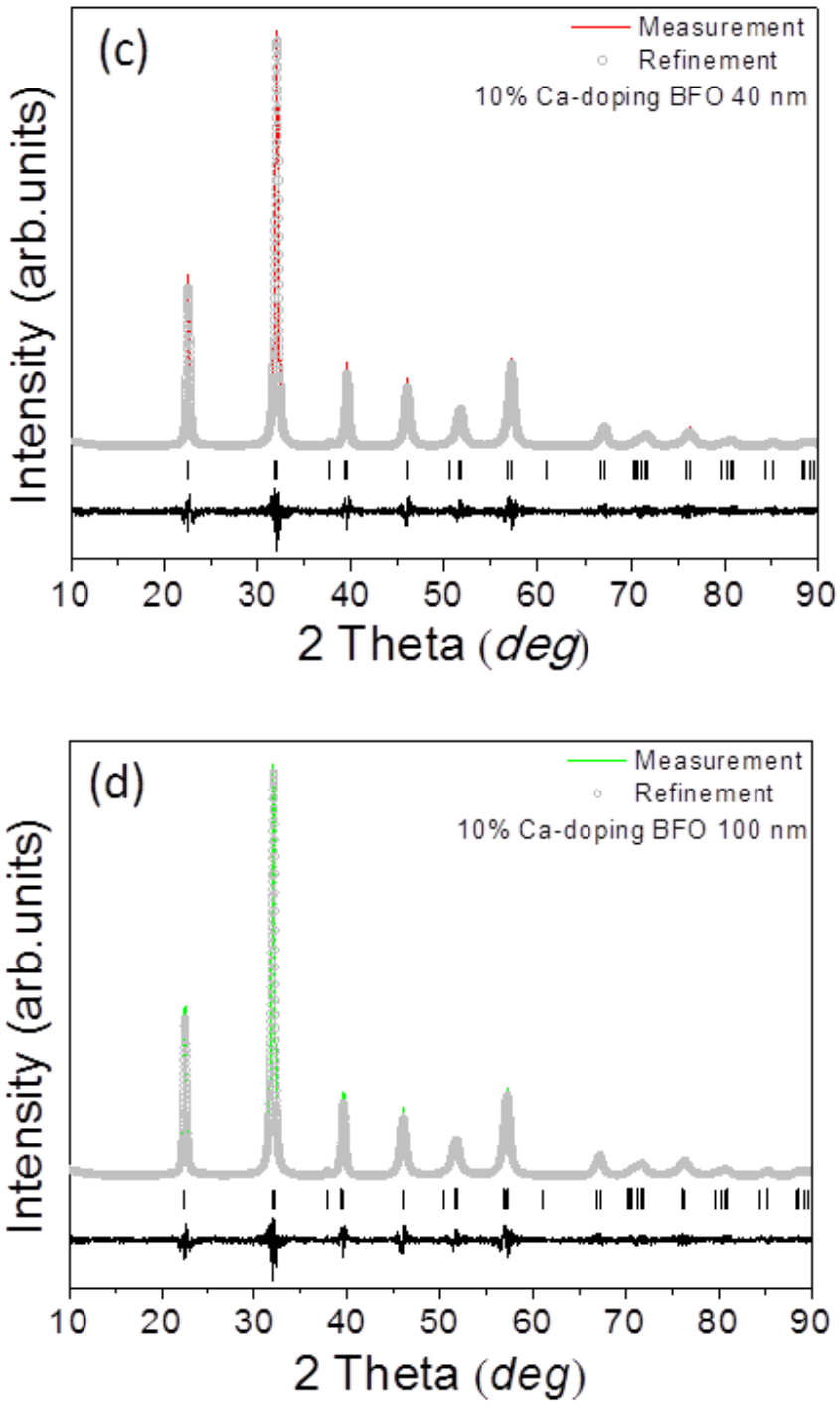


Figure 6.4 X-ray diffraction analysis for 10% La and Ca doping $BiFeO_3$ samples at different particle size by Rietveld method.

Table 6.2 Structural parameters $a_{hex}$ and $c_{hex}$ in hexagonal notation, pseudocubic tetragonality $c_c / a_c$ calculated from corresponding pseudocubic $c_c$ and $a_c$ unit cell values, unit cell volume $V_{hex}$, crystallite size and micro-strain for different doped nano-sized $BiFeO_3$ particles

| | **La 5% 35 nm** | **La 5% 100 nm** | **La 10% 35nm** | **La 10% 100 nm** |
|---|---|---|---|---|
| $a_{hex}$ **(Å)** | 5.5761(5) | 5.5771(0) | 5.5757(4) | 5.5762(8) |
| $c_{hex}$ **(Å)** | 13.8443(8) | 13.8366(9) | 13.8703(7) | 13.8080(3) |
| $a_c$ **(Å)** | 3.9429(3) | 3.9436(1) | 3.9426(4) | 3.9430(3) |
| $c_c$ **(Å)** | 3.9965(3) | 3.9943(1) | 4.0040(3) | 3.9860(3) |
| $c_c/a_c$ | 1.0135(9) | 1.0128(6) | 1.0155(7) | 1.0109(1) |
| $V_{hex}$ **(Å$^3$)** | 372.7(9) | 372.7(2) | 371.9(0) | 371.8(4) |
| $R_p$**(%)** | 11.08 | 8.08 | 9.07 | 11.06 |
| $R_{wp}$**(%)** | 17.76 | 13.48 | 14.04 | 17.82 |
| **Crystallite (nm)** | 30±5 | 43±5 | 28±5 | 40±5 |
| **Microstrain (*ε*)** | (60.4±2.3)·$10^{-4}$ | (40.2±1.5) $10^{-4}$ | (62.3±2.3)·$10^{-4}$ | (43.8±1.5) $10^{-4}$ |

| | **Ca 5% 40 nm** | **Ca 5% 100 nm** | **Ca 10% 40nm** | **Ca 10% 100 nm** |
|---|---|---|---|---|
| $a_{hex}$ **(Å)** | 5.5722(1) | 5.5725(2) | 5.5750(6) | 5.5699(2) |
| $c_{hex}$ **(Å)** | 13.8391(0) | 13.8294(2) | 13.7545(5) | 13.7497(5) |
| $a_c$ **(Å)** | 3.9401(4) | 3.9430(3) | 3.9421(6) | 3.9385(3) |
| $c_c$ **(Å)** | 3.9950(0) | 3.9860(3) | 3.9706(0) | 3.9692(1) |
| $c_c/a_c$ | 1.0155(7) | 1.0109(1) | 1.0072(1) | 1.0077(9) |
| $V_{hex}$ **(Å$^3$)** | 372.1(8) | 371.9(1) | 370.2(3) | 369.4(2) |
| $R_p$**(%)** | 10.97 | 12.22 | 12.50 | 11.43 |
| $R_{wp}$**(%)** | 16.75 | 18.47 | 17.91 | 16.55 |
| **Crystallite (nm)** | 21±5 | 30±5 | 21±6 | 28±5 |
| **Microstrain (*ε*)** | (79.9±2.3)·$10^{-4}$ | (57.1±1.5) $10^{-4}$ | (84±2.4)·$10^{-4}$ | (62.9±1.3)·$10^{-4}$ |

From Table 6.2, compare to lattice parameter of $BiFeO_3$ synthesizing at same temperature in Table 6.1, it is clear that the crystallite size decreases with larger doping. The interaction between the dopants and surface/grain boundaries may decrease surface energy/crystallite boundary energy, thus the particle size is smaller than for pure $BiFeO_3$ synthesized at the same temperature (seen chapter 5.2). Comparing the $c_c/a_c$ values of samples with different doping and dopants, it can be seen that these values are weakly changed and close to $BiFeO_3$ ones, meaning that the polarization linked to such structure is expected to be roughly the same between samples presenting La or Ca doping. However, comparing microstrain values of these

samples to $BiFeO_3$ ones, those of La/Ca doped $BiFeO_3$ samples are increased by an order of magnitude, which is expected to be caused not only by the size decrease but also by the increase of disorder induced by the doping.

### 6.1.3 Temperature dependence of X-ray diffraction results of different size $BiFeO_3$ particles

Temperature dependence of X-ray diffraction parameters of different size $BiFeO_3$ particles are shown in Figure 6.5-Figure 6.7. The crystal parameters ($a_{hex}$, $c_{hex}$ and $V$) of different size $BiFeO_3$ particles at different temperature are determined using JANA 2006, with the same procedure as for the X-ray diffraction experiments and analysis performed at room temperature. From Figure 6.5-Figure 6.7, it can be seen that the value of crystal lattice parameters increase with temperature increasing, which is in well agreement with earlier data from Bucci *et al*[64]., the variation rate of crystallite lattice parameter are shown in Table 6.3. It can be seen that there are almost no change but a small jump around Néel temperature for different size samples in $a_{hex}$ and $c_{hex}$ lattice parameters with temperature increasing. The cell parameters describe a quasilinear temperature evolution with similar expansion coefficients for $a_{hex}$ and $c_{hex}$ (Table 6.3). This result is in agreement with the earlier observation of Bucci *et al*[64] and Haumont *et* al.[175]. It is remarkable that this is a support of the strong spin-lattice coupling, and it is still more important to underline our results since the investigated samples were nanoparticles and the experiments were carried out using a laboratory diffraction setup. The bond length can weakly change at the antiferromagnetic to paramagnetic transition as reported by Haumont *et al.*[175], being this transition characterized by a continuous magnetic structure change from a particular temperature $T^*$ and achieving the actual Néel transition at $T_N$. In our results, although the unit cell changes are very subtle for nanoparticles data, this temperature can be clearly evidenced through the lattice parameters analysis *vs* T ($a_{hex}$, $c_{hec}$ and $V$) shown in Figures 6.4-6.6, depicting an inflection point. Through above analysis, we deduce that the magnetic structure arranges itself continuously between $T^* \sim 390K$ and $T_N \sim 580K$ for smaller particles and between $T^* \sim 400K$ and $T_N$

~ 610K for larger particles, all these characteristic temperatures depending on the particle size are summarized in Table 6.3.

We want to comment on another intriguing point related to the variation of $T_N$ values as the particle size changes, also shown in Table 6.3; $T_N$ decreases from ~ 650 K for micro-$BiFeO_3$ to ~ 580 K for 30 nm $BiFeO_3$. Similar results have been reported by Sverre *et al.*[79] and Landers *et al*[36] through X-ray diffraction and Mössbauer spectroscopy. The finite size effects on structure properties and Néel temperature, which is the major effect factor in our case. Antiferromagnetic domains can be controlled by electric field induced switching of ferroelastic domains, and antiferromagnetic planes in $BiFeO_3$ are perpendicular to the polar axis[176]. Phase transition in $BiFeO_3$ nanoparticles has observed to a high-symmetry paraelectric phase with particle size decreasing[80], which can influence the magnitude of polarization. Meanwhile, the antiferromagnetic ordering may thus be influenced by the polarization. The decrease in $T_N$ could be associated with the decrease in spontaneous polarization, in addition to the decrease in the number of the antiferromagnetic interactions with decreasing particle volume. This is in agree with the dielectric anomalies at $T_N$ in $BiFeO_3$[177]. The $T_N$ anomaly for 50 nm $BiFeO_3$ is related to the Dzyalonshinkii-Moriya (DM) interaction when particle size approaches to 62 nm, which will be explained in chapter 6.4.

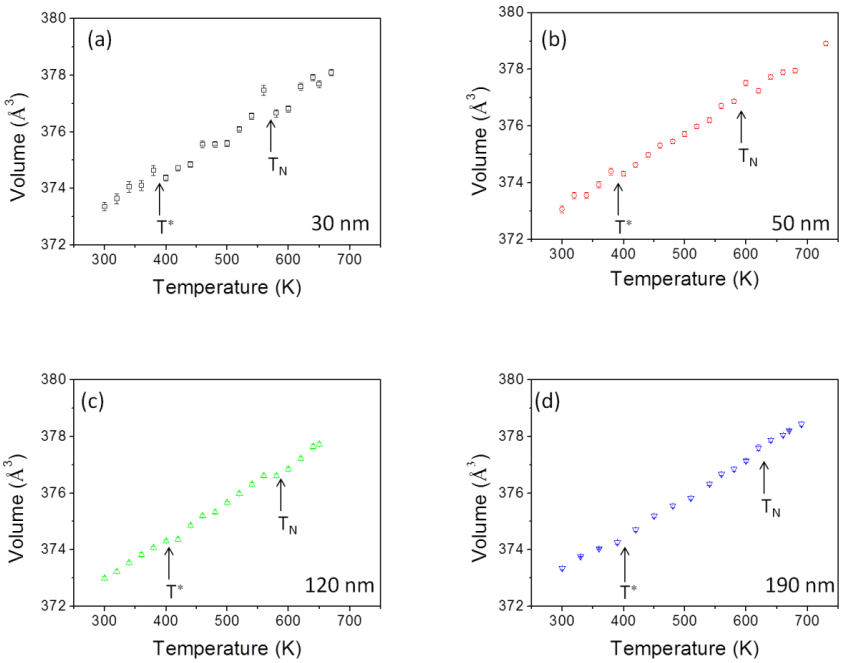


Figure 6.5 Volume variation (hexagonal notation) of different size $BiFeO_3$ as a function of temperature, (a) 30 nm; (b) 50 nm; (c) 120 nm; and (d) 190 nm.

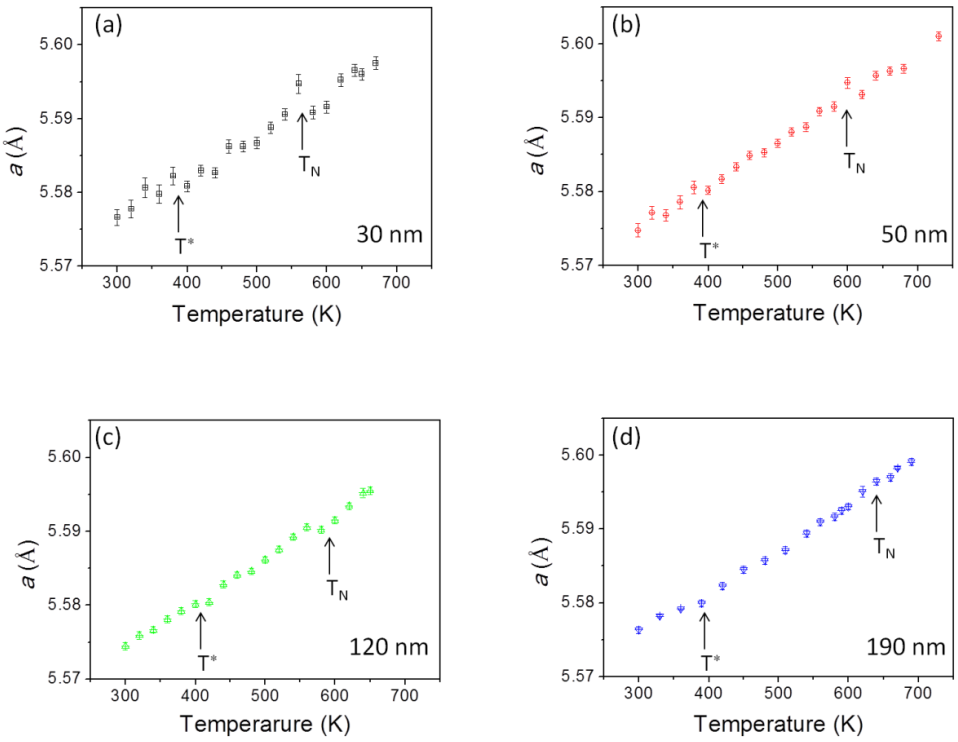


Figure 6.6 Parameter $a_{hex}$ variation of different size $BiFeO_3$ as a function of temperature, (a) 30 nm; (b) 50 nm; (c) 120 nm; and (d) 190 nm.

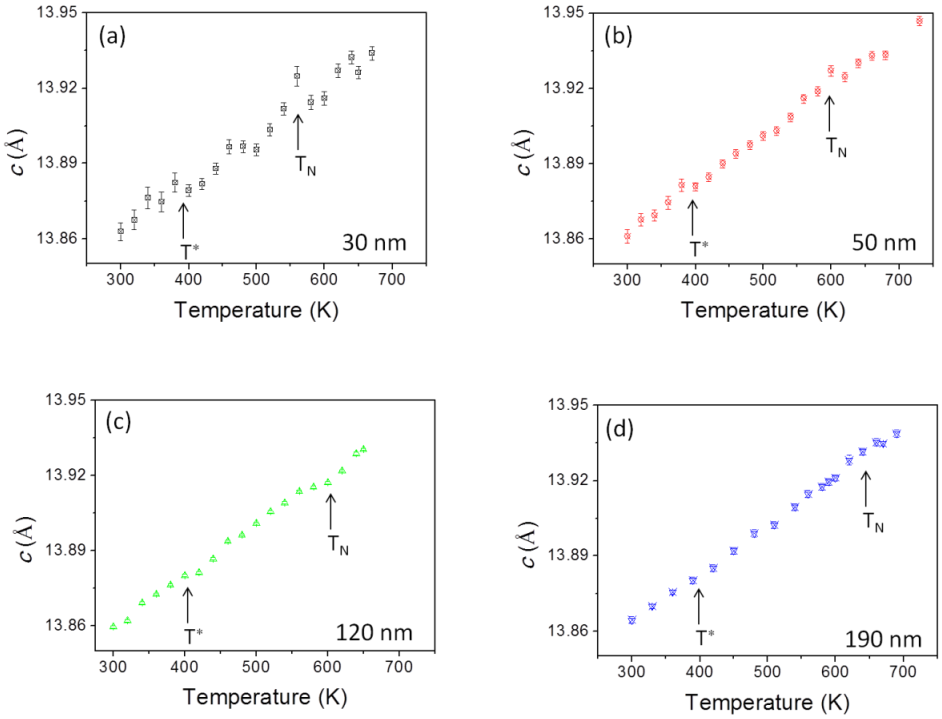


Figure 6.7 Parameter $c_{hex}$ variation of different size $BiFeO_3$ as a function of temperature, (a) 30 nm; (b) 50 nm; (c) 120 nm; and (d) 190 nm.

Table 6.3 Lattice expansion coefficients of different size $BiFeO_3$ particles

| Sample | $\alpha_{hex}\times10^{-5}$ (Å/K) | $c_{hex}\times10^{-5}$ (Å/K) | $V\times10^{-3}$ (Å$^3$/K) | $T^*$ | $T_N$ |
|---|---|---|---|---|---|
| 30 nm | 5.7(2)±0.2 | 19.3(4)±0.8 | 12.9(8)±0.5 | ~390 K | ~580 K |
| 50 nm | 5.9(9)±0.1 | 19.6(6)±0.4 | 13.3(7)±0.3 | ~390 K | ~600 K |
| 120 nm | 5.9(7)±0.1 | 19.9(5)±0.3 | 13.4(4)±0.2 | ~400 K | ~600 K |
| 190 nm | 5.9(2)±0.08 | 19.3(8)±0.2 | 13.1(8)±0.2 | ~400 K | ~610 K |
| Micro | 6.0(8)±0.1 | 21.4(0)±0.2 | 13.9(8)±0.3 | ~400 K | ~650 K |

## 6.2 Raman spectra for different size $BiFeO_3$

As mentioned before, for $BiFeO_3$, the ferroelectric order originates from the stereochemical activity of Bi lone electron pair. The A site $Bi^{3+}$ ion shows a valence electron configuration of $6s^26p^0$, the lone $6s^2$ electrons of $Bi^{3+}$ ion hybridize with both empty $6p^0$ orbitals of $Bi^{3+}$ ion and the $2p^6$ electrons of $O^{2-}$ ion to form Bi-O covalent bonds, which leading a structure distortion and ferroelectric order[69-70]. This ferroelectric mechanism is different from other conventional perovskite oxide ferroelectrics.

For $BiFeO_3$[132, 133], we identify phonon modes containing information of different atomic distortions, sensitive to structural phase transition, but also to magnetic order. About the available optical modes from the group theory, it is predicted that $BiFeO_3$, belonging to *R3c* space group, it should display optical phonon modes given by[178-179]:

$$\Gamma_{opt}(R3c) = 4A_1^{IR,R} + 9E^{IR,R} + 5A_2 \qquad [6.1]$$

The $A_1$ and $E$ modes are both IR and Raman active, whereas the $A_2$ modes are both IR and Raman inactive. Further, to detect these different phonons, propagation direction against light polarization can be used. In fact, the $A_1$ modes are polarized along *z* and the doubly degenerate *E* modes polarized in the *x*-*y* plane. Thus typically $A_1$ phonon modes detected are longitudinal optical (LO) phonons and *E* are transverse optical (TO) vibrational modes.

### 6.2.1 Room temperature Raman spectra of $BiFeO_3$ nanoparticles

First of all, Figure 6.8 shows the Raman spectrum for $BiFeO_3$ micrometric particles, which provides a reference for the investigation on $BiFeO_3$ nanoparticles. We note that the number of Raman modes in Raman spectrum are more than 13 modes expected in *R3c* space group. Given the high sample quality and the fact the no Raman modes are observed from impurity phases ($Bi_2O_3$, $Fe_2O_3$, $Fe_3O_4$ *etc*.), we conclude that all recorded Raman modes belong to $BiFeO_3$. On the other hands, all the Raman modes are infrared-active, as a conclusion, the LO-TO splitting is expected as a result of long range electrostatic forces[180], which can insert other modes in the Raman spectrum.

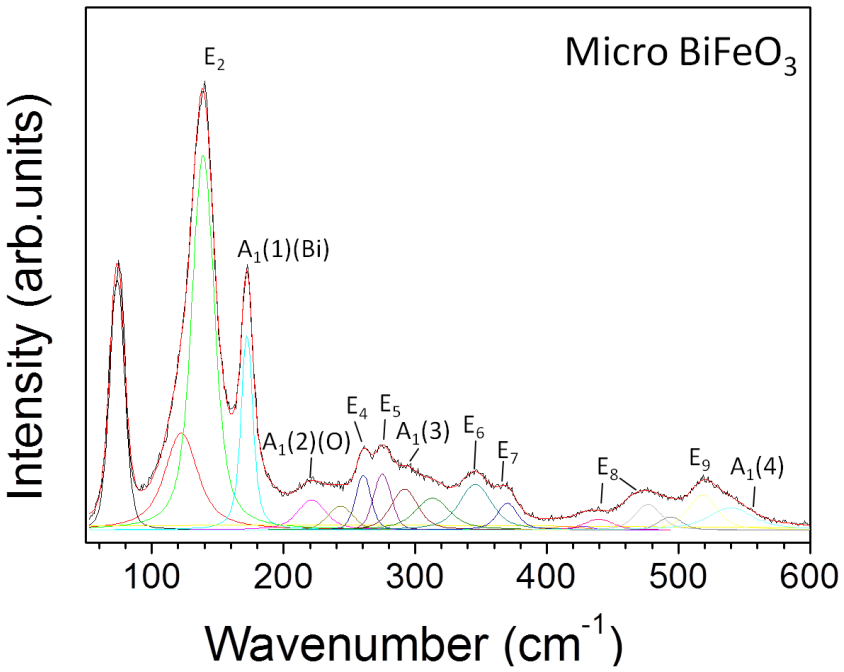


Figure 6.8 Room temperature Raman spectra of micrometric size $BiFeO_3$ powders in the spectral range 50-600 $cm^{-1}$. The first order Γ-point phonons are visible below 600 $cm^{-1}$, together with mode symmetries taken from Ref.[181] and predominantly involving atomic species taken from the first-principles study in Ref.[132]. The modes are numbered according to ascending frequency.

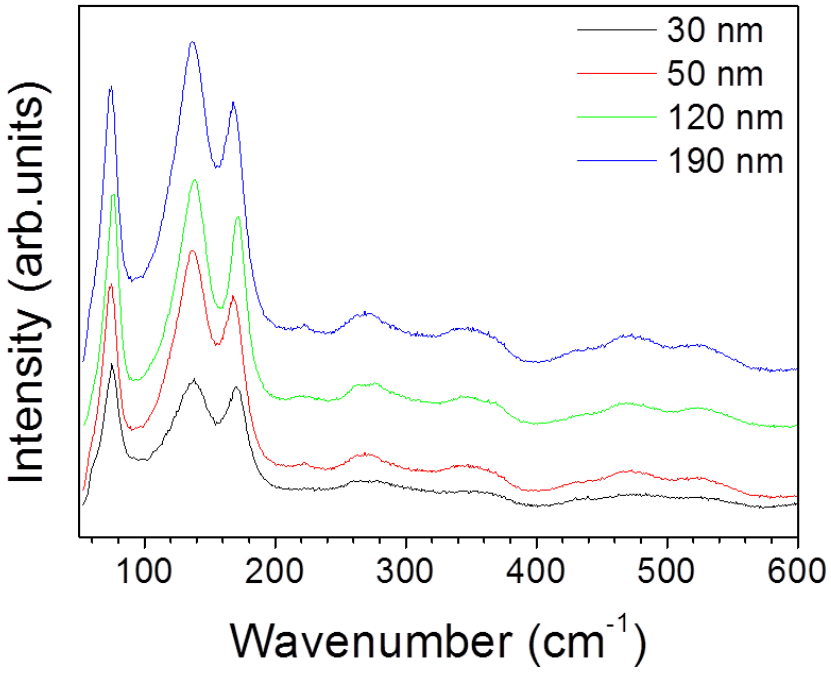


Figure 6.9 Room temperature Raman spectra of different size $BiFeO_3$ nanoparticles in the spectral range 50-600 $cm^{-1}$.

Compared to $BiFeO_3$ micro-particles data (Figure 6.8), $BiFeO_3$ nanoparticles (Figure 6.9) have the same spectrum assignment as a whole. However, differences also exist form the details which will be analyzed in the following. Even though $BiFeO_3$ has been extensively studied with Raman spectroscopy, the assignment of the phonons is still controversial. In this work, we will adopt the assignments from Refs. [181] and [132] as our starting point. The peak assigned as *A*1 and *E* features are also in reasonable agreement with calculated and experimental results[132, 182]. For $BiFeO_3$ Raman spectra which have been largely reported[183-186], the lower wavenumber vibration modes below 170 $cm^{-1}$ give the information about Bi atoms and the oxygen motion strongly dominates in the modes above 267 $cm^{-1}$. The Fe atoms are mainly involved in the modes between 152 and 261 $cm^{-1}$ and also contribute to some high wavenumber modes. We attribute the low modes to the *E* ($LO_2$) one at 140 $cm^{-1}$, and to the $A_1$ ($TO_1$) one at 170 $cm^{-1}$, which overlap with the A-site displacement caused by the activation of Bi lone pair. These low modes are predominantly linked to the Bi atom. The mode at 220 $cm^{-1}$ has been assigned as the oxygen mode with $A_1$ symmetry which is related to the structure distortion away from the ideal $Pm\bar{3}m$ structure, which has been assigned to $A_1$ (O). The mode at 260 $cm^{-1}$ is assigned as *E* mode with is related to the Fe-O covalent bond and corresponding Fe-O-Fe angle. The modes higher than 600 $cm^{-1}$ belong to the second-order Raman scattering which is related to the electron-phonon interaction in $BiFeO_3$. If the structure distortion happened, the spin-phonon and electron-phonon coupling will happened[178] and obvious Raman modes change can be observed in the second-order scattering, which will explain in detail in the doping $BiFeO_3$ sample. The computed frequencies of the $A_2$ modes are 109, 261, 308, 446, and 579 $cm^{-1}$, respectively. These frequencies, however, cannot be compared to experimental values since no experimental inelastic scattering data are presently available.

We want to qualitately focus on the shape, intensity and wavenumber values of the peaks between the multi-crystal $BiFeO_3$ microparticles spectrum (Figure 6.8) and the $BiFeO_3$ nanoparticles spectra (Figure 6.9). For micro-$BiFeO_3$, Voigt functions have been used for fitting the Raman modes and different modes have been marked (Figure 6.8). A notable intensity change in the peaks with varying size has been

observed. Obviously, the peaks are intensified with crystal size increasing. A similar phenomenon has been reported in Refs. [35, 157]. The increase in peak intensity and slight change of wavenumber of normal $A_1$ mode with increasing crystal size implies the enhancement in the contribution of the Bi-O vibrational mode, which might be caused by different lattice distributions and change in the spin-phonon coupling in the different size $BiFeO_3$ nanoparticles[80]. We recall that the first order $\Gamma$-point phonons are visible below 620 $cm^{-1}$ and thus we can obtain detailed information on the structure of the sample. Since the Raman spectra of nano-$BiFeO_3$ (Figure 6.9), has the same mode assignment than the micro-$BiFeO_3$ (Figure 6.8), we conclude that the crystal structure doesn't change when the particle size is reduced to 30 nm, keeping the *R3c* structure[79-80]. However, when observed in detail, some fine disparities can be found. Compared to the micro $BiFeO_3$ spectrum, for the nano-$BiFeO_3$ two modes at ~360 $cm^{-1}$ and two other ones at ~270 $cm^{-1}$ are merged together with decreasing the particle size. Another difference is observed on the relative intensity of the modes between 470 $cm^{-1}$ and 530 $cm^{-1}$. The mode at ~360 $cm^{-1}$ is related to the oxygen chain of octahedra and relative intensity variation means the octahedral environment has changed as particle size decreases. Although in our work the second order Raman scattering is not shown because of the wavenumber limit, for the purpose of understanding the present data, we note Johan *et al.*[178] reported mode combination between first order scattering (below 900 $cm^{-1}$) and second order (above 900 $cm^{-1}$). According to their results, the mode at ~470 $cm^{-1}$ and ~530 $cm^{-1}$ are combined with the mode at 950 $cm^{-1}$ and 1150 $cm^{-1}$. However, in our result, the mode at ~530 $cm^{-1}$ is still ambiguous. The relative intensity variation of modes at ~470 $cm^{-1}$ and ~530 $cm^{-1}$ means the different electron-phonon interaction which can be explained by Fröhlich mechanism[187]. Some articles have reported that there exists a critical particle size (~8 nm) for phase transition of $BiFeO_3$ when particle size decreasing[79-80]. As shown in our case, through the relationship between Raman modes and crystal structure, the shifts of the Raman modes with decreasing the particle size in the low wavenumber range from ~100 to ~200 $cm^{-1}$ is presented in Figure 6.9.

Figure 6.10 displays the Raman spectrum of the low wavenumber region (80 $cm^{-1}$ to 200 $cm^{-1}$) of micro-$BiFeO_3$ (Figure 6.10 (a)) together with the wavenumber values of the corresponding peaks for the different nano-$BiFeO_3$ samples (Figure 6.10 (b)). Striking finite length scale effects are evident from the observed nanoparticle response in this wavenumber range. From the fitting results (Figure 6.10 (b)), we distinguish that the Raman mode *E* (TO) near 110 $cm^{-1}$ has shifted to lower wavenumber values with particle size decreasing.

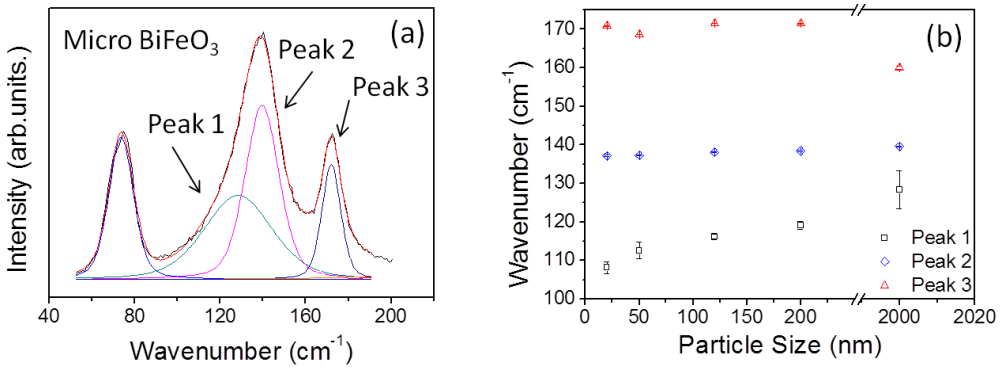


Figure 6.10 (a) Raman spectrum and corresponding fitting of micro $BiFeO_3$ at low wavenumber from 80 $cm^{-1}$ to 200 $cm^{-1}$; (b) Shifts of the Raman modes with particle size increasing for the three different Raman modes shown in (a).

Like mentioned above, the low wavenumber vibrational modes below ~170 $cm^{-1}$ give the information about Bi atoms. For the rhombohedral of $BiFeO_3$, Bi cations move out-of-phase with respect to $FeO_6$ octahedral along the polar direction, while the two adjacent $FeO_6$ octahedral counter rotate about the [111] axis. Fe cation displacements are fairly large, so they move off-center in the octahedral. These displacements can be evidenced by displacive phonons[80, 179]. The systematic red shift of the *E* (TO) vibrational mode (Figure 6.10 (b)) and the relative intensity change of the Raman modes at 360 $cm^{-1}$, 470 $cm^{-1}$ and 530 $cm^{-1}$ with decreasing size (Figure 6.9) strongly support its assignment as the soft mode driving the ferroelectric transition. Moreover, the *E* mode is under damped in the smallest particle size 30 nm $BiFeO_3$, suggesting a first order nature. This means that the stereochemical activity of the Bi lone electron pair plays a main role in the change of Bi-O covalent bond.

According to the above analysis and based on the observed phonon shift trend, decreasing the crystal size implies a change of the Bi-O covalent bonds as a result of

the decline in the stereochemical activity of the Bi lone electron pair. This change weakens the intensity and broadens the width of the Raman modes, special for low wavenumber ones.

### 6.2.2 Temperature dependence of $BiFeO_3$ Raman spectrum

Since the Raman spectra are sensitive to atomic displacements, the shift in Raman modes with temperature can provide valuable information about lattice distortions and electric polarization.

From now on, to simplify the temperature dependence analysis and get qualitative information on the thermal evolution of low wavenumber range of the Raman spectra of different size nano-$BiFeO_3$, we have fitted these data with Asy2sig functions. Representative Raman spectra deconvolution for different size $BiFeO_3$ at room temperature is shown in Figure 6.11, where a strong asymmetry for the low wavenumber modes is observed. It can be seen that the phonon anomaly is very pronounced for the band at ~140 $cm^{-1}$.

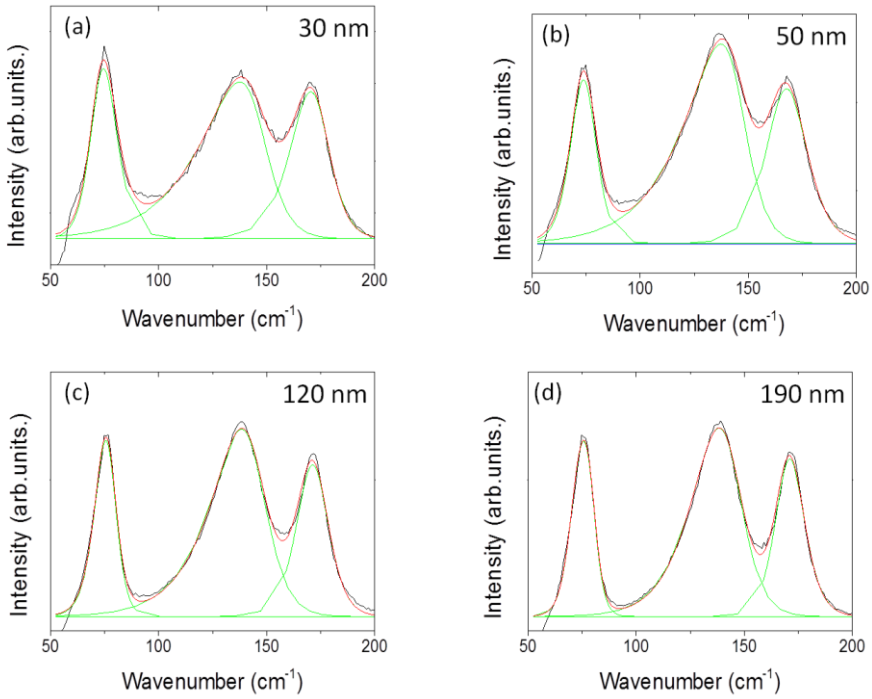


Figure 6.11 Below 200 $cm^{-1}$ raw Raman spectra (black lines) and deconvolution using Asy2sig functions (green and red lines) for different size $BiFeO_3$ nanoparticles.

To emphasize on these anomalies, Figure 6.12 presents a more detailed view of the temperature dependence of the modes at ~140 $cm^{-1}$ and ~170 $cm^{-1}$. For different $BiFeO_3$ nanoparticles, a closer inspection of these data reveals a noticeable spectral change in the vicinity of 500-550 K. The anomalies in the full width at half maximum (FWHM) (Figure 6.13) and in intensity (not shown) also clearly point out two changes of regime. We note that the earlier reported phonon anomalies for the $BiFeO_3$ ceramic at low temperature (140 K and 201 K) link to surface confined phase transition[188], and another transition of $BiFeO_3$ related to its surface layer has been confirmed using impedance analysis and grazing incidence x-ray diffraction at 550 K[189]. Due to the surface has its own symmetry and undergoes its particular phase transition, surface-sensitive probes such as backscattering Raman have shown an onset of phonon softening at 543 K[182].

To figure out if these anomalies are related to the surface effects, we analyze the data from different size nanoparticles. At first sight, the considerable spectral changes at $T^*$[182] suggest a structural rearrangement which has to be subtle on a local level. From the X-ray diffraction data (chapter 6.1.1), the $T^*$ transition for $BiFeO_3$ nanoparticles has also been deduced from X-ray diffraction analysis, with very similar $T^*$ values (~400 K) for different size $BiFeO_3$ (Figure 6.5-Figure 6.7, Table 6.3). However, it is hard to detect surface layer properties transitions for nanoparticles by X-ray diffraction using laboratory setups, since it is essentially sensitive to the volume of the crystal. Moveover, the crystalline size of the nanoparticles being in the nanometric scale, the width of the X-ray diffraction peak of these powders is intrinsically large due to size effects, thus any surface effect is smeared out. We note that it is also difficult to detect this transition from the optical characterization in the UV and visible range (allowing us to determine the band gap value and Urbach energy), corresponding data and analysis are included in chapter 7. Adding all these effects, these anomalies seen by Raman spectroscopy are speculated to be related to the skin layer structure of $BiFeO_3$, since the elongated out-of-plane lattice parameter has been verified within a few nanometers from the surface[188-189].

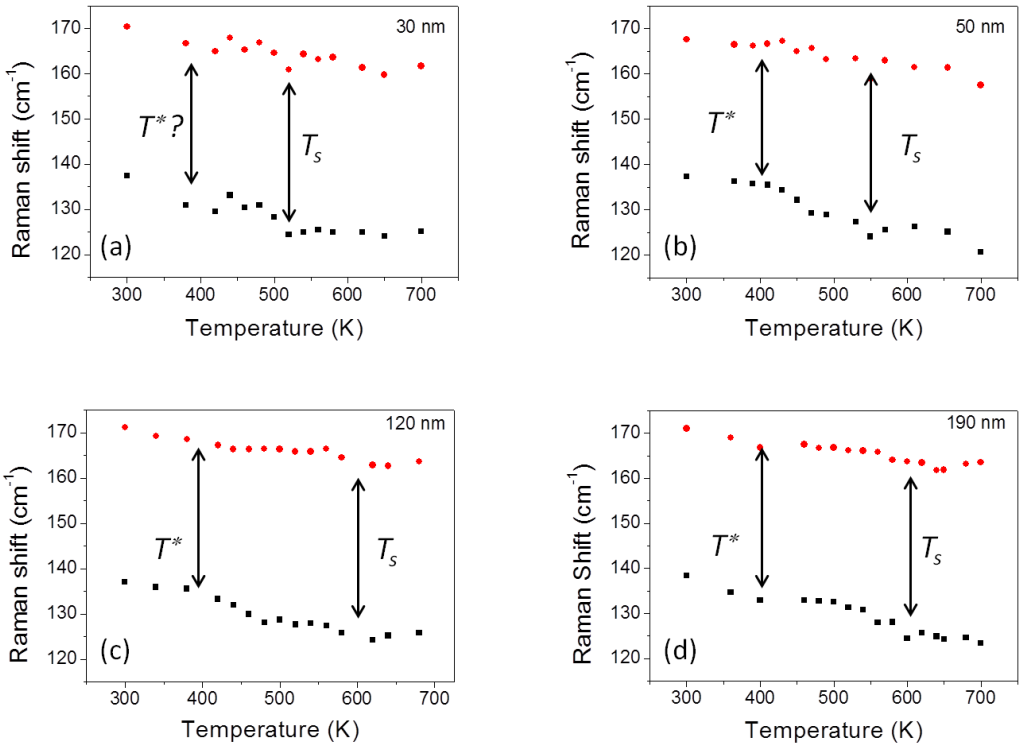


Figure 6.12 Temperature dependence of Raman modes (~140 $cm^{-1}$ and ~170 $cm^{-1}$) shift for different particle size: (a) 30 nm, (b) 50 nm, (c) 120 nm and (d) 190 nm

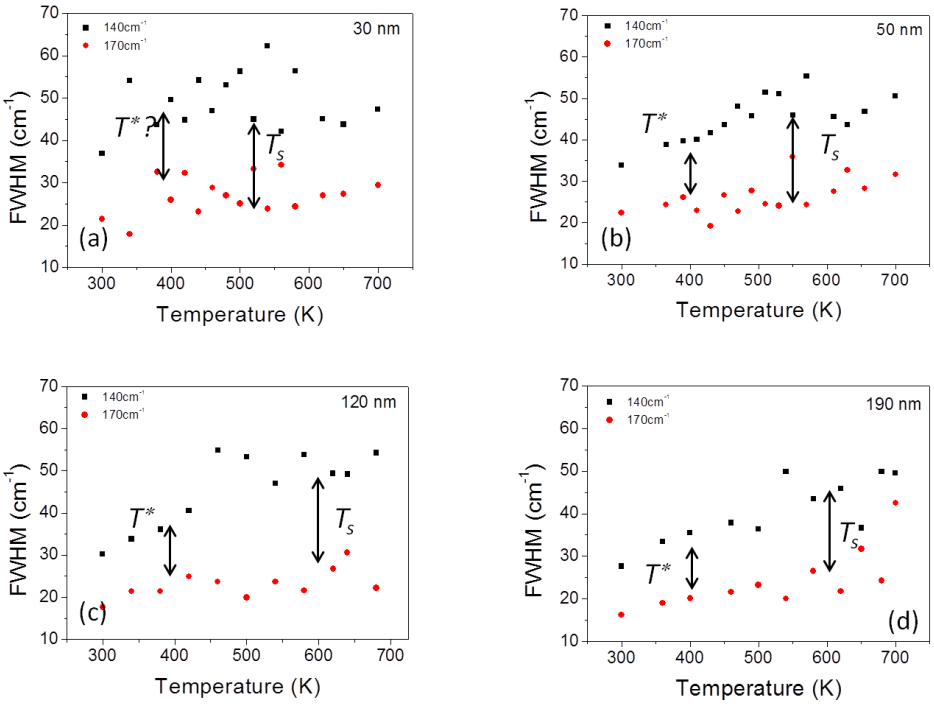


Figure 6.13 Temperature dependence of the full width at half maximum (FWHM) for different Raman modes (~140 $cm^{-1}$ and ~170 $cm^{-1}$) of different particle size: (a) 30 nm, (b) 50 nm, (c) 120 nm and (d) 190 nm

It is known that any static and dynamic changes in the structures should, in principle, lead to a variation in the phonon behavior, and the analysis of the wave number, intensity, and line width evolution of the whole spectra as a function of temperature. A weak thermal transition region, limited by two Raman anomalies is observed from $T^*$ to $T_s$, $T_s$ being the transition temperature related to relaxation energy and magnetic properties at the surface, in different size $BiFeO_3$ nanoparticles (Figure 6.12 and Figure 6.13). The summary of the values of these anomalies are shown in Table 6.4. We speculate that this $T_s$ transition is related to the $BiFeO_3$ skin layer and thus it should be sensitive to the surface to volume ratio of the particles. Thus, comparing the Raman shifts and the corresponding FWHM data of different size nanoparticles (Figure 6.12 and Figure 6.13), we notice that the upper value of this region, $T_s$, for different size nanoparticles decreases with particle size decreasing. Indeed, $T_s$ is reduced from ~600 K to ~510 K. It means that the different size $BiFeO_3$ nanoparticles have different phonon energy state for the skin layer. The skin will more strongly contribute to the Raman spectra on samples with a large surface to volume ratio. It has been reported that if a skin layer exists, a core-shell structure composed by a bulk-like $BiFeO_3$ core and a $BiFeO_3$-skin layer shell represents quite accurately any $BiFeO_3$ nanoparticle. The magnetic properties of these nanoparticles have been measured evaluating the zero-field cooling and field cooling magnetization experiments, and with particle size decreasing, the surface contribution of smaller particle is predominant[35]. In our case, from the Figure 6.12 and Table 6.4, lower $T_s$ values can be observed for smaller size nanoparticles, which is in agreement with the reported data on other $BiFeO_3$ nanoparticles.

Table 6.4 Temperature transitions observed from low wavenumber Raman modes (~140 $cm^{-1}$ and ~170 $cm^{-1}$) for different size $BiFeO_3$ nanoparticles

| **Sample** | $T^*$ **(K)** | $T_s$ **(K)** |
|---|---|---|
| 30 nm | ~390 | ~520 |
| 50 nm | ~400 | ~550 |
| 120 nm | ~400 | ~600 |
| 190 nm | ~400 | ~610 |

As mentioned begin, the Raman modes at these low wavenumbers are mainly related to the phonon of Bi atom, the observed phonon anomalies as a function of temperature illustrate a difference of Bi state in the surface and in the bulk due to surface reconstruction/relaxation and some other local defects being also possible, but in any case essentially being predominant at the surface. Jarrier *et al*.[188] have already reported that the some defects exist at the surface of $BiFeO_3$ samples due to bismuth volatility, the most probable defects are Bi vacancies due to bismuth volatility. In our case, due to the low temperature synthesis of our samples, Bi should be in a stoichiometric state. Nevertheless, other surface effects can be claimed to produce similar polar effects as those reported in Ref [188]. For instance, as we will see in chapters 6.2.3 and 6.2.4, a change on the Fe valence at the surface compared to the bulk of the nanoparticle is possible, as well as the stabilization of other absorbates, such as FeOOH. Thus, we note that these surface effects can effectively change the local electronic structure and bonding energy. As it has been seen in Ref [189], the variation of lattice parameter at the surface, as indicated by the grazing incidence XRD, induce the strong uniaxial strain in the surface[189], which further induces the creation of a shallow impurity level resulting in the structure release at the surface. Similar effects are the possible disorder origin in our systems, affecting the surface structure and changing the Bi sublattice with decreasing the particle size[80], which is likely to be a plausible explanation for the different surface transition temperatures as a function of the particle size.

### 6.2.3 Raman spectra of A-site doped $BiFeO_3$ particles

The discovery of the unusual multiferroic together with an observed magnetoelectric coupling in $BiFeO_3$ have generated a large amount of scientific research. Among different effects, isovalent and non-equivalent atomic substitution on the Bi and/or Fe site can destroy the spin cycloid and affect the magnetoelectric coupling[76, 190-191]. Upon substitution on the $Bi^{3+}$-site, this induced distortion can eventually lead to a perturbation of the Bi 6*s* lone pair electrons and a concurrent of a change in the space group form the polar *R3c* to nonpolar space groups, depending on the nature of the substituting element. In this work, $La^{3+}$ and $Ca^{2+}$ ions have been used for

substitution atoms on the $Bi^{3+}$-site, for different reasons: $La^{3+}$ ions represent an isovalent substitution with a small change in the ionic radius from 116 pm to 117 pm between $La^{3+}$ and $Bi^{3+}$, whereas $Ca^{2+}$ ions present a different valence state and very different ionic radius, which implies that the substitution introduces a significant lattice distortions as well as perturbing the electronic landscape and in particular the band gap.

Here, La and Ca doping of $BiFeO_3$ samples have been achieved following the synthesis presented in chapter 4, keeping a low dopant concentration (5 mol% and 10 mol%). The purity and crystal structure of the $Bi_{1-x}La_xFeO_3$ ($0 \leq x \leq 0.1$) and $Bi_{1-x}Ca_xFeO_{3-\delta}$ ($0 \leq x \leq 0.1$) samples prepared for the Raman measurements were assessed on the basis of the long scan XRD data (chapter 5, Figure 5.14). For these dopants and keeping a dopant concentration lower than 10%, the diffraction pattern was characteristic of *R3c* symmetry, similar results being reported in Ref. [78, 128, 174, 178].

The allowed Raman modes of La and Ca doped $BiFeO_3$ compounds have been analyzed. Because $Bi_{1-x}La_xFeO_3$ ($0 \leq x \leq 0.1$) and $Bi_{1-x}Ca_xFeO_3$ ($0 \leq x \leq 0.1$) keep the same space group than $BiFeO_3$, Raman modes depicted by doped samples are similar to those of the $BiFeO_3$. We note that only the position and intensity of the modes are affected by this doping. In particular, the number of Raman allowed modes of doped samples is as follows[178-179]:

$$\Gamma_{opt}(R3c) = 4A_1^{IR,R} + 9E^{IR,R} + 5A_2 \qquad [6.2]$$

which are the same as those of $BiFeO_3$. We recall that in $BiFeO_3$, the low $A_1$ (TO) mode at 170 $cm^{-1}$, overlapping with the A-site displacement caused by the activation of the Bi lone pair , corresponds predominantly to Bi motions. The atomic motions of the modes at 220 $cm^{-1}$ originate from the relative soft oxygen mode with $A_1$ symmetry. Thus, these two modes will be affected by the A-site doping.

Firstly, in Figure 6.14, the Raman spectra for La doped $BiFeO_3$ nanoparticles for different concentrations and sizes (Figure 6.14 (a) and (b)) are presented and compared to the corresponding data for $BiFeO_3$ micro and nanoparticles (Figure 6.14 (c) and (d)). At the low wavenumber range (Figure 6.14 (a) and (c)), it can be seen

that the $E_2$ ~140 $cm^{-1}$ and $A_1$ ~170 $cm^{-1}$ modes of La doped $BiFeO_3$ nanoparticles are shifted to lower wavenumbers compared to those of $BiFeO_3$ micro and nanoparticles, in particular for La 10% doped $BiFeO_3$ (mode position indicated by vertical line and arrows). The decrease of size of the La-doped nanoparticles affects in the same way these modes as for $BiFeO_3$ nanoparticles, and we notice a similar increase on the width of the modes. For the high wavenumber range (Figure 6.14 (b)), a close examination of the mode at 350 $cm^{-1}$ reveals a gradual shift to lower wavenumber with La doping concentration increasing, when compared to $BiFeO_3$ micro and nanoparticles spectra in the same range (Figure 6.14(d)) (reference mode position indicated by vertical lines and corresponding shifts by arrows). We also note that the intensity of the mode at 620 $cm^{-1}$ (vertical line) is strengthen for all La doped samples presenting 35 nm-particle size, this latter effect has also been observed for 30 nm-$BiFeO_3$ nanoparticles (arrows).

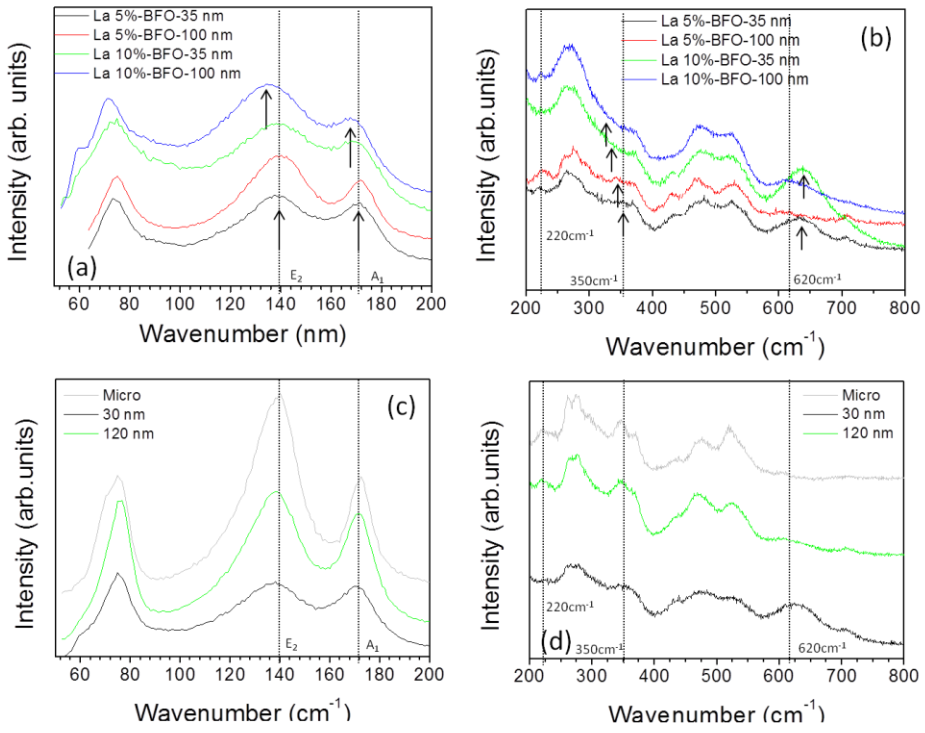


Figure 6.14 Room temperature Raman spectra of: [(a) and (b)] La doped $BiFeO_3$ nanoparticles with different La content and size, as indicated in the legend, and [(c) and (d)] pure $BiFeO_3$ micro and nanoparticles, with sizes indicated in the legend. The Raman spectra have been separated into different panels, for low spectral range (below 200 $cm^{-1}$) [(a) and (c)], and for high spectral range (200 $cm^{-1}$ to 800 $cm^{-1}$) [(b) and (d)]. Vertical dotted lines indicate the mode reference position for the pure $BiFeO_3$ . Closest arrows indicate the evaluated position for the La doped $BiFeO_3$ nanoparticles.

A general feature of $BiFeO_3$ based compounds when doping on the A-site is realized[178] is a strong shift of the $A_1$ mode, which is identified by first-principle calculations as arising from both Bi motions and oxygen octahedra tilts in *R3c* $BiFeO_3$[132]. From Figure 6.14, the $A_1$ mode at ~220 $cm^{-1}$ decreases in intensity for doped and undoped samples with smaller size. However, this $A_1$ mode is weakly affected by the La doping, whereas the doping strongly affects the position of $A_1$ mode at lower wavenumber ~170 $cm^{-1}$ but also that of the E mode at 140 $cm^{-1}$. This result can be expected based on the fact that the ionic radius of La and Bi are very close, thus Bi-sublattice and oxygen octahedra tilt distortions at low doping level is relatively weak. We point out that weaker shifts on the B-site can be noticed, such as on the *E* mode at ~260 $cm^{-1}$ associated to the Fe-O covalent bond[174, 178], indirectly related to the Fe-O-Fe bond angle, which may affect the antiferromagnetic order, potentially seen from a larger spin canting effect, leading to the existence of a weak ferromagnetism stabilized by the La doping but also by the increase of the surface in smaller nanoparticles[36].

Continuing the study on oxygen motion modes, comparing the *E* Raman mode at ~350 $cm^{-1}$ of La doped samples against $BiFeO_3$ micro and nanoparticles in Figure 6.14(b) and (d), respectively, it can be seen that the mode frequency shifts towards lower values with increasing the La doping. This significant variation in *E* modes due to La substitution signals that there is a significant destabilization of the oxygen octahedra chains, which in-turn affects the local $FeO_6$ octahedral environment. Here we must remember that the activation of the Bi lone pair electrons and the corresponding [111] displacement of the Bi atoms depends on a Bi *s*-O *p*/*s* hybridization that, in itself, affects unit cell parameters and polarization. Loss of the Bi *6s* lone pair electrons with the $La^{3+}$ substitution will thus alter the oxygen octahedra arrangement even in the absence of direct lattice deformations, thus causing a contraction of the unit cell, resulting in the observed weakening of the *E* mode. Besides, ferroelectric polarization will be consequently decreased by the La doping.

When comparing the high wavenumber range Raman spectra of different La doped samples with those of $BiFeO_3$ nanoparticles, it can be found that the relative

intensity of the ~620 $cm^{-1}$ mode increases with decreasing the particle size. Nevertheless, a more detailed mode assignment is lacking for this vibrational mode at ~620 $cm^{-1}$, which is not fitted in the expected allowed Raman first $\Gamma$-point phonons. Bielecki *et al.*[178] have reported that in the polar *R3c* structure, though there can be found completely Raman silent $A_2$ modes, infrared active vibrations can also be Raman active due to the loss of inversion center and the existence of Fröhlich mechanism related to the second-order scattering. Therefore, the mode at ~620 $cm^{-1}$ is expected to be a Fröhlich activated mode[187], following first-principles calculations that predicts the highest $A_2$ mode may lie between 620 $cm^{-1}$ and 700 $cm^{-1}$, depending on the functional used[132]. Moreover, it can be seen that the intensity of this mode at ~620 $cm^{-1}$ is independent of the La dopant concentration. Here, we speculate that from the similar radius values of $Bi^{3+}$ and $La^{3+}$, weak effects are expected on the oxygen octahedra chains, then the LO-scattering becomes more relevant and allowed through Fröhlich mechanism[187] in smaller $BiFeO_3$ nanoparticles (doped and undoped).

Ca doped $BiFeO_3$ nanoparticles have also been investigated in this work. Divalent cation substituted $Bi_{1-x}A_xFeO_{3-\delta}$ (A = Ca, Sr, Pb, and Ba) compounds have been already studied[78, 192]. Yang *et al.*[129] showed the presence of a ferroelectric-paraelectric boundary in Ca doped $BiFeO_3$ thin films with an atomic fraction of ~0.125. Since the high doping will cause strong structural distortions due to the large difference in ionic radius, in order to study the rhombohedral phase for our nanoparticles, we limited the Ca doping to low concentration values (5%, 10%).

Figure 6.15 shows the Raman spectra of different Ca dopant concentrations (5%, 10%) and different size nanoparticles at low wavenumber (50 to 200 $cm^{-1}$) and high wavenumber (200 to 800 $cm^{-1}$) (Figure 6.15(a) and (b), respectively) compared to the corresponding data for $BiFeO_3$ micro and nanoparticles (Figure 6.15(c) and (d), respectively) . It can been seen that, compared to $BiFeO_3$ particles, one new mode appears at low wavenumber at ~90 $cm^{-1}$ and the modes are shifted to higher wavenumber (vertical line and arrows at 90 $cm^{-1}$, Figure 6.15(a)). Still within the low wavenumber range, the $E_2$ ~140 $cm^{-1}$ and $A_1$ ~170 $cm^{-1}$ are shifted from their ideal

values even for 5% Ca doped samples, but the shift sign depends on the size of the nanoparticles. In fact, for 10% Ca doped nanoparticles, the broadening of these modes is larger than for the 5% Ca doped ones, but for the 10% Ca doped ones spectra, these modes keep the reference center positions at 140 $cm^{-1}$and 170 $cm^{-1}$. We also notice other mode shifts and broadening, in particular the *E* mode at ~350$cm^{-1}$ towards lower wavenumbers and the ~470 $cm^{-1}$ and ~520 $cm^{-1}$ modes towards higher wavenumbers, with the increase of doping.

The structure of $BiFeO_3$ is rhombohedral at room temperature, and the influence of Ca doping is to reduce both the volume and the rhombohedral distortion of the unit cell, which has been demonstrated by XRD patterns and corresponding analysis (chapter 6.1.2, Table 6.2). Published works have already reported that the Fe ions preserve their $Fe^{3+}$ oxidation state[78, 129] and, due to the divalent ions substituted in the doped compound, in order to equilibrate the charge balance, oxygen vacancies can be produced[76, 128-129]. Thus, we speculate that the observed broadness of the Raman modes, modes shifts to higher/lower wavenumber values and the appearance of a new mode in the low wavenumber range with the increase of Ca doping might be all caused by the reduction of the stereochemical activity of Bi lone pair electrons caused by a strong A-site lattice disorder and by the creation of oxygen vacancies.

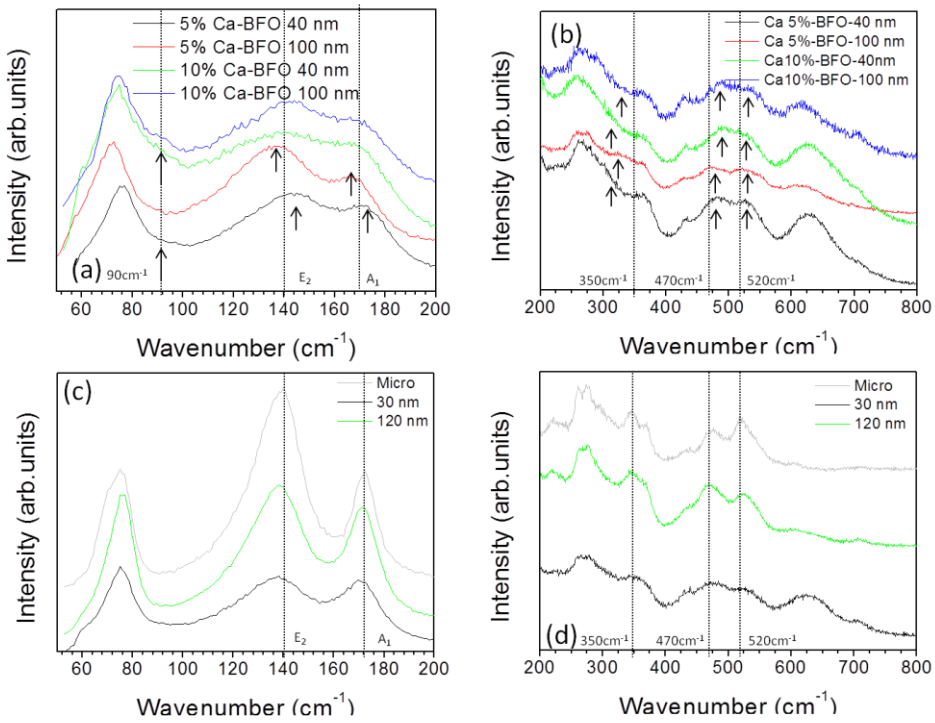


Figure 6.15 Room temperature Raman spectra of: [(a) and (b)] Ca doped $BiFeO_3$ nanoparticles with different Ca content and size, as indicated in the legend, and [(c) and (d)] pure $BiFeO_3$ micro and nanoparticles, with sizes indicated in the legend. The Raman spectra have been separated into different panels, for low spectral range (below 200 $cm^{-1}$) [(a) and (c)], and for high spectral range (200 $cm^{-1}$ to 800 $cm^{-1}$) [(b) and (d)]. Vertical dotted lines indicate the mode reference position for the pure $BiFeO_3$ . Closest arrows indicate the evaluated position for the Ca doped $BiFeO_3$ nanoparticles.

The Ca-doping will probably affect the magnetic properties of $BiFeO_3$, thus, which also can be detected by Raman spectrum analysis[78]. In Figure 6.15(b), within the spectral range from 200 $cm^{-1}$ to 600 $cm^{-1}$, the Raman spectra mainly reflect the information of Fe, O and Fe-O-Fe bonds[178], and it can be analyzed in view of the effect in the magnetic order. Similarly to La doping effects, at ~350 $cm^{-1}$, this *E* mode shifts to lower wavenumbers with the increase of Ca doping, which means the oxygen octahedra environment is changed by Ca doping. Since the Fe ions preserve their $Fe^{3+}$ oxidation state, the substitution of $Bi^{3+}$ by $Ca^{2+}$ has at least two structural effects, and probably indirect charge effects. Firstly, it contracts the lattice and it straightens the Fe-O-Fe bond angle. Secondly, it distorts the oxygen octahedra, and lastly it creates oxygen vacancies to keep charge neutrality.

From Figure 6.15(b), it also can be seen that the Raman modes at 470 $cm^{-1}$ and 520 $cm^{-1}$ are shifted to higher wavenumbers and present larger widths with Ca doping

concentration increasing. Divalent doping on the A-site in Fe and Cr perovskites have been deduced to be an effect of the oxygen vacancies and the local distortions that they induce[187]. Due to these local distortions of the oxygen network, the Ca doping on the Bi-site should influence the Fe-O-Fe bond angle, straightening it. In ceramics samples, it has even been already reported an increase of the Néel temperature $T_N$ with Ca doping[78]. Moreover, since the Bi sublattice is also strongly affected by the loss of the Bi *s*-O *p*/*s* hybridization, the ferroelectric polarization and Curie temperature $T_C$ of these compounds are thus expected to present a lower value compared to undoped $BiFeO_3$. From all these results, we can then speculate that for Ca doped samples the magnetoelectric coupling may be enhanced by this simultaneous increase of $T_N$ and decrease of $T_C$[193].

## 6.3 Nanostructure through Electron Microscopies

### 6.3.1 High Resolution Scanning Transmission Electron Microscopy for atomic scale structural characterization

Figure 6.16 shows the as-acquired High Resolution Scanning Transmission Electron Microscopy (HRSTEM) images on pure $BiFeO_3$ nanoparticles (120 nm) for two different indices of crystallographic plane, one oriented such that the incident electron beam is along $<001>_c$ (zone axis, Figure 6.16 (a) and (b)), and the second oriented along $<111>_c$ zone axis (Figure 6.16(c)). Figure 6.16(b) shows the HAADF STEM image from a region of the nanoparticle shown in Figure 6.16(a) (indicated in blue). It must be noted that contrast in HAADF STEM images emanates out of electron channeling along the atomic columns with $I \sim Z^2$, where $I$ is the intensity of a bright spot on a dark background and $Z$ is the effective atomic number of an atomic column along the zone axis[139]. In Figure 6.16(b), the brightest circles correspond to Bi atoms in $<001>_c$ columns, and the relatively dimmer contrast corresponds to Fe atoms along $<001>_c$ columns. From the structural projection of $BiFeO_3$ along the $<001>_c$ direction (Figure 6.16(a), inset), we simulated the HAADF STEM contrast by JEMS software (Figure 6.16 (b), inset). The square-like lattice pattern of Bi atoms in the simulation (Figure 6.16(b), inset) is in agreement with what is observed experimentally (Figure 6.16 (b)). Similarly, the hexagonal-like lattice in HAADF STEM pattern of $BiFeO_3$ structure simulated along $<111>_c$ zone axis (Figure 6.16(c), inset) depicts the corresponding experiment results (Figure 6.16(c)). It is important to realize that along the $<111>_c$ zone axis, every atomic column consists of equal number of Bi and Fe atoms, giving rise to the same intensity for all the columns.

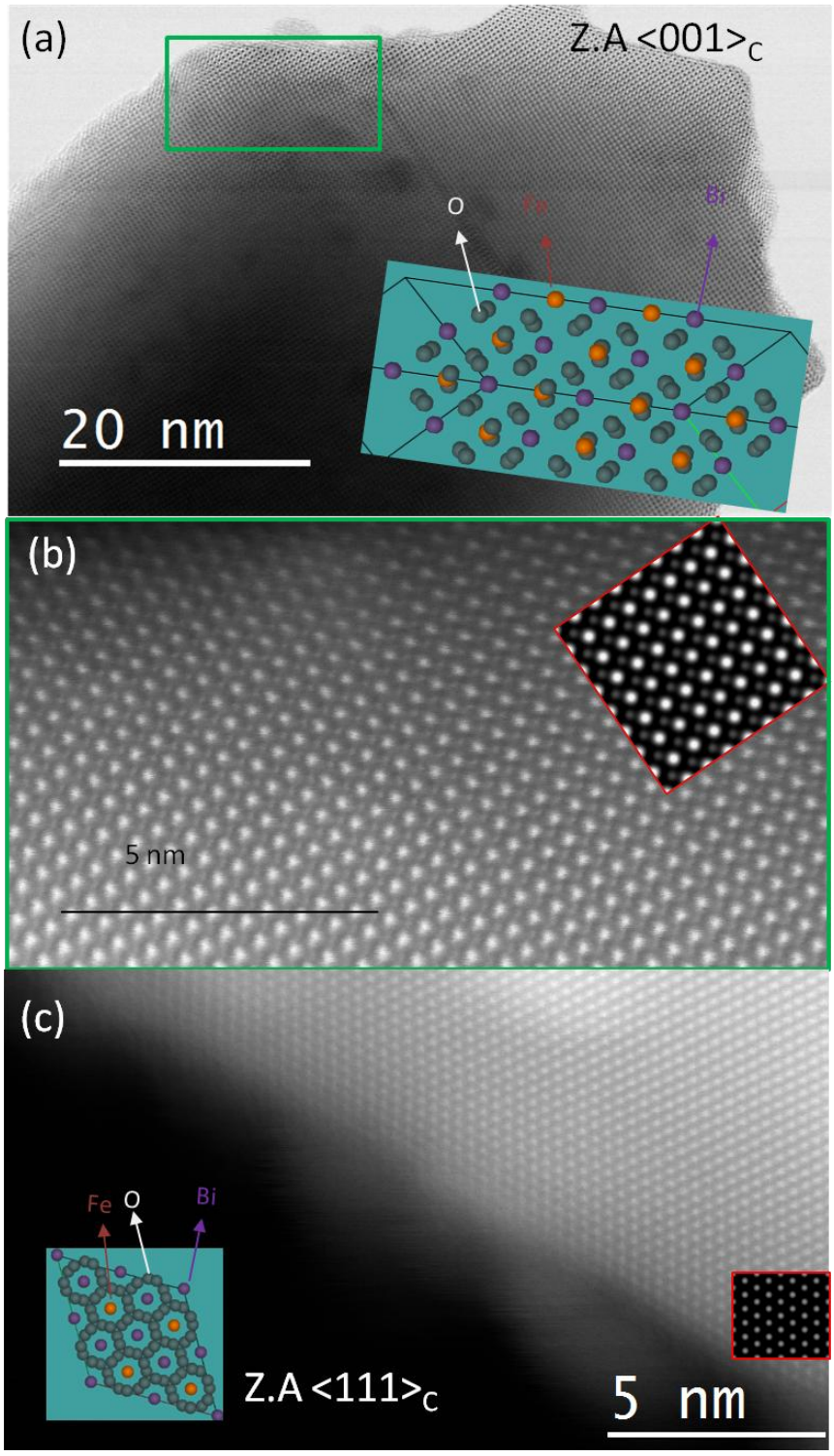


Figure 6.16 The as-acquired HRSTEM images on pure $BiFeO_3$ nanoparticles (120 nm) with two different crystallographic plane indices, one oriented such that the incident electron beam is along $<001>_c$ zone axis, (a) and (b), and the second oriented along $<111>_c$ zone axis, (c). We include simulated images (insets with red squares in (b) and (c)) and atomic structural models (blue sketches in (a) and (c)), obtained using JEMS software.

Owing to the energy minimization of elastic and electrostatic, coexistence of various ferroelastic and ferroelectric domains can be observed in $BiFeO_3$ samples. Polarization should lie along $[111]_c$ directions, thus, the interesting zone axis to

observe any atomic displacement should be $<001>_c$. To characterize the nature of domains, the first step in this direction was filtering both the low and high frequency noise from the HAADF STEM images shown in Figure 6.16. Figure 6.17 (a) shows such a processed image from a selected part of Figure 6.16 (b), presenting a nanoparticle along $<001>_c$ zone axis. It can be seen from the simulated HAADF STEM image (Figure 6.17 (b)) of a monodomain $BiFeO_3$ along $<001>_c$ zone axis that Fe atoms are all displaced in a particular $<110>_c$ direction from the center of the Bi square-like lattice, which is a projection of its original displacement along $[111]_c$ directions in *R3c* $BiFeO_3$. The existence of Fe displacements along different diagonals in different regions of the image reveals the coexistence of ferroelectric domains. To understand such Fe displacements, we performed a line scan over 11.5 nm along a $[1\text{-}10]_c$ direction connecting 20 Bi atoms, on the processed image (Figure 6.17 (a) and (c)). For the first 7 nm along the considered line, it can be seen from the Bi and Fe intensities that the Fe off-centering is indeed along the diagonal of the Bi lattice, pointing towards the bottom right Bi atom of every square-like Bi lattice, denoted precisely as $[110]_c$ (arrow in Figure 6.17(a)). The long and short bond distances between Bi and Fe are 3.2 and 2.5 Å respectively. Subsequently, from 7 to 9.5 nm along the line, we see a complete flip of Fe off-centering to $[\text{-}1\text{-}10]_c$ direction, resulting in a reversal of short bond and long bond ordering. Clearly, atoms in 7 to 9.5 nm and atoms in the first 7 nm belong to different ferroelectric domains. Beyond 9.5 nm along the line, we observe no contrast of Fe atoms, revealing a shift of Fe atoms along the other diagonal $[1\text{-}10]_c$ (arrows in the Figure 6.17(a)), and hence belonging to another (or other set of) ferroelectric domain(s). Furthermore, we also observe a smeared out of Fe contrast from 7 to 9.5 nm which can be modeled as a combination of Fe displacements along $[\text{-}1\text{-}10]_c$ and $[1\text{-}10]_c$ directions (off-centering towards top-right Bi), suggesting the coexistence of ferroelectric domains in the thickness direction, too. All in all, based on $<001>_c$ zone HAADF STEM image processing on a 40 $nm^2$ area of the sample, we can identify the coexistence of at least three different ferroelectric domains. This is our first strong evidence to show that our $BiFeO_3$ nanoparticles synthesized via sol-gel processing present ferroelectric domains.

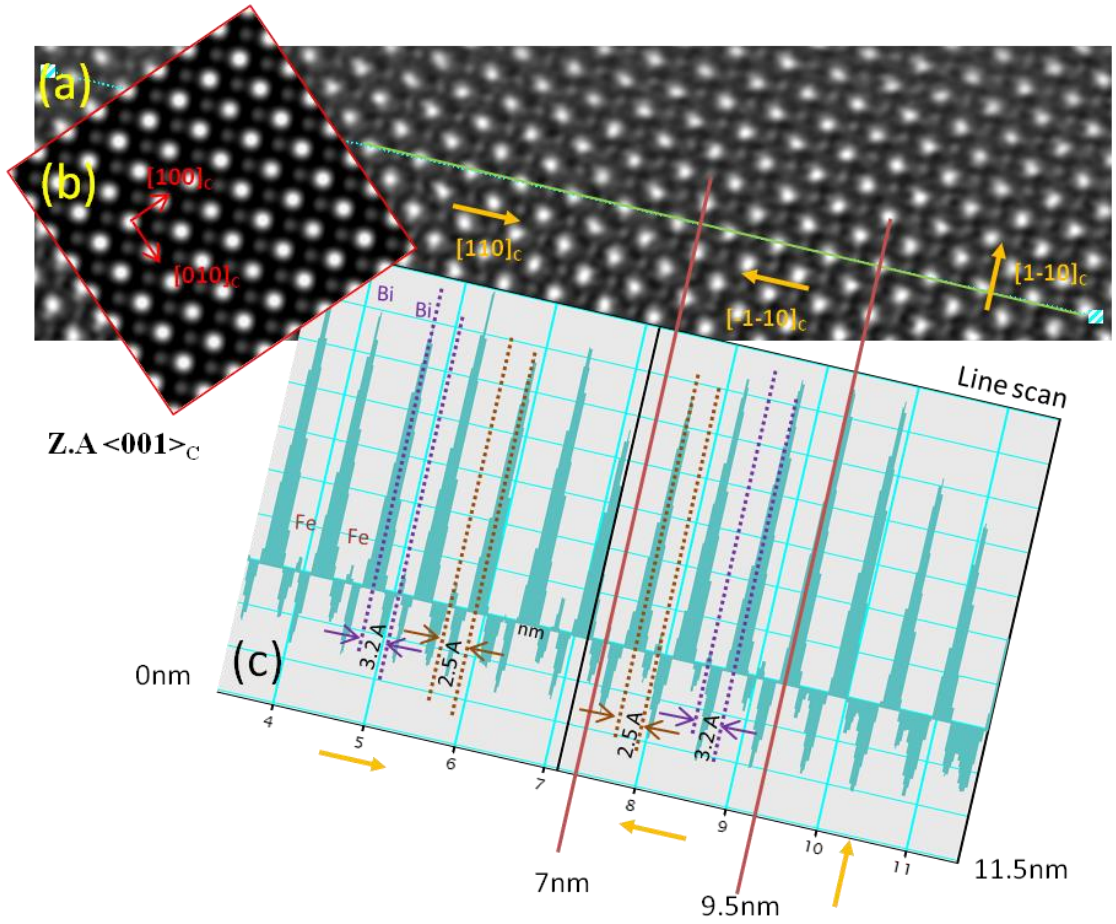


Figure 6.17 HAADF STEM image from a selected part of Figure 6.16 (b) after filtering both low and high frequency noise. The existence of Fe displacements along different diagonals in different regions of the image are observed, which reveals the coexistence of ferroelectric domains in $BiFeO_3$ nanoparticles.

### 6.3.2 Chemical analysis of pure $BiFeO_3$ and 10% La doped $BiFeO_3$ nanoparticles by Electron Energy Loss Spectroscopy

In the attempt to understand if the A site doping was homogenous and the possible electronic and chemical effects on the Fe site, we characterized 10%La (A-site) doped ferroelectric $BiFeO_3$ nanoparticles. To facilitate an easy comparison with our STEM and Electron Energy Loss Spectroscopy (EELS) results on pure $BiFeO_3$ nanoparticles, we selected 100 nm size particles, and observed them along $<001>_c$ zone axis. The first question we attempted to answer was whether La doping was uniform through the sample. For this, we generated energy filtered maps using EELS spectrum images of La distribution in the nanoparticle. A spectrum image (SI) is essentially HAADF STEM image, with every pixel additionally containing information on energy loss spectrum in a certain energy range. The loss peak at ~120 eV corresponds to a

delayed La N edge and thus we have used it to map La-distribution. By selecting the energy slice from 95 to 125 eV, and replotting the spatial information already available in the SI, we obtain the spatial map of La distribution (Figure 6.18 (b)). When compared with Fe maps generated from the energy slices around $L_{2,3}$ edges of Fe (Figure 6.18 (a)), we can see that while Fe is spatially very uniform, La is almost uniformly distributed with minor inhomogeneities within the inner part of the nanoparticle (indicated by red circles on the image).

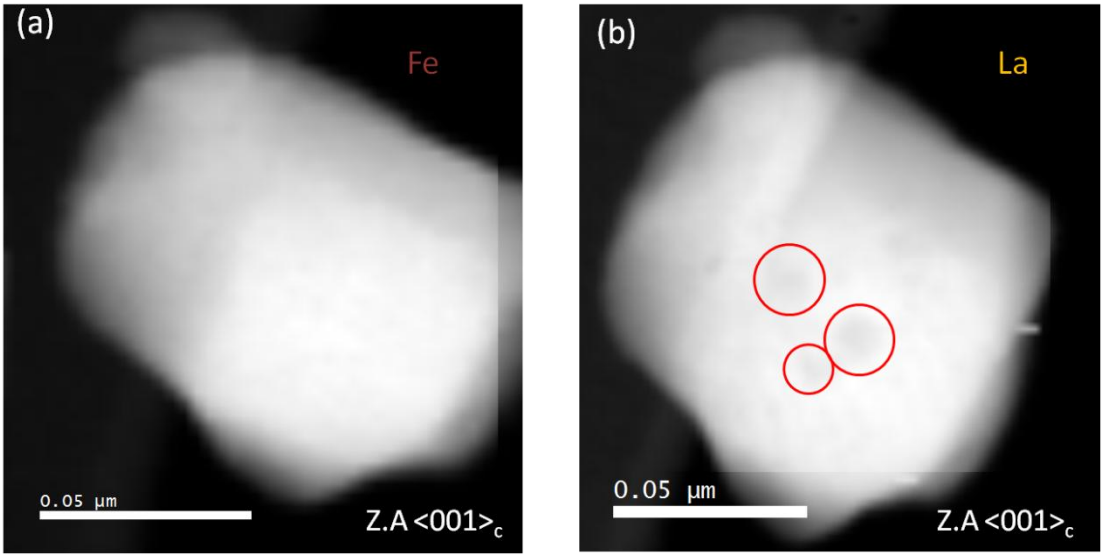


Figure 6.18 Spatial map of Fe (a) and La (b) distributions in 10% La doped $BiFeO_3$ obtained from EELS spectrum images.

Finally, we sought to understand the effect of La doping on the structure and chemistry of $BiFeO_3$. For this, we use EELS data and compared the Fe $L_{2,3}$ edges of pure $BiFeO_3$ and 10% La doped $BiFeO_3$ nanoparticles (Figure 6.19) and observed similar features. The energy split of 13 eV between $L_2$ and $L_3$ in both doped and pure particles is attributed to the spin-orbit coupling, and it is consistent with EELS observations on other Fe-O containing compounds. Each of these individual peaks further consists of fine structure. For $L_3$ edge shows a shoulder followed by a more intense peak, and can be deconvoluted into two Lorentzians ($L_{3a}$ and $L_{3b}$) separated by 1.6 eV. This separation results from octahedral crystal field splitting of $Fe^{3+}$ 3d orbitals into a lower energy triplet with $t_{2g}$ symmetry, and a higher energy states with $e_g$ symmetry[194]. Conversely, such fine structure of $L_3$ peaks proves the existence of $Fe^{3+}$ in an octahedral ligand field, the ligand here being oxygen. The intensity

ratios of these paeaks ($L_{3a}/L_{3b}$) are 0.40 and 0.38 for pure $BiFeO_3$ and 10% La doped $BiFeO_3$, respectively, from fitted Lorentzian peaks indicated as $L_{3a}$ and $L_{3b}$ in Figure 6.19. These values are comparable to that of a standard hematite ore ($Fe_2O_3$, $L_{3a}/L_{3b}$ = 0.38) which also has $Fe^{3+}$ in an octahedral oxygen environment. These results unequivocally show that La constitutes an A-site substitution, and that is does not alters neither the oxidation state of Fe (remaining as $Fe^{3+}$), nor its octahedral oxygen environment within the volume of the nanoparticles.

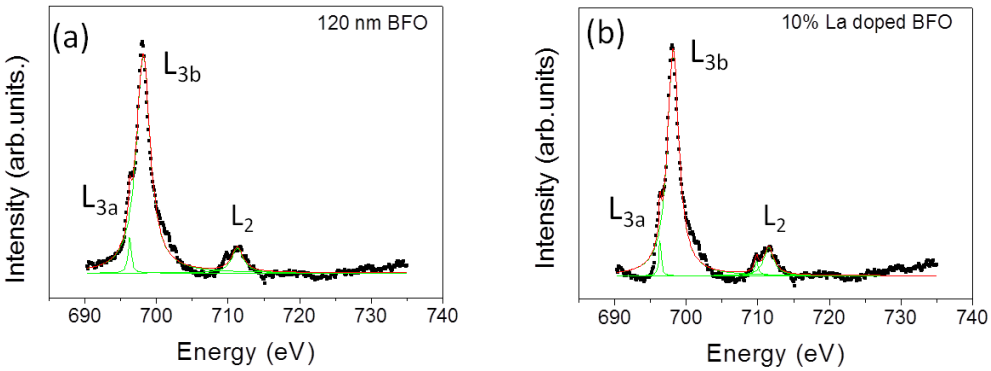


Figure 6.19 EELS spectra of pure $BiFeO_3$ (120 nm) and 10% La doped $BiFeO_3$ (100 nm) nanoparticles.

### 6.3.3 Surface chemical states from X-ray photoelectron spectroscopy

The Fe valence state in our different size samples are investigated by measuring the Fe 2p core level X-ray photoelectron spectroscopy (XPS). The representative survey scans of different size $BiFeO_3$ are given in Figure 6.20. It can be seen at first glance that the spectra of different size $BiFeO_3$ are same in the whole scanning range. In the following, though being the atomic species in $BiFeO_3$ presenting the highest sensitivity to surface effects and practically less complex to be analyzed than oxygen, we focus our study on the Fe states.

The valence state of Fe 2p core level spectra of $Fe^{2+}$ and $Fe^{3+}$ in different materials have been largely reported [195-199]. Figure 6.21 shows the typical Fe 2p XPS core spectra for $BiFeO_3$ 30 nm and 190 nm nanoparticles. Fe 2p spectra show mostly the features of $Fe^{3+}$ oxidation state as determined from the binding energy obtained for Fe $2p_{3/2}$ (at 710.6 eV) for all samples. The peak at 712.1 eV is attributed to Fe(OH) or FeO(OH)[200] or Fe atoms in $BiFeO_3$ occupying both octahedral and tetrahedral sites[201].

In general, satellite peaks appear at 8 eV above $2p_{3/2}$ for $Fe^{3+}$ and 6 eV above $2p_{3/2}$ for $Fe^{2+}$. In our samples, the wide peak at 718.3 eV is the corresponding satellite peak of the $Fe^{3+}$. However, from fitting core level spectra, the peak at 714.9 eV was attributed to the $Fe^{2+}$ contribution[201-202].

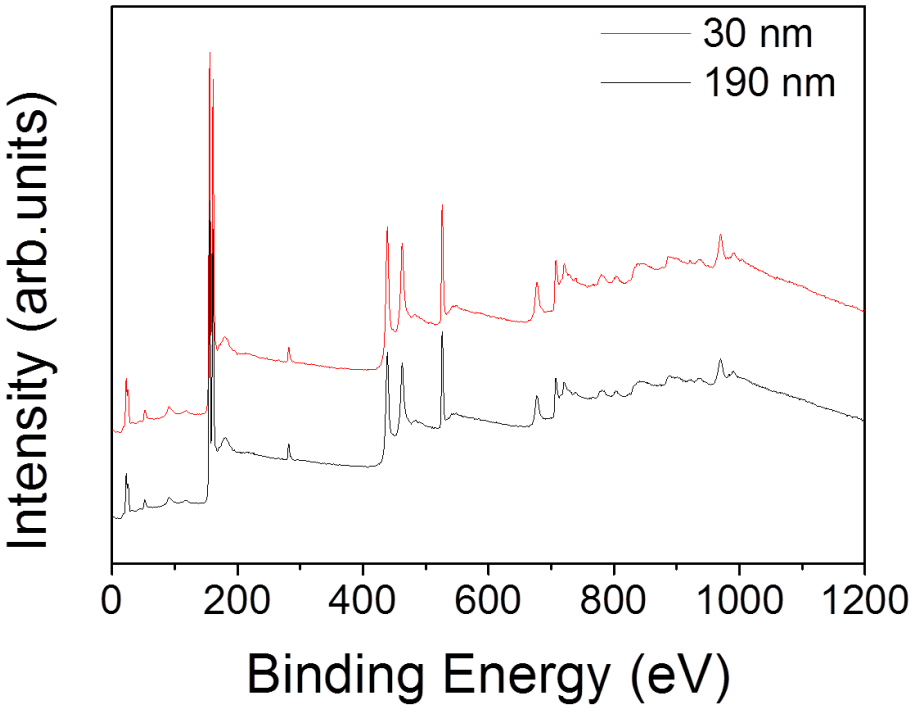


Figure 6.20 Survey XPS scans of 30 nm (red line) and 190 nm (black line) $BiFeO_3$ nanoparticles.

The XPS analysis evidences the existence at the surface of a mixed $Fe^{2+}$-$Fe^{3+}$ valence state in different size $BiFeO_3$ particles (Figure 6.21(c)), which is different from reported results on $BiFeO_3$ nano-samples[195]. In our case, the origin of $Fe^{2+}$ could be due to the occurrence of oxygen vacancies[201]. The $Fe^{2+}/Fe^{3+}$ content of different size $BiFeO_3$ were obtained through the fitting results in Figure 6.21 (a) and (b). A summary of the corresponding results are shown in Table 6.5.

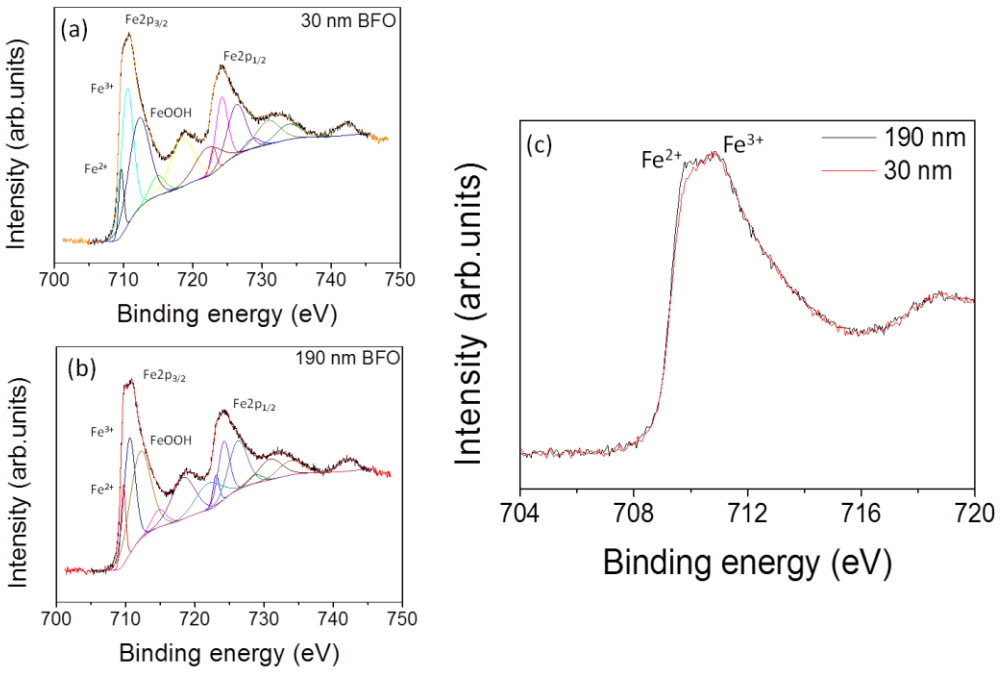


Figure 6.21 Fe 2p XPS core spectra for (a) 30 nm and (b) 190 nm $BiFeO_3$ nanoparticles, and(c) detail of the corresponding Fe $2p_{3/2}$ region for 30 nm (red line) and 190 nm (black line) $BiFeO_3$ nanoparticles.

Table 6.5 XPS fitting results of detail of the Fe 2p regions of 30 nm and 190 nm $BiFeO_3$.

| Sample | $Fe^{2+}$ (%) | $Fe^{3+}$ (%) | $Fe^{3+}$ from FeOOH (%) | $Fe^{2+}/Fe^{3+}$ |
|---|---|---|---|---|
| $BiFeO_3$ 30nm | 5.4 | 27.7 | 31.1 | 0.09 |
| $BiFeO_3$ 190nm | 7.1 | 24.5 | 33.6 | 0.12 |

From Table 6.5, it can be seen that a particle size dependence of the $Fe^{2+}/Fe^{3+}$ ratio (from 0.09 to 0.12) in $BiFeO_3$, thus reflecting the increase of $Fe^{2+}$ content relatively to $Fe^{3+}$ as particle size increases. Though by EELS analysis (chapter 6.3.3) clearly indicate that the core of 120 nm $BiFeO_3$ nanoparticles are essentially constituted by $Fe^{3+}$ ions, we can localize this $Fe^{2+}$ signature to arise from the very last unit cells of the nanoparticles. Such $Fe^{2+}$ coming from the outer surface of the nanoparticles, it indicates that slightly larger $Fe^{2+}$ regions may be found on larger nanoparticles. However, we also notice from the study of the FeOOH signature, which correspond to a $Fe^{3+}$ state, that for larger nanoparticles the FeOOH signature is also larger. A chemical and electronic surface reconstruction of a given oxide under different environmental conditions is expected. Interestingly, a FeOOH compound may eventually play a significant role in separating electron and holes in the event of a photocatalytic process as it happens for $TiO_2$[203]. Both effects ($Fe^{2+}$ and FeOOH

stabilization) may differently affect the photocatalytic properties. These results will be presented and analyzed in chapter 8.

## 6.4 Magnetism from magnetometry and Mössbauer spectroscopy

### 6.4.1 Magnetometry

To investigate the magnetic properties of $BiFeO_3$ nanoparticles, magnetic measurements were performed on these samples using a SQUID magnetometer. Figure 6.22 shows magnetic field dependences of the mass magnetization *M* for $BiFeO_3$ powders with different sizes obtained at room temperature. For large particles an almost linear hysteresis-loops are observed, similar to those obtained from bulk $BiFeO_3$[157]. For sample size below 120 nm (inset, Figure 6.22), it can be seen that a larger remnant magnetization appears. This result can be explained by two possible facts: (i) with particle size reduced, sample becomes dimensionally smaller than the characteristic period length of 62 nm of the spiral modulated spin structure of $BiFeO_3$[35-36], and (ii) the spin canting and consequently the effective remnant magnetization becomes more relevant since this effect is strongly correlated to surfaces, and the surface to volume ratio increases for smaller nanoparticles[34]. In addition, from the inspection of the magnetization hysteresis loops at 300 K and 5 K for the smallest nanoparticles (Figure 6.23), it is clearly seen that this effects is kept down to low temperature and even increased (larger remnant magnetization at low temperature). We can thus conclude that $BiFeO_3$ nanoparticles present a weak ferromagnetic behavior.

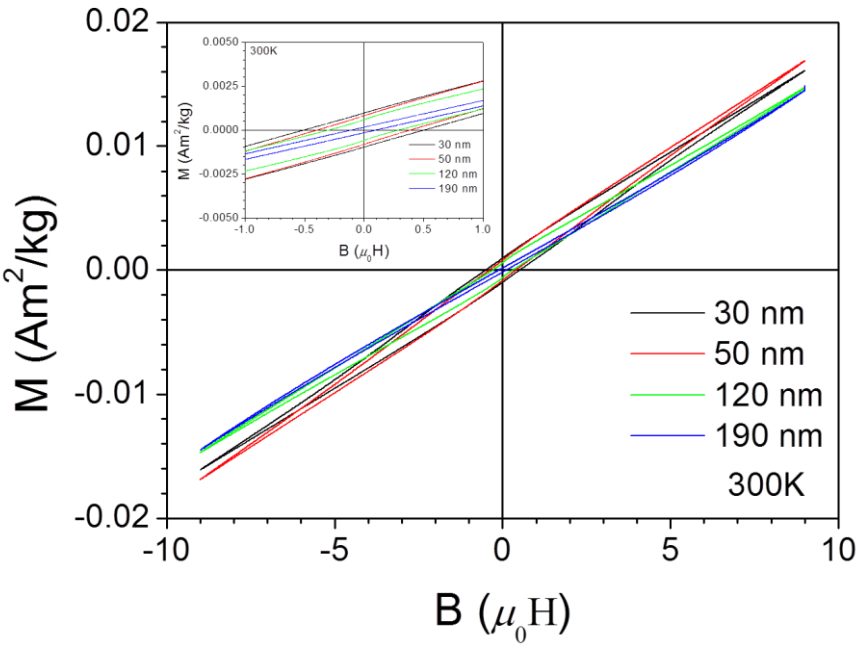


Figure 6.22 Hysteresis loops at 300 K for $BiFeO_3$ nanoparticles with indicated sizes. The inset shows a zoom of the low field magnetization loops.

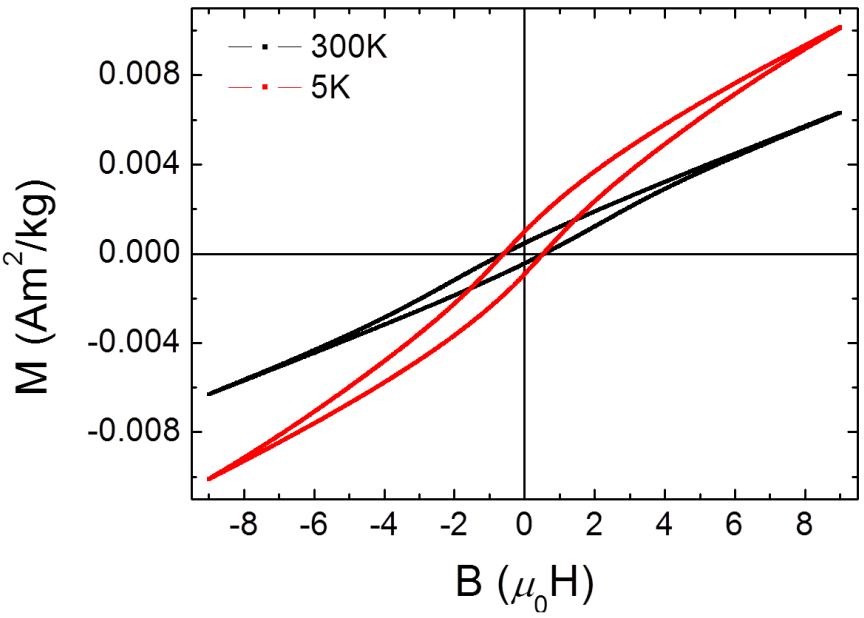


Figure 6.23 Magnetization hysteresis loops for the 30 nm-nanoparticles at 5 K and 300 K, respectively.

As particle size decreases, micro strain increases (chapter 6.1.1; Table 6.1); introducing ionic coordination distortions and lattice disorder throughout the nanoparticle, including the surface, with the net result being that canted spin

structures; leading to the increase of the remnant magnetization, coexist with the underlying $BiFeO_3$ antiferromagnetic order.

Temperature dependent magnetization studies are shown in Figure 6.24 for different size $BiFeO_3$. Magnetization measurements were carried out while heating the sample from lowest temperature at large applied magnetic field (9 T), after cooling down under no field (zero-cooling, ZFC) and after cooling down under field (field cooling, FC). This large magnetic field ensures the measurement of the saturation magnetization and allows the study of the overall magnetic response.

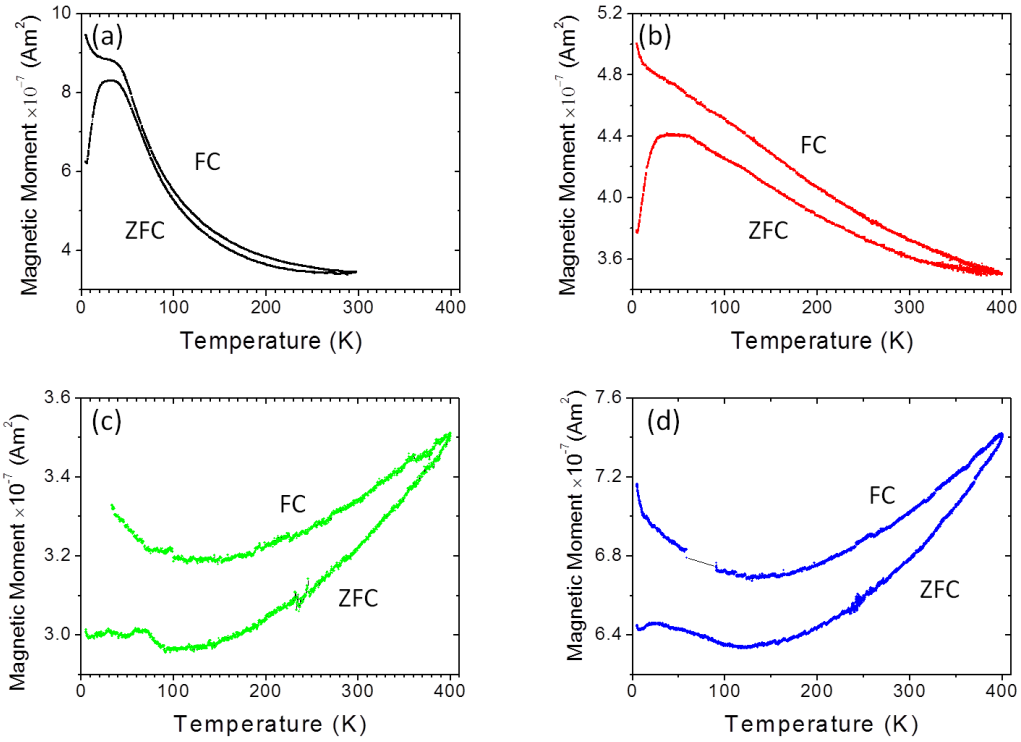


Figure 6.24 Temperature dependence of the magnetization for $BiFeO_3$ nano particles of varying size, showing zero field cooling (ZFC) and field cooling (FC) curves, with an applied magnetic field set at 9T. (a) 30 nm, (b) 50 nm, (c) 120 nm, (d) 190 nm

Firstly, there are three features worth mentioning: (1) the splitting in the ZFC and FC magnetization curves are observed for all the $BiFeO_3$ samples; (2) the magnetization from ZFC and FC curves for 190 nm and 120 nm samples decreases from 300 K, while for 50 nm and 30 nm, their corresponding magnetization values increase; and (3) for all the $BiFeO_3$ samples, in the ZFC curves, we can observe a maximum of magnetic moment at low temperature, being more evident for smaller nanoparticles (50 and 30nm).

We can explain these different features as follows. First, the splitting of the ZFC and FC curves usually appears in the co-existent system of antiferromagnetic and ferromagnetic phases, like the core-shell structure with antiferromagnetic core and ferromagnetic surface[35]. Secondly, from magnetic point of view, samples with sizes larger than 62 nm are expected to follow the bulk behavior, since this size allows the existence of a bulk-like spin cycloid. Finally, the presence of the broad peak in ZFC curves can be attributed to the magnetic blocking mechanism induced by the competition between thermal energy and magnetic anisotropy energy in nanoparticles[34, 157], strongly enhanced for samples with larger values of surface/volume ratios. For this last feature, we note that $BiFeO_3$ nanoparticles (30 nm and 50 nm), their corresponding curves exhibit a broad magnetization maximum around $T_{max}$ = 50 K. Park *et al.*[157] have reported that this is not the superparamagnetic relaxation process. On the contrary, $T_{max}$ represents a spin-glass-like freezing temperature due to the high packing volume fraction as well as a complex interplay between finite size effects, possible interparticle interactions, and a random distribution of anisotropy axes in our nanoparticle assembly. Vijayanand *et al.*[204] proved that the above mentioned peak is not associated with any spin glass or phase transition by a series of ZFC and FC magnetization measurement, and they propose that it corresponds to some changes associated with domain structure. After these statements, the broad magnetic peak of our $BiFeO_3$ nanoparticles may be related to the magnetic domain pinning effect, which is well known in magnetic materials[205], added to the disorder induced by the strain. Additionally, aggregation can be observed in different size nanoparticles from SEM (chapter 5.3.1), the interparticle interactions within the nanoparticle assemblies become stronger, which can affect the magnetic properties in nanoparticles. It is suggested to be due to the interparticle dipolar and exchange interactions between the particles in the aggregations.

### 6.4.2 Mössbauer spectroscopy

In order to obtain closer insight into the atomistic nature of the magnetic state of $BiFeO_3$ nanoparticles, Mössbauer spectroscopy is performed at room temperature. And Mössbauer spectra of different size $BiFeO_3$ are shown in Figure 6.25. In the Mössbauer spectra, superposition of quadrupolar (doublet) and magnetic (sextet) absorption spectra are observed (Figure 6.25, lines).

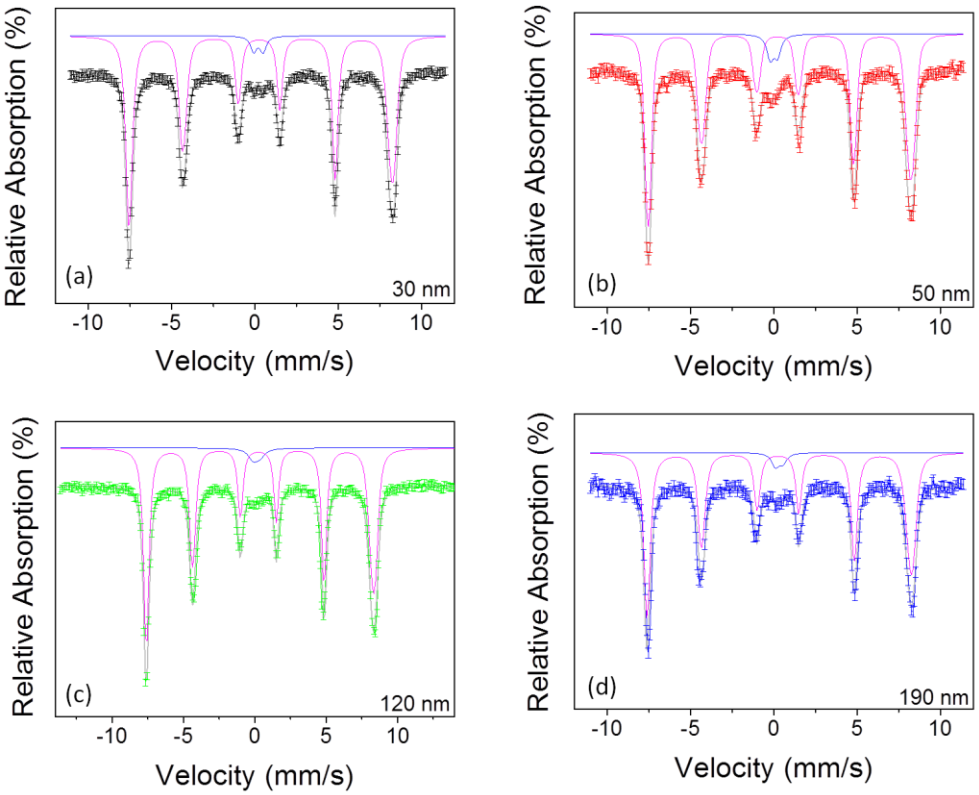


Figure 6.25 Room temperature Mössbauer spectra of $BiFeO_3$ nanoparticles, annealed at different temperature: (a) 30 nm, (b) 50 nm, (c) 120 nm, (d) 190 nm. Measurements performed in zero applied magnetic field. The solid lines are least-squares fits of the experimental data to theoretical spectra. Deduced Mössbauer parameters are summarized in Table 6.6.

Table 6.6 Mössbauer parameters of different size $BiFeO_3$ nanoparticles

| Sample | Magnetic hyperfine field ($H_{hf}$) (T) | Isomer shift ($\delta$) (mm/s) | Quadrupole splitting ($\Delta E_Q$) (mm/s) |
|---|---|---|---|
| 30 nm | 48.9(6)±0.03 | $0.29(8)\pm3.2\times10^{-5}$ | $0.09(4)\pm2.8\times10^{-3}$ |
| 50 nm | 48.9(0)±0.01 | $0.28(1)\pm3.0\times10^{-4}$ | $0.11(0)\pm1.2\times10^{-2}$ |
| 120 nm | 49.3(1)±0.03 | $0.29(3)\pm4.8\times10^{-4}$ | $0.10(2)\pm3.1\times10^{-3}$ |
| 190 nm | 49.1(5)±0.04 | $0.29(0)\pm6.3\times10^{-4}$ | $0.08(4)\pm4.0\times10^{-3}$ |

The magnetic spectral signature corresponds to high-spin $Fe^{3+}$ ions in a oxygen octahedra environment, typical for $BiFeO_3$ crystal lattice[206]. In such case, an absorption sextet is observed, characterized by an asymmetry in the relative absorption value of all absorptions, as for instance it is seen between for the first peak (on the left) and the last peak (on the right). This has been attributed to the presence of $Fe^{3+}$ in two different crystallographic environments that differ primarily in the size of the electric field gradient, through the Dzyalonshinkii-Moriya (DM) interaction, creating a cycloid spin structure, with an uncommensurate period compared to the antiferromagnetic unit cell[34].

In Figure 6.25, we include the least-square fits of our experimental data to theoretical spectra based on antiferromagnetic $Fe^{3+}$ in an octahedral crystal field (red lines) plus a paramagnetic contribution (blue lines). The fitting gives values for the isomer shift ($\delta$), quadrupole splitting ($\Delta E_Q$), and magnetic hyperfine field ($H_{hf}$) consistent with the presence of high-spin $Fe^{3+}$ ions[34]. The fitting results are included in Table 6.6. We note similar results for all nanoparticles for the quadrupole splitting values, varying $\Delta E_Q$ between 0.09 and 0.11 mm/s (compared to literature values in $BiFeO_3$ nanoparticles[34]), and for the isomer shift values, varying $\delta$ between 0.28 and 0.29 mm/s (which is slightly lower than bulk $BiFeO_3$)[206]. On the other hand, the hyperfine field $H_{hf}$ has a relatively lower value for 30 and 50 nm nanoparticles, compared to the corresponding values for 120 and 190 nm ones. We argue that these values have the same origin as the increase of the remnant magnetization for smaller samples seen in magnetometry measurements (previous chapter, Figure 6.22), being related to a larger spin canting in samples with larger surface-to-volume ratio. Further experiments as a function of temperature are necessary to confirm the exact nature of the spin arrangement. As for magnetometry measurements, low temperature Mössbauer experiments can provide information on the spin cycloid. From the values shown in Table 6.6, the apparently non monotonic evolution of the isomer shifts and quadrupole splitting should be related to a different cycloid and spin canting state in smaller samples (30 and 50 nm).

From the above analysis of the magnetic data (magnetometry and Mössbauer spectroscopy), we can conclude that as the particle size diminishes and the surface-to-volume ratio increases, the increase of magnetization is due to the contribution of uncompensated spins at the surface, caused by strain and the inavoidable larger contribution of the surface in smaller particles. Consequently, surface spins dominate the magnetic behavior in smaller particles.

## 6.5 Conclusion

In this part, the structure and chemical and electronic states of different size $BiFeO_3$ and doped samples are analyzed through XRD experiments and Raman spectra at different temperature, and HRTEM-EELS and XPS. The size and morphology of different size $BiFeO_3$ are observed by FE-SEM, which has shown that the particle size is increasing with synthesis temperature increases. Compare with the crystallite size from XRD, particle size is larger for the particle size larger than 50 nm, which means that a particle contains several crystals. Structure and Raman analysis indicates the existence of characteristic *R3c* structure for all samples, but presenting different strain states, with transitions seen to depend on the sample size. From HRTEM imaging, we prove the existence of ferroelectric domains in pure $BiFeO_3$ nanoparticles. The chemical and electronic state of Fe is studied from HRTEM-EELS and XPS experiments. We notice that at the nanoparticles surface we find $Fe^{2+}$ and characteristic features of FeOOH ligands, whereas the core of the nanoparticles keeps $Fe^{3+}$ ions. The analysis of these EELS and XPS results signals the existence of a surface layer, *i.e.* skin layer, with different chemical/electronic states than the core of the particle. Finally, the study of magnetic properties through magnetometry and Mössbauer experiments has proved the existence of antiferromagnetic order for pure $BiFeO_3$ samples. The smaller size samples show distinguishing spin canting behavior because of finite size effect, strain and other defects, arising from uncompensated spins at the surface.

# 7 Light interaction with $BiFeO_3$ particles

## 7.1 Mechanisms for charge transition in $Fe^{3+}$ oxides

Transition metal oxides are materials belonging to the family of oxides with strong electron-electron correlation and electron-phonon coupling[207], which lead to many complex phenomena. $BiFeO_3$ is one of the typical multiferroic materials which exhibit colossal magnetoelectricity coupling and photoferroelectricity[1, 49]; Moreover, these different properties may even be sensitive to a size effect. The size effects reflect different critical physical lengths and behaviors that are fingerprints of the varied elementary excitations and interactions[59]. In this part, we try to understand light induced properties of $BiFeO_3$ compounds with different micrometric and nanometric size.

In $BiFeO_3$, $Fe^{3+}$ ions are kept in oxygen octahedra, then Fe ions exhibit strong inter-reactions with close oxygen ions and adjacent $Fe^{3+}$. It is well established that three types of electronic transitions occur in the optical absorption spectra of $Fe^{3+}$ substances, that is, the $Fe^{3+}$ ligand field transitions or the *d-d* transitions, the ligand to metal charge transfer transitions, and the pair excitations resulting from the simultaneous excitation of two neighboring $Fe^{3+}$ cations that are magnetically coupled. We detail in the following these different transitions.

### 7.1.1 $Fe^{3+}$ ligand field transitions or $Fe^{3+}$ *d-d* transitions

In octahedral coordination, the Fe 3*d* atomic orbitals are split into two sets of orbitals labeled as $t_{2g}$ and $e_g$. The $t_{2g}$ and $e_g$ orbitals are each of them split by the exchange energy and the energy separation is the 10D*q* ligand field parameter or crystal field splitting. The energies of the different states of $Fe^{3+}$ under this ligand field as a function of 10D*q* are shown schematically in the Tanabe-Sugano diagram shown in Figure 7.1. The exchange splitting results in two sets of $t_{2g}$ and $e_g$ orbitals, one for majority spin (spin-up or $\alpha$-spin) and the other for the minority spin (spin-down or $\beta$-spin) electrons. The ligand field transitions are those relating states which arise from the different possible electronic configurations of the $t_{2g}$ and $e_g$ orbitals.

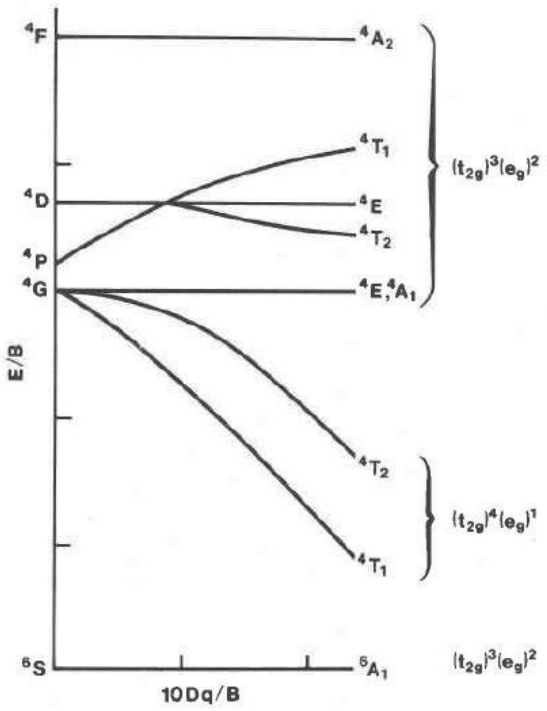


Figure 7.1 Tanabe-Sugano diagram for high-spin $Fe^{3+}$ in octahedral coordination.

The ground $^6A_1$ ($^6S$) state in Figure 7.1 arises from the ground state $(t_{2g}^{\alpha})^3(e_g^{\alpha})^2$ configuration of high-spin $Fe^{3+}$ ions. The first possible excited state is $(t_{2g}^{\alpha})^3(e_g^{\alpha})^1(t_{2g}^{\beta})^1$. This configuration gives the $^4T_1$ ($^4G$) and $^4T_2$ ($^4G$) states in Figure 7.1. the remaining states in Figure 7.1 result from the "spin-flip" configuration $(t_{2g}^{\alpha})^2(t_{2g}^{\beta})^1(e_g^{\alpha})^2$ and $(t_{2g}^{\alpha})^3(e_g^{\alpha})^1(e_g^{\beta})^1$[208].

All of the transitions from the ground $^6A_1$ ($^6S$) state to the excited ligand field states are, in principle, both spin and parity forbidden. However, in practice these transitions may occur with a finite transition probability and become allowed through other mechanisms, such as the magnetic coupling of electronic spins of nearest $Fe^{3+}$ ions in the crystal[209-211].

A qualitative understanding of the state associated with $Fe^{3+}$-$Fe^{3+}$ pairs can be obtained by assuming that the coupling between two $Fe^{3+}$ centers is through the Heisenberg Hamiltonian[212]:

$$H = -J\vec{S}_a \cdot \vec{S}_b \qquad [7.1]$$

Here, $\vec{S}_a$ and $\vec{S}_b$ are the spins of the two $Fe^{3+}$ cations and *J* is the Heisenberg exchange integral between this spins. We simplify the analysis and use of the Hamiltonian, in the view of antiparallel spin configuration of $Fe^{3+}$ cations and being *J* negative for antiferromagnetic interaction. From now on, we consider the absolute value of *J* and use the modulus of the both spins $\vec{S}_a$ and $\vec{S}_b$., thus $S_a$ and $S_b$. The application of this Hamiltonian as a perturbation to the ligand field states of the uncoupled $Fe^{3+}$ cations yields a set of states for the Fe-pairs with energies given by:

$$E = (J/2)[S(S+1) - S_a(S_a+1) - S_b(S_b+1)] \qquad [7.2]$$

Where *S* is the net spin of the pair with values $|S_a + S_b|$, $|S_a + S_b - 1|$,....., $|S_a - S_b|$. If both $Fe^{3+}$ cations are in their ground $^6A_1$ states (high-spin), $S_a$=$S_b$=5/2, the resulting pair-states derived by coupling the two $Fe^{3+}$ cations will have *S*=0, 1, 2, 3, 4, and 5. Now, if one of the $Fe^{3+}$ cations in the pair is excited to a quartet ligand field state, $S_a$=3/2 and $S_b$=5/2, the two $Fe^{3+}$ cations would therefore couple to give a set of pair states with *S*=1, 2, 3, and 4. Transition from *S*=1, 2, 3, and 4 states in the $Fe^{3+}(^6A_1)$-$Fe^{3+}(^6A_1)$ pair state manifold to the states in the excited-single-ion pair-state manifold can therefore, occur with $\Delta S$=0 and be spin allowed. The relative energies of the states in the ground and excited-single-ion manifolds are shown in Figure 7.2.

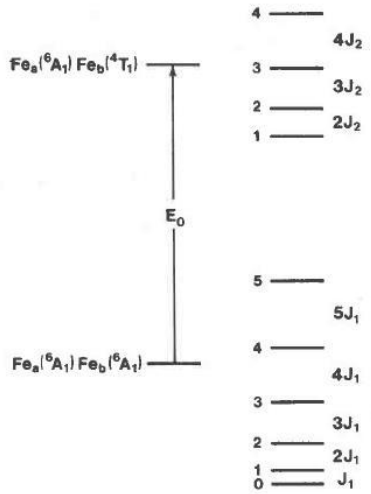


Figure 7.2 States of an $Fe^{3+}$-$Fe^{3+}$ pair assuming that the $Fe^{3+}$ cations are coupled via Heisenberg Hamiltonian $H=-J\cdot S_a\cdot S_b$. $E_0$ is the energy difference between the ground $^6A_1$ state and an arbitrary quartet state of an isolated, uncoupled $Fe^{3+}$ cation. The number next to each level indicate the spin quantum number (*S*) of the pair state.

In $BiFeO_3$, the $O^{2-}$ ions lie between the neighboring $Fe^{3+}$ ions, and, through the super-exchange mechanism, allow the $Fe^{3+}$-$Fe^{3+}$ magnetic coupling. The existence of the hybridization of Fe 3*d* and O 2*p* orbitals relaxes the parity forbidden transitions to some extent. Therefore, both the spin and parity selection rules for the $Fe^{3+}$ ligand field transitions can be relaxed by the magnetic coupling of adjacent $Fe^{3+}$ cations and covalent bonding with oxygen. Moreover, this relaxation through the covalent bonding may be enhanced by decreasing size and surface modification[33, 75].

### 7.1.2 Pair excitations or double exciton processes

An additional phenomenon resulting from the magnetic coupling of adjacent $Fe^{3+}$ cations is the presence of absorption features corresponding to the simultaneous excitation of two $Fe^{3+}$ centers[213]. These features occur at energies given approximately by the sum of two single-ion $Fe^{3+}$ ligand field transitions and are often referred as "double exciton processes." These transitions are also spin allowed: if both $Fe^{3+}$ cations are excited to a quartet ligand field state so that $S_a$=$S_b$=3/2, the pair states resulting from coupling the two $Fe^{3+}$ cations will have *S* values of 0, 1, 2, and 3. Transitions to these pair states can therefore occur from the *S*=0, 1, 2, and 3 states in the $Fe^{3+}(^6A_1)$-$Fe^{3+}(^6A_1)$ ground state manifold.

### 7.1.3 Ligand to metal charge-transfer transitions

According to molecular orbital theory, the transitions at energy higher than most of the ligand field transitions are the ligand to metal charge-transfer transitions. For $BiFeO_3$, since the bulk band gap is ~2.6 eV (or ~476 nm), bands above 3.0 eV (or ~400 nm) in energy were assigned to ligand to metal charge-transfer transitions. However, this charge-transfer band tail may extend to lower energy (longer wavelength) regions through the magnetic coupling.

### 7.1.4 Band edge and narrow *d* bands

The band edge of an inorganic solid is located at the low energy end of the conduction band above the valence band. It is difficult to determine the band edge for transition metal oxides particularly those presenting magnetic order, because

there are narrow *d* bands in the gap, leading to transitions implying localized charges that to some extend can be excited with infrared radiation with a finite probability. The transitions induced by these photons include the *d*-*d* transitions, pair excitation, and finally the charge transfer or optical band gap. The first two transitions mentioned previously arise from the narrow *d* bands.

## 7.2 Optical properties of pure $BiFeO_3$: effect of particle size and temperature

Optical spectroscopy is a well-known non-contact probe to study the charge and bonding in solids. When charge and spin degrees of freedom are strongly coupled, it they are also influenced by magnetic excitations or by spin order transition[141, 214]. The coupling between different types of orders in multiferroics, which in the case of $BiFeO_3$, simultaneous possess antoferromagnetic and ferroelectric orders, gives rise to several interesting coupling phenomena. $BiFeO_3$, with its high temperature antiferromagnetic and ferroelectric transitions, besides the fact to present a band gap in the visible range, provides a set of interesting parameters to be studied and optically triggered, including spin, charge and lattice couplings[33].

In this part, the band structure of different size $BiFeO_3$ has been investigated by ultraviolet-visible light spectrometry exploiting diffuse reflectance experiments at different temperature. The disorder of the different samples has been investigated by Urbach analysis. The different optically induced transitions, from the band gap to different interband or other charge-transfer transitions at high energy as well as magnon excitations at low energy will be presented.

### 7.2.1 Room temperature behavior

The band structure and other charge transition of oxides can be deduced from optical properties using photons with different energies[83]. To the present study on $BiFeO_3$, the wavelength range of the photons used on the diffuse reflectance spectroscopy was from 200 to 900 nm. The experiments were carried out at room temperature for different size samples, being shown in Figure 7.3.

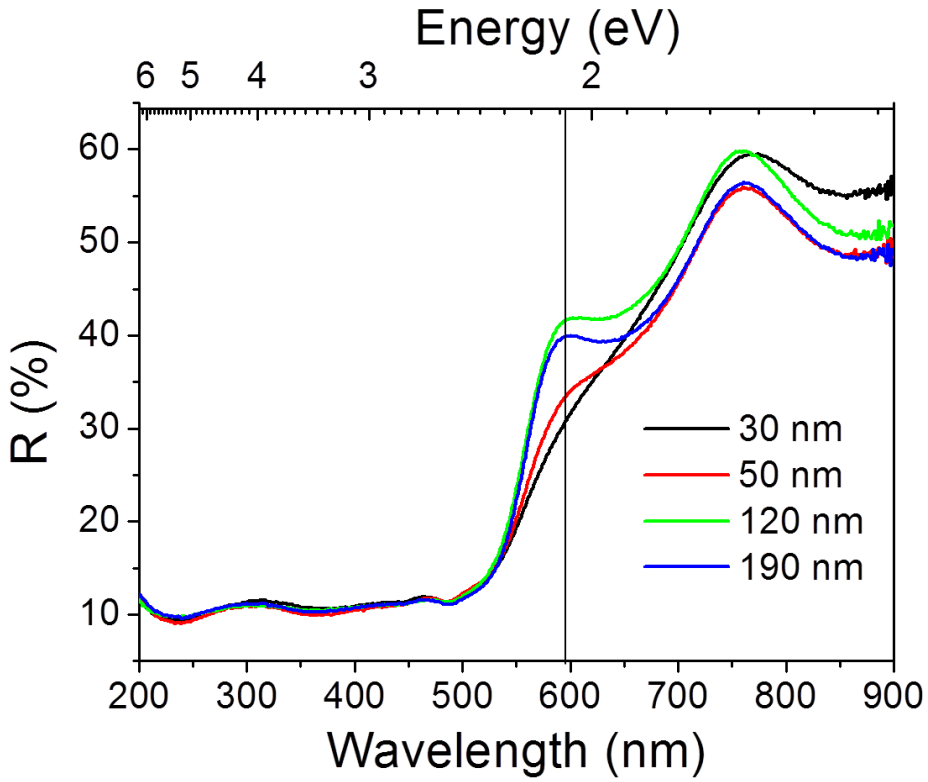


Figure 7.3 Diffuse reflectance spectra for different size $BiFeO_3$, as indicated. The vertical line is a guide for the eye, indicating the energy (top) or wavelength (bottom) for which the more obvious variation of reflectance intensity is measured.

One obvious variation of the reflectance measured for different size samples is found for ~600 nm (~2.06 eV). We notice that the shape of the reflectance curves in this region strongly changes, evolving from an almost linear dependence on the energy for 30 nm particles towards a plateau for corresponding data for 190 nm ones. From this simple examination of the reflectance curves, we deduce that different charge transition mechanisms may exists for different size $BiFeO_3$, which we analyze below.

In order to obtain the band gap value of different size sample, Kubelka-Munk (KM) function is used [215]

$$F(R) = \frac{(1-R)^2}{2R} \qquad [7.3]$$

where *R* is the experimental reflectance referred to the $BaSO_4$ standard. We recall that K-M function is also known as the reemission function. From now on, the K-M function (or *F(R)* curves) will be considered as proportional to the optical absorption. The different *F*(*R*) curves are shown in Figure 7.4 as a function of the photon energy.

Information on the complex charge transitions and on the electronic structure can be deduced from the *F*(*R*) curves, since considered as the absorption, provide information on the electronic states. These features will be analyzed in the following.

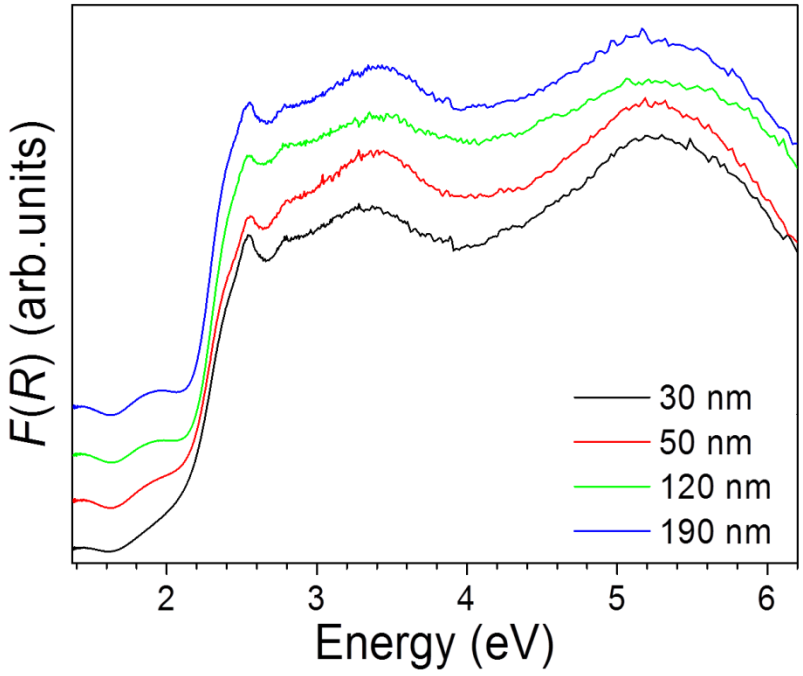


Figure 7.4 K-M functions of different size $BiFeO_3$ at room temperature.

In order to study the band gap, we represent the *F(R)* curves using the Tauc plot[195] according to the relation

$$\left(F(R)h\nu\right)^n = A\left(h\nu - E_g\right) \qquad [7.4]$$

where *F*(*R*) corresponds to the experimental K-M function, *A* is a constant value, *h* is the Plank's constant, $\nu$ is the photon frequency, $E_g$ is the band gap and the *n* is the exponential coefficient related to the band gap transition nature (*n*=2 for direct band gap). Using the direct band gap approach with our set of data, the band gap values have been determined from linear fits of the band gap edge of the different Tauc plots, the effective band gap values as a function of the particles size have been obtained and shown in Figure 7.5.

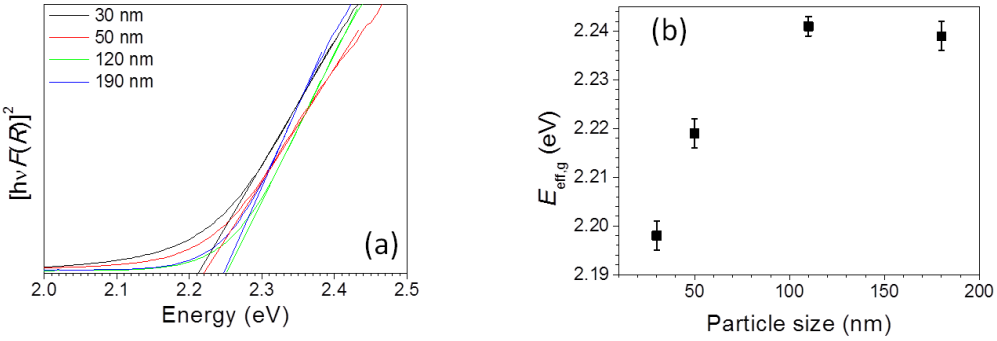


Figure 7.5 (a) Tauc plots of different size $BiFeO_3$, presenting the linear fits used for determining the effective band gap values. (b) Size dependence of the effective band gap.

It can be seen that the band gap value increases with the increase of the particle size, to further stabilize its value for nanoparticles with size larger than 120 nm, which is consistent with previous reports[195], but still these values are lower than the usual $E_g$ values obtained from single crystals and thin films[216-217]. Our band gap results, even though they are dependence on the particle size, holding around ~2.20-2.25 eV.

In order to investigate the electronic states and the charge transitions below the band gap, the K-M function can be further analyzed to depict the electronic disorder near the band gap edge. From the Urbach energy, it is possible to obtain important information about the dynamics of the electronic excitations and to determine, for instance, the effect of defects on the electronic excitations[143]. In $BiFeO_3$, oxygen vacancies and oxygen interstitials are assigned as possible defects which have also been reported in other oxides[101, 218]. Generally, the oxygen vacancies in materials create an intra gap, localized state. It can be simply explained from the fact that the positive vacancy $V_O^{\bullet\bullet}$, the net positive charge induces other closer cation to relax away from the vacancy site, raising the defect state energy[219]. Recent experimental results would favor a vacancy level in the upper gap edge[101]. In a general view, in oxides, oxygen (anion) vacancies are surrounded by metal (cation) site, whereas in a covalent solid, anion vacancies would leave cation dangling bonds. With increasing ionicity, cation dangling bond states lie nearer the conduction band. Additionally, in even more ionic solids, the charge screening weakens, the coulomb potential is stronger, all this causes the vacancy states to become more localized inside the vacancy itself and less delocalized onto the cation states. Thus, larger iconicity is

typically related to type-s and type-p metal oxides, leading the vacancy level to lie deeper in the band gap, whereas type-d metal oxides present less ionicity (larger covalency), leading the vacancy level to lie near the conduction band, even above it.[219].

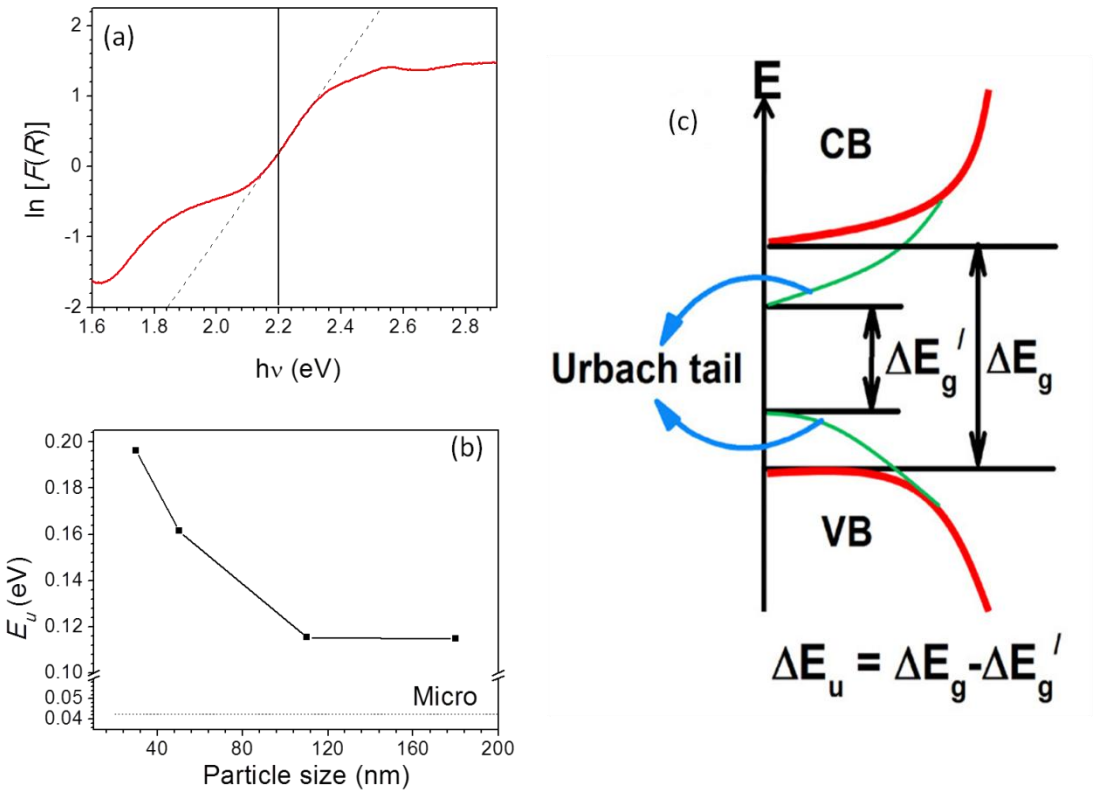


Figure 7.6 (a) *ln[F(R)]* plot as a function of the photon energy for 50 nm $BiFeO_3$ nanoparticles, allowing to determine the Urbach energy $E_U$ from the linear fit in the band gap energy range, the slope being proportional to ($1/E_U$). (b) Dependence of the Urbach energy on the particle size. The dotted line is the $E_U$ value for the corresponding data of $BiFeO_3$ microparticles. (c) Schematic view of the energy diagram, Urbach tails lying close to the conduction band and valence bands.

From the different K-M curves, we can determine the Urbach energy $E_U$ related to the disorder of the energy levels close to the conduction and/or valence bands. The disorder sources can be point defects, strain related effects on the electronic states, morphology effects, etc. A schematic view of the Urbach energy is shown in Figure 7.6 (c). Figure 7.6 (a) shows the typical plot to determine the Urbach energy, and Figure 7.6 (b) includes the Urbach energy as a function of particle size.

We recall the Urbach analysis relationship, based on

$$\ln F(R) = h\nu / E_U \qquad [7.5]$$

where *F(R)* is the K-M function, *h* is the Plank's constant, $\nu$ is the photon frequency, and $E_U$ is the Urbach energy. $E_U$ vales are found to vary from 0.11 eV to 0.20 eV for 190 nm to 30 nm particle sizes, respectively. These latter $E_U$ values are in very good agreement with X-ray photoelectron spectroscopy measurements on $BiFeO_3$ revealing the presence of defect trapped states at 0.2 eV below the conduction band that have been attributed to defects at the grain boundaries[218].

Continuing with the analysis of the K-M curves shown in Figure 7.4, we notice that below ~ 2.2 eV, two other absorption onsets can be seen at ~1.9 eV and ~1.4 eV. In Figure 7.7 (a) and (b), we include the *F(R)* for different size $BiFeO_3$ samples this intragap energy range. Because of the limited infrared range of our spectrophotometer to 900nm (~1.4 eV) (Figure 7.7(b)), in order to provide further evidence on the existence of this low energy transition, we have used another spectrophotometer (PerkinElmer Lambda 950 UV Vis NIR), capable to illuminate and detect within the near infrared range and up to 1800 nm (Figure 7.7(a)). We can thus confirm that the different absorption peaks at ~1.4 eV and ~ 1.9 eV exist in all $BiFeO_3$ particles, being attributed to $^6A_{1g} \rightarrow {}^4T_{1g}$ and $^6A_{1g} \rightarrow {}^4T_{2g}$ crystal-field transitions, respectively (Figure 7.7 (c)). Strikingly, in contrast to the other absorption bands, low-energy crystal-field bands at ~1.9 eV are obviously affected by the decrease of the particle size, the positions are red-shifted and the intensity is also decreased (within the detection limits), as shown in the Figure 7.7 (b). We cannot rule out that the effect of higher disorder near the band gap edge increases the band gap absorption onset, affecting the shape of the curve and making it difficult to determine the energy position of the transition at ~1.9 eV. On the other hand, compared to the transition at ~1.9 eV, the lower energy transition at ~1.4 eV clearly holds the same energy for different size $BiFeO_3$ particles, which is shown in Figure 7.7 (a).

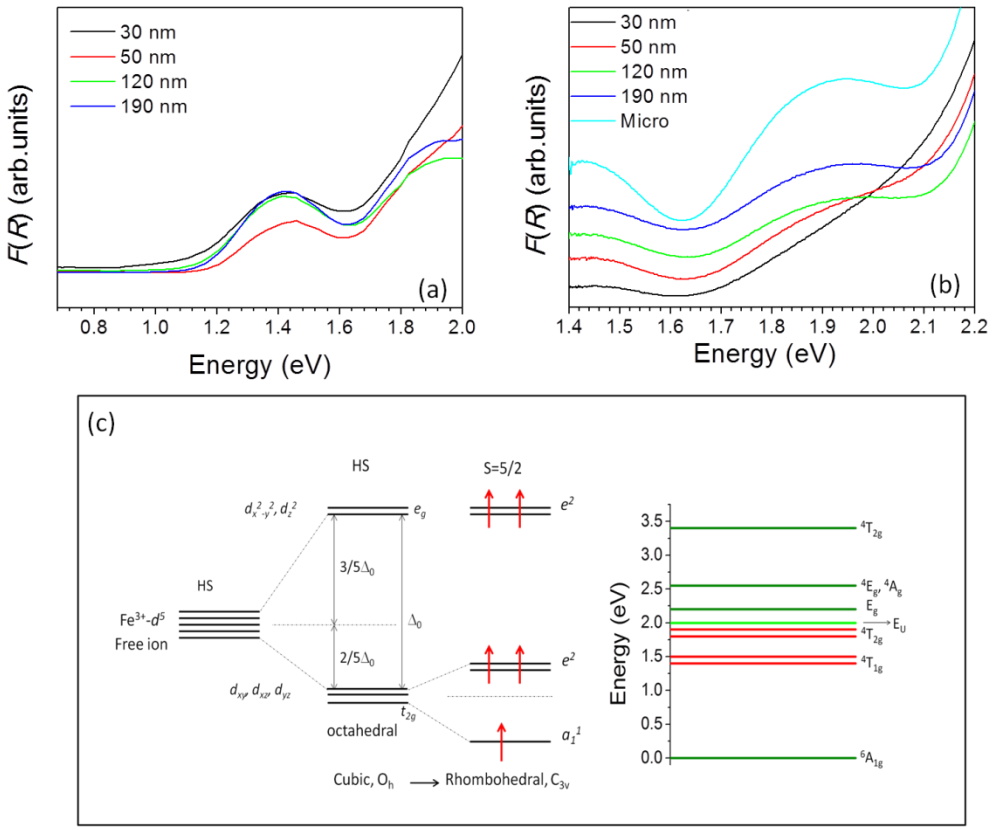


Figure 7.7 [(a) and (b)] K-M functions at low energy range, observed peaks correspond to the *d-d* transitions ${}^6A_{1g} \rightarrow {}^4T_{1g}$ (~1.4 eV) and ${}^6A_{1g} \rightarrow {}^4T_{2g}$ (~1.9 eV); (c) Schematic representation of the crystal-field effect lowering the symmetry from cubic octahedral $O_h$ to rhombohedral $C_{3v}$ environment and the energy levels involved in $BiFeO_3$. $E_c$ and $E_v$ indicate the expected bottom conduction and top valence band, respectively. $E_U$ corresponds to the Urbach energy.

These bands have been demonstrated to be magnetically sensitive and, more interestingly, by using an oscillator strength analysis involving electron-phonon coupling[216], it has been also shown that their temperature dependent behavior changes at 150 K; Raman scattering has highlighted a similar anomaly behavior near 140 K which has been interpreted as a spin reorientation transition. And it also remarkably corresponds to the temperature value of one of the transitions reported for the skin-layer of $BiFeO_3$[188]. We note that the magnetic changes have been previously attributed to the skin-layer at this peculiar temperature[188], which means the electrons state between skin layer and bulk is different. In addition, some *d-d* transitions may exhibit a finite size effect due to the different spin orientation at the surface. Moreover, since such a skin-layer is also known to be the site of trapped states for charge carriers, we propose here that the defect states evidenced from

our Urbach analysis at room temperature could be mainly located in the skin-layer. Therefore, both the Urbach energy and low-energy bands changes for different particle size could suggest that the skin-layer and the defects trapped in it plays a major role in modifying the optical response of $BiFeO_3$ particles.

Further analysis on the K-M functions shown in Figure 7.4 as a whole is thus related to above band gap transitions. In detail, above ~2.2 eV, the absorption suddenly increases and shows two broad bands at ~3.4 eV and ~5.2 eV. On its low-energy side, the *p-d* charge-transfer band at ~3.4 eV is affected by the $^4T_{2g}$ crystal-field electronic level localized at ~3.3 eV as well as additional bands previously reported at ~2.8 eV, 2.9 eV and 3.1 eV by second-harmonic-generation measurements and explained by electronic states and multimagnon couplings[220]. The band at ~5.2 eV can be assigned to (*p*+*d*)-*p* charge-transfer[221] and the tail on the left-side energy at ~4.5eV is explained by *p-d* charge-transfer excitations[222]. As previously mentioned, while the charge band gap is expected at ~2.6-2.8 eV[101, 222], a narrow *d-d* band absorption at ~2.55 eV corresponding to ($^4E_g$, $^4A_g$) crystal field levels and a shoulder at ~2.4 eV in the linear spectra above ~2.2 eV due to *d-d* charge-transfer (and possibly to double-excitons) can be observed[220]. From this analysis, the resulting electronic energy-level scheme for the $Fe^{3+}$ ions is summarized in Table 7.1.

Table 7.1 Summary of the different energy levels optically probed in $BiFeO_3$ particles

| **Type of energy levels/Transitions** | **Energy (eV)** |
|---|---|
| Crystal-field levels of $Fe^{3+}$ in $BiFeO_3$ | ~1.4, ~1.9 |
| Charge gap, $E_{eff,g}$ | ~2.2 |
| Double-exciton/charge transfer bands | ~2.4 |
| $^4E_g$, $^4A_g$ crystal field levels | ~2.55 |
| Multimagnon coupling | ~2.8, ~2.9, ~3.1 |
| *p-d* charge transfer | ~3.4, ~4.5 |
| *(p+d)-p* charge-transfer | ~5.2 |

Due to the superimposition of charge transfer excitation bands associated with interatomic transitions between O 2*p*, Fe 3*d*, Bi 6*s* and Bi 5*p* levels and absorption

bands (*d-d* bands transitions) originating from on-site $Fe^{3+}$ (high-spin $3d^5$) crystal-field transitions linked to its rhombohedral symmetry environment (Figure 7.7 (c)), $BiFeO_3$ reveals a complex and puzzling electronic structure. Since the rhombohedral structure, $Fe^{3+}$ displaces away from the central location in octahedral, the electronic configuration of free $Fe^{3+}$ ions will evolve from the typical $t_{2g}^3 e_g^2$ high spin configuration in the cubic octahedral environment to the $a^1e^2e^2$ one, as belonging to the rhombohedral environment $C_{3v}$ space group. In addition, the lowering of the local symmetry by defects/strains can lead to a shift of the energy levels, lift off of the degeneracy (*e* orbitals can split) and/or insertion of localized intragap energy levels, thus adding some extra absorption features.

From the above analysis and the optical reflectance spectra in the ultraviolet-visible-near infrared range of as-synthesized $BiFeO_3$ particles, it is clear that four unambiguous absorption regions appear in the absorption that can be adscribed to different processes. In Figure 7.4, region 1 (250-400 nm) mainly includes the ligand to metal charge-transfer transitions and partly the contributions of the $Fe^{3+}$ ligand field transitions ${}^6A_1 \rightarrow {}^4T_1$(4P) at 290-310 nm, ${}^6A_1 \rightarrow {}^4E$(4D) and ${}^6A_1 \rightarrow {}^4T_2$(4D) at 360-380 nm. Region 2 (400-600 nm) is considered to include the pair excitation processes ${}^6A_1 + {}^6A_1 \rightarrow {}^4T_1$(4G)+${}^4T_1$(4G) at 485-550 nm, possibly overlapped to the contributions of ${}^6A_1 \rightarrow {}^4E$, ${}^4A_1$(4G) ligand field transitions at 430 nm and the charge-transfer band tail. Region 3 (600-750 nm) is assigned to include the ${}^6A_1 \rightarrow {}^4T_2$(4G) transition at about 640 nm. Finally, region 4 (750-900 nm) covers the ${}^6A_1 \rightarrow {}^4T_1$(4G) transition at about 900 nm. Moreover, the absorption values in regions 1 and 2 are far larger than those in regions 3 and 4, which indicates that the absorption from the charge-transfer transitions or the pair excitations is far stronger than that from the ligand field transitions due to the selection rules.

Interestingly, though $BiFeO_3$ presents a G-type antiferromagnetic structure and belongs to the *R3c* space group, the spin-orbit interactions and the presence of a spin cycloid and spin canting[35], these effects give rise to more relaxed parity-forbidden transitions[216]. All this can lead to large transition probabilities for the spin-allowed single-ion excitation and simultaneous double-ion excitation (pair

excitations or double exciton processes) of two $Fe^{3+}$ centers. In the case of $BiFeO_3$, the transition at 500 nm is responsible for the double exciton [$^6A_1$+$^6A_1$→$^4T_1$ (4G)+$^4T_1$(4G)]. In the long wavelength (low energy) region, from 600 nm to 900 nm, just the spin-allowed single-ion excitations and relaxed parity-forbidden transitions of the $Fe^{3+}$ ligand field transitions can occur. The defects combined with uncompensated spins on the surface induce weak ferromagnetic interaction between interstitial $Fe^{3+}$ ions, which cause the *d-d* charge transition between the ground $^6A_1$ state and the excited states $^4T_2$(4G).

### 7.2.2 High temperature behavior

The band gap of $BiFeO_3$ single crystal and thin film has been extensively studied, found to be ~2.6-2.8 eV. For our $BiFeO_3$ nanoparticles, the analysis of the diffuse reflectance data at room temperature indicates the existence of a skin layer, where defects, local distortions, surface reconstructions, *etc*. can be located, and indeed they can affect the optical absorption of $BiFeO_3$ by shifting and/or splitting energy levels. Using the direct band gap approach and using Tauc plots with our set of data, an effective band gap of $E_{g,eff}$ ~2.2 eV has been obtained for $BiFeO_3$ nanoparticles. From Figure 7.5 (b), it can be seen that the variation of band gap is weak as a function of particle size. Because of the spin-charge-lattice coupling, the band structure of $BiFeO_3$ is sensitivity to the external factors, such as temperature and stress[223-224]. The obvious metal-insulator transition of $BiFeO_3$ single crystal has been confirmed by investigating the variation of band gap value as a function of temperature.

In order to find out the temperature dependence of band gap and any optically probed transition in $BiFeO_3$ nanoparticles, diffuse reflectance spectra have been measured for temperatures between 300 and 680 K for our samples (Figure 7.8). From the diffuse reflectance result, curves are characterized by a redshift, the shape of the curves indicating that the shoulder at ~600 nm disappears with higher temperature.

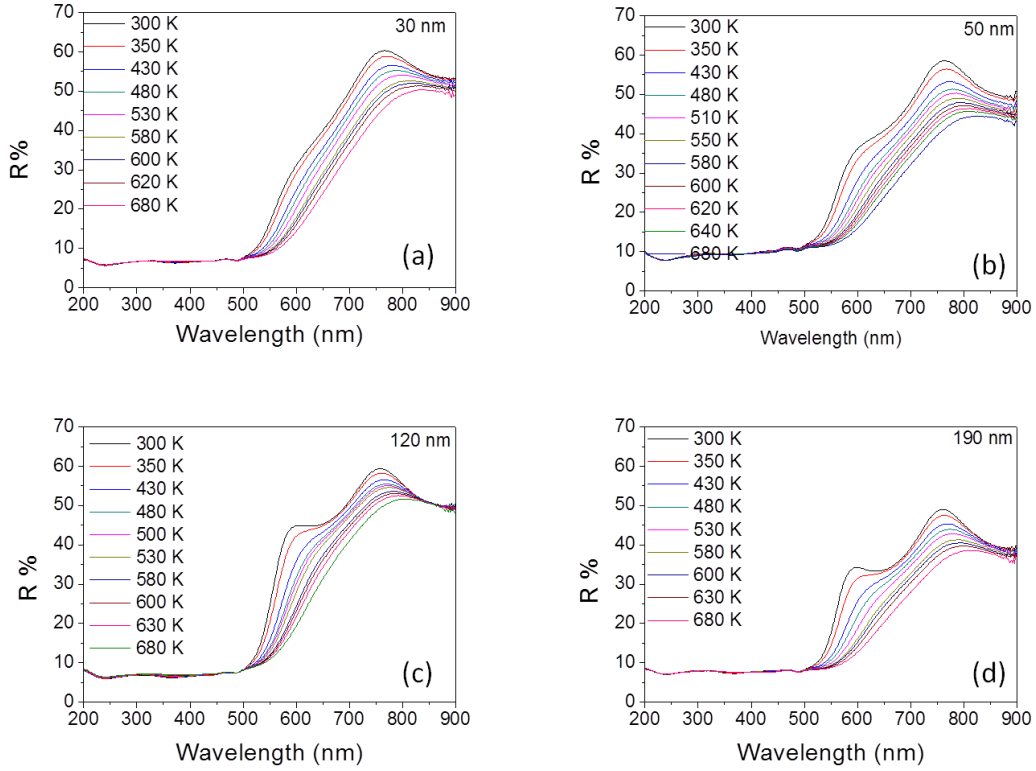


Figure 7.8 Diffuse reflectance spectra as a function of temperature for different size $BiFeO_3$ nanoparticles : (a) 30 nm, (b) 50 nm, (c) 120 nm, and (d) 190 nm.

From Figure 7.9, the band gap values of different sizes samples as a function of temperature have been determined from the corresponding linear fits of the Tauc plots. From Figure 7.9, we notice that the band gap decreases as temperature increases, similarly to what has been reported for $BiFeO_3$ single crystals[223]. The temperature dependence of the band gap values for different particle size samples is shown in Figure 7.10. It can be seen that with increasing the temperature, the band gap for all $BiFeO_3$ nanoparticles decrease almost linearly, with no discontinuity. Considering these dependences as linear ones, the fitting results have provided variation rate constants for the band gap (Table 7.2). Comparing the overall band gap variation rates from nanoparticles, we notice that these values are constraint between $-5.12\times10^{-4}$ and $-6.74\times10^{-4}$ eV/K, whereas the corresponding value for microparticles is that of a much pronounced slope, $-9.66\times10^{-4}$ eV/K.

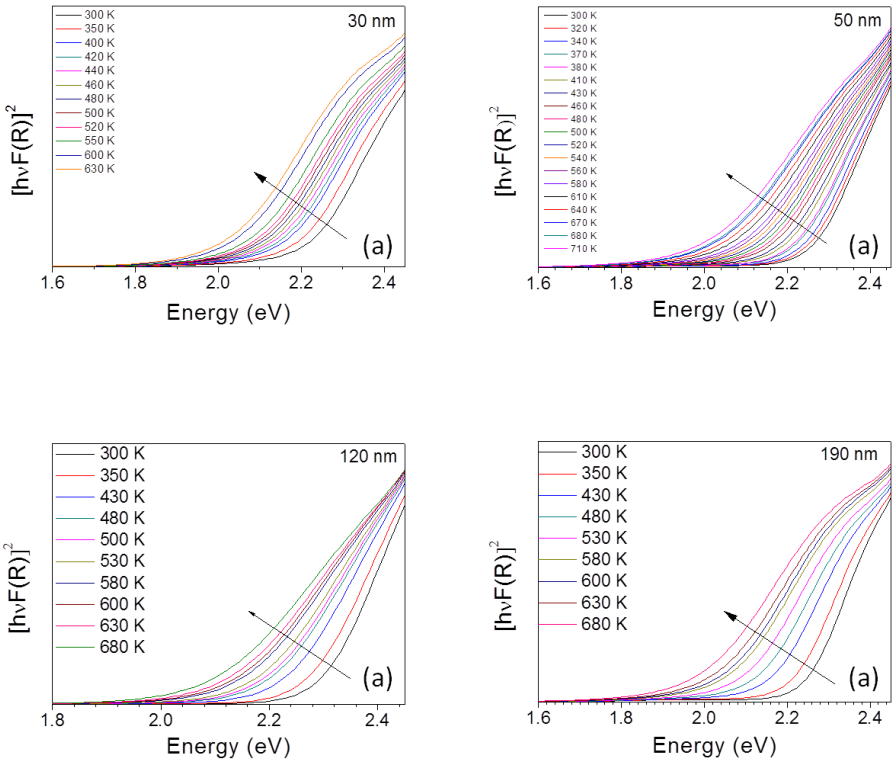


Figure 7.9 (a) Temperature dependence of the Tauc plots of different size $BiFeO_3$ nanoparticles: (a) 30 nm, (b) 50 nm, (c) 120 nm, and (d) 190 nm. The arrow indicates the different spectra as the temperature increases.

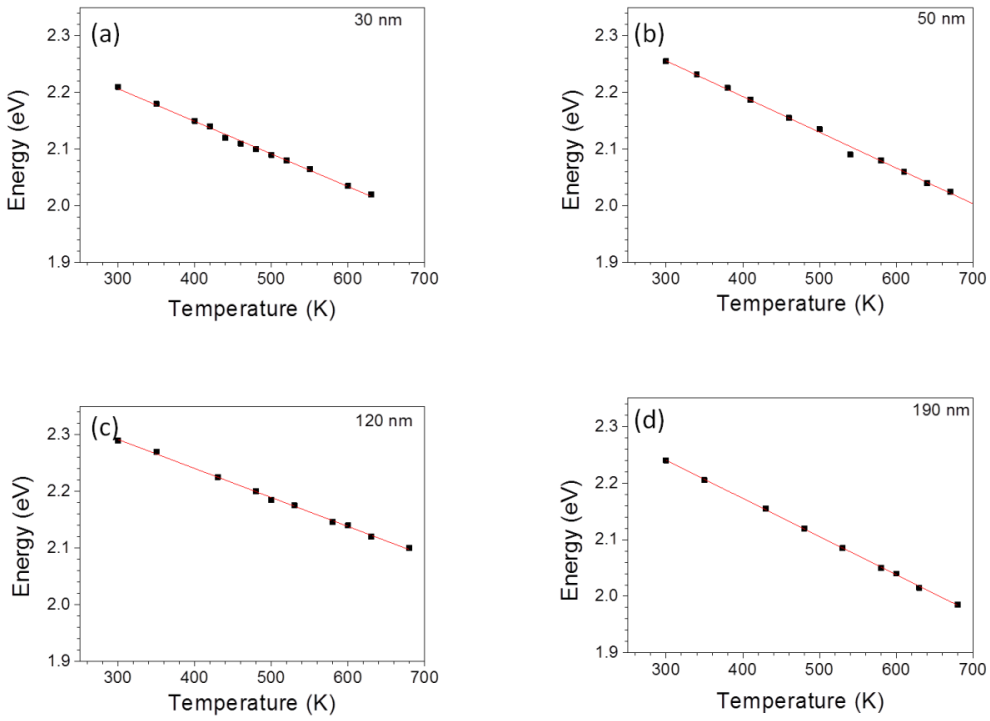


Figure 7.10 Band gap values as a function of temperature of different size $BiFeO_3$ nanoparticles: (a) 30 nm, (b) 50 nm, (c) 120 nm, and (d) 190 nm.

Table 7.2 Thermal variation rates of band gap, Urbach energy and low energy transition

| Sample | Variation rate×$10^{-4}$ (eV/K) (band gap) | Variation rate×$10^{-4}$ (eV/K) (Urbach energy) | Variation rate×$10^{-4}$ (eV/K) (low energy *d-d* transition) |
|---|---|---|---|
| 30 nm | -5.97 | 1.97 | -5.35 |
| 50 nm | -6.31 | 3.68 | -4.60 |
| 120 nm | -5.12 | 2.69 | -4.90 |
| 190 nm | -6.74 | 3.87 | -4.79 |
| Micro | -9.66 | 9.22 | -3.96 |

The room temperature band gap values as a function of particle size shown in Figure 7.5 (b), and the fact that below a given particle size the band gap decreases, were previously explained by the existence of defect-induced energy levels between conduction and valence bands, more specifically energy levels close to the conduction band. These shallow levels can reduce the effective band gap for smaller particles, if their density is high enough. The presence of non-uniform micro strain in the particles but also surface reconstructions or other surface effects modify the energy levels, influencing the absorption band edge[195]. As mentioned in chapter 6.1, and it can be seen that micro-strain increases with particle size decreasing, this result also being reported in Ref. [195]. In general, the micro-strain in nano-crystallites is caused by several factors, like non-uniform lattice distortions, dislocations, anti-phase domain boundaries, grain surface relaxation, *etc*. In $BiFeO_3$, the most common defects such as oxygen vacancies are major contributions to the micro-strain, these oxygen vacancies reportedly at lower energy level than the adjacent Fe 3*d* levels, resulting in sub-band gap defect states, analyzed in chapter 7.2.1. Another contribution to the micro-strain comes from the unsaturated bonds on the surface of the nanoparticles, which create deep and shallow levels within the band gap[225], helping to stabilize other valence states for the cations, as $Fe^{2+}$, or adsorbed molecules, such as FeOOH (chapter 6.3.4).

For the high temperature band gap analysis, the 120 nm nanoparticle data indicate an inflection point in the observed trend as a function of particle size. In fact, the electron confinement, coulomb interactions, and binding energy effects dominate each other in different particle size regimes[33, 226-227]. Thus, because of the weak variation of band gap at room temperature (~2.2 eV) and the high temperature

variation rates (from $-5.12\times10^{-4}$ to $-6.74\times10^{-4}$ eV/K) for different particle size, we speculate that variation trend of the electron configuration for all nanoparticles as a function of temperature is the same within the studied temperature range. That is, compared to $BiFeO_3$ microparticles, all $BiFeO_3$ nanoparticles present the same defect configuration. To study these defects (disorder) in $BiFeO_3$ particles, the Urbach energy has been studied as a function of temperature, and it will be presented below (Figure 7.11 and Figure 7.12).

Similarly to the analysis performed for the room temperature data, from the different Kubelka-Munk curves, we can determine the Urbach energy $E_U$ related to variations of the energy levels close to the conduction and/or valence bands (affected by different sources of disorder), as a function of temperature. Figure 7.11 depicts the corresponding Urbach energy plots for $BiFeO_3$ nanoparticles at different temperatures.

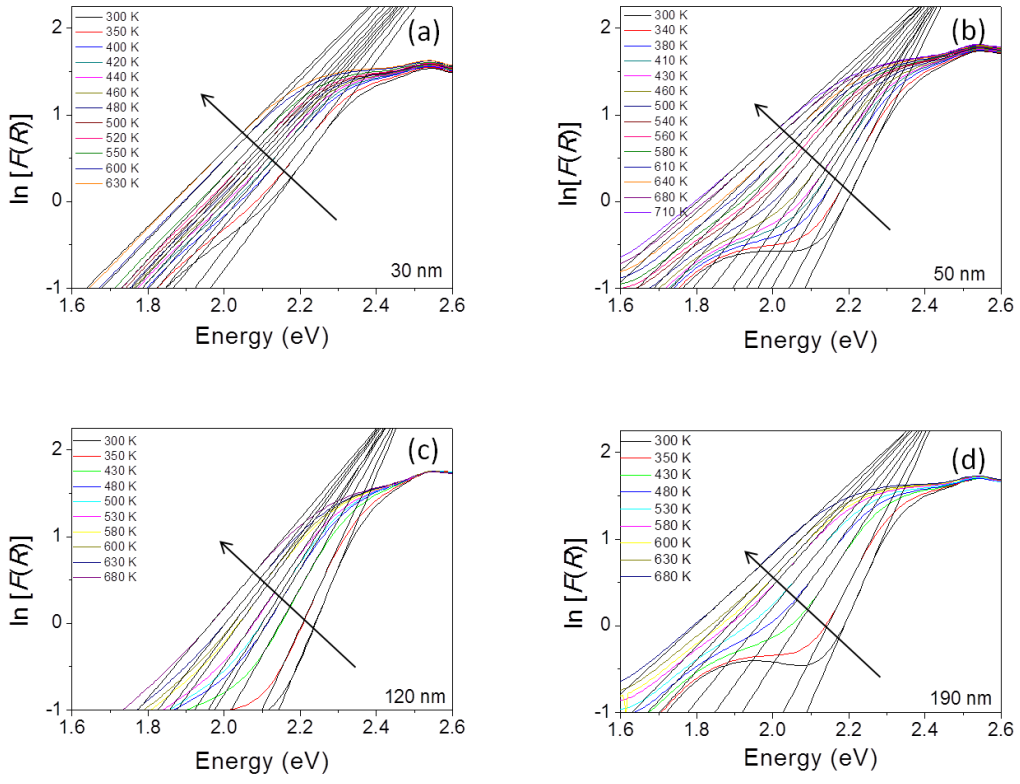


Figure 7.11 *ln[F(R)]* plots as a function of temperature for different size $BiFeO_3$ nanoparticles: (a) 30 nm, (b) 50 nm, (c) 120 nm, and (d) 190 nm. The arrow indicates the different spectra as the temperature increases.

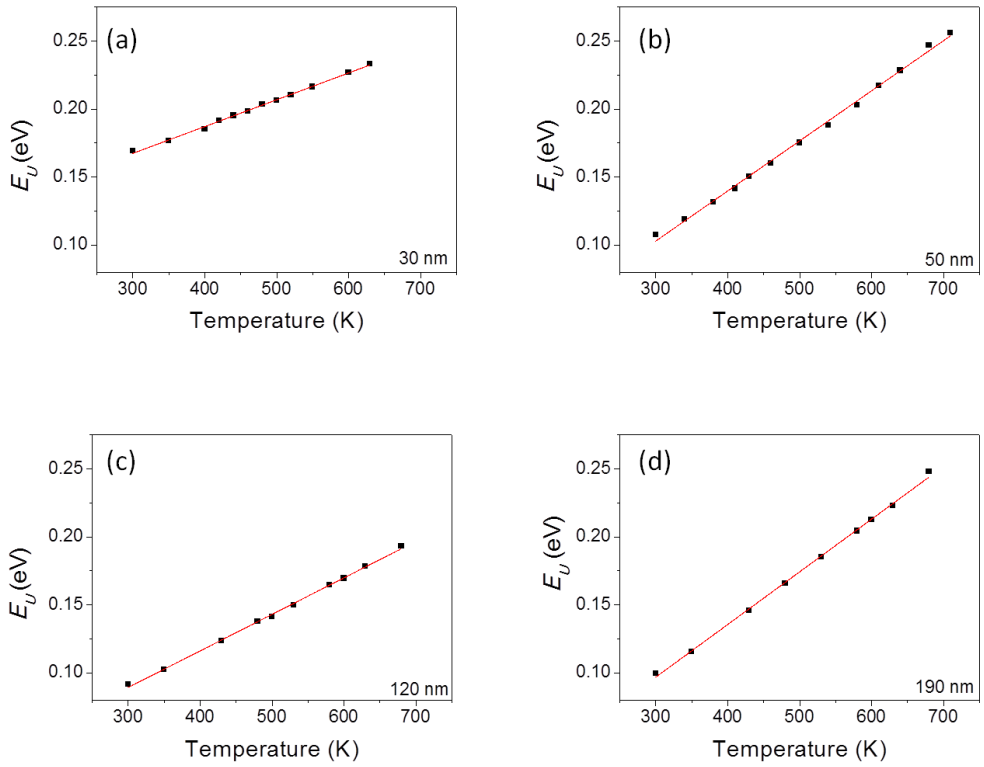


Figure 7.12 Urbach energy $E_U$ values as a function of temperature of different size $BiFeO_3$ nanoparticles: (a) 30 nm, (b) 50 nm, (c) 120 nm, and (d) 190 nm.

According to the Urbach rule in crystalline solids (equation 7.5), the Urbach behavior happens to be seen as tails near valence and conduction bands (Figure 7.6 (c)). The shape and size of these tails depend on the presence of different types of disorder. In Figure 7.11, we study the absorption tails of the absorption spectra and to apply Urbach rule (linear fit) to determine the characteristic $E_U$ values. The slope of the linear fits corresponds to $(1/E_U)$, and since it decreases with increasing the temperature, the Urbach energy thus increases as a function of temperature. In Figure 7.12, we present the temperature dependence of the Urbach energy for $BiFeO_3$ nanoparticles, the corresponding temperature variation of the $E_U$ values is summarized in Table 7.2. From the values of Urbach energy rate constant, it is difficult to find a clear trend on the nanoparticle size. However, taking a close look at Table 7.2 and comparing Urbach energy variation rate constants and the absolute values of the band gap ones for all nanoparticle data, we evidence a similar dependence: increasing band gap/Urbach below 120 nm nanoparticles, then slight decrease. Similarly, the corresponding rate constant for the microparticles is larger than that of nanoparticles. These results indicate a different nature of the electronic

defects observed by optical probes on nano and microparticles, differing also in their temperature dependence.

As a comparison with larger size particles, the reflectance spectra of $BiFeO_3$ microparticles have been also investigated as a function of temperature (Figure 7.13). The band gap of micro-$BiFeO_3$ decreases with increasing the temperature. However, we point out that obvious differences from nano size $BiFeO_3$ data is that the absolute value of the band gap and the Urbach energy variation rates are much larger for micro than for nanoparticles (Table 7.2).

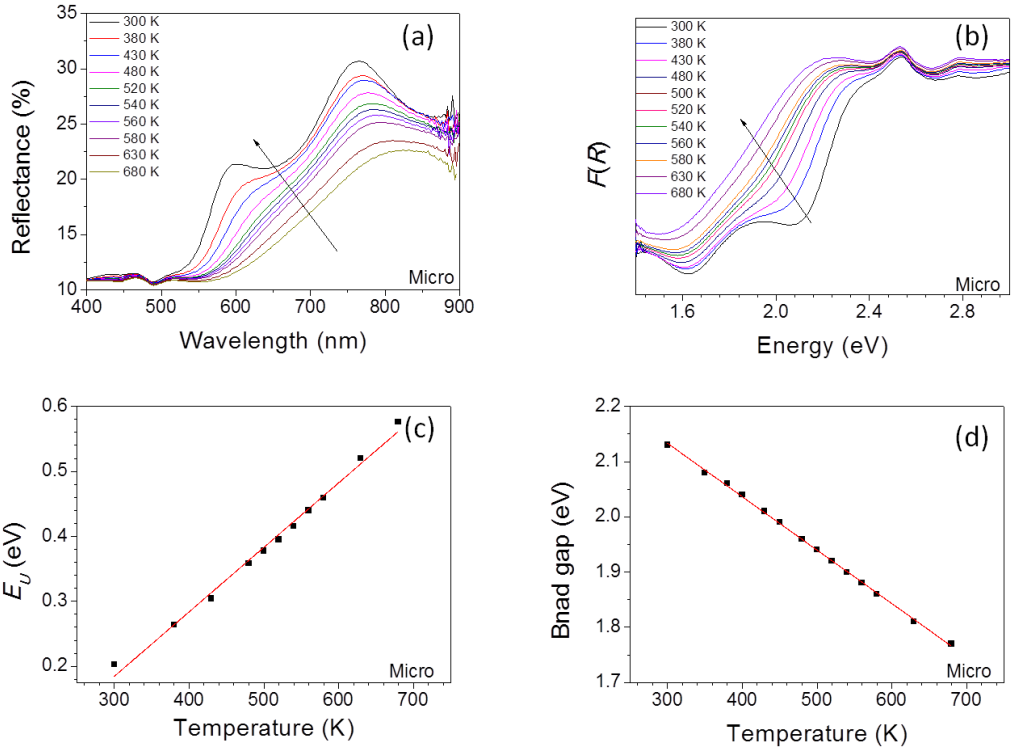


Figure 7.13 For micro-$BiFeO_3$, as a function of temperature: (a) reflectance spectra, (b) corresponding K-M functions, and fitted values of (c) Urbach energy, and (d) band gap.

On top of the investigation of the band gap and electronic disorder near it, we have studied the low energy electronic transition $^6A_1 \rightarrow {}^4T_2$ as a function of temperature (Figure 7.14 (a)), through detailed investigation of the second derivative of the KM spectra (Figure 7.13 (b)). We have proceeded in the same manner for the KM data from $BiFeO_3$ nanoparticles. In Table 7.2 we include the variation rates of this low energy electronic transition. Remarkably, these values are almost the same for nano- and micro-$BiFeO_3$. In Figure 7.14, we compare the temperature dependences of the

band gap and low energy *d-d* transition values together for micro and nanoparticles. It is seen that increasing the temperature, the low energy transition values intersect those of the band gap for $BiFeO_3$ microparticles at ~640 K (Figure 7.14 (a)). However, this effect is not observed for $BiFeO_3$ nanoparticles (Figure 7.14 (b)).

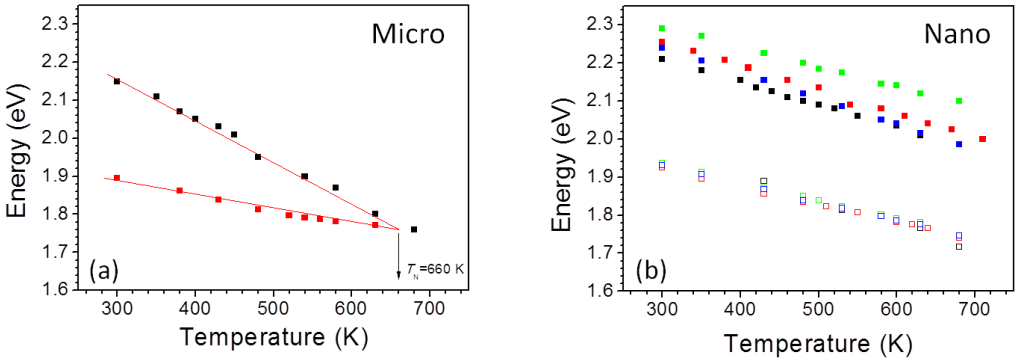


Figure 7.14 The variation of band gap and low energy *d-d* transition as a function of temperature for micron (a) and nano (b) $BiFeO_3$

In order to better understand this electronic *d-d* transition as a function of temperature for micro-$BiFeO_3$, the schematic energy diagram as a function of temperature is shown in Figure 7.15. Due to the different temperature variation rates of band gap of micro- and nano-$BiFeO_3$, the electronic band transition ($^6A_1 \rightarrow {}^4E_g$, $^4A_g$) and low energy transition band ($^6A_1 \rightarrow {}^4T_2$) merge together at high temperature.

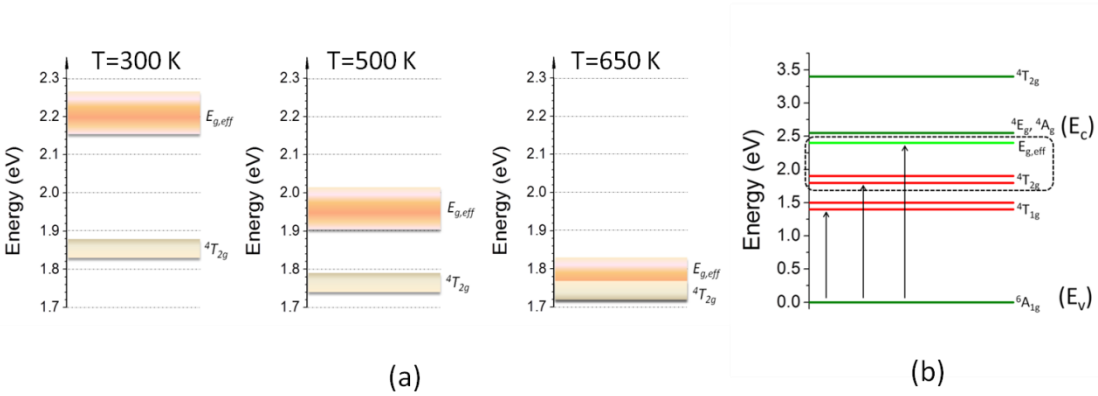


Figure 7.15 (a) Sketch of two different bands transition three different arbitrary temperatures for micro-$BiFeO_3$ (b) Band structure for $BiFeO_3$ below 3.5 eV, three arrows corresponding to the low energy *d-d* transition ($^6A_1 \rightarrow {}^4T_1$, $^6A_1 \rightarrow {}^4T_2$) and effective band gap transition.

Moreover, from the temperature dependence of the electronic conductivity (in air) of micro-$BiFeO_3$ (Figure 7.16) [thesis work of Romain Jarrier (SPMS)], as temperature

increases, around 640 K, there is no change in the absolute value of conductivity. Nevertheless, Arrhenius plots show a change in the slope, with a knee point at 640 K. The activation energy of the charge carriers changes from 0.4 to 0.85 eV as the sample is heated above 640K. We suggest that this effect is related to the band structure change increasing the temperature.

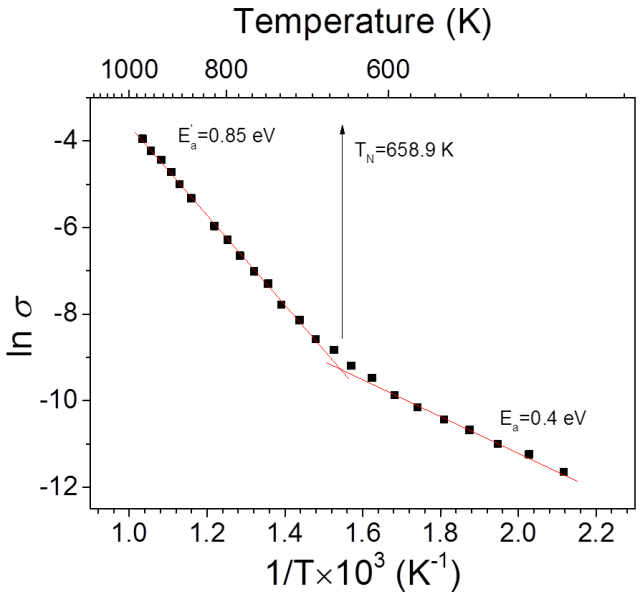


Figure 7.16 Arrhenius plot of the electric conductivity σ dependence on temperature of a pressed pellet of micro-$BiFeO_3$. The different activation energy $E_a$ values below and after the knee at 658.9 K and calculated from linear fits are also indicated

From Figure 7.14 (a) and Table 7.2, we have pointed out that the different variation rates for the band gap and low energy *d-d* transition with temperature for $BiFeO_3$ microparticles leads to a crossing point at 640 K for these energies. In other words, both $^6A_1 \rightarrow {}^4E_g$, $^4A_g$ and $^6A_1 \rightarrow {}^4T_2$ transitions continually reduce, thus the conductivity increases, and when temperature reaches 640 K, the two bands merge together, thus the electron transfer through the $^6A_1 \rightarrow {}^4E_g$ transition is easily performed. More excited electrons populate the conduction band, further increasing the conductivity. This may explain why there is a knee point in the 640 K in Figure 7.16.

For nano-$BiFeO_3$, from Figure 7.14 and Table 7.2, both variation rates for $^6A_1 \rightarrow {}^4E_g$, $^4A_g$ and $^6A_1 \rightarrow {}^4T_2$ are similar. Thus, it cannot be observed any crossing point in the temperature range under study. Electric conductivity measurements for nano-$BiFeO_3$

was not possible since the sintering in pellets induces particle growth, thus losing the interest in the particle effect. The conductivity of $BiFeO_3$ as a function of temperature has been reported in Ref. [33], in which the magnetic order affects the conductivity band gap, the knee point being assigned as the Néel temperature. Meanwhile, the Néel temperature decreasing with particles size decreasing has also been reported. However, according to our results, we did not observe the intersection between the two transitions, $^6A_1 \rightarrow {}^4E_g$, $^4A_g$ and $^6A_1 \rightarrow {}^4T_2$, at the temperature range where the Néel temperature is expected, which is contradictory with reported results. From these results, further investigations on the correlation between band gap and magnetic order in nano-$BiFeO_3$ is needed.

### 7.2.3 Band gap as a function of temperature for $BiFeO_3$ nano and microparticles

In this part, the explanation on the different temperature dependence of the band gap for different size $BiFeO_3$ samples will be given.

The band gap values of nano- and micro-$BiFeO_3$ as a function of temperature are shown in Figure 7.17. The band gap variation rate as temperature increases is different for nano and micro samples (Table 7.2), with faster rates for microparticles than the corresponding ones for nanoparticles. The combination of finite size effects on lattice parameters and atomic positions has been proved from the atomic bond lengths and angles determined from calculations and neutron diffraction analysis[80, 228]. The $Fe^{3+}$ ion displacement is more sensitive to size than the $Bi^{3+}$ ion one, thus being of interest to focus on the Fe-O bond length and Fe-O-Fe angle of two corner-sharing $FeO_6$ octahedra, as shown in Figure 7.18. From crystal structure analysis, with decreasing size, the short Fe-O bond length decreases and the long Fe-O bond length increases, and the Fe-O-Fe angle decreases with decreasing crystallite size[79]. In a band structure picture, increasing the band gap with decreasing particles size arises naturally from the structural changes at the nanoscale, since the increase of long Fe-O bond lengths and the decrease of Fe-O-Fe angles weaken the Fe-O-Fe superexchange mechanism by reducing the Fe 3*d*-O 2*p* orbital overlapping and increasing the bandwidth[29]. Thus, all this accounts for the slightly larger effective band gap observed in nanoparticles.

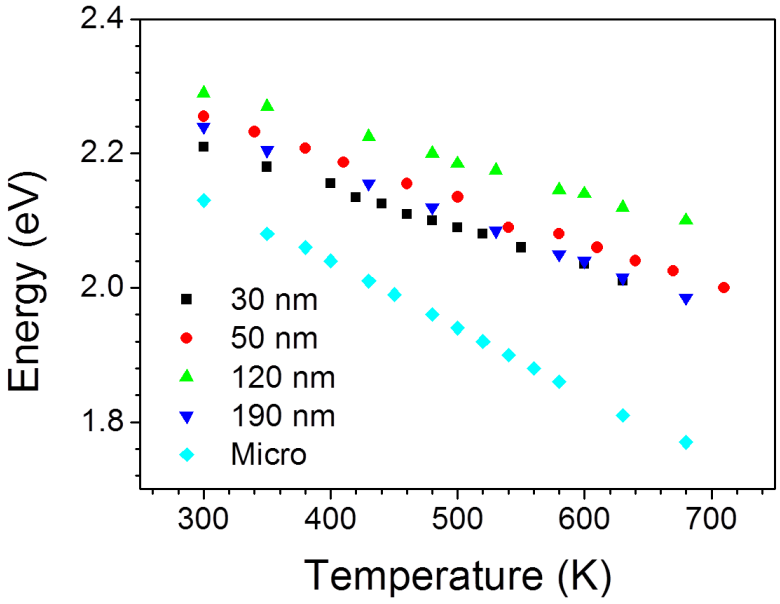


Figure 7.17 Band gap of different size $BiFeO_3$ particles as a function of temperature. Error bar

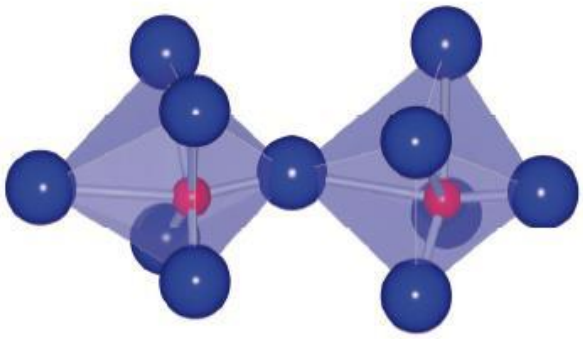

Figure 7.18 Sketch of two adjacent $FeO_6$-octahedra showing the two different Fe-O bond lengths caused by the polar displacement of $Fe^{3+}$ with respect to the center of the oxygen octahedron and the Fe-O-Fe angle < 180°

The band gap evolution as a function of temperature has been reported by Palai *et al.*[223]. However, they mainly focused on the metal-insulator transition at high temperature. In this study, different wavelength Raman spectra have been used to analyze the band gap evolution as a function of temperature[229]. According to the investigation of first and second order Raman scattering, the optical absorption changes in temperature are related to a shrinking of the indirect band gap, while the direct band gap is almost insensitive to temperature. In our case, the band gap values of nano and microparticles are all shrinking with temperature (Figure 7.17), but the variation rates are different. We explain this through the different Fe-O-Fe

angle variation in temperature. The key structure is likely to be the straightening of the Fe-O-Fe angle, which leads to the increase of the orbital overlapping between oxygen *p* the iron *d* orbitals, thus facilitating the charge transfer. This angle is known to play a key role in the functional properties of transition metal perovskite oxides. Weber *et al.*[229] have reported that the band gap decrease in temperature is caused by the modification of the valence band. They claim that this can happen because the highest valence band states predominantly originate from oxygen *p*-states, while the light relative mass of the oxygen atom will naturally lead to the largest nuclear displacements in the corresponding phonon modes. Increasing the temperature, the Fe-O-Fe angle increases, which means that it facilitates the vibration of the oxygen atom, and the phonon energy increases. Furthermore, because of the different Fe-O-Fe angle between the nano and micro-$BiFeO_3$, it can make the band gap variation rate different for different size samples.

High temperature reflectance spectra below the corresponding synthesis temperature of micro-$BiFeO_3$ were performed to investigate this high temperature transitions. In Figure 7.19, the determined band gap values for micro-$BiFeO_3$ are shown to decrease monotonously until ~875 K. Then, after this temperature, the band gap variation rate changes and we can observe a plateau, almost unchanged. Palai's results[223] signal that an analogy can be created between optical band gap and an insulator to conductor transition. Weber *et al.*[229] have proposed that the temperature-dependent modification of the valence band is primary based on a band gap value variation. In our case, the band gap value of 2.09 eV is observed for micro-$BiFeO_3$ at room temperature, which is much smaller than the reported band gap values of thin films and single crystals[224, 230]. It has been known that the oxygen vacancies are a familiar defect for the high temperature synthesis of $BiFeO_3$. Thus, the smaller band gap value shall then correspond to an intragap electronic states, caused by charge defect related to oxygen vacancies, being also in agreement with the 2.2 eV value predicted by first-principles calculations[231]. Finally, we assign this band gap value change at high temperature to a defect transition involving oxygen vacancies located at near the valence band.

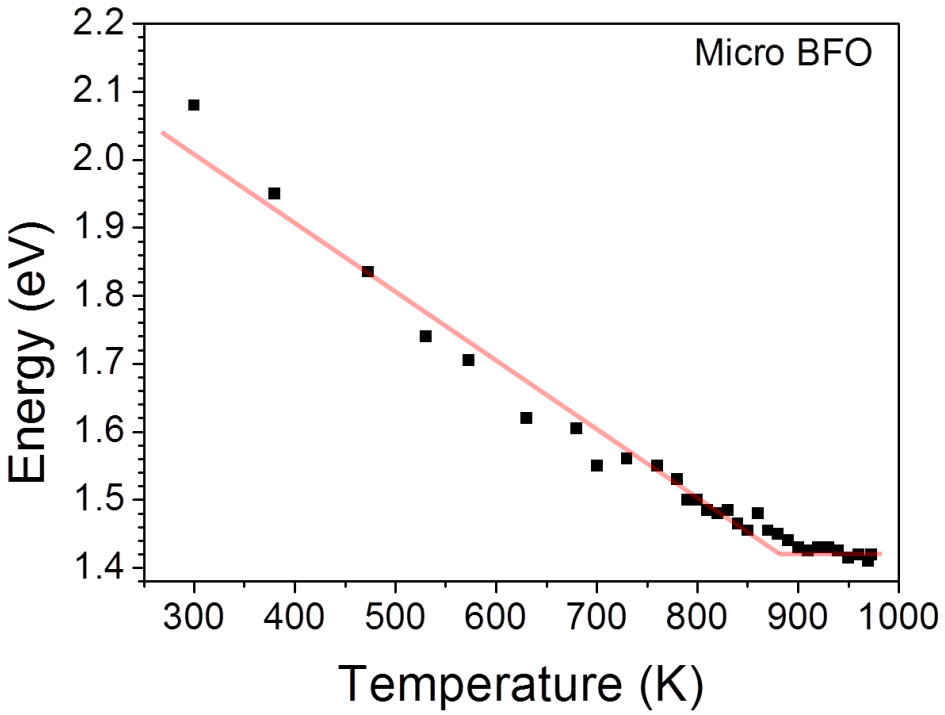


Figure 7.19 Band gap values of micro $BiFeO_3$ as a function of temperature. The line is a guide for the eye.

Using high annealing temperatures, the appearance of oxygen vacancies in $BiFeO_3$ has been largely reported [101, 232-233], concomitant to this effect, the sublimation/evaporation of Bi happens and thus the appearance of Bi vacancies[108, 233]. The conjunction of oxygen and bismuth vacancies shall affect the band structure of oxide. In view of the above mentioned facts, we propose that oxygen and bismuth vacancies appear in our micro-$BiFeO_3$ sample, simultaneously. From semi-conductor theory, in $BiFeO_3$ as the donor (*n*-type) oxygen vacancies are expected to be located close to the bottom of conduction band, on the other hand, the bismuth vacancies are acceptors (*p*-type), thus located close to the top of valence band. Generally, the Fermi level can be modulated by the relative content of donors ($\delta_d$) and acceptors ($\delta_a$)[129], and when the amount of donors and acceptors is high, the transition from non-degenerate state to degenerate state can occur, changing the position of Fermi level. Following this semi-conductor view, different Fermi level positions can be set as a function of the donor/acceptor content: (1) if there are no defects or the concentration of oxygen vacancies and hole carriers is in equilibrium ($\delta_d$=$\delta_a$), the Fermi level is located in the middle of the valence and conduction bands; (2) for

larger donor concentration (oxygen vacancies) than acceptor one (bismuth vacancies) $\delta_d > \delta_a$, the Fermi level is close to or even within the conduction band (3) for larger acceptor concentration (bismuth vacancies) than donor one (oxygen vacancies) $\delta_d < \delta_a$, the Fermi level is close to or so far as within the valence band. According to the position of Fermi level, band structure and conductivity may be confirmed. A schematic diagram of density of states is shown in Figure 7.20, the three different Fermi level positions mentioned above are presented.

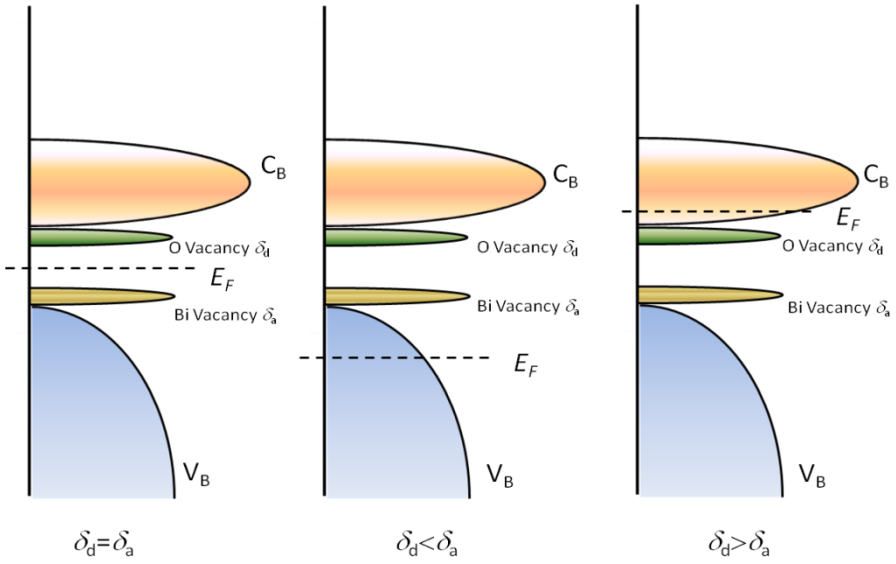


Figure 7.20 The band filling and position of the virtual Fermi level $E_F$, at representative contents of oxygen vacancies ($\delta_d$) and holes ($\delta_a$). The oxygen vacancy band is expected to be kept below the conduction band $C_B$ at room temperature.

Figure 7.21 shows the Kubelka-Munk functions of micro-$BiFeO_3$ before(after) annealing the sample at 1073 K. This procedure allows, in principle, to freeze(compensate) the oxygen vacancies created at high temperature. First, the spectrum is broader for the annealed sample than for the non-annealed one, and at ~2.2 eV, and one obvious small bump arises for the annealed one. This energy range corresponds to the aforementioned oxygen vacancies band below the conduction band. Furthermore, this phenomenon confirms that the emergence of oxygen vacancies in $BiFeO_3$ at high temperature is unavoidable under the ordinary conditions. From Mössbauer analysis at high temperature by Landers *et al.*[36], it can be seen that the isomer shift is less than 0.4 mm/s at high temperature, which is a value close to that of our samples at room temperature. This study reported that the

valence of the Fe ion is held at trivalent for the whole temperature range, which also can be affirmed by the works presented in Ref.[78, 234]. The valence state of Fe ion in Ca doping $BiFeO_3$ in A site holds as $Fe^{3+}$ (the Ca concentration is 10%)[78], which further confirm that the invariance of valance state of $Fe^{3+}$ in $BiFeO_3$. However, from our XPS results for nano $BiFeO_3$ particles, the characteristic peak of $Fe^{2+}$ is observed, although it arises essentially from the surface and it is shown even in pure $BiFeO_3$ nanoparticles. It does not affect our analysis, since the role of $Fe^{2+}$ is same as Bi vacancies, which contributes to the hole concentration in $BiFeO_3$. From analysis above, it confirms that the Bi vacancies arise with the generation of oxygen vacancies, which could also affect the Fermi level in the band structure.

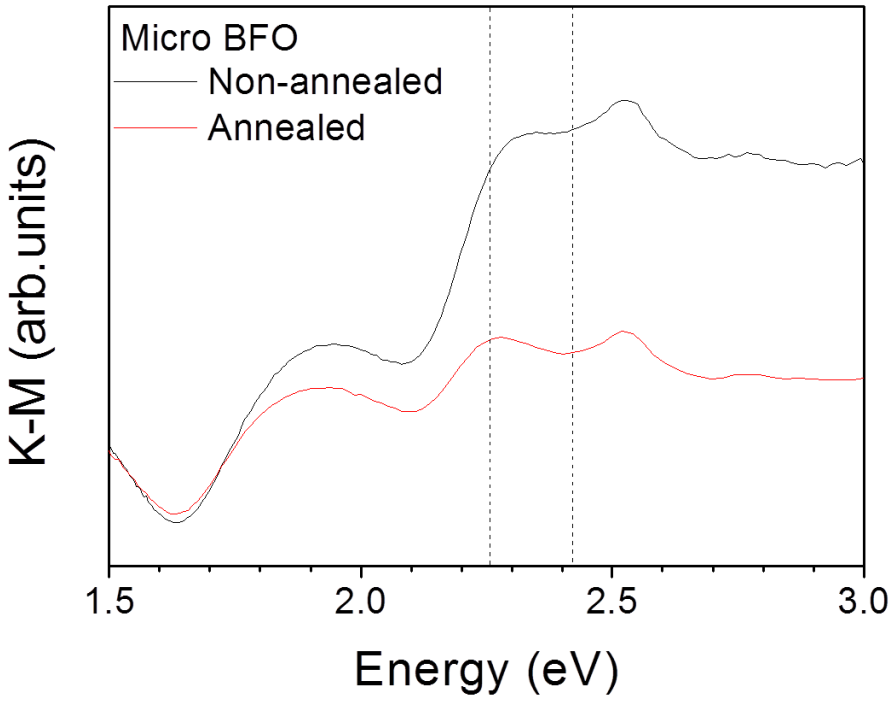


Figure 7.21 Comparison of Kubelka-Munk functions of micro $BiFeO_3$ for annealed (800 °C, 10 h) and non-annealed. Dotted lines are guide for the eye.

We now come back to the observed band gap transition at high temperature (Figure 7.19). The temperature dependence of the band gap evolution can be separated in two different behaviors, below and above ~875 K, below this temperature presenting a linear trend, and above being almost unchanged. These different trends can be understood in terms of an electronic localization (below ~875 K)-

delocalization (above ~875 K) through the different evolution of the electronic bands, leading to a Fermi level that at high temperature crosses both absorption bands (Figure 7.20). We have proposed that the explanation of this aforementioned effect is the existence of two different defects in $BiFeO_3$: bismuth and oxygen vacancies. The position of Fermi level is controlled then by the relative concentration and activation of donor oxygen vacancies ($\delta_d$) and acceptor bismuth vacancies ($\delta_a$). In our case, in order to explain the band gap values as a function of temperature, below and above ~875 K, two arguments need to be recalled. In fact, for temperatures below ~875 K, the band gap decreases with temperature increasing, caused by (1) the excitation energy form valence band to defect state involving oxygen vacancies decreases with temperature, and/or (2) the excitation energy from a defect state near the valence band caused by bismuth vacancies towards the conduction band decreases. To determine the most probable scenario and shed light on the role of vacancies in the $BiFeO_3$ band structure, we compare the temperature dependence of the band gap for samples with different vacancy content, *i.e.* for annealed and non-annealed $BiFeO_3$ (Figure 7.22).

First, we notice that annealed $BiFeO_3$ microparticles depict a smaller band gap than those of non-annealed samples. Interestingly, both series of data exhibit the same trend in temperature, with the inflection point at ~875 K. The concentration of bismuth vacancies can be larger after annealing for a rather long time (10 h) at high temperature (1073 K), and oxygen vacancies may not have been completely compensated and present a larger bandwidth, all these effects contributing to the shrinkage of the effective band gap for the annealed sample. In order to explain the observed plateau values for the band gap above ~875 K (Figure 7.19 and Figure 7.22), one possible explanation is that the Fermi level becomes affected by high temperature activated states in the valence (conduction) band and is kept at the middle of the forbidden band. As a matter of fact, we notice that the shape of the curves is very similar for both samples, thus the nature of the defects should be essentially the same for both samples, though the population and width of the defect states is clearly larger due to the high temperature annealing. Consequently, at ~875 K, the Fermi energy level should sit at the middle of the forbidden band

though the compensated effect of both defect states (oxygen vacancies at the conduction band, bismuth vacancies at the valence band), these states becoming saturated, leading to the invariant band gap value observed above ~875 K.

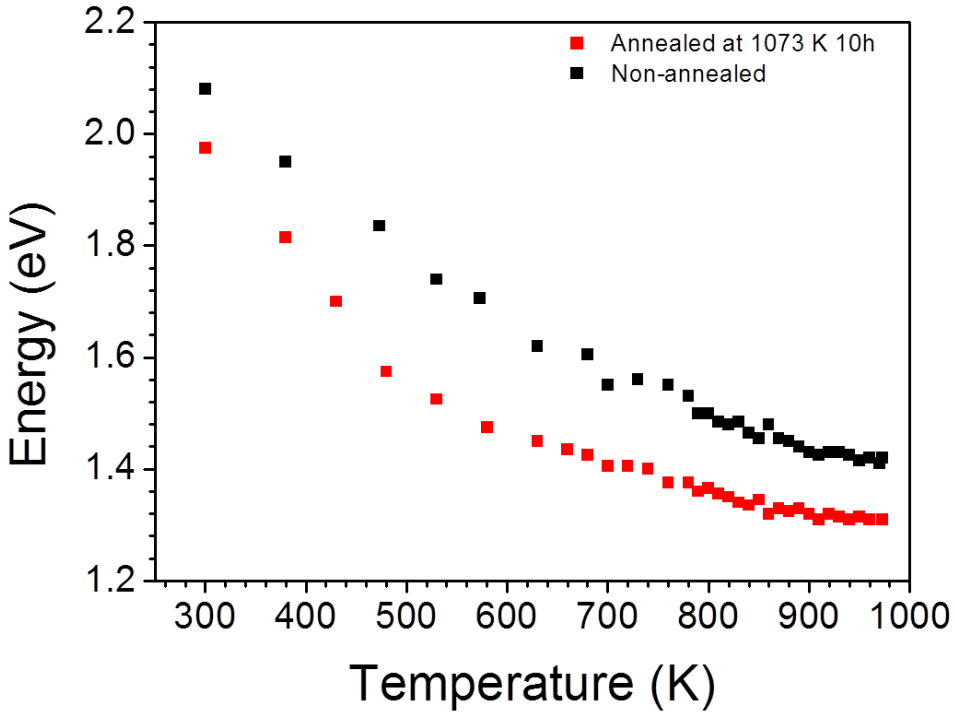


Figure 7.22 Comparison of band gap variation as a function of temperature for annealed and non-annealed $BiFeO_3$.

From the above analysis, we speculate that annealed $BiFeO_3$ microparticles can be considered more as a room temperature *p*-type semiconductor, since the high temperature annealing may primarily create new bismuth vacancies and the observed curves of annealed (1073 K, 10h) and non-annealed samples are barely the same. At room temperature, the holes concentration caused by bismuth vacancies is thus higher than the concentration of oxygen counterparts. In other words, the amount of acceptors is higher than the amount of donors. The Fermi energy level could lie much closer to the valence band, and with temperature increasing, the transition from degenerate state to non-degenerate state occurs at ~875 K. Although the band gap variation of the annealed $BiFeO_3$ as a function of temperature has the similar variation trend as non-annealed $BiFeO_3$, we conclude that the band gap values of the annealed $BiFeO_3$ are smaller compared to the non-annealed one due to

the enlargement of the width of the defect bands and the increase of the population of oxygen vacancy states.

### 7.2.4 Low energy *d-d* transition as a function of temperature for $BiFeO_3$ nano and microparticles

In order to investigate the *d-d* transition at low energy of different size $BiFeO_3$ particles as a function of temperature, we have fitted the diffuse reflectance spectrum using Bi-Gaussian functions, the spectrum from the maximum temperature experiment for each sample has been used as the baseline for every spectrum at any other temperature. As an example, the fitting procedure corresponding to the reflectance spectra from microparticles is shown in Figure 7.23.

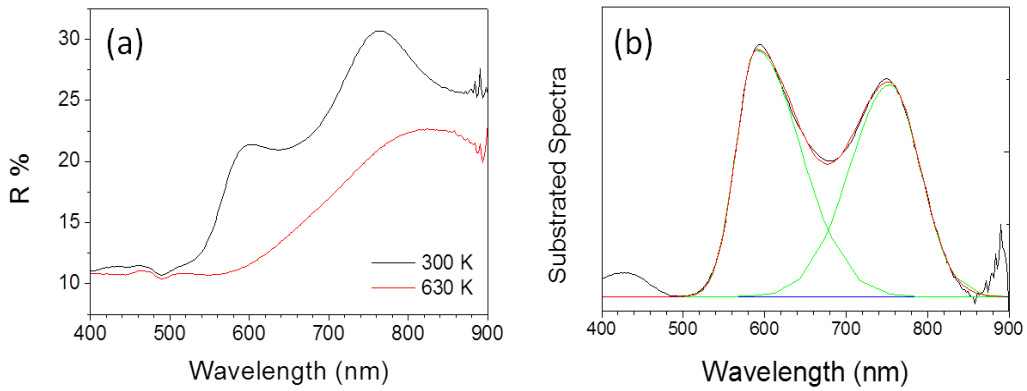


Figure 7.23 Reflectance spectra of $BiFeO_3$ microparticles: (a) for 300 K and 630 K (higher temperature experiment, data used as baseline), (b) corrected spectrum using the 300 K spectrum and removing the 630K one in (a), and the corresponding fitting result using Bi-gaussian functions.

The reflectance peak centers of the corresponding Bi-Gaussians as a function of temperature of different size $BiFeO_3$ are shown in Figure 7.24. It can be clearly seen that, compared to the reflectance peak at ~750 nm, the reflectance peak at ~600 nm shifts in temperature with a faster rate. Interestingly, the temperature dependences of both peaks present an anomaly at ~550 K-600 K for all size samples. The skin layer, which has its own lattice parameter and electronic structure, has been found in single crystals and nanotubes of $BiFeO_3$, with reported transitions happening at 140.3 K, 201 K and 550 K[188-189] and related to its variation of the electron density and elongation of the out-of-plane lattice parameter. The transition seen in our diffuse

reflectance spectra as a function of temperature is not to be a coincidence, on the contrary, we argue it is related to the phase transition of the skin layer of different size samples.

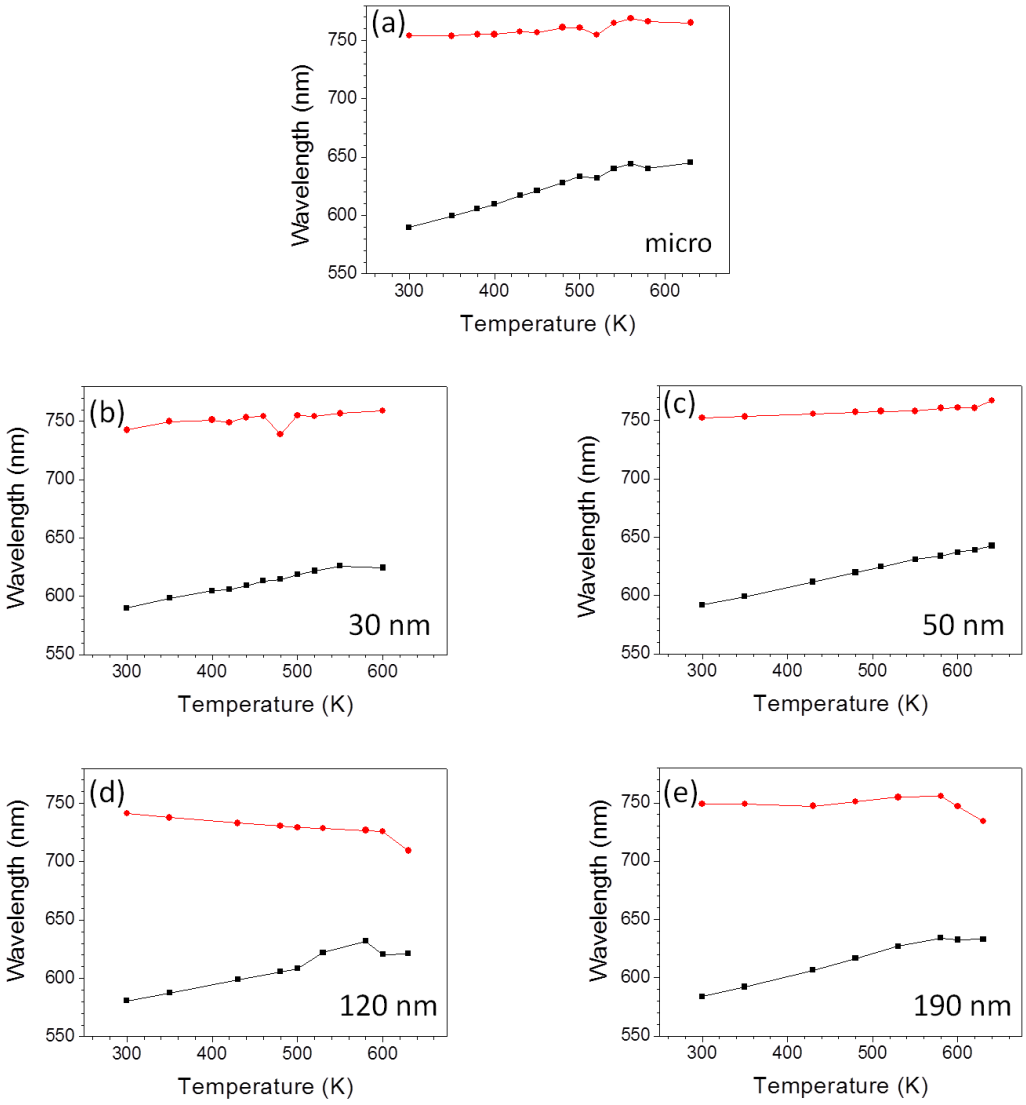


Figure 7.24 Center positions of the low energy transitions as a function of temperature obtained from fitting the two reflectance peaks at ~600 nm and ~750 nm for different size samples: (a) micro, (b) 30 nm, (c) 50 nm, (d) 120 nm, and (e) 190 nm.

In Figure 7.25 (a) we show the reflectance spectra together with the corresponding Kubelka-Munk (K-M) functions for $BiFeO_3$ nanoparticles. Remarkably, the reflectance peaks previously fitted correspond in the K-M functions to the energy interval identified for the low energy *d-d* transition. Thus, computing the center position difference (wavelength difference) for the different samples and as a function of temperature will provide us information on this transition. The wavelength

difference for different size samples in temperature are included in Figure 7.25 (b)-(f). It can be seen that the width (wavelength difference) of the *d-d* electron transition decreases in temperature, meaning that the *d-d* transition weakens compared to the background (high temperature baseline). Some anomalies are more clearly seen in these wavelength difference plots. In particular, we notice that the data from microparticles depicts two clear anomalies, identified by two inflection points, whereas the data from nanoparticles present much weaker effects. These results are in agreement with the *d-d* transitions analyzed previously in chapter 7.2.2 for different size samples, being different between micro and nanoparticles.

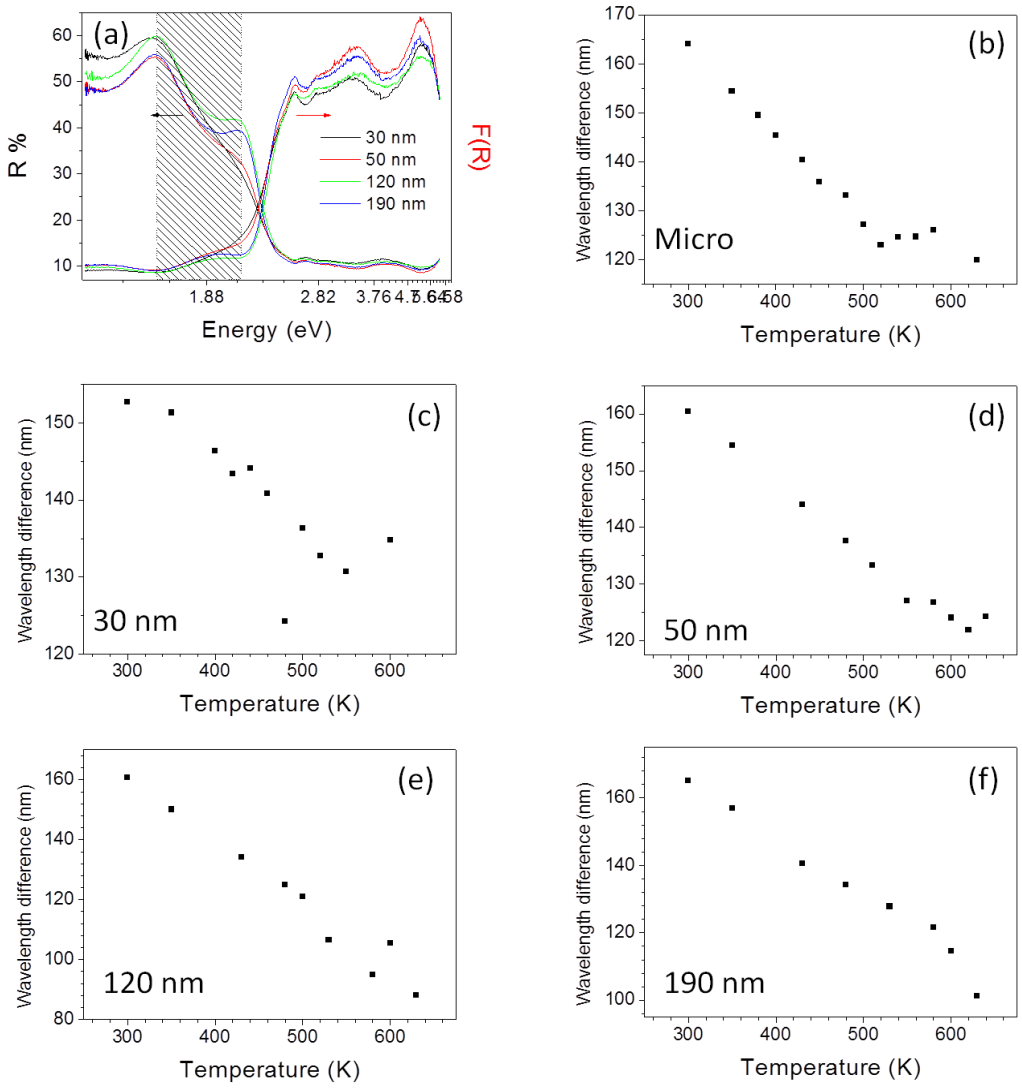


Figure 7.25 (a) Reflectance and Kubelka-Munk spectra of different size $BiFeO_3$, the shadowed part is the correspond area of low energy *d-d* transition in reflectance and Kubelka-Munk spectra; (b)-(f) are the reflectance difference as a function of temperature of different size $BiFeO_3$.

We recall that a surface transition has been identified from Raman spectroscopy of different size samples as a function of temperature (chapter 6.2.2, Figure 6.12 and Figure 6.13, Table 6.4). It is known that any static and/or dynamic changes in the structure should, in principle, lead to a variation in the phonon behavior, and the analysis of the wavenumber, intensity, and/or linewidth evolution of the whole spectra as a function of temperature is expected to give insight into those change[188]. The Raman modes transition temperatures (Figure 6.12 and Figure 6.13, Table 6.4) for different size samples are comparable to the anomalies seen in Figure 7.25 (b)-(e), all round 550 K. The Raman modes at low wavenumber corresponding to Bi mode activity in $BiFeO_3$. Ab initio calculations[188] suggesting that Bi vacancies may be at the origin of the defect state levels and the variation of out-of-plane lattice parameter related to Bi sublattices, combined to our Raman modes (140 $cm^{-1}$ and 170 $cm^{-1}$) anomaly with increasing the temperature, all this means that a strong uniaxial strain at the surface is expected around 550 K[189]. With the surface transition at ~550 K being confirmed by impedance analysis and grazing incidence X-ray diffraction[189], the temperature dependences of our reflectance data and K-M function analysis of *d-d* transition at 550 K provide another proof of the existence of a high temperature surface transition related to Bi vacancies at the surface.

## 7.3 Optical properties of A-site doped $BiFeO_3$

### 7.3.1 Low energy *d-d* transition as a function of temperature for A-site doped $BiFeO_3$ nano and microparticles

In this section, the low energy *d-d* transition as a function of temperature for doped and non doped $BiFeO_3$ sample are compared. As mentioned above, from K-M spectrum, below the band gap, there exist two weak bands at ~1.39 eV and ~1.92 eV, which are assigned to $3d^5$-intraconfigurational $^6A_1 \rightarrow {}^4T_1$ and $^6A_1 \rightarrow {}^4T_2$ crystal-field transition[235], respectively. Originally, these transition are spin and parity forbidden in centrosymmetric systems, the exchange mechanism between $Fe^{3+}$ pairs in concentrated systems and nonconcentrosymmetric crystal-field distortion around $Fe^{3+}$ such as those attained in $BiFeO_3$ and $Fe_2O_3$ both relax the spin and parity forbiddingness, enhancing the transition oscillator strengths[216]. The integrated band

transition energy for $^4T_2$ has been obtained by second derivative for K-M spectrum. Figure 7.26 (a) and (b) shows the temperature dependence of the K-M spectrum of 10% La and 10% Ca doping $BiFeO_3$ (100 nm) synthesizing at 600 °C. Two relevant features are observed: (1) the $^4T_2$ bands redshift with temperature, (2) $^6A_1 \rightarrow {}^4T_2$ the transition intensity associated with $^4T_2$ transition is notably changed with temperature.

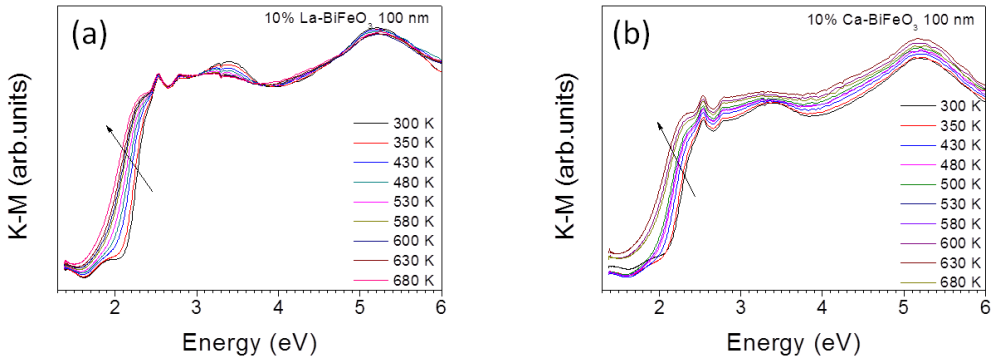


Figure 7.26 Kubelka-Munk spectra of (a) 10% La and (b) 10% Ca doped $BiFeO_3$ nanoparticles synthesized at 600 °C.

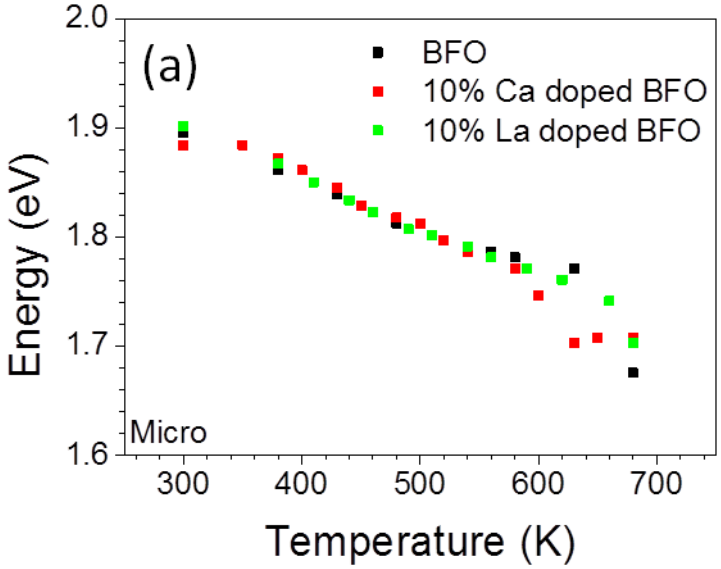

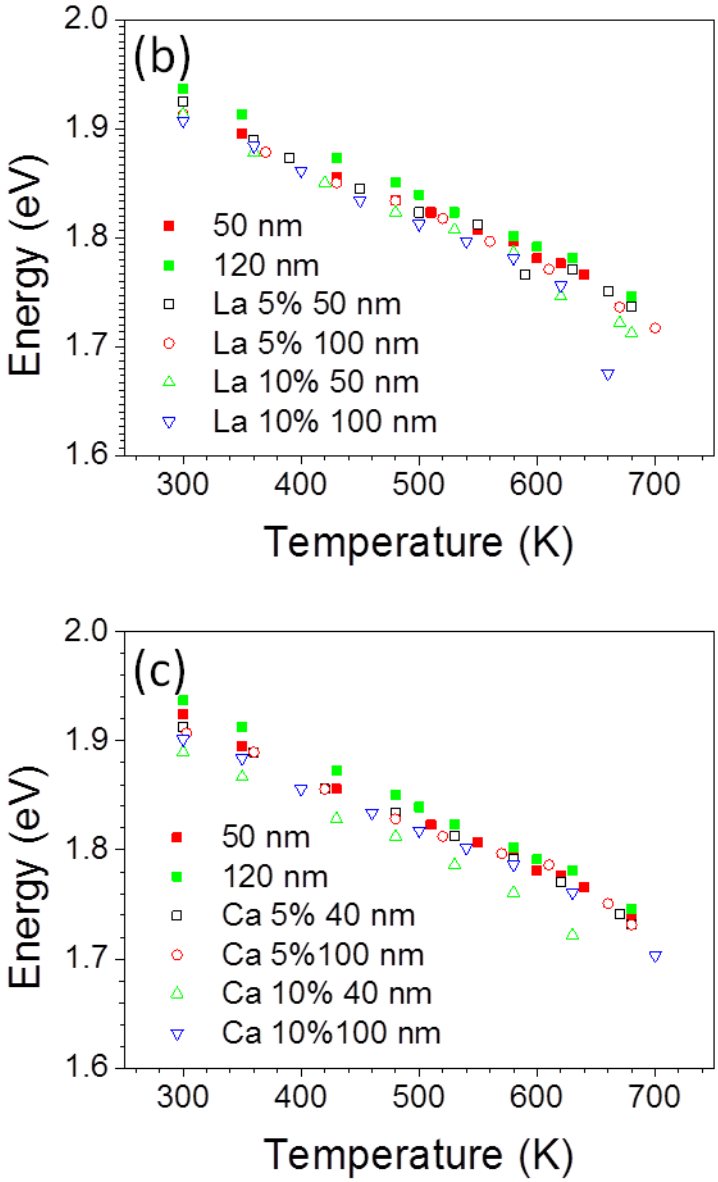


Figure 7.27 Low energy *d-d* transition as a function of temperature for La and Ca doped micro (a) and nano-$BiFeO_3$, corresponding size and doping as indicated.

Figure 7.27 shows the temperature dependence of the low energy *d-d* transition obtained from the study of the second derivative of the K-M functions for micro and nano La and Ca doping $BiFeO_3$. Figure 7.27 (a) shows the low energy *d-d* transition for doped and pure micro-$BiFeO_3$. It is clear that the band energy keeps the same variation trend for all micro-samples below 600 K, with an anomaly after 600 K. It has been shown that the Ca and La doping can induce a change of Néel temperature[78, 236], which caused by the variation of the crystal field environment of $Fe^{3+}$. Besides, the low energy *d-d* transition in $BiFeO_3$ is related to crystal field

distortion. From the above analysis, the Néel temperature transition can be seen by this low energy *d-d* transition as a function of temperature. Figure 7.27 (b) and (c) show the low energy *d-d* transition for different crystal size doped and pure nano-$BiFeO_3$. It can be seen that, whatever the crystal size for $BiFeO_3$, the band position of *d-d* transition keep the same energy. However, when doping with Ca or La in the A-site of $BiFeO_3$, the band energy of *d-d* transition is slightly lower than the pure samples for the whole temperature range. We have mentioned that this *d-d* transition is related to the crystal-field distortion caused by the loss of centrosymmetric arrangement. From the *d-d* transitions determined from the doped samples, we confirm that it is another clear evidence of the Ca and La doing effect on the octahedral crystal structure. Unfortunately, it is difficult to make conclusive remarks on how these size and doping effects affect the *d-d* transition.

### 7.3.2 Band gap as a function of temperature for A-site doped $BiFeO_3$ microparticles

In this part, the band gap of Ca and La doped $BiFeO_3$ have been studied as a function of temperature. Because of different valence of $Ca^{2+}$ and $La^{3+}$, the doping effect for forbidden band is different. Since the doping concentration in $BiFeO_3$ is set below 10%, from X-ray diffraction (chapter 6), it has been shown that the space group of different doping sample are still *R3c*. Thus, we can remove the effect to band gap from a structural phase transition up to a certain limit. The band gap values of differently doped samples are obtained from analysis of Kubelka-Munk functions combined with Tauc plots. Figure 7.28 shows the band gap values for 10% Ca and 10% La doped micro-samples as a function of temperature. It can be seen that at whole temperature range, the band gap of 10% Ca doped $BiFeO_3$ microparticles is unexpectedly higher than those of 10% La doped ones and of pure $BiFeO_3$ ones.

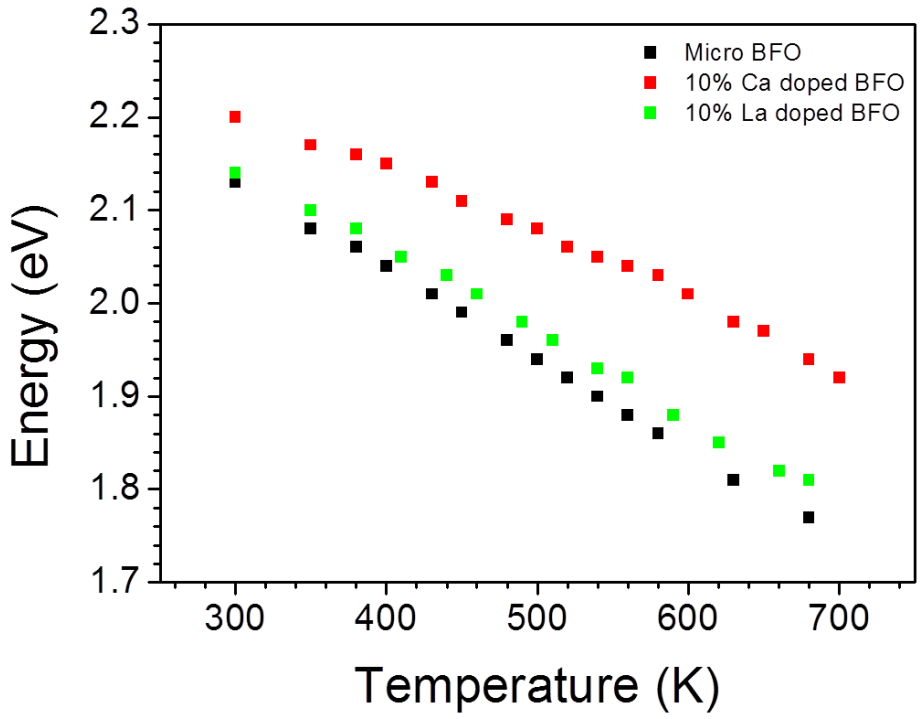


Figure 7.28 Band gap values of 10% La and 10% Ca doped $BiFeO_3$ microparticles as a function of temperature.

Firstly, we focus on the 10% Ca doping sample ($Bi_{0.9}Ca_{0.1}FeO_{3-\delta}$). In order to understand why Ca-doped sample has a higher band gap value having the same space group than the other compounds, the band structure and its Fermi level is analyzed. Because of the divalent cation $Ca^{2+}$ occupying the $Bi^{3+}$ site, holes could be produced. Moreover, oxygen vacancies can be created to maintain charge neutrality. Ionization of oxygen vacancies in Ca-doped $BiFeO_3$ yields electrons to compensate hole carriers introduced by Ca to maintain the 3+ valence state of iron ions. As donors, the oxygen vacancies are thermodynamically highly confined near the conduction band. As acceptors, the hole carriers caused by calcium doping are located at the top of valence band. The relative content of oxygen vacancies ($\delta_{VO}$) and hole carriers ($\delta_h$) can control the Fermi energy level position. When the concentration of oxygen vacancies is lower than the concentration of hole carries ($\delta_{VO}<\delta_h$), the Fermi level is thus located close to valence band even within the valence band; when $\delta_{VO}>\delta_h$, the Fermi level is located close to conduction band or within the conduction band; when $\delta_{VO}=\delta_h$, the Fermi energy is expected to be located in the middle of the forbidden band, as shown in Figure 7.20.

The Ca doping in the A site of $BiFeO_3$, compared to $BiFeO_3$ (chapter 7.2.3), more hole carriers can be produced, which means the Fermi level will be located preferentially in the valence band, deeper, at room temperature. With increasing the temperature, the Fermi level raises continually corresponding to the band gap decreasing, as expected. It explains why the Ca doped $BiFeO_3$ samples have a larger band gap within the whole temperature range. Another possible scenario is that the $Ca^{2+}$ has the different radius with $Bi^{3+}$, then in Ca doped $BiFeO_3$, Ca contracts the lattice and straighten the Fe-O-Fe bond angle. In chapter 7.2.3, we have analyzed the relationship between Fe-O-Fe angle and band gap values in $BiFeO_3$. In Ca doped case, from the result of band gap values as a function of temperature, it can be found that this result is opposed to the effect expected from a Fe-O-Fe angle variation. From the above analysis, the structural effects induced by Ca doping are not the dominant mechanism for the band gap variation, but the electronic (holes) ones.

Although La ion (1.16 Å) has almost the same ionic radius that Bi ion (1.17 Å) according to their tabulated Shannon radii, La doping in $BiFeO_3$ could make the crystal structure more symmetric, the $FeO_6$ octahedron can become progressively more uniform and decrease the local structural distortion, the loss of the Fe-O bond anisotropy (*e.g.*, the difference in the bond length between Fe-$O_1$ and Fe-$O_2$), reduced significantly upon the substitution of La on Bi at the A site of perovskites[76, 174]. The Fe-O-Fe angles become large and enhances the overlap between Fe 3*d* $e_g$ and $O^{2-}$ 2*p* orbitals. The structural consequences of La substitution resemble those of a small hydrostatic pressure. The effect of pressure on the band gap and the local $FeO_6$ environment in $BiFeO_3$ has reported in Ref. [224], in contrast to band gap, the $Fe^{3+}$ crystal field energy mainly depends on the $FeO_6$ local structure. This fact points out how the band gap, as a crystal bulk property, depends on the crystal structure and thus it is an appropriate probe for detecting phase transition. La doping can also reduce the leakage current, which is caused by a conducting mechanism at the bulk of the grains. This suggests that the change in the resistivity of the La doped $BiFeO_3$ does not stem from minor amounts of secondary phases at grain boundaries. Our XRD data also support the absence of any minority phase. The splitting of the $(104)/(202)_{hex}$ and the $(006)/(202)_{hex}$ reflections decreases, pointing to a less

distorted crystal structure with increasing the La content. According to this idea, the observed increase in the electrical resistivity (decrease of the optical band gap) can be attributed to a reduction in the concentration of minor hole carriers, which means that the amount of oxygen vacancies is depressed. In the schematic diagram of the electronic density of states, the oxygen vacancy impurity band is less populated. According to the aforementioned analysis, the band gap value of La doping $BiFeO_3$ depend on the relative degree of oxygen vacancies impurities and holes created by A-site vacancies. In our case, it can be seen that the band gap values, to a certain extent, are higher than for $BiFeO_3$. Thus, it can be deduced that, for the whole temperature range, the oxygen vacancies impurity band level is virtually shifted upwards, and hole carriers, if any, are less populated though less La vacancies are expected than their Bi counterparts. Thus, the band gap value of La doped $BiFeO_3$ is higher than pure $BiFeO_3$.

In conclusion, the band gap values of Ca and La doped $BiFeO_3$ are investigated as a function of temperature. The band gap values decrease in temperature for two differently doped and different size samples. From our analysis, for Ca doping, due to the acceptor impurity doping, compared to $BiFeO_3$, more holes are produced in Ca doped $BiFeO_3$ compounds. Meanwhile, oxygen vacancies also exist naturally. Because of the concentration of holes is larger than oxygen vacancies, compared to $BiFeO_3$, the Fermi level lies deeper in the valence band for Ca doped $BiFeO_3$ samples. Thus, the band gap value of Ca doped $BiFeO_3$ is higher than the band gap of $BiFeO_3$. For La doped $BiFeO_3$ samples, the band gap values depend mainly on the density of state changes related to the less populated oxygen vacancy impurity bands and the lower amount of holes existing in the La-doped $BiFeO_3$ samples, thus making the band gap of such samples larger than for the $BiFeO_3$ ones.

## 7.4 Conclusion

The photo-induced properties, and in particular the effective band gap and low energy *d-d* transition as a function of temperature, have been analyzed for different size and differently doped $BiFeO_3$. As a reference, micro $BiFeO_3$ samples have also been studied. The low energy *d-d* transition values of micro-$BiFeO_3$ decrease quicker

than the nano $BiFeO_3$ ones. The band gap variation of micro $BiFeO_3$ is analyzed at high temperature, and we give the result that the band gap variation is caused by Fermi energy level position change as a function of the nature and population of the oxygen and bismuth vacancy levels. Finally, transitions of La and Ca doped $BiFeO_3$ compounds are studied as a function of temperature. We notice that the whereas the band gap is larger for doped $BiFeO_3$ than for pure ones, being explained by the fact that the Fermi level depends on the defect states created by this different substitution.

# 8 Photocatalysis using $BiFeO_3$ nanoparticles on Rhodamine B dye

Among useful ferroelectrics for photo-induced applications, $BiFeO_3$ is the most promising candidate because of its relatively small band gap ($E_g$ ~ 2.6-2.8 eV) in comparison to other classical ferroelectric oxides like $BaTiO_3$, $PbZrTiO_3$ or $LiNbO_3$ ($E_g$ > 3 eV) allowing to benefit from a wider part of the sunlight spectrum and its larger polarization value (P ~ 100 $\mu C/cm^2$)[33], ensuring a more efficient separation of the photogenerated charge carriers. While intensively studied as thin film form for its ferroelectric, magnetic and magnetoelectric properties as well as most recently for its photovoltaicity, there is an increasing interest for photocatalytic and photolysis processes under visible light illumination using this material, that might become an alternative to the widely investigated photocatalytic material $TiO_2$ which suffers from its large band gap allowing to use only ~ 4 % of the solar spectrum.

However, to make $BiFeO_3$ a good photocatalyst requires to enhance the surface area and reactivity by simultaneously keeping or even increasing its absorption capability in order to guarantee an efficient charge transfer to surrounding foreign molecules and participate in oxidation-reduction processes leading to molecule decomposition[53]. It has been demonstrated that using different $BiFeO_3$ particles, from nanosized to core shells structures, can indeed be beneficial for enhancing the photocatalytic activity[93, 237]. The nanosize shaping produces a lowering of the band gap which might cause a larger absorption of the sunlight. Moreover, the particle morphology is also a contributing parameter as it has been shown on micron-sized $BiFeO_3$ particles because of the more efficient photoabsorption of cubic like facets[238]. Core-shell nanostructures based on $BiFeO_3$ coated with $TiO_2$ have been also used to enhance surface reactivity[93]. However, despite growing research in this field, the coupling between nanosize, shaping, optical and photocatalytic responses in $BiFeO_3$ has been not demonstrated yet. Here, by investigating at room temperature $BiFeO_3$ nanopowders with sizes ranging from 30 to 190 nm.

The time dependent photo-degradation of the Rhodamine B (RhB) dye under visible light irradiation while in solution with $BiFeO_3$ nanoparticles of different size has been

shown in Figure 8.1(a). It can be seen that the typical intensity variation of the absorbance peak of RhB under visible-light irradiation that decreases with increasing the time indicating that RhB has been decomposed by $BiFeO_3$ with reaction time. In order to evaluate the degradation efficiency of RhB, the maximum intensity ratio $C/C_0$ is plotted in Figure 8.1 (b). Compared with the blank test for equivalent time dependences obtained from the light induced degradation of pure RhB in aqueous solution, it can be seen that the RhB degradation becomes efficiently accelerated by up to 50 % by using $BiFeO_3$ particles. However, unexpectedly, the degradation is found to be less efficient once the particle size is reduced. This is clearly seen in Table 8.1 through the continuous decrease of $(C_0\text{-}C)/C_0$ ratio, *i.e.* the degradation efficiency, with particle size decreasing.

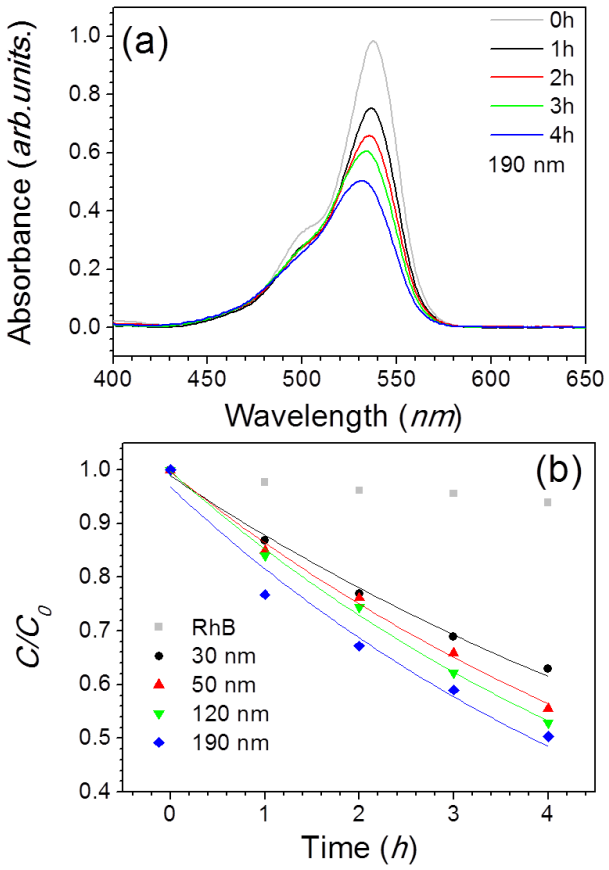


Figure 8.1 (a) Absorption spectra of RhB under visible-light irradiation in solution with ~ 190 nm $BiFeO_3$ nanopowders. (b) Photodegradation of RhB as a function of the illuminated time when in solution with BFO nanopowders of different particle sizes. The curves are fitting results using the first order kinetic equation $C/C_0 = \exp(-kt)$

The degradation efficiency is strongly lowered by over 30 % from the 190 nm sample to the 30 nm one. A first order kinetic reaction law i.e. $C/C_0 = \exp(-kt)$ where $k$ is the kinetic rate and $t$ the time, is used to fit the data in Figure. 8.1(b). Table 8.1 reports the constant $k$ obtained for the different particle size. It appears that the faster reaction occurs for the bigger particles although a lower surface area is exposed to the RhB dye. Reducing the particle size is generally beneficial for photocatalysis, as it leads to quadratic growth of the specific surface area and thus enhances the surface reaction. However, it is not always the case that the smaller the particle size, the higher the efficiency. Nevertheless, here, in contrast to previous reports[238], the shape of the particle is similar, which has been shown in Figure 8.2, and the lowering of the degradation efficiency cannot be accounted to a better light absorption from some specific facets with higher surface energy.

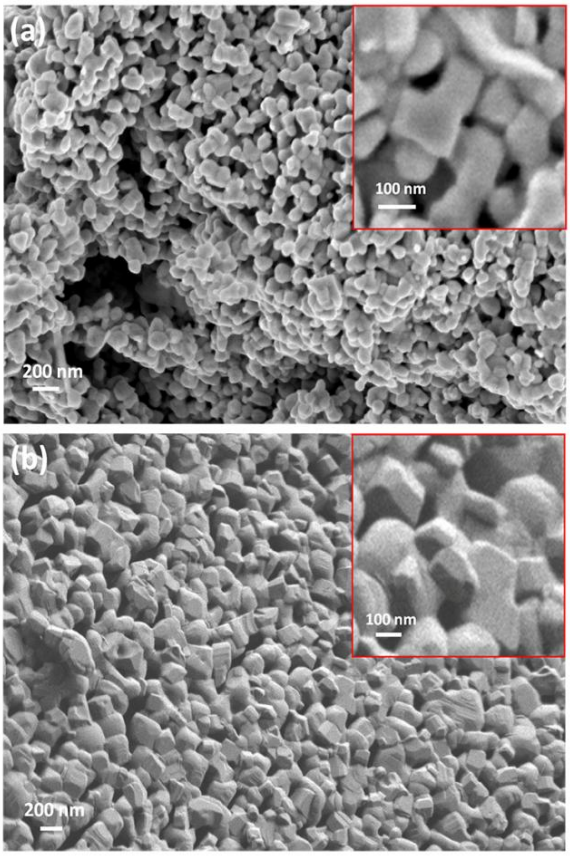


Figure 8.2 FE-SEM images of $BiFeO_3$ powders with average nanoparticles of (a) 50 nm (b) 190 nm. The corresponding inset figures are selected focused areas depicting that similar surface morphology is observed for different particle sizes.

Table 8.1 Sample name of $BiFeO_3$ nanoparticles and their corresponding synthesis temperature, particle size, crystalline size, lattice parameters, $c_c/a_c$ ratio, cubic-like distortion, and local inhomogeneous distortion

| Sample name | Synthesis Temperature (°C) | Mean Particle Size (SEM) (nm) | Crystalline Size (XRD) (nm) | $a_c$ (Å) | $c_c$ (Å) | $c_c/a_c$ | Local inhomogeneous distortion $(c_c-a_c)/c_c$ | Inhomogeneous strain $\varepsilon$ |
|---|---|---|---|---|---|---|---|---|
| 30 nm | 450 | 32±7 | 28+/-5 | 3.9452(5) | 4.0040(1) | 1.0148(9) | 14.6(8)% | $(24.7\pm4.8)\cdot10^{-4}$ |
| 50 nm | 500 | 48±8 | 39+/-5 | 3.9443(5) | 4.0030(4) | 1.0149(7) | 14.7(5)% | $(14.6\pm2.5)\cdot10^{-4}$ |
| 120 nm | 550 | 120±22 | 46+/-6 | 3.9450(4) | 4.0042(7) | 1.0150(1) | 14.7(9)% | $(8.4\pm3.0)\cdot10^{-4}$ |
| 190 nm | 600 | 189±38 | 61+/-2 | 3.9443(6) | 4.0034(3) | 1.0149(8) | 14.7(6)% | $(8.2\pm2.8)\cdot10^{-4}$ |

Besides, the polarization, which is expected to only vary slightly, if any, with the change of the nanocrystallite size, cannot be considered as a parameter that could here affect the charge carrier separation. In contrast, some defects and their corresponding local strains revealed by the broadening of the Bragg peaks do exist and their amount and/or strength increases by decreasing the particle size. These defects, if localized at the surface, may indeed favor the recombination of electron-hole charge carriers reducing the reaction activity between $BiFeO_3$ and the RhB molecules. Moreover, the defects localized in the inner part of the particle can trap the charge carriers created within the particle, limiting their mean free path and thus their migration towards the surface. In addition, the local distortions surrounding associated to these defects can also affect the electronic structure, which has been presented in chapter 7.2.1, by shifting or lifting the degeneracy of existing energy levels or by creating new extra ones that can be localized within the band gap. Additionally, from Figure 8.3, although the total absorption is similar for different size samples, a great number of defects in smaller size sample could lead to greater scattering of carriers and this deduces the light efficiency, which will lead to a change on the light absorption properties of $BiFeO_3$ particles. Thus, defects will lead to a change on the light absorption properties of $BiFeO_3$ particles. It is worth mentioning that their nature cannot be straightforwardly determined and further efforts are required to answer to this question. Here, we note that the more plausible origin of these defects are the oxygen vacancies[195], as they are usually expected in oxides as point defects, although others may also account like the so-called skin-layer[188, 239].

This skin-layer having its own phase transitions is believed to be the site of trapping centers for charge carriers and interestingly it is associated to strong local distortions. Increasing the surface/volume ratio by decreasing the particle size might make the skin-layer to have a role on (1) the average increase of the local distortions, becoming more relevant in smaller particles (Table 8.1), and (2) the development of more local defects, *i.e.* more efficient trapping centers for the photogenerated charge carriers, as observed from the decrease of the degradation efficiency and the rate constant in such particles (Table 8.2).

Table 8.2 Sample name and corresponding values of photodegradation efficiency ($C_0$-$C$)/$C_0$, (deduced after 4 h of irradiation), kinetics rate $k$, effective band gap $E_{g,eff}$, Urbach energy $E_U$, and absorption area below 2.95 eV.

| **Sample** | **Photodegradation $(C_0-C)/C_0$ (%)** | **Rate constant $k$ ($h^{-1}$)** | **Absorption onset energy $E_{abs}$ (eV)** | **Urbach Energy $E_U$ (eV)** | **Absorption area** |
|---|---|---|---|---|---|
| 30 nm | 33% | 0.12 | 2.18(1) | 0.19(1) | 2.40(1) |
| 50 nm | 41% | 0.14 | 2.21(1) | 0.16(1) | 2.47(1) |
| 120 nm | 44% | 0.16 | 2.22(1) | 0.11(1) | 2.58(1) |
| 190 nm | 46% | 0.17 | 2.24(1) | 0.11(1) | 2.94(1) |

In order to get further insights into the possible mechanisms involved in the decrease of the photocatalytic activity with particle size reduction, we studied the modifications of the optical properties related to particle size changes in $BiFeO_3$. The absorption spectra of $BiFeO_3$ nanoparticles are analyzed through the corresponding Kubelka-Munk function $F(R)$, which is proportion to the absorption. The different $F(R)$ curves are presented in Figure 8.3 as a function of the photon energy. Different low energy onsets can be seen in the inset of Figure 8.3.

Because of the spin-charge-lattice couplings, $BiFeO_3$ absorption spectrum reveals a complex and puzzling electronic structure[75, 101, 230], which has been analyzed in chapter 7. Actually, according to the complex charge transition, the determination of the band gap is not straightforward. Typically, the band gap is determined using Tauc plots according to the relation $(F(R)h\nu)^n=A(h\nu-E_g)$ (chapter 7). Using the direct band gap approach with our set of data provides an effective band gap of $E_{g,eff}$ ~2.2 eV, in agreement with previous reports but lower than the usual $E_g$ values obtained from

single crystals or thin films[220]. Even though this effective band gap is lower than that seen in crystalline materials, it is relatively close to the absorption onset noted there. Our results show a very weak decrease, if any, with the particle size reduction from 190 nm to 30 nm, as summarized in Table 8.2.

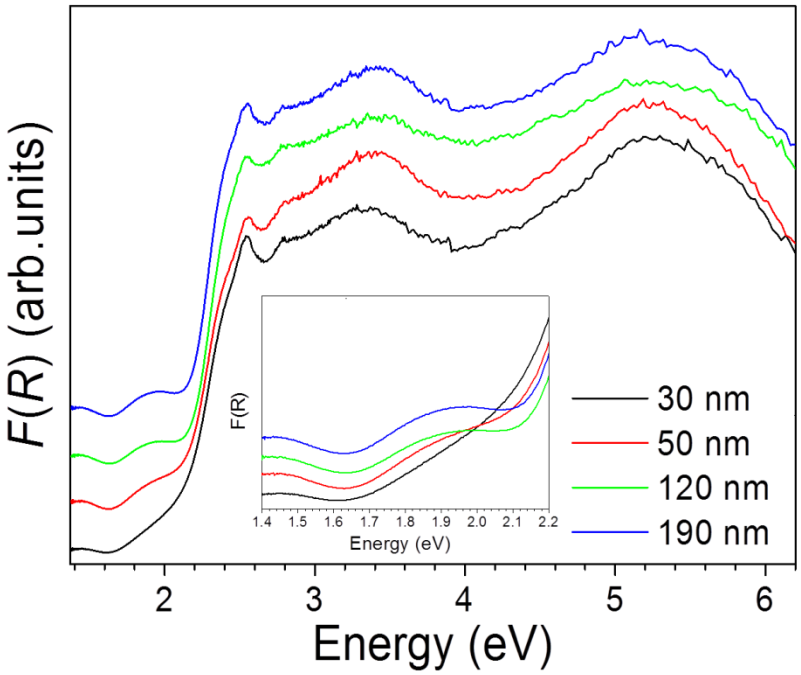


Figure 8.3 Room temperature UV-Vis absorption spectra of different size $BiFeO_3$ samples derived from the diffuse reflectance (*R*) spectra using Kubelka-Munk functions *F(R)*. The inset shows the low energy crystal-field transition bands for samples with different average particle sizes.

From the different Kubelka-Munk curves, we can determine the Urbach energy $E_U$ related to the variation of the energy levels close to the conduction and/or valence bands, being affected by different sources of disorder. Using Urbach analysis through $\ln F(R)=h\nu/E_U$ relationship, the Urbach energy is found to vary from 0.11 eV to 0.2 eV from 190 nm to 30 nm, respectively (Table 8.2). These latter $E_U$ values are in very good agreement with x-ray photoelectron spectroscopy measurements[218] on $BiFeO_3$ revealing the presence of defect trapped states at 0.2 eV below the conduction band that have been attributed to defects at the particle boundaries.

Below ~ 2.2 eV, the low energy transitions located at ~1.4 eV and ~1.9 eV (Figure 8.3) are magnetically sensitive. Strikingly and in contrast to the other absorption bands, these low-energy crystal-field bands are obviously affected by the decrease of the particle size; the positions are red-shifted and the intensity is also decreased (within the detection limits), as shown in the inset of Figure 8.3. More interestingly, by using an oscillator strength analysis involving electron-phonon coupling[216], it has been also shown that their temperature dependent behavior changes at 150 K, which remarkably corresponds to the temperature value of one of the transitions reported for the skin-layer of $BiFeO_3$[188]. We note that the magnetic changes have been previously attributed to the skin-layer at this peculiar temperature[188]. Moreover, as such a skin-layer is also known to be the site of trapped states for charge carriers, we propose here that the defect states evidenced from our Urbach analysis could be mainly located in the skin-layer. Therefore, both the Urbach energy and low-energy bands changes when the particle size is varied could suggest that the skin-layer and the defects trapped in it plays a major role in modifying the optical response of BFO particles. However, we should consider other mechanisms accounting for these different surface effects. As a matter of fact, the variation of the polarization state near the surface or through the nanoparticles, related to the ferroelectric domain configuration, will lead to a polarization gradient. Secondly, these nanoparticles should present Stern layers developed in the solution during the photocatalytic experiments that should influence the path and recombination of carriers within the solution. Additionally, nanoparticle aggregation could change the surface area contacting with the light, which also can affect the photocatalytic properties. From SEM images of different size nanoparticles (chapter 5.3.1), it can be observed that the different aggregation degree for different particle size $BiFeO_3$. To unveil the contribution of these effects, further investigations are in process.

Figure 8.4 shows the absorption area above 420 nm (*i.e*. energies below 2.95 eV) determined using $F(R)$ and corresponding to the total optical energy absorbed by $BiFeO_3$ particles in our photocatalysis experiment in comparison to the degradation efficiency. It appears that the absorption by $BiFeO_3$ particles decreases with the reduction of the particle size. Therefore, the decrease of degradation efficiency of

RhB molecules with particle size reduction can be simply explained by the decrease of $BiFeO_3$ capability to absorb the light once the particle size is reduced.

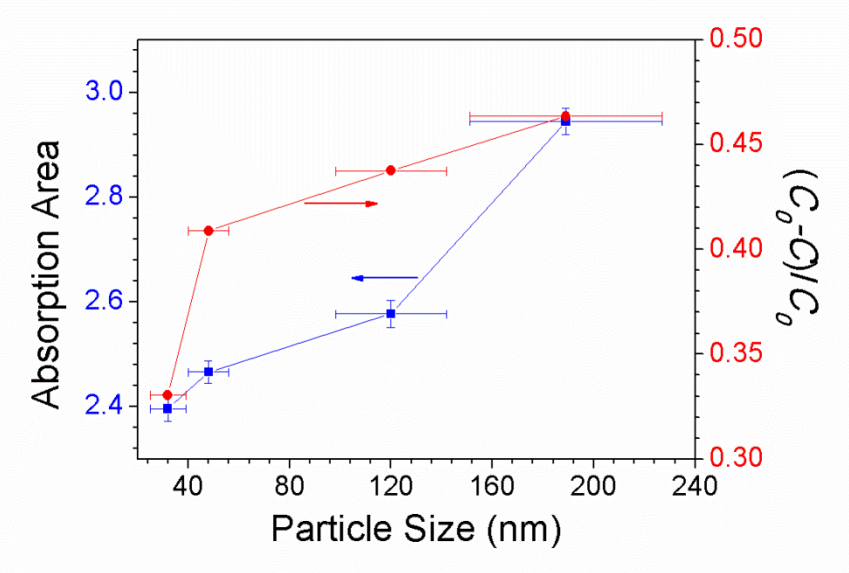


Figure 8.4 The absorption area extracted from $F(R)$ above 420 nm (*i.e.* below 2.95 eV) and photodegradation efficiency $(C_0\text{-}C)/C_0$ as a function of the different average particle size.

Therefore, both the Urbach energy and low-energy bands changes when the particle size is varied could suggest that the skin-layer and the defects trapped in it plays a major role in modifying the optical response of $BiFeO_3$ particles. Such skin-layer which is the site of defects and local distortions can indeed affect the optical absorption of $BiFeO_3$ by shifting and/or splitting energy levels because of local symmetry reduction and inserting extra in-gap levels that can trap the charge carriers. By decreasing the particle size, the average shape, polarization, distortion and band gap are only weakly altered, if any, while the skin-layer is believed to vary substantially (Urbach energy and low-energy bands) leading to the observed decrease of degradation capabilities of $BiFeO_3$ nanoparticles.

In conclusion, a detailed optical and photocatalytic investigation on different particle sized $BiFeO_3$ particles is conducted. While the particle size is reduced and thus the surface reaction is increased, the photocatalytic activity of $BiFeO_3$ is found to decrease in the investigated particle size range. Such unexpected behavior is explained by changes occurring in the optical response of $BiFeO_3$ due to the existence of a skin-layer which is the site of trapped defects and local distortions.

Decreasing the particle size affects the skin-layer response while the global properties (polarization, strain, band gap) are only weakly affected. The skin-layer being an inherent property of many other compounds should be then taken into account for further investigation and use in future photocatalysis applications of other functional oxides with the $ABO_3$ perovskite structure like $BiFeO_3$.

# 9 Summary

Multiferroic materials combine two or more of the ferroic properties which affect reciprocally. These materials are prime candidates for future computer memory concepts, as well as for sensors and spintronic devices. Recently, coupling to other degree of freedom, such as light, is now under intense scrutiny, in the quest for multifunctional materials. The perovskite bismuth ferrite ($BiFeO_3$) is the most studied mutiferroic material. $BiFeO_3$ is ferroelectric below 830 °C and antierromagnetic below 370 °C. Epitaxial thin films of $BiFeO_3$ have attract tremendous interest from the scientific community, but a thorough understanding of photo-induced properties and electron and charge transition at different energy and different temperature has received comparative less attention.

The aim of this work has been to prepare phase pure bulk and nanocrystalline $BiFeO_3$ and to investigate the electron/charge optically proved transitions as a function of temperature. Moreover, different size La/Ca doped $BiFeO_3$ samples have also been studied for in the same manner.

Simple aqueous synthesis routes to obtain phase pure nanocrystalline $BiFeO_3$ were developed using nitrate solution as metal precursors. The tartaric acid and ethylene glycol were found to complex both Bi and Fe cations. Preparation of pure phase bulk $BiFeO_3$ by solid state reaction synthesis from $Bi_2O_3$ and $Fe_2O_3$ has been also obtained. The XRD and Raman spectroscopy techniques have been used for analyzing the sample quality and structure variation as a function of temperature. From the Raman spectra, we determine that the Fe-O-Fe angle depends on the size and in temperature it presents different anomalies related to the surface effects of different size $BiFeO_3$. From XRD pattern, small changes of the lattice have been observed at the Néel temperature, which is an evidence of the spin-lattice coupling even observed in nanoparticles. EELS and XPS techniques have been used to study the volume and surface chemistry, respectively. Different ratios of $Fe^{2+}/Fe^{3+}$ in the surface of different size $BiFeO_3$ have been detected, whereas the core of the nanoparticles is constituted by $Fe^{3+}$ ions, thus indicating that different surface

properties can be expected for different size $BiFeO_3$ while keeping similar core properties. STEM technique has been used. From STEM images, ferroelectric domains in $BiFeO_3$ nanoparticles have been observed. From the EELS results of La doped $BiFeO_3$ and pure $BiFeO_3$ nanoparticle, it can be seen that the distribution of La ion is almost uniform in doped samples and $Fe^{3+}$ state remains unchanged.

The optical properties, especially, the effective band gap and low energy *d-d* transition as a function of temperature have been analyzed for different size $BiFeO_3$. As a comparison, micro $BiFeO_3$ has also been studied, which exhibits different band structure transition with temperature increasing. The low energy *d-d* transition of micro $BiFeO_3$ is reducing quicker than nano $BiFeO_3$, and one sketch is used to explain this difference variation. The band gap variation of micro $BiFeO_3$ is analyzed at high temperature, the result being that the band gap variation is caused by a shift of the Fermi energy level depending on the concentration of oxygen vacancies and holes in these materials. Moreover, electronic and charge transitions of La/Ca doped $BiFeO_3$ have been studied as a function of temperature. The band gap difference is explained by the existence of different defects that can be controlled by the doping in the materials.

Finally, a detailed optical and photocatalytic investigation on different particle sized $BiFeO_3$ particles is conducted. While the particle size is reduced and thus the surface reaction area is increased, the photocatalytic activity of $BiFeO_3$ is found to decrease in the investigated particle size range. Such unexpected behavior is explained by changes occurring in the optical response of $BiFeO_3$ due to the existence of a skin-layer which is the site of trapped defects and local distortions. Decreasing the particle size affects the skin-layer response while the global properties (polarization, strain, band gap) are only weakly affected. The skin-layer being an inherent property of many other compounds should be then taken into account for further investigation and use in future photocatalysis applications of other functional oxides with the $ABO_3$ perovskite structure like $BiFeO_3$.

## References


1. Eerenstein, W.; Mathur, N.; Scott, J. F., Multiferroic and Magnetoelectric Materials. *nature* **2006**, *442*, 759-765.
2. Scott, J., Applications of Modern Ferroelectrics. *science* **2007**, *315*, 954-959.
3. Velev, J.; Jaswal, S.; Tsymbal, E., Multi-Ferroic and Magnetoelectric Materials and Interfaces. *Philosophical Transactions of the Royal Society A: Mathematical, Physical and Engineering Sciences* **2011**, *369*, 3069-3097.
4. Lines, M. E.; Glass, A. M., *Principles and Applications of Ferroelectrics and Related Materials*; Clarendon press Oxford, 2001.
5. Khomskii, D., Classifying Multiferroics: Mechanisms and Effects. *Physics* **2009**, *2*, 1-8.
6. Li, C.; Soh, K. C. K.; Wu, P., Formability of $ABO_3$ Perovskites. *Journal of Alloys and Compounds* **2004**, *372*, 40-48.
7. Wu, P.; Li, C., Stability and Formability of Complex Oxides in $M_2O_3$-$M'_2O_3$ Systems. *Calphad* **2003**, *27*, 201-211.
8. Goldschmidt, V. M., Die Gesetze Der Krystallochemie. *Naturwissenschaften* **1926**, *14*, 477-485.
9. Yokokawa, H.; Kawada, T.; Dokiya, M., Thermodynamic Regularities in Perovskite and K2nif4 Compounds. *Journal of the American Ceramic Society* **1989**, *72*, 152-153.
10. Cohen, R. E., Origin of Ferroelectricity in Perovskite Oxides. **1992**.
11. Glazer, A., The Classification of Tilted Octahedra in Perovskites. *Acta Crystallographica Section B* **1972**, *28*, 3384-3392.
12. Zhou, J.-S.; Goodenough, J., Intrinsic Structural Distortion in Orthorhombic Perovskite Oxides. *Physical Review B* **2008**, *77*, 132104.
13. Goodenough, J. B., Electronic and Ionic Transport Properties and Other Physical Aspects of Perovskites. *Reports on Progress in Physics* **2004**, *67*, 1915.
14. Kubel, F.; Schmid, H., Structure of a Ferroelectric and Ferroelastic Monodomain Crystal of the Perovskite $BiFeO_3$. *Acta Crystallographica Section B* **1990**, *46*, 698-702.
15. Bokov, A.; Ye, Z.-G., Recent Progress in Relaxor Ferroelectrics with Perovskite Structure. In *Frontiers of Ferroelectricity*, Springer: 2007; 31-52.
16. Petkov, V.; Selbach, S. M.; Einarsrud, M. A.; Grande, T.; Shastri, S. D., Melting of Bi Sublattice in Nanosized $BiFeO_3$ Perovskite by Resonant X-Ray Diffraction. *Phys. Rev. Lett.* **2010**, *105*, 185501.
17. Long, Y.; Shimakawa, Y., Intermetallic Charge Transfer between A-Site Cu and B-Site Fe in a-Site-Ordered Double Perovskites. *New Journal of Physics* **2010**, *12*, 063029.
18. Charge Disproportionation and Charge Transfer in A-Site Ordered Perovskites Containing Iron. *Zeitschrift für anorganische und allgemeine Chemie* **2009**, *635*, 1882.
19. Burns, G.; Scott, B. A., Lattice Modes in Ferroelectric Perovskites: $PbTiO_3$. *Physical Review B* **1973**, *7*, 3088.
20. Picozzi, S.; Yamauchi, K.; Sergienko, I. A.; Sen, C.; Sanyal, B.; Dagotto, E., Microscopic Mechanisms for Improper Ferroelectricity in Multiferroic Perovskites: A Theoretical Review. *Journal of Physics-Condensed Matter* **2008**, *20*.
21. Hill, N. A.; Rabe, K. M., First-Principles Investigation of Ferromagnetism and Ferroelectricity in Bismuth Manganite. *Physical Review B* **1999**, *59*, 8759-8769.
22. Cohen, R. E., Theory of Ferroelectrics: A Vision for the Next Decade and Beyond. *Journal of Physics and Chemistry of Solids* **2000**, *61*, 139-146.
23. Jonker, G. H.; Van Santen, J. H., Ferromagnetic Compounds of Manganese with Perovskite Structure. *Physica* **1950**, *16*, 337-349.
24. Khaliullin, G.; Kilian, R., Theory of Anomalous Magnon Softening in Ferromagnetic Manganites. *Physical Review B* **2000**, *61*, 3494-3501.

25. Comstock, R., Review Modern Magnetic Materials in Data Storage. *Journal of Materials Science: Materials in Electronics* **2002**, *13*, 509-523.
26. Pimenov, A.; Mukhin, A.; Ivanov, V. Y.; Travkin, V.; Balbashov, A.; Loidl, A., Possible Evidence for Electromagnons in Multiferroic Manganites. *Nature Physics* **2006**, *2*, 97-100.
27. Spaldin, N. A., *Magnetic Materials: Fundamentals and Applications*; Cambridge University Press, 2010.
28. O'handley, R. C., *Modern Magnetic Materials: Principles and Applications*; Wiley New York, 2000; Vol. 830622677.
29. Treves, D.; Eibschütz, M.; Coppens, P., Dependence of Superexchange Interaction on $Fe^{3+}$-$O^{2-}$-$Fe^{3+}$ Linkage Angle. *Physics Letters* **1965**, *18*, 216-217.
30. Moriya, T., Anisotropic Superexchange Interaction and Weak Ferromagnetism. *Physical Review* **1960**, *120*, 91-98.
31. Cullity, B. D.; Graham, C. D., *Introduction to Magnetic Materials*; John Wiley & Sons, 2011.
32. Dionne, G. F., *Magnetic Oxides*; Springer, 2009.
33. Catalan, G.; Scott, J. F., Physics and Applications of Bismuth Ferrite. *Advanced Materials* **2009**, *21*, 2463-2485.
34. Castillo, M. E.; Shvartsman, V. V.; Gobeljic, D.; Gao, Y.; Landers, J.; Wende, H.; Lupascu, D. C., Effect of Particle Size on Ferroelectric and Magnetic Properties of $BiFeO_3$ Nanopowders. *Nanotechnology* **2013**, *24*, 10.
35. Huang, F., et al., Peculiar Magnetism of BiFeO3 Nanoparticles with Size Approaching the Period of the Spiral Spin Structure. *Sci. Rep.* **2013**, *3*.
36. Landers, J.; Salamon, S.; Castillo, M. E.; Lupascu, D. C.; Wende, H., Mossbauer Study of Temperature-Dependent Cycloidal Ordering in $BiFeO_3$ Nanoparticles. *Nano Lett.* **2014**, *14*, 6061-6065.
37. Jaiswal, A.; Das, R.; Vivekanand, K.; Mary Abraham, P.; Adyanthaya, S.; Poddar, P., Effect of Reduced Particle Size on the Magnetic Properties of Chemically Synthesized $BiFeO_3$ Nanocrystals. *The Journal of Physical Chemistry C* **2010**, *114*, 2108-2115.
38. Gavriliuk, A. G. e.; Struzhkin, V.; Lyubutin, I. S. e.; Troyan, I., Equation of State and Structural Transition at High Hydrostatic Pressures in the $BiFeO_3$ Crystal. *JETP Letters* **2007**, *86*, 197-201.
39. Lyubutin, I. S. e.; Gavriliuk, A. G. e.; Struzhkin, V., High-Spin-Low-Spin Transition and the Sequence of the Phase Transformations in the $BiFeO_3$ Crystal at High Pressures. *JETP letters* **2008**, *88*, 524-530.
40. Carlson, D. E.; Wronski, C., Amorphous Silicon Solar Cell. *Appl. Phys. Lett.* **1976**, *28*, 671-673.
41. Grinberg, I.; West, D. V.; Torres, M.; Gou, G.; Stein, D. M.; Wu, L.; Chen, G.; Gallo, E. M.; Akbashev, A. R.; Davies, P. K., Perovskite Oxides for Visible-Light-Absorbing Ferroelectric and Photovoltaic Materials. *Nature* **2013**, *503*, 509-512.
42. Sah, C.-T.; Noyce, R.; Shockley, W., Carrier Generation and Recombination in Pn Junctions and Pn Junction Characteristics. *Proceedings of the IRE* **1957**, *45*, 1228-1243.
43. Kreisel, J.; Alexe, M.; Thomas, P. A., A Photoferroelectric Material Is More Than the Sum of Its Parts. *Nature materials* **2012**, *11*, 260-260.
44. Bennett, J. W.; Grinberg, I.; Rappe, A. M., New Highly Polar Semiconductor Ferroelectrics through *d* 8 Cation-O Vacancy Substitution into $PbTiO_3$: A Theoretical Study. *Journal of the American Chemical Society* **2008**, *130*, 17409-17412.
45. Young, S. M.; Zheng, F.; Rappe, A. M., First-Principles Calculation of the Bulk Photovoltaic Effect in Bismuth Ferrite. *Phys. Rev. Lett.* **2012**, *109*, 236601.
46. Bhatnagar, A.; Roy Chaudhuri, A.; Heon Kim, Y.; Hesse, D.; Alexe, M., Role of Domain Walls in the Abnormal Photovoltaic Effect in Bifeo3. *Nat Commun* **2013**, *4*.
47. Fridkin, V. M., *Photoferroelectrics*; Springer, 1979.

48. Schneider, J.; Matsuoka, M.; Takeuchi, M.; Zhang, J.; Horiuchi, Y.; Anpo, M.; Bahnemann, D. W., Understanding Tio2 Photocatalysis: Mechanisms and Materials. *Chemical reviews* **2014**, *114*, 9919-9986.
49. Hung, C.-M.; Tu, C.-S.; Yen, W. D.; Jou, L. S.; Jiang, M.-D.; Schmidt, V. H., Photovoltaic Phenomena in $BiFeO_3$ Multiferroic Ceramics. *J. Appl. Phys.* **2012**, *111*, 07D912.
50. Poosanaas, P.; Tonooka, K.; Uchino, K., Photostrictive Actuators. *Mechatronics* **2000**, *10*, 467-487.
51. Yang, S.; Seidel, J.; Byrnes, S.; Shafer, P.; Yang, C.-H.; Rossell, M.; Yu, P.; Chu, Y.-H.; Scott, J.; Ager, J., Above-Bandgap Voltages from Ferroelectric Photovoltaic Devices. *Nature nanotechnology* **2010**, *5*, 143-147.
52. Seidel, J.; Fu, D.; Yang, S.-Y.; Alarcón-Lladó, E.; Wu, J.; Ramesh, R.; Ager, J. W., Efficient Photovoltaic Current Generation at Ferroelectric Domain Walls. *Phys. Rev. Lett.* **2011**, *107*, 126805.
53. Tong, H.; Ouyang, S.; Bi, Y.; Umezawa, N.; Oshikiri, M.; Ye, J., Nano-Photocatalytic Materials: Possibilities and Challenges. *Advanced Materials* **2012**, *24*, 229-251.
54. Ferromagnetic and Photocatalytic Behaviors Observed in Ca-Doped $BiFeO_3$ Nanofibres. *J. Appl. Phys.* **2013**, *113*, 146101.
55. Ravindran, P.; Vidya, R.; Kjekshus, A.; Fjellvåg, H.; Eriksson, O., Theoretical Investigation of Magnetoelectric Behavior in $BiFeO_3$ *Physical Review B* **2006**, *74*, 224412.
56. Haumont, R.; Bouvier, P.; Pashkin, A.; Rabia, K.; Frank, S.; Dkhil, B.; Crichton, W.; Kuntscher, C.; Kreisel, J., Effect of High Pressure on Multiferroic $BiFeO_3$. *Physical Review B* **2009**, *79*, 184110.
57. Muneeswaran, M.; Jegatheesan, P.; Gopiraman, M.; Kim, I.-S.; Giridharan, N., Structural, Optical, and Multiferroic Properties of Single Phased $BiFeO_3$. *Applied Physics A* **2014**, *114*, 853-859.
58. Zeches, R.; Rossell, M.; Zhang, J.; Hatt, A.; He, Q.; Yang, C.-H.; Kumar, A.; Wang, C.; Melville, A.; Adamo, C., A Strain-Driven Morphotropic Phase Boundary in $BiFeO_3$. *science* **2009**, *326*, 977-980.
59. Kundys, B.; Viret, M.; Colson, D.; Kundys, D., Light-Induced Size Changes in BiFeO3 Crystals. *Nature materials* **2010**, *9*, 803-805.
60. Michel, C.; Moreau, J.-M.; Achenbach, G. D.; Gerson, R.; James, W. J., The Atomic Structure of $BiFeO_3$. *Solid State Communications* **1969**, *7*, 701-704.
61. Kubel, F.; Schmid, H., Structure of a Ferroelectric and Ferroelastic Monodomain Crystal of the Perovskite $BiFeO_3$. *Acta Crystallographica Section B: Structural Science* **1990**, *46*, 698-702.
62. Moreau, J.-M.; Michel, C.; Gerson, R.; James, W. J., Ferroelectric $BiFeO_3$ X-Ray and Neutron Diffraction Study. *Journal of Physics and Chemistry of Solids* **1971**, *32*, 1315-1320.
63. Thomas, N. W.; Beitollahi, A., Inter-Relationship of Octahedral Geometry, Polyhedral Volume Ratio and Ferroelectric Properties in Rhombohedral Perovskites. *Acta Crystallographica Section B: Structural Science* **1994**, *50*, 549-560.
64. Bucci, J.; Robertson, B.; James, W., The Precision Determination of the Lattice Parameters and the Coefficients of Thermal Expansion of $BiFeO_3$. *J. Appl. Crystallogr.* **1972**, *5*, 187-191.
65. Ismailza, IG., X-Ray Diffraction Study of Phase Transitions in Bismuth Ferrite. *DOKLADY AKADEMII NAUK SSSR* **1966**, *170*, 85-87.
66. Teague, J. R.; Gerson, R.; James, W. J., Dielectric Hysteresis in Single Crystal $BiFeO_3$. *Solid State Communications* **1970**, *8*, 1073-1074.
67. Kumar, M. M.; Palkar, V. R.; Srinivas, K.; Suryanarayana, S. V., Ferroelectricity in a Pure $BiFeO_3$ Ceramic. *Appl. Phys. Lett.* **2000**, *76*, 2764-2766.
68. Lebeugle, D.; Colson, D.; Forget, A.; Viret, M.; Bonville, P.; Marucco, J.-F.; Fusil, S., Room-Temperature Coexistence of Large Electric Polarization and Magnetic Order in $BiFeO_3$ Single Crystals. *Physical Review B* **2007**, *76*, 024116.

69. Neaton, J.; Ederer, C.; Waghmare, U.; Spaldin, N.; Rabe, K., First-Principles Study of Spontaneous Polarization in Multiferroic $BiFeO_3$. *Physical Review B: Condensed Matter and Materials Physics* **2005**, *71*, 014113.1-014113.8.
70. Ravindran, P.; Vidya, R.; Kjekshus, A.; Fjellvåg, H.; Eriksson, O., Theoretical Investigation of Magnetoelectric Behavior in $BiFeO_3$. *Physical Review B* **2006**, *74*, 224412.
71. Shvartsman, V.; Kleemann, W.; Haumont, R.; Kreisel, J., Large Bulk Polarization and Regular Domain Structure in Ceramic $BiFeO_3$. *Appl. Phys. Lett.* **2007**, *90*, 172115-172115.
72. Wang, J.; Neaton, J.; Zheng, H.; Nagarajan, V.; Ogale, S.; Liu, B.; Viehland, D.; Vaithyanathan, V.; Schlom, D.; Waghmare, U., Epitaxial $BiFeO_3$ Multiferroic Thin Film Heterostructures. *Science* **2003**, *299*, 1719-1722.
73. Kamba, S.; Nuzhnyy, D.; Savinov, M.; Šebek, J.; Petzelt, J.; Prokleška, J.; Haumont, R.; Kreisel, J., Infrared and Terahertz Studies of Polar Phonons and Magnetodielectric Effect in Multiferroic $BiFeO_3$ Ceramics. *Physical Review B* **2007**, *75*, 024403.
74. Megaw, H. D.; Darlington, C. N. W., Geometrical and Structural Relations in the Rhombohedral Perovskites. *Acta Crystallographica Section A* **1975**, *31*, 161-173.
75. Neaton, J. B.; Ederer, C.; Waghmare, U. V.; Spaldin, N. A.; Rabe, K. M., First-Principles Study of Spontaneous Polarization in Multiferroic $BiFeO_3$. *Physical Review B* **2005**, *71*, 014113.
76. Yang, C.-H.; Kan, D.; Takeuchi, I.; Nagarajan, V.; Seidel, J., Doping $BiFeO_3$: Approaches and Enhanced Functionality. *Physical Chemistry Chemical Physics* **2012**, *14*, 15953-15962.
77. Jacobson, A. J.; Fender, B. E. F., A Neutron Diffraction Study of the Nuclear and Magnetic Structure of $BiFeO_3$. *Journal of Physics C: Solid State Physics* **1975**, *8*, 844.
78. Catalan, G.; Sardar, K.; Church, N. S.; Scott, J. F.; Harrison, R. J.; Redfern, S. A. T., Effect of Chemical Substitution on the N\'Eel Temperature of Multiferroic $Bi_{1-x}Ca_xFeO_3$. *Physical Review B* **2009**, *79*, 212415.
79. Selbach, S. M.; Tybell, T.; Einarsrud, M. A.; Grande, T., Size-Dependent Properties of Multiferroic $BiFeO_3$ Nanoparticles. *Chem. Mat.* **2007**, *19*, 6478-6484.
80. Chen, P.; Xu, X.; Koenigsmann, C.; Santulli, A. C.; Wong, S. S.; Musfeldt, J. L., Size-Dependent Infrared Phonon Modes and Ferroelectric Phase Transition in $BiFeO_3$ Nanoparticles. *Nano Lett.* **2010**, *10*, 4526-4532.
81. Rubio-Marcos, F.; Del Campo, A.; Marchet, P.; Fernández, J. F., Ferroelectric Domain Wall Motion Induced by Polarized Light. *Nat Commun* **2015**, *6*.
82. Choi, W. S.; Chisholm, M. F.; Singh, D. J.; Choi, T.; Jellison Jr, G. E.; Lee, H. N., Wide Bandgap Tunability in Complex Transition Metal Oxides by Site-Specific Substitution. *Nature communications* **2012**, *3*, 689.
83. Kundys, B.; Viret, M.; Meny, C.; Da Costa, V.; Colson, D.; Doudin, B., Wavelength Dependence of Photoinduced Deformation in $BiFeO_3$. *Physical Review B* **2012**, *85*, 092301.
84. Nebel, C. E., Photocatalysis: A Source of Energetic Electrons. *Nature materials* **2013**, *12*, 780-781.
85. Qu, Y.; Duan, X., Progress, Challenge and Perspective of Heterogeneous Photocatalysts. *Chemical Society Reviews* **2013**, *42*, 2568-2580.
86. Bell, N. J.; Ng, Y. H.; Du, A.; Coster, H.; Smith, S. C.; Amal, R., Understanding the Enhancement in Photoelectrochemical Properties of Photocatalytically Prepared $TiO_2$-Reduced Graphene Oxide Composite. *The Journal of Physical Chemistry C* **2011**, *115*, 6004-6009.
87. Cui, Y.; Briscoe, J.; Dunn, S., Effect of Ferroelectricity on Solar-Light-Driven Photocatalytic Activity of $BiFeO_3$ Influence on the Carrier Separation and Stern Layer Formation. *Chem. Mat.* **2013**, *25*, 4215-4223.
88. Gao, F.; Chen, X.; Yin, K.; Dong, S.; Ren, Z.; Yuan, F.; Yu, T.; Zou, Z.; Liu, J.-M., Visible-Light Photocatalytic Properties of Weak Magnetic $BiFeO_3$ Nanoparticles. *ADVANCED MATERIALS-DEERFIELD BEACH THEN WEINHEIM-* **2007**, *19*, 2889.

89. Zhang, S.; Audebert, P.; Wei, Y.; Lauret, J.-S.; Galmiche, L.; Deleporte, E., Synthesis and Optical Properties of Novel Organic-Inorganic Hybrid Uv $(R\text{-}NH_3)_2$ $PbCl_4$ Semiconductors. *Journal of Materials Chemistry* **2011**, *21*, 466-474.
90. Deng, J.; Banerjee, S.; Mohapatra, S. K.; Smith, Y. R.; Misra, M., Bismuth Iron Oxide Nanoparticles as Photocatalyst for Solar Hydrogen Generation from Water. *Journal of Fundamentals of Renewable Energy and Applications* **2011**, *1*, 1-10.
91. Lou, X. W.; Wang, Y.; Yuan, C.; Lee, J. Y.; Archer, L. A., Template-Free Synthesis of $SnO_2$ Hollow Nanostructures with High Lithium Storage Capacity. *Advanced Materials* **2006**, *18*, 2325-2329.
92. Liu, Z.; Qi, Y.; Lu, C., High Efficient Ultraviolet Photocatalytic Activity of $BiFeO_3$ Nanoparticles Synthesized by a Chemical Coprecipitation Process. *Journal of Materials Science: Materials in Electronics* **2010**, *21*, 380-384.
93. Li, S.; Lin, Y.-H.; Zhang, B.-P.; Li, J.-F.; Nan, C.-W., $BiFeO_3/TiO_2$ Core-Shell Structured Nanocomposites as Visible-Active Photocatalysts and Their Optical Response Mechanism. *J. Appl. Phys.* **2009**, *105*, 054310-054310-5.
94. Li, D.; Zhao, M. H.; Garra, J.; Kolpak, A.; Rappe, A.; Bonnell, D.; Vohs, J., Direct in Situ Determination of the Polarization Dependence of Physisorption on Ferroelectric Surfaces. *nature materials* **2008**, *7*, 473-477.
95. Shin, J.; Nascimento, V. B.; Geneste, G.; Rundgren, J.; Plummer, E. W.; Dkhil, B.; Kalinin, S. V.; Baddorf, A. P., Atomistic Screening Mechanism of Ferroelectric Surfaces: An in Situ Study of the Polar Phase in Ultrathin $BiFeO_3$ Films Exposed to $H_2O$. *Nano Lett.* **2009**, *9*, 3720-3725.
96. Stock, M.; Dunn, S., Influence of the Ferroelectric Nature of Lithium Niobate to Drive Photocatalytic Dye Decolorization under Artificial Solar Light. *The Journal of Physical Chemistry C* **2012**, *116*, 20854-20859.
97. Inoue, Y., Photocatalytic Water Splitting by $RuO_2$-Loaded Metal Oxides and Nitrides with *d* 0-and *d* 10-Related Electronic Configurations. *Energy & Environmental Science* **2009**, *2*, 364-386.
98. Ji, W.; Yao, K.; Lim, Y.-F.; Liang, Y. C.; Suwardi, A., Epitaxial Ferroelectric $BiFeO_3$ Thin Films for Unassisted Photocatalytic Water Splitting. *Appl. Phys. Lett.* **2013**, *103*, 062901.
99. Stock, M.; Dunn, S., $LiNbO_3$ a New Material for Artificial Photosynthesis. *Ultrasonics, Ferroelectrics, and Frequency Control, IEEE Transactions on* **2011**, *58*, 1988-1993.
100. Hong, K.-S.; Xu, H.; Konishi, H.; Li, X., Piezoelectrochemical Effect: A New Mechanism for Azo Dye Decolorization in Aqueous Solution through Vibrating Piezoelectric Microfibers. *The Journal of Physical Chemistry C* **2012**, *116*, 13045-13051.
101. Clark, S. J.; Robertson, J., Band Gap and Schottky Barrier Heights of Multiferroic Bifeo3. *Appl. Phys. Lett.* **2007**, *90*, 132903.
102. Guo, R. Q.; Fang, L.; Dong, W.; Zheng, F. G.; Shen, M. R., Enhanced Photocatalytic Activity and Ferromagnetism in Gd Doped $BiFeO_3$ Nanoparticles. *J. Phys. Chem. C* **2010**, *114*, 21390-21396.
103. Lin, H.; Huang, C.; Li, W.; Ni, C.; Shah, S. I.; Tseng, Y.-H., Size Dependency of Nanocrystalline $TiO_2$ on Its Optical Property and Photocatalytic Reactivity Exemplified by 2-Chlorophenol. *Applied Catalysis B: Environmental* **2006**, *68*, 1-11.
104. Beydoun, D.; Amal, R.; Low, G.; McEvoy, S., Role of Nanoparticles in Photocatalysis. *Journal of Nanoparticle Research* **1999**, *1*, 439-458.
105. Xian, T.; Yang, H.; Dai, J. F.; Wei, Z. Q.; Ma, J. Y.; Feng, W. J., Photocatalytic Properties of $BiFeO_3$ Nanoparticles with Different Sizes. *Materials Letters* **2011**, *65*, 1573-1575.
106. Wei, J.; Li, H.; Mao, S.; Zhang, C.; Xu, Z.; Dkhil, B., Effect of Particle Morphology on the Photocatalytic Activity of $BiFeO_3$ Microcrystallites. *Journal of Materials Science-Materials in Electronics* **2012**, *23*, 1869-1874.

107. Morozov, M. I.; Lomanova, N. A.; Gusarov, V. V., Specific Features of $BiFeO_3$ Formation in a Mixture of Bismuth(iii) and Iron(iii) Oxides. *Russian Journal of General Chemistry* **2003**, *73*, 1676-1680.
108. Rojac, T.; Bencan, A.; Malic, B.; Tutuncu, G.; Jones, J. L.; Daniels, J. E.; Damjanovic, D., $BiFeO_3$ Ceramics: Processing, Electrical, and Electromechanical Properties. *Journal of the American Ceramic Society* **2014**, *97*, 1993-2011.
109. Zhang, X.; Zhang, D. L.; Wang, Y. H.; Miao, J.; Xu, X. G.; Jiang, Y., Dependence of Bifeo 3 Thickness on Exchange Bias in $BiFeO_3/CO_2$ Feal Multiferroic Structures. *Journal of Physics: Conference Series* **2011**, *263*, 012008.
110. Zhonghua, D.; Yukikuni, A., Electrical Properties of Multiferroic $BiFeO_3$ Ceramics Synthesized by Spark Plasma Sintering. *Journal of Physics D: Applied Physics* **2010**, *43*, 445403.
111. Hardy, A.; Gielis, S.; Van den Rul, H.; D'Haen, J.; Van Bael, M.; Mullens, J., Effects of Precursor Chemistry and Thermal Treatment Conditions on Obtaining Phase Pure Bismuth Ferrite from Aqueous Gel Precursors. *Journal of the European Ceramic Society* **2009**, *29*, 3007-3013.
112. Selbach, S. M.; Einarsrud, M. A.; Tybell, T.; Grande, T., Synthesis of $BiFeO_3$ by Wet Chemical Methods. *Journal of the American Ceramic Society* **2007**, *90*, 3430-3434.
113. Wang, Y.; Zhou, L.; Zhang, M.; Chen, X.; Liu, J.-M.; Liu, Z., Room-Temperature Saturated Ferroelectric Polarization in $BiFeO_3$ Ceramics Synthesized by Rapid Liquid Phase Sintering. *Appl. Phys. Lett.* **2004**, *84*, 1731-1733.
114. Matsumoto, K.; Yamaguchi, K.; Fujii, T.; Ueno, A., Preparation of Bismuth Substituted Yttrium Iron Garnet Powders by the Citrate Gel Process. *J. Appl. Phys.* **1991**, *69*, 5918-5920.
115. Gülgün, M. A.; Nguyen, M. H.; Kriven, W. M., Polymerized Organic-Inorganic Synthesis of Mixed Oxides. *Journal of the American ceramic society* **1999**, *82*, 556-560.
116. Babooram, K.; Ye, Z.-G., New Soft Chemical Routes to Ferroelectric $SrBi_2Ta_2O_9$. *Chem. Mat.* **2006**, *18*, 532-540.
117. Cushing, B. L.; Kolesnichenko, V. L.; O'Connor, C. J., Recent Advances in the Liquid-Phase Syntheses of Inorganic Nanoparticles. *Chemical reviews* **2004**, *104*, 3893-3946.
118. Rajamathi, M.; Seshadri, R., Oxide and Chalcogenide Nanoparticles from Hydrothermal Solvothermal Reactions. *Current Opinion in Solid State and Materials Science* **2002**, *6*, 337-345.
119. Komarneni, S.; Roy, R.; Li, Q., Microwave-Hydrothermal Synthesis of Ceramic Powders. *Materials Research Bulletin* **1992**, *27*, 1393-1405.
120. Suslick, K. S.; Price, G. J., Applications of Ultrasound to Materials Chemistry. *Annual Review of Materials Science* **1999**, *29*, 295-326.
121. Paraschiv, C.; Jurca, B.; Ianculescu, A.; Carp, O., Synthesis of Nanosized Bismuth Ferrite ($BiFeO_3$) by a Combustion Method Starting from $Fe(NO_3)_3{\cdot}9H_2O$-$Bi(NO_3)_3{\cdot}9H_2O$-Glycine or Urea Systems. *Journal of thermal analysis and calorimetry* **2008**, *94*, 411-416.
122. Selbach, S. M.; Einarsrud, M.-A.; Grande, T., On the Thermodynamic Stability of $BiFeO_3$. *Chem. Mat.* **2008**, *21*, 169-173.
123. Silva, J.; Reyes, A.; Esparza, H.; Camacho, H.; Fuentes, L., $BiFeO_3$: A Review on Synthesis, Doping and Crystal Structure. *Integrated Ferroelectrics* **2011**, *126*, 47-59.
124. Effect of a Site and B Site Doping on Structural, Thermal, and Dielectric Properties of $BiFeO_3$ Ceramics. *Journal of Alloys and Compounds* **2011**.
125. Effect of Ion Doping in Different Sites on the Morphology and Photocatalytic Activity of $BiFeO_3$ Microcrystals. *Journal of Alloys and Compounds* **2013**, *570*, 57.
126. Jiang, Q.-H.; Nan, C.-W.; Shen, Z.-J., Synthesis and Properties of Multiferroic La-Modified $BiFeO_3$ Ceramics. *Journal of the American Ceramic Society* **2006**, *89*, 2123-2127.
127. Schiemer, J.; Withers, R.; Noren, L.; Liu, Y.; Bourgeois, L.; Stewart, G., Detailed Phase Analysis and Crystal Structure Investigation of a $Bi_{1-X}Ca_XFeO_{3-X/2}$ Perovskite-Related Solid

Solution Phase and Selected Property Measurements Thereof. *Chem. Mat.* **2009**, *21*, 4223-4232.
128. Kothari, D.; Reddy, V. R.; Gupta, A.; Sathe, V.; Banerjee, A.; Gupta, S.; Awasthi, A., Multiferroic Properties of Polycrystalline $Bi_{1-X}Ca_XFeO_3$. *Appl. Phys. Lett.* **2007**, *91*, 202505.
129. Yang, C. H., et al., Electric Modulation of Conduction in Multiferroic Ca-Doped $BiFeO_3$ Films. *Nat Mater* **2009**, *8*, 485-493.
130. Petricek, V.; Dusek, M.; Palatinus, L., Crystallographic Computing System Jana2006: General Features. *Z. Kristall.* **2014**, *229*, 345-352.
131. Williamson, G. K.; Hall, W. H., X-Ray Line Broadening from Filed Aluminium and Wolfram. *Acta Metallurgica* **1953**, *1*, 22-31.
132. Hermet, P.; Goffinet, M.; Kreisel, J.; Ghosez, P., Raman and Infrared Spectra of Multiferroic Bismuth Ferrite from First Principles. *Physical Review B* **2007**, *75*, 220102.
133. Moskovits, M., Surface‐Enhanced Raman Spectroscopy: A Brief Retrospective. *Journal of Raman Spectroscopy* **2005**, *36*, 485-496.
134. Amer, M., *Raman Spectroscopy for Soft Matter Applications*; John Wiley & Sons, 2009.
135. Colthup, N., *Introduction to Infrared and Raman Spectroscopy*; Elsevier, 2012.
136. Long, D. A., Raman Spectroscopy. *New York* **1977**, 1-12.
137. Watts, J. F.; Wolstenholme, J., *An Introduction to Surface Analysis by XPS and AES,. 224. ISBN 0-470-84713-1. Wiley-VCH, May 2003.* **2003**, *1*.
138. Reimer, L., *Scanning Electron Microscopy: Physics of Image Formation and Microanalysis*; Springer, 1998.
139. Fultz, B.; Howe, J. M., *Transmission Electron Microscopy and Diffractometry of Materials*; Springer Science & Business Media, 2012.
140. Williams, D. B.; Carter, C. B., *The Transmission Electron Microscope*; Springer, 1996.
141. Wooten, F., *Optical Properties of Solids*; Academic press, 2013.
142. Pankove, J. I., *Optical Processes in Semiconductors*; Courier Corporation, 2012.
143. Kurik, M. V., Urbach Rule. *physica status solidi (a)* **1971**, *8*, 9-45.
144. Studenyak, I.; Kranjec, M.; Kurik, M., Urbach Rule in Solid State Physics. *International Journal of Optics and Applications* **2014**, *4*, 76-83.
145. Dexter, D. L., Interpretation of Urbach's Rule. *Phys. Rev. Lett.* **1967**, *19*, 1383-1385.
146. Ortiz-Quiñonez, J. L.; Díaz, D.; Zumeta-Dubé, I.; Arriola-Santamaría, H.; Betancourt, I.; Santiago-Jacinto, P.; Nava-Etzana, N., Easy Synthesis of High-Purity $BiFeO_3$ Nanoparticles: New Insights Derived from the Structural, Optical, and Magnetic Characterization. *Inorganic chemistry* **2013**, *52*, 10306-10317.
147. Ivanda, M.; Musić, S.; Popović, S.; Gotić, M., Xrd, Raman and Ft-Ir Spectroscopic Observations of Nanosized $TiO_2$ Synthesized by the Sol-Gel Method Based on an Esterification Reaction. *Journal of Molecular structure* **1999**, *480*, 645-649.
148. Bruno, J. A. J., Esterification Process. Google Patents: 1953.
149. Kao, C.-F.; Yang, W.-D., Preparation of Barium Strontium Titanate Powder from Citrate Precursor. **1999**.
150. WANG, W.; ZHOU, Y.; CHEN, S.; Ye, F.; JIA, D., Preparation of Strontium Bismuth Tantalum (SBT) Fine Powder by Sol-Gel Process Using Bismuth Subnitrate as Bismuth Source. *Journal of Materials Science and Technology, 2001, 17 (1):* **2001**.
151. Harris, J. M., *Poly (Ethylene Glycol) Chemistry: Biotechnical and Biomedical Applications*; Springer Science & Business Media, 2013.
152. Popa, M.; Crespo, D.; Calderon-Moreno, J. M.; Preda, S.; Fruth, V., Synthesis and Structural Characterization of Single Phase $BiFeO_3$ Powders from a Polymeric Precursor. *Journal of the American Ceramic Society* **2007**, *90*, 2723-2727.
153. Gonzalez, A.; Simões, A.; Cavalcante, L.; Longo, E.; Varela, J. A.; Riccardi, C., Soft Chemical Deposition of $BiFeO_3$ Multiferroic Thin Films. *Appl. Phys. Lett.* **2007**, 3.

154. Liu, T.; Xu, Y.; Feng, S.; Zhao, J., A Facile Route to the Synthesis of $BiFeO_3$ at Low Temperature. *Journal of the American Ceramic Society* **2011**, *94*, 3060-3063.
155. Wang, X.; Lin, Y.; Zhang, Z.; Bian, J., Photocatalytic Activities of Multiferroic Bismuth Ferrite Nanoparticles Prepared by Glycol-Based Sol-Gel Process. *Journal of sol-gel science and technology* **2011**, *60*, 1-5.
156. Dhir, G.; Lotey, G.; Uniyal, P.; Verma, N. K., Size-Dependent Magnetic and Dielectric Properties of Tb-Doped $BiFeO_3$ Nanoparticles. *Journal of Materials Science: Materials in Electronics* **2013**, *24*, 4386-4392.
157. Park, T.-J.; Papaefthymiou, G. C.; Viescas, A. J.; Moodenbaugh, A. R.; Wong, S. S., Size-Dependent Magnetic Properties of Single-Crystalline Multiferroic $BiFeO_3$ Nanoparticles. *Nano Lett.* **2007**, *7*, 766-772.
158. Marotta, A.; Buri, A., Kinetics of Devitrification and Differential Thermal Analysis. *Thermochimica Acta* **1978**, *25*, 155-160.
159. Matusita, K.; Tashiro, M., Effect of Added Oxides on Crystallization of $Li_2O$-$2SiO_2$ Glasses. *Physics and Chemistry of Glasses* **1973**, *14*, 77.
160. Matusita, K.; Sakka, S., Kinetic Study of the Crystallization of Glass by Differential Scanning Calorimetry. *Physics and Chemistry of Glasses* **1979**, *20*, 81.
161. Matusita, K.; Sakka, S.; Matsui, Y., Determination of the Activation Energy for Crystal Growth by Differential Thermal Analysis. *Journal of Materials Science* **1975**, *10*, 961-966.
162. Fine, M. E., *Introduction to Phase Transformations in Condensed Systems*; Macmillan, 1964.
163. Matusita, K.; Sakka, S., Study on Crystallization Kinetics in Glass by Differential Thermal Analysis. *Thermochimica Acta* **1979**, *33*, 351-354.
164. Kudo, A.; Niishiro, R.; Iwase, A.; Kato, H., Effects of Doping of Metal Cations on Morphology, Activity, and Visible Light Response of Photocatalysts. *Chemical Physics* **2007**, *339*, 104-110.
165. Qi, X.; Zhou, J.; Yue, Z.; Gui, Z.; Li, L., Auto-Combustion Synthesis of Nanocrystalline $LaFeO_3$. *Materials chemistry and physics* **2003**, *78*, 25-29.
166. Xiao, S. H.; Jiang, W. F.; Li, L. Y.; Li, X. J., Low-Temperature Auto-Combustion Synthesis and Magnetic Properties of Cobalt Ferrite Nanopowder. *Materials Chemistry and Physics* **2007**, *106*, 82-87.
167. Haile, S.; Staneff, G.; Ryu, K., Non-Stoichiometry, Grain Boundary Transport and Chemical Stability of Proton Conducting Perovskites. *Journal of Materials Science* **2001**, *36*, 1149-1160.
168. Buban, J.; Matsunaga, K.; Chen, J.; Shibata, N.; Ching, W.; Yamamoto, T.; Ikuhara, Y., Grain Boundary Strengthening in Alumina by Rare Earth Impurities. *Science* **2006**, *311*, 212-215.
169. Di, Z.; Chen, X.; Chen, J.; Xia, Y.; Pu, S., Suppressing the Field-Induced Agglomeration in the Magnetic Fluid by Doping the Nonmagnetic Particles. *Appl. Phys. Lett.* **2007**, *90*, 161129.
170. Chen, P. L.; Chen, I. W., Grain Growth in $CeO_2$: Dopant Effects, Defect Mechanism, and Solute Drag. *Journal of the American Ceramic Society* **1996**, *79*, 1793-1800.
171. Chen, P. L.; Chen, I. W., Grain Boundary Mobility in $Y_2O_3$: Defect Mechanism and Dopant Effects. *Journal of the American Ceramic Society* **1996**, *79*, 1801-1809.
172. Khomchenko, V.; Kiselev, D.; Vieira, J.; Jian, L.; Kholkin, A.; Lopes, A.; Pogorelov, Y.; Araujo, J.; Maglione, M., Effect of Diamagnetic Ca, Sr, Pb, and Ba Substitution on the Crystal Structure and Multiferroic Properties of the $BiFeO_3$ Perovskite. *J. Appl. Phys.* **2008**, 024105-024105-6.
173. Schiemer, J. A.; Withers, R. L.; Liu, Y.; Carpenter, M. A., Ca-Doping of $BiFeO_3$: The Role of Strain in Determining Coupling between Ferroelectric Displacements, Magnetic Moments, Octahedral Tilting, and Oxygen-Vacancy Ordering. *Chem. Mat.* **2013**, *25*, 4436-4446.

174. Lee, J.-H.; Choi, H. J.; Lee, D.; Kim, M. G.; Bark, C. W.; Ryu, S.; Oak, M.-A.; Jang, H. M., Variations of Ferroelectric Off-Centering Distortion and 3d-4p Orbital Mixing in La-Doped $BiFeO_3$ Multiferroics. *Physical Review B* **2010**, *82*, 045113.
175. Haumont, R.; Kornev, I. A.; Lisenkov, S.; Bellaiche, L.; Kreisel, J.; Dkhil, B., Phase Stability and Structural Temperature Dependence in Powdered Multiferroic $BiFeO_3$. *Physical Review B* **2008**, *78*, 134108.
176. Zhao, T.; Scholl, A.; Zavaliche, F.; Lee, K.; Barry, M.; Doran, A.; Cruz, M.; Chu, Y.; Ederer, C.; Spaldin, N., Electrical Control of Antiferromagnetic Domains in Multiferroic $BiFeO_3$ Films at Room Temperature. *Nature materials* **2006**, *5*, 823-829.
177. Palkar, V.; John, J.; Pinto, R., Observation of Saturated Polarization and Dielectric Anomaly in Magnetoelectric $BiFeO_3$ Thin Films. *Appl. Phys. Lett.* **2002**, *80*, 1628-1630.
178. Bielecki, J.; Svedlindh, P.; Tibebu, D. T.; Cai, S.; Eriksson, S.-G.; Börjesson, L.; Knee, C. S., Structural and Magnetic Properties of Isovalently Substituted Multiferroic $BiFeO_3$: Insights from Raman Spectroscopy. *Physical Review B* **2012**, *86*, 184422.
179. Haumont, R.; Kreisel, J.; Bouvier, P., Raman Scattering of the Model Multiferroic Oxide $BiFeO_3$: Effect of Temperature, Pressure and Stress (Vol 79, Pg 1043, 2006). *Phase Transit.* **2009**, *82*, 496-496.
180. Porporati, A. A.; Tsuji, K.; Valant, M.; Axelsson, A. K.; Pezzotti, G., Raman Tensor Elements for Multiferroic $BiFeO_3$ with Rhombohedral *R3c* Symmetry. *Journal of Raman Spectroscopy* **2010**, *41*, 84-87.
181. Hlinka, J.; Pokorny, J.; Karimi, S.; Reaney, I. M., Angular Dispersion of Oblique Phonon Modes in $BiFeO_3$ from Micro-Raman Scattering. *Physical Review B* **2011**, *83*, 020101.
182. Haumont, R.; Kreisel, J.; Bouvier, P.; Hippert, F., Phonon Anomalies and the Ferroelectric Phase Transition in Multiferroic $BiFeO_3$. *Physical Review B* **2006**, *73*, 132101.
183. Fukumura, H.; Matsui, S.; Harima, H.; Takahashi, T.; Itoh, T.; Kisoda, K.; Tamada, M.; Noguchi, Y.; Miyayama, M., Observation of Phonons in Multiferroic $BiFeO_3$ Single Crystals by Raman Scattering. *Journal of Physics: Condensed Matter* **2007**, *19*, 365224.
184. Beekman, C.; Reijnders, A. A.; Oh, Y. S.; Cheong, S. W.; Burch, K. S., Raman Study of the Phonon Symmetries in $BiFeO_3$ Single Crystals. *Physical Review B* **2012**, *86*, 020403.
185. Yang, Y.; Bai, L. G.; Zhu, K.; Liu, Y. L.; Jiang, S.; Liu, J.; Chen, J.; Xing, X. R., High Pressure Raman Investigations of Multiferroic $BiFeO_3$. *Journal of Physics: Condensed Matter* **2009**, *21*, 385901.
186. Haumont, R.; Kreisel, J.; Bouvier, P., Raman Scattering of the Model Multiferroic Oxide $BiFeO_3$: Effect of Temperature, Pressure and Stress. *Phase Transit.* **2006**, *79*, 1043-1064.
187. Andreasson, J.; Holmlund, J.; Rauer, R.; Käll, M.; Börjesson, L.; Knee, C. S.; Eriksson, A. K.; Eriksson, S.-G.; Rübhausen, M.; Chaudhury, R. P., Electron-Phonon Interactions in Perovskites Containing Fe and Cr Studied by Raman Scattering Using Oxygen-Isotope and Cation Substitution. *Physical Review B* **2008**, *78*, 235103.
188. Jarrier, R., et al., Surface Phase Transitions in $BiFeO_3$ Below Room Temperature. *Physical Review B* **2012**, *85*, 184104.
189. Martí, X.; Ferrer, P.; Herrero-Albillos, J.; Narvaez, J.; Holy, V.; Barrett, N.; Alexe, M.; Catalan, G., Skin Layer of $BiFeO_3$ Single Crystals. *Phys. Rev. Lett.* **2011**, *106*, 236101.
190. Chauhan, S.; Kumar, M.; Chhoker, S.; Katyal, S.; Singh, H.; Jewariya, M.; Yadav, K., Multiferroic, Magnetoelectric and Optical Properties of Mn Doped $BiFeO_3$ Nanoparticles. *Solid State Communications* **2012**, *152*, 525-529.
191. Gabbasova, Z. V.; Kuz'min, M. D.; Zvezdin, A. K.; Dubenko, I. S.; Murashov, V. A.; Rakov, D. N.; Krynetsky, I. B., $Bi_{1-X}R_xFeO_3$ (R=Rare Earth): A Family of Novel Magnetoelectrics. *Physics Letters A* **1991**, *158*, 491-498.
192. Khomchenko, V.; Kiselev, D.; Vieira, J.; Kholkin, A.; Sá, M.; Pogorelov, Y., Synthesis and Multiferroic Properties of $Bi_{0.8}A_{0.2}FeO_3$(A= Ca, Sr, Pb) Ceramics. *Appl. Phys. Lett.* **2007**, *90*.
193. Schmid, H., Multi-Ferroic Magnetoelectrics. *Ferroelectrics* **1994**, *162*, 317-338.

194. Pailloux, F.; Couillard, M.; Fusil, S.; Bruno, F.; Saidi, W.; Garcia, V.; Carrétéro, C.; Jacquet, E.; Bibes, M.; Barthélémy, A., Atomic Structure and Microstructures of Supertetragonal Multiferroic $BiFeO_3$ Thin Films. *Physical Review B* **2014**, *89*, 104106.
195. Mocherla, P. S. V.; Karthik, C.; Ubic, R.; Rao, M. S. R.; Sudakar, C., Tunable Bandgap in $BiFeO_3$ Nanoparticles: The Role of Microstrain and Oxygen Defects. *Appl. Phys. Lett.* **2013**, *103*.
196. Mills, P.; Sullivan, J., A Study of the Core Level Electrons in Iron and Its Three Oxides by Means of X-Ray Photoelectron Spectroscopy. *Journal of Physics D: Applied Physics* **1983**, *16*, 723.
197. Moulder, J. F.; Chastain, J.; King, R. C., *Handbook of X-Ray Photoelectron Spectroscopy: A Reference Book of Standard Spectra for Identification and Interpretation of XPS Data*; Perkin-Elmer Eden Prairie, MN, 1992.
198. Schedel-Niedrig, T.; Weiss, W.; Schlögl, R., Electronic Structure of Ultrathin Ordered Iron Oxide Films Grown onto Pt (111). *Physical Review B* **1995**, *52*, 17449.
199. Graat, P.; Somers, M. A., Quantitative Analysis of Overlapping XPS Peaks by Spectrum Reconstruction: Determination of the Thickness and Composition of Thin Iron Oxide Films. *Surface and interface analysis* **1998**, *26*, 773-782.
200. Brundle, C. R.; Chuang, T. J.; Wandelt, K., Core and Valence Level Photoemission Studies of Iron Oxide Surfaces and the Oxidation of Iron. *Surface Science* **1977**, *68*, 459-468.
201. Thery, J.; Dubourdieu, C.; Baron, T.; Ternon, C.; Roussel, H.; Pierre, F., Mocvd of $BiFeO_3$ Thin Films on $SrTiO_3$. *Chemical Vapor Deposition* **2007**, *13*, 232-238.
202. Yamashita, T.; Hayes, P., Analysis of XPS Spectra of $Fe^{2+}$ and $Fe^{3+}$ Ions in Oxide Materials. *Applied Surface Science* **2008**, *254*, 2441-2449.
203. Hoffmann, M. R.; Martin, S. T.; Choi, W.; Bahnemann, D. W., Environmental Applications of Semiconductor Photocatalysis. *Chemical reviews* **1995**, *95*, 69-96.
204. Vijayanand, S.; Mahajan, M.; Potdar, H.; Joy, P., Magnetic Characteristics of Nanocrystalline Multiferroic $BiFeO_3$ at Low Temperatures. *Physical Review B* **2009**, *80*, 064423.
205. Sankar, C. R.; Joy, P., Magnetic Properties of the Self-Doped Lanthanum Manganites $La_{1-X}$ $MnO_3$. *Physical Review B* **2005**, *72*, 024405.
206. Blaauw, C.; Van der Woude, F., Magnetic and Structural Properties of $BiFeO_3$. *Journal of Physics C: Solid State Physics* **1973**, *6*, 1422.
207. Zener, C., Interaction between the d-Shells in the Transition Metals. Iv. The Intrinsic Antiferromagnetic Character of Iron. *Physical Review* **1952**, *85*, 324-328.
208. Sherman, D. M., The Electronic Structures of $Fe^{3+}$ Coordination Sites in Iron Oxides: Applications to Spectra, Bonding, and Magnetism. *Physics and Chemistry of Minerals* **1985**, *12*, 161-175.
209. Ferguson, J.; J. Guggenheim, H.; Tanabe, Y., The Effects of Exchange Interactions in the Spectra of Octahedral Manganese. II. Compounds. *Journal of the Physical Society of Japan* **1966**, *21*, 692-704.
210. Krebs, J.; Maisch, W., Exchange Effects in the Optical-Absorption Spectrum of $Fe^{3+}$ in $Al_2O_3$. *Physical Review B* **1971**, *4*, 757.
211. Lohr, L. L., Spin-Forbidden Electronic Excitations in Transition Metal Complexes. *Coordination Chemistry Reviews* **1972**, *8*, 241-259.
212. Sherman, D. M.; Waite, T. D., Electronic Spectra of $Fe^{3+}$ Oxides and Oxide Hydroxides in the near Ir to near Uv. *American Mineralogist* **1985**, *70*, 1262-1269.
213. Schugar, H. J.; Rossman, G. R.; Thibeault, J.; Gray, H. B., Simultaneous Pair Electronic Excitations in a Binuclear Iron (Iii) Complex. *Chemical Physics Letters* **1970**, *6*, 26-28.
214. Galuza, A.; Beznosov, A.; Eremenko, V., Optical Absorption Edge in alpha-$Fe_2O_3$ the Exciton-Magnon Structure. **1998**.
215. Wendlandt, W. W.; Hecht, H. G., *Reflectance Spectroscopy*; Interscience New York, 1966; Vol. 80.

216. Xu, X.; Brinzari, T.; Lee, S.; Chu, Y.; Martin, L.; Kumar, A.; McGill, S.; Rai, R.; Ramesh, R.; Gopalan, V., Optical Properties and Magnetochromism in Multiferroic $BiFeO_3$. *Physical Review B* **2009**, *79*, 134425.
217. Kumar, A.; Rai, R. C.; Podraza, N. J.; Denev, S.; Ramirez, M.; Chu, Y.-H.; Martin, L. W.; Ihlefeld, J.; Heeg, T.; Schubert, J., Linear and Nonlinear Optical Properties of $BiFeO_3$. *Appl. Phys. Lett.* **2008**, *92*, 121915-121915-3.
218. Ramachandran, B.; Dixit, A.; Naik, R.; Lawes, G.; Rao, M. R., Charge Transfer and Electronic Transitions in Polycrystalline $BiFeO_3$. *Physical Review B* **2010**, *82*, 012102.
219. Seeger, K., *Semiconductor Physics: An Introduction*; Springer Science & Business Media, 2013; Vol. 40.
220. Ramirez, M.; Kumar, A.; Denev, S.; Podraza, N.; Xu, X.; Rai, R.; Chu, Y.; Seidel, J.; Martin, L.; Yang, S.-Y., Magnon Sidebands and Spin-Charge Coupling in Bismuth Ferrite Probed by Nonlinear Optical Spectroscopy. *Physical Review B* **2009**, *79*, 224106.
221. Chen, P.; Podraza, N.; Xu, X.; Melville, A.; Vlahos, E.; Gopalan, V.; Ramesh, R.; Schlom, D.; Musfeldt, J., Optical Properties of Quasi-Tetragonal $BiFeO_3$ Thin Films. *Appl. Phys. Lett.* **2010**, *96*, 131907-131907-3.
222. Pisarev, R.; Moskvin, A.; Kalashnikova, A.; Rasing, T., Charge Transfer Transitions in Multiferroic $BiFeO_3$ and Related Ferrite Insulators. *Physical Review B* **2009**, *79*, 235128.
223. Palai, R.; Katiyar, R.; Schmid, H.; Tissot, P.; Clark, S.; Robertson, J.; Redfern, S.; Catalan, G.; Scott, J., B Phase and Γ-B Metal-Insulator Transition in Multiferroic $BiFeO_3$. *Physical Review B* **2008**, *77*, 014110.
224. Gómez-Salces, S.; Aguado, F.; Rodríguez, F.; Valiente, R.; González, J.; Haumont, R.; Kreisel, J., Effect of Pressure on the Band Gap and the Local $FeO_6$ Environment in $BiFeO_3$. *Physical Review B* **2012**, *85*, 144109.
225. Sattler, K.; Nalwa, H., Handbook of Thin Films Materials. *Nanomaterials and Magnetic Thin Films* **2002**, *5*.
226. Kayanuma, Y., Quantum-Size Effects of Interacting Electrons and Holes in Semiconductor Microcrystals with Spherical Shape. *Physical Review B* **1988**, *38*, 9797-9805.
227. Nosaka, Y., Finite Depth Spherical Well Model for Excited States of Ultrasmall Semiconductor Particles: An Application. *The Journal of Physical Chemistry* **1991**, *95*, 5054-5058.
228. Palewicz, A.; Przenioslo, R.; Sosnowska, I.; Hewat, A. W., Atomic Displacements in $BiFeO_3$ as a Function of Temperature: Neutron Diffraction Study. *Acta Crystallographica Section B* **2007**, *63*, 537-544.
229. Weber, M. C.; Guennou, M.; Toulouse, C.; Cazayous, M.; Gillet, Y.; Gonze, X.; Kreisel, J., Temperature Evolution of the Band-Gap in $BiFeO_3$ Traced by Resonant Raman Scattering. *arXiv preprint arXiv:1510.03754* **2015**.
230. Basu, S.; Martin, L.; Chu, Y.; Gajek, M.; Ramesh, R.; Rai, R.; Xu, X.; Musfeldt, J., Photoconductivity in $BiFeO_3$ Thin Films. *Appl. Phys. Lett.* **2008**, *92*, 091905.
231. Clark, S. J.; Robertson, J., Energy Levels of Oxygen Vacancies in $BiFeO_3$ by Screened Exchange. *Appl. Phys. Lett.* **2009**, *94*, 022902.
232. Wang, Y.; Zhou, L.; Zhang, M.; Chen, X.; Liu, J.; Liu, Z., Room-Temperature Saturated Ferroelectric Polarization in $BiFeO_3$ Ceramics Synthesized by Rapid Liquid Phase Sintering. *Appl. Phys. Lett.* **2004**, *84*, 1731-1733.
233. Benfang, Y.; Meiya, L.; Jun, L.; Dongyun, G.; Ling, P.; Xingzhong, Z., Effects of Ion Doping at Different Sites on Electrical Properties of Multiferroic $BiFeO_3$ Ceramics. *Journal of Physics D: Applied Physics* **2008**, *41*, 065003.
234. Pokatilov, V. S.; Sigov, A. S.; Konovalova, A. O., NMR and Mössbauer Study of Multiferroic $BiFeO_3$. *Bull. Russ. Acad. Sci. Phys.* **2010**, *74*, 347-351.
235. Marusak, L. A.; Messier, R.; White, W. B., Optical Absorption Spectrum of Hematite, alpha-$Fe_2O_3$ near Ir to Uv. *Journal of Physics and Chemistry of Solids* **1980**, *41*, 981-984.

236. Cheng, Z.; Li, A.; Wang, X.; Dou, S. X.; Ozawa, K.; Kimura, H.; Zhang, S.; Shrout, T. R., Structure, Ferroelectric Properties, and Magnetic Properties of the La-Doped Bismuth Ferrite. **2008**.
237. Xian, T.; Yang, H.; Dai, J. F.; Wei, Z. Q.; Ma, J. Y.; Feng, W. F., Photocatalytic Properties of $BiFeO_3$ Nanoparticles with Different Sizes. *Materials Letters* **2011**, *65*, 1573-1575.
238. Li, S.; Lin, Y.-H.; Zhang, B.-P.; Wang, Y.; Nan, C.-W., Controlled Fabrication of $BiFeO_3$ Uniform Microcrystals and Their Magnetic and Photocatalytic Behaviors. *The Journal of Physical Chemistry C* **2010**, *114*, 2903-2908.
239. Martí, X.; Ferrer, P.; Herrero-Albillos, J.; Narvaez, J.; Holy, V.; Barrett, N.; Alexe, M.; Catalan, G., Skin Layer of $BiFeO_3$ Single Crystals. *Phys. Rev. Lett.* **2011**, *106*, 236101.